Number: 20
Redalyc 3.0
ESCI Web of science
UNIVERSIDAD POLITÉCNICA SALESIANA ECUADOR
pISSN : 1390-650X
eISSN : 1390-860X
july / december 2018

INGENIUS

Revista de Ciencia y Tecnología

Ingenius

Ingenius • Número 20 • july/december 2018. Semester Journal of Science and Tecnology of the Universidad Politécnica Salesiana of Ecuador. Publication dedicated to studies related to the Sciences of Mechanical Engineering, Electrical Engineering, Electronic Engineering, Mechatronic Engineering, Systems Engineering and Industrial Engineering.

Reviewers board

Editorial

Editorial Abya Yala (Quito-Ecuador),
Av. 12 de octubre N422 y Wilson,
Bloque A, UPS Quito, Ecuador.
Casilla 17-12-719 Telfonos: (593-2) 3962800 ext. 2638
email: editorial@abyayala.org

Translator

Valentina Bravo

Tiraje: 800 ejemplares

Typographic system used in the composition of this document LaTeX.

Ingenius

Journal of Science and Technology

Número 20, july – december 2018

ISSN impreso 1390-650X / ISSN electrónico 1390-860X

The administration of the journal is done through the following parameters:

The journal uses the academic anti-plagiarism system

The articles have an identification code (Digital Object Identifier)

The editorial process is managed through the Open Journal System

The articles of the present edition can be consulted in
http://revistas.ups.edu.ec/index.php/ingenius

Universidad Politécnica Salesiana del Ecuador

INGENIUS Journal, is indexed in the following Databases and scientific information systems:

SELECTIVE DATABASES

REVIEWS EVALUATION PLATFORMS

SELECTIVE DIRECTORIES

SELECTIVE SERIAL LIBRARY

SCIENTIFIC LITERATURE SEARCHERS OPEN ACCESS

OTHER BIBLIOGRAPHICAL DATABASES

CATALOG OF INTERNATIONAL UNIVERSITY LIBRARIES

Editorial

Dear readers:

The responsibility and ethics involved in editorial work have led the INGENIUS Journal team to strengthen the aspects that allow readers, authors and reviewers to interact in a relevant, objective and agile way. This approach favors an integrated work model, making it possible to improve the quality of the contributions and their diffusion.

From March onwards, the entire journal has been migrated to the OJS 3.0 system (Open Journal Systems). This was accomplished through an efficient process, without loss of data and minimizing errors in the presentation of previous issues. The changes generated with this version provide the user with a new, more agile and simplified interface: a fluid, time effective communication with the editorial team. The system presents a new software architecture, with new security features which make it modern and efficient. The new layout allows the readers to have an improved reading experience, making it easier to access and download all documents, and providing statistics for each publication.

Another key aspect that reaffirms the journal's commitment to quality is the integration to REDALYC (Network of Scientific Journals of Latin America and the Caribbean, Spain and Portugal). As stated on their website: «The concrete proposal of redalyc.org materializes in the creation, design and maintenance of an open access online scientific information system, which functions as a meeting point for all who are interested in reconstructing the scientific knowledge of and about Latin America. The web portal, which is the most visible part of this effort, was formally launched to the public during the first quarter of 2003, as part of an initiative derived from a group of researchers and editors concerned about the low visibility of the research results generated in and about the region».

As part of the efforts to continue moving forward, the journal has also been indexed in the Emerging Source Citation Index (ESCI), a database of all journals being evaluated for inclusion in the Web of Science Core Collections: Science Citation Index (SCIE), Social Science Citation Index (SSCI) and Arts & Humanities Citation Index (AHCI). The objective of this index is to contribute to visibility and citation, and to favor a transparent selection process.

In addition, from this issue onward, the journal will be completely published in two languages, Spanish and English. This will increase the number of readers and authors, and will enable greater coverage in the dissemination of research papers published in INGENIUS.

The work carried out by all members of the journal's team has begun to bear fruit, leading to an increased number of submissions and to greater geographical diversification, as can be seen in this issue which includes participants from Mexico, Brazil, Argentina, and Ecuador.

John Calle Sigüencia, MSc

EDITOR IN CHIEF

Contents

Scientific Paper / Artículo Científico

UNIVERSIDAD POLITÉCNICA SALESIANA ECUADOR
INGENIUS
Revista de Ciencia y Tecnología
https://doi.org/10.17163/ings.n20.2018.01
pISSN: 1390-650X / eISSN: 1390-860X

Implementation of an algorithm for Ecuadorian traffic sign detection: Stop, Give-way and Velocity cases

Implementación de un algoritmo para la detección de señales de tránsito del Ecuador: Pare, Ceda el paso y Velocidad

Marco Flores-Calero[1,2,*], Cristian Conlago[3], Jhonny Yunda[3],
Milton Aldás[4], Carlos Flores[5]

Abstract

This paper presents a system prototype for traffic sign detection (SDST) on-board a moving vehicle. Therefore, a new approach to the development of an SDST is presented, using the following innovations: i) an efficient method of color segmentation for regions of interest (ROIs) generation based on k-NN with , ii) a new version of the HOG descriptor for feature extraction and iii) SVM training for stage multi-classification. The proposed approach has been specialized and tested on a subset of Regulatory (Stop, Give-way and Velocity) Ecuadorian signs. Many experiments have been carried out in real driving conditions, under different lighting changes such as normal, sunny and cloudy. This system has showed a global performance of 98.7% for segmentation, 99.49% for classification and an accuracy of 96% for detection.

Keywords: Accidents, Ecuador, HOG, $k-NN$, $K_m-means$, SVM, Traffic sign, Stop, Give way, Velocity.

Resumen

Este artículo presenta un prototipo de un sistema embarcado en un vehículo para la detección de señales de tránsito (SDST). Por lo tanto, un nuevo enfoque para la construcción de un SDST se presenta usando las siguientes innovaciones, i) un método eficiente de segmentación por color para la generación de regiones de interés (ROI) basado en los algoritmos $k-NN$, $K_m-means$ con , ii) una nueva versión del descriptor HOG para la extracción de características, y iii) el entrenamiento del algoritmo SVM no-lineal para multiclasificación. El enfoque propuesto ha sido probado sobre un subconjunto de las señales de tránsito ecuatorianas de regulación (Pare, Ceda el paso y Velocidad). Varios experimentos han sido desarrollados en condiciones reales de conducción en varias ciudades ecuatorianas, bajo tres condiciones de iluminación: normal, soleado y nublado. Este sistema ha mostrado un desempeño global del 98,7 % para la segmentación, 99,49 % para la clasificación y una precisión global del 96 % en la detección.

Palabras clave: Accidentes, Ecuador, HOG, $k-NN$, $K_m-means$, señales de tránsito, SVM, Pase, Ceda el paso, Velocidad.

[1,*]Department of Electrics and Electronics, Universidad de las Fuerzas Armadas-ESPE. Sangolquí – Ecuador
Author for correspondence ✉: mjflores@espe.edu.ec, http://orcid.org/0000-0001-7507-3325
[2]Departamento de Sistemas Inteligentes, Tecnologías I&H. Latacunga, Ecuador.
[3]Electronic Engineering, Automation and Control Major, Universidad de las Fuerzas Armadas-ESPE
http://orcid.org/0000-0002-7772-5259, http://orcid.org/0000-0003-0498-9656
[4]Faculty of Civil and Mechanical Engineering, Universidad Técnica de Ambato, Ambato – Ecuador.
http://orcid.org/0000-0003-2726-4092
[5]Traffic Accident Investigation Service (SIAT), Policía Nacional del Ecuador, Latacunga – Ecuador.
http://orcid.org/0000-0003-2131-6883

Received: 02-04-2018, accepted after review: 21-05-2018

Suggested citation: Flores-Calero, M.; Conlago, C.; Yunda, J.; Aldás, M. y Flores, C. (2018). «Implementation of an algorithm for Ecuadorian traffic sign detection: Stop, Give-way and Velocity cases». Ingenius. N.°20, (july-december). pp. 9-20. doi: https://doi.org/10.17163/ings.n20.2018.01.

1. Introduction

1.1. Notation

The notation used throughout this article is presented in Table 1.

Table 1. Notation

Name	Acronym
K-nearest neigborhood	k-NN
Partitioning method in K m means	K m -means
Support Vector Machine	SVM
Principal Component Analysis	PCA
Support Vector Regression	SVR
Convolutional Neural Network	CNN
Extreme Learning Machine	ELM
Multi-Layer Perceptron	MLP
Adaptive Boosting	Adaboost
Histogram of Oriented Gradient	HOG
Pyramidal Histogram of Oriented Gradient	PHOG
Aggregate Channel Features	ACF
Speeded Up Robust Features	SURF
Integral Channel Features	ICF
Discrimiative Codeword Selection	DSC
Region Of Interest	ROI
Color space Red, Green, Blue	RGB
Luminance color space, with chrominance Cb and Cr	YCbCr
Luminance color space, a* between red and green and b* between yellow and blue	L*a*b*
Color space Hue, Saturation, Intensity	HIS
Color space Hue, Saturation, Value	HSV
Receiver Operating Characteristic	ROC
Area under a ROC curve	AUC
Traffic sign detection systems	TSDS

1.2. Motivation

The purpose of traffic signs is to help the orderly and safe movement of actors, allowing a continuous flow of both vehicle and pedestrian traffic. Each of these signals presents instructions, which provide information about routes, destinations, points of interest, prohibitions, alerts, etc. These signals must be respected by all road users in order to avoid unexpected and unfortunate accidents, and above all, have a reliable and safe circulation [1]. The risk of an adult pedestrian dying after being hit by a car is less than 20% at a speed of 50 km/h, and about 60% at 80 km/h, so it is essential for drivers to take into account the speed established by traffic signs [2].

Currently, Ecuador has the best road network in South America [3]. This includes regulatory Stop, Give-way and Speed traffic signs at the intersections of roads, roundabouts and access points through secondary roads. Despite this important road infrastructure, Ecuador exceeds the death rate in traffic accidents by 3.14% with respect to the average of other Andean countries. Thus, traffic accidents are a constant problem, due to several critical factors, such as the imprudence of drivers when driving with excessive speed and not respecting traffic signs [4]. In 2015, 13.75% of all traffic accidents happened at road intersections [5], generating 8.14% of deaths under this type of mishap. On the other hand, an adult pedestrian has less than a 20% chance of dying if he is struck by a car at less than 50 km/h, but almost a 60% risk of dying if they are hit at 80 km/h [2].

TSDSs are of increasing importance [6, 7] because they can help in the prevention and reduction of traffic accidents [8]. However, these systems are still far from perfect, and must be specialized by country, adapted to the particularities of the transit signage design of each nation [9].

Therefore, this research presents a TSDS specialized in three types of traffic signs from Ecuador, which are the Stop, Give-way and Speed signs. Being able to detect them is important because it allows the driver to be alerted that they will cross an area with a high potential for collision with another vehicle. In the case of the Stop disk, the driver must stop completely; in the case of Give-way, the driver must become vigilant, and in the case of Speed the driver must respect the speed limits of 50 km/h and 100 km/h in urban and motorway zones, respectively. The speed signal of 50 km/h is the most common daily limit in urban environments, and 100 km/h is the most common on motorways.

For the implementation of TSDS, modern techniques of computer vision and artificial intelligence have been used to cover all cases that arise while driving during the day, such as: variability of lighting, partial occlusion and deterioration of signals. The document is organized as follows: the second section corresponds to the previous works regarding the detection of traffic signs. Section three presents a new system for the detection of traffic signs for the case of the Ecuadorian traffic signs of Stop, Give-way and Speed. Then, the next section shows the experimental results in real driving conditions. Finally, the last part is dedicated to conclusions and future work.

2. Materials and methods

2.1. Previous works

For the development of systems for automatic detection of traffic signs, the problem is usually divided into two parts, segmentation and recognition/classification [10].

a) In the case of segmentation, one of the predominant characteristics in the visible spectrum, is color, where color spaces and different computer vision techniques have been used to generate regions with a high possibility of containing a traffic sign. Such is the case that most of the techniques based on color seek to be robust against

the variations of lighting during the day, in different scenarios such as sunny, cloudy, etc. Thus, Salti et al. [11] have used three color spaces derived from RGB, the first to highlight traffic signs with predominance of blue and red colors, the second for signals with intense red and the third for bright blues. Li et al. [12] have constructed a space where the objects dominated by the blue-yellow and green-red colors stand out, on which, using the K-means clustering algorithm [13] they construct a color classification method for the generation of ROI. Nguyen et al. [6] have used the HSV space with several thresholds to generate a set of ROI looking for red and blue colors. Lillo et al. [14] have used the L*a*b* spaces and HSI to detect signals where the colors red, white and yellow predominate, using the components a* and b* to build a classifier for these colors. Chen and Lu [15] have used multiresolution and AdaBoost techniques to merge two sources of information, visual and spatial localization; in the visual they construct two color spaces based on RGB called outgoing color maps, in spatial they have used the gradient with different orientations. Finally, Han et al. [16] have used the H component of the HSI space, to generate an interval where the traffic signs stand out, and to construct a gray image where the ROIs are located. Villalón et al. [17] have implemented a filter using the normalized RGB color space, on which, by calculating statistical parameters, they have generated the red regions and thus have obtained the ROI.

b) In the recognition/classification scenario, some methods have been used for the extraction of characteristics in conjunction with a learning-machine algorithm [18–20], in order to classify and recognize the different types of signals. This stage is divided into two parts: i) method of extracting characteristics and, ii) choice of classification algorithm. In the first case there is a wide variety of proposals. Thus, Salti et al. [11], Huang et al. [21], Shi and Li [22] have used the descriptor HOG [23] with three variants specialized in traffic signs. Li et al. [12] have used the PHOG descriptor, which is a variation of HOG in a pyramidal scheme. Lillo et al. [14] have implemented feature extraction using the discrete Fourier transform. Han et al. [16] have used the SURF method [24]. Chen and Lu [15] used iterative DSC for the generation of the feature vector. Mongoose et al. [9] jointly implemented ICF and ACF to generate the characteristics. Pérez et al. [10] have used the PCA technique for the reduction of the dimension and the choice of dominant characteristics. Finally, Lau et al. [25] have used a weighting of neighboring pixels to highlight the characteristics of the object of interest. In the second question, the preferred algorithms are: SVM [13, 20], used in the works of Salti et al. [11], Li et al. [12], Lillo et al. [14] and Shi and Li [26]. SVR used in Chen and Lu [15], [20] implemented in the investigations of Han et al. [16] Artificial neural networks, used by Huang et al. [21] with the ELM case and Pérez et al. [10] with the MLP implementation. Adaboost with decision trees used in the work of Mogelmose et al. [9] Villalón et al. [17] have developed a statistical template based on a probability-adjusted model on the normalized YCbCr and RGB spaces. In recent years, the techniques based on deep learning are gaining more importance, so much so that CNN and its variations are used for automatic classification, where the vector of characteristics is extracted without direct human intervention. Such is the case of the works of Lau et al. [25], Zhu et al. [27] and Zuo et al. [28]

c) Regarding the traffic sign databases, it can be mentioned that each country has its own regulations in terms of signaling, divided into the categories of information, mandatory, prohibitive and warning [9,11,14,15,27]. At present, the main databases present in the bibliography correspond to countries such as Germany [10, 21], Italy [11], Spain [14], Japan [6], United States [9], Sweden [27], Malaysia [25]; an isolated case is that of Chile [17]. This bibliographic review demonstrates that there is no important, and even less reliable, information from developing countries, as is the case of Ecuador, with respect to the traffic sign data bases; this generates a challenge to raise this type of information, which must also be relevant to ensure road safety and maintenance of road infrastructure.

2.2. Methods for the construction of the traffic sign detection system

The scheme of the system proposed in this research is presented in Figure 1, which shows the segmentation (location) and recognition (classification) stages. In the segmentation process, a set of ROI is generated, which will then be sent to the classification stage for recognition. This proposal only works in the restricted case of the Stop, Give-way and Speed of 50 km/h and 100 km/h traffic signs. These signs have the color red in common, and belong to the prohibition type.

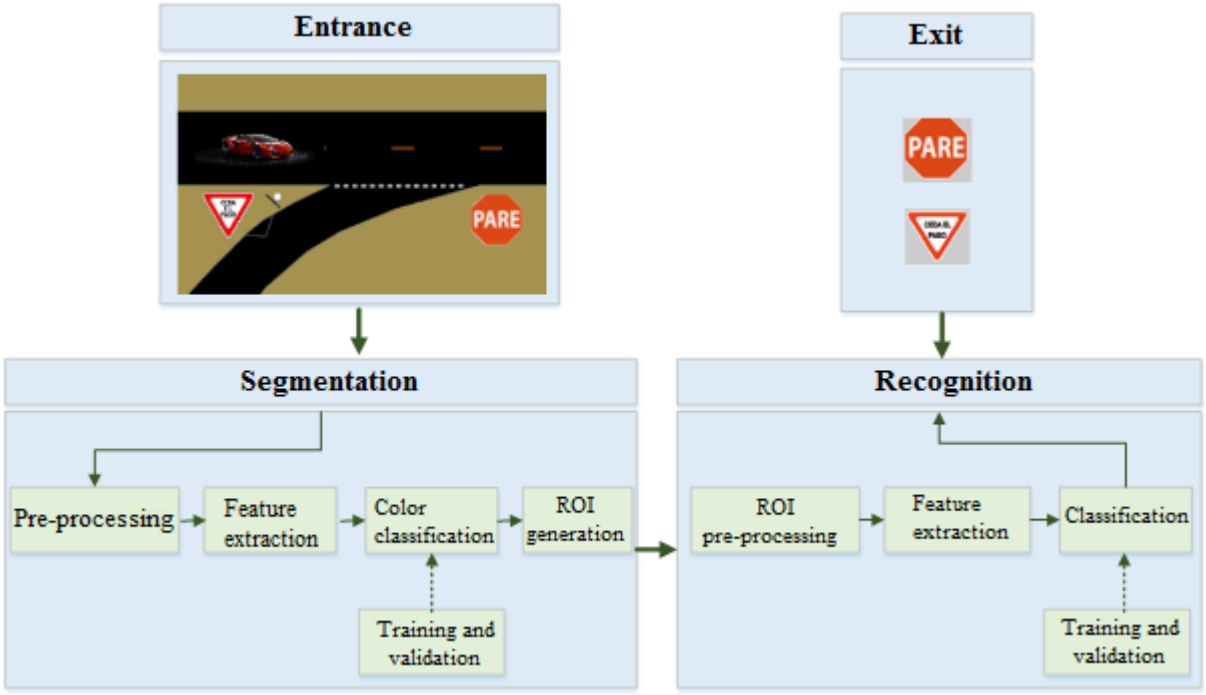

Figure 1. Proposed scheme for the location and recognition of traffic signs at road intersections in Ecuador in the visible spectrum, for the Stop and Give-way cases; and its subsequent extension to the case of Speed at 50 km/h and 100 km/h.

2.2.1. Segmentation by color and ROI generation

Figure 1 (left) shows the segmentation scheme described below.

Segmentation is done by discriminating the red color of the background from the rest of the colors. Experimentally, the RGBN color space has been chosen because it has a more compact distribution in the channels B_n and G_n, whose values are within the and intervals, respectively. Figure 2a shows the distribution of the red color according to normal, sunny and dark lighting conditions. Figure 2b show the distributions of the classes, where red represents the interest class and blue identifies the non-interest class.

1) **1) Representative points in space B_n and G_n:** To generate a small number of representative points of each class, the grouping algorithm K_m-means is used [19]; in this way, K_m centroids for each of the classes are obtained. The efficient value of K_m has been determined experimentally using the methods of Calinski-Harabasz [29], Davies-Bouldin [30], Gap [31] and Silhouettes [32], obtaining the following values, 30 and 40 for the red and not red (other colors) classes, respectively. Figure 2b shows the centroids of the two classes generated with K_m. To generate this figure, samples have been used in three lighting conditions: sunny, normal and dark.

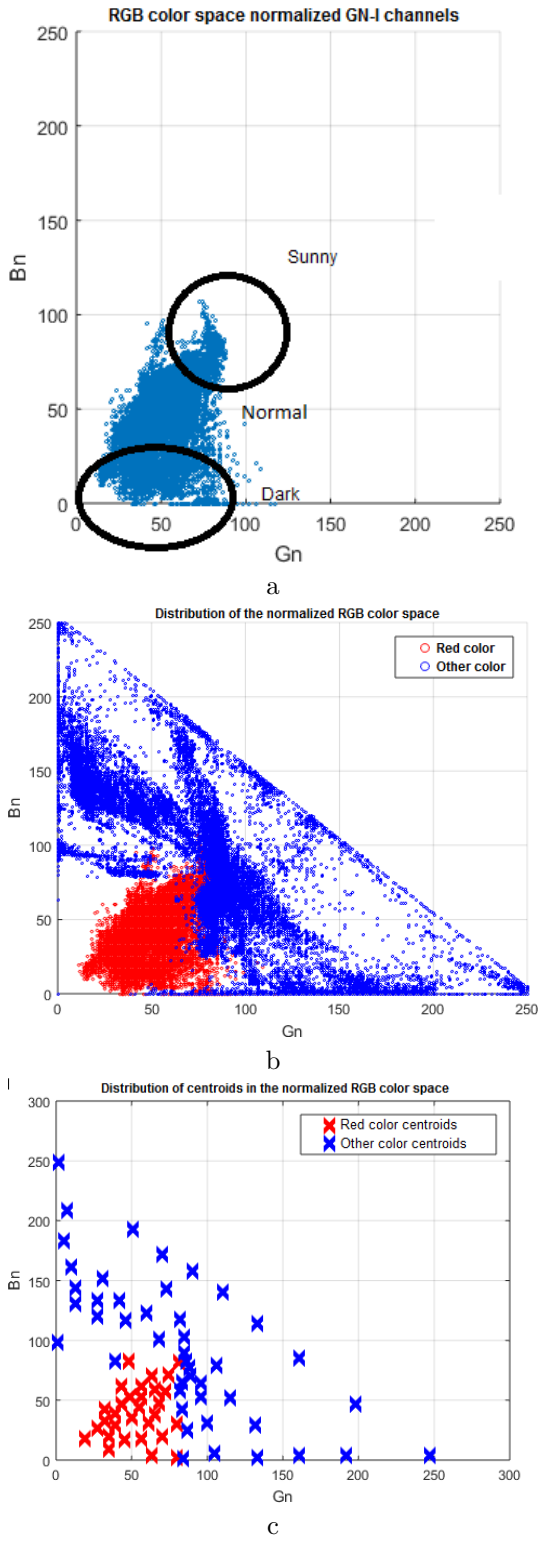

Figure 2. Color distribution in the normalized RGB space B_n and G_n, (a) distribution according to lighting conditions, (b) representation of the interest and non-interest classes, (c) graph of the centroids generated with $K_m - means$.

2) **2) Classifier design based on** $k - NN$**:** To design this classifier it is important to choose an adequate value of to allow the improvement of discrimination between the interest classes and the background. In this sense, the value of the area under the curve, known as the AUC index, of the ROC curve [33] has been used. The values used for this procedure are between 1 and 8. Table 2 shows the results to choose the best value for k.

Table 2. Choice of the K parameter in K- NN

k	**1**	**2**	**3**	**4**
AUC	0.985	0.931	0.986	0.987
k	**5**	**6**	**7**	**8**
AUC	0.985	0.983	0.982	0.983

3) **Post-processing of bodies:** Afterwards, using the morphological operators of dilation and erosion [26], certain bodies that do not meet specific size characteristics are eliminated as candidates for traffic signs. Experimental has set several thresholds for this procedure.

4) **Geometric constraints:** Finally, the bodies that do not fulfill the height/width relation are eliminated, using thresholds determined experimentally; Table 3 shows the necessary parameters as a function of the reference distance. This distance is part of the collision risk zone of a vehicle.

Table 3. Geometric characteristics that a ROI must fulfill over an image of 640 × 480 size depending on the reference distance

Characteristic	**Minimum value**	**Maximum value**
Area	400 pixels	10000 pixels
Width/height ratio	0,6	1,4
Reference distance	20 meters	5 meters

2.2.2. Recognition of traffic signs

In this stage, the ROIs coming from the segmentation stage are classified to determine if they correspond to a Stop, Give-way or Speed sign, or to another object that is not of interest.

Figure 1 (right) shows the recognition scheme, which consists of the following parts:

1) **Preprocessing of candidates:** The images corresponding to the gray scale ROI are transformed, then they are normalized to a size of 32×32 pixels and then the histogram equalization is performed

to obtain an image with a uniform distribution of gray levels. This process allows for an increase in the contrast of the image and a reduction of abrupt illumination changes.

2) **Feature extraction:** A new version of the HOG descriptor [34] is used to find the representative characteristics of a traffic sign. The innovation developed on this descriptor focuses on varying the size of the cells and the orientations, and finding the best combination adapted to the traffic signs. In this sense, the cells take values of 2×2, 4×4, 8×8 and 16×16 pixels. Figure 3 shows this form of division in the four cases. Orientation is obtained by dividing the orientation range without sign of $[-90°; 90°]$ or $\left[\frac{-\pi}{2}; \frac{\pi}{2}\right]$ in 3,6,9,12 and 15 intervals.

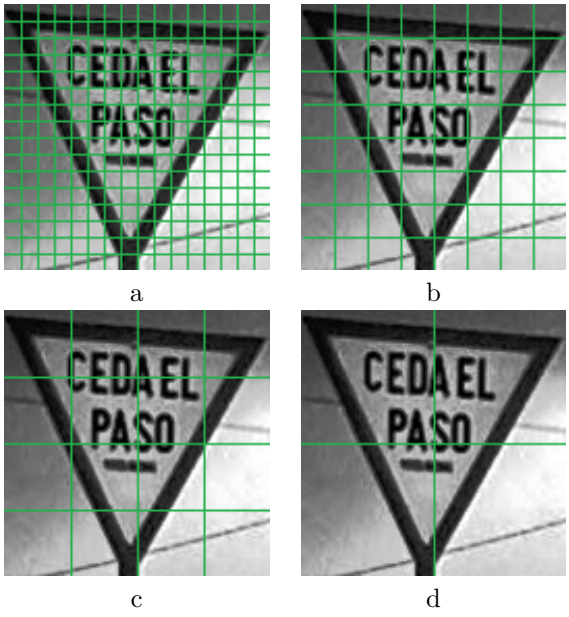

Figure 3. Cell size variation on images of 32×32 pixels: (a) 2×2, (b)4×4, (c) 8×8 (d) 16×16.

3) **Classification training based on SVM:** SVM [18–20] is used with three different cores to try out the best option: linear, polynomial and RBF. For training, three data sets are used that correspond to the Stop, Give-way, and Speed signs and other elements that do not belong to the previous cases.

The best option is chosen over this range of parameters using the AUC index [33]. In total, 60 cases are evaluated combining points 2 and 3, from which the ones that generate the best results are extracted in the next section.

3. Results and discussion

3.1. Perception and processing system

The total traffic sign detection system is presented in Figure 4. The perception system consists of a webcam with USB input at 25 frames per second, a display screen and a camera support. The processing system is a computer installed on the experimental vehicle ViiA. This vehicle incorporates a 12 V-120 AC power source that continuously supplies electrical power for the operation of the road system.

Figure 4. System of traffic sign detection in Ecuador, for the Stop, Give-way and Speed (50 and 100) signs, installed on the windshield of an experimental vehicle.

Currently, this system is easy to install in any type of vehicle and does not interfere with driving thanks to its small size.

3.2. Training, validation and experimentation database

The training and validation databases have been built with images of traffic signs from Ecuador, taken in the cities of Latacunga, Ambato, Salcedo, Quito and Sangolquí, in real driving scenarios, in different lighting conditions during the day. These conditions correspond to the cases of normal, sunny and cloudy. More details are found in Table 4.

Table 4. Environmental conditions for the acquisition of images

Ambient	Real time on cities and highways
Climate conditions	Normal, sunny and cloudy
Capture time	5.30 a. m. to 7.30 p. m.
Camera capture speed	25 frames per second
Image size	640 x 480 pixels
Image background	Complex, not fixed
Size of the traffic signs	Varying
Conditions of	Faded, blurred,
traffic signs	damaged, occluded
Type of	Stop, Give-way and
traffic signs	Speed of 50 and 100

Table 5 shows the size of the training and validation sets obtained by means of the Holdout method [35] and in Figure 5 several positive and negative examples are observed.

Table 5. Size of the training sets and validation by Stop, Give-way and negative signs

	Number of samples					Total
	Stop	**Give-way**	**Speed 50**	**Speed 100**	**Negatives**	
Training	700	700	700	700	2800	5600
Validation	300	300	300	300	1200	2400
Total	1000	1000	1000	1000	4000	8000

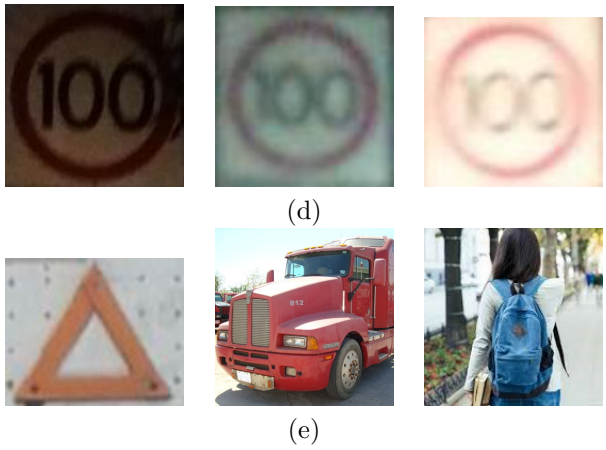

Figure 5. Examples of the traffic sign database for Ecuador under different lighting and status conditions, (a) Stop, (b) Give-way, (c) limit of 50 km/h, (d) limit of 100 km/h and (e) negative examples.

To increase the size of the training set, the images were randomly rotated to a total of five times the original size. In this way, the variability of the database is increased.

Subsequently, to verify the operation of the system, a database with videos was built in real driving situations, in the visible spectrum under different lighting conditions. This base consists of five specimens under different lighting conditions, where the signals have been manually located for evaluation purposes [33].

3.3. Analysis of results

The results can be summarized in the following points:

1) For the case of color segmentation, the classification algorithm generates an AUC of 0.986, with $k = 4$ and $K_m = 30$ for red class and $k = 4$ and $K_m = 30$ for other colors class.

2) For the classification, the best parameters of the HOG descriptor are cells of 8×8 pixels, blocks of 2×2 cells with simple overlap, 9 unsigned orientations and $C = 215, r = 0, \gamma = 1/m$ polynomial SVM parameters, where m is the size of the feature vector. Table 6 presents the results for the case of 8×8 pixels, where the best result is highlighted in bold.

Table 6. Classification results with HOG characteristics with cells of 8×8 pixels in all orientations.

Orientations	**Tipe of core**		
	Linear	**Polynomial**	**RBF**
3	0,9603	0,9913	0,9755
6	0,9784	0,9947	0,9834
9	0,9798	**0,9949**	0,9784
12	0,9762	0,9921	0,9827
15	0,9834	0,9971	0,9819

To measure the detection power, the curve of the false negative rate (loss rate) versus the false positive rate, in a logarithmic scale in the range of 0.01–1m [36], is presented in Figure 6. This shows that the best performance is on normal days with a loss rate of 13% and the worst execution is on sunny days with a loss rate of 28%.

The system has an excellent performance, with an average accuracy of 96%. The worst accuracy is achieved in sunny conditions, since the excess of light prevents a correct segmentation for the generation of ROIS, see Table 7.

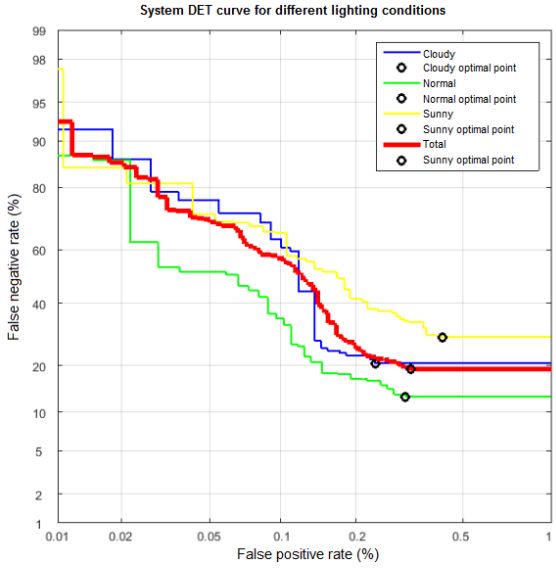

Figure 6. DET curve of the traffic sign detection system, separated in different lighting conditions and globally.

Table 7. Results of the traffic sign detection system in different lighting scenarios during the day

	TRPa	TFNb	TRNc	TFPd	Exe	Prf
Día normal	0,87	0,13	0,997	0,003	0,98	0,97
Día soleado	0,72	0,28	0,995	0,005	0,97	0,9
Día nublado	0,79	0,21	0,997	0,003	0,97	0,96
Sistema total	0,81	0,19	0,997	0,003	0,98	0,96

a Real positive rate, b False negative rate
c Real negative rate, d False positive rate
e Accuracy, f Precision

Several examples generated by the system can be seen in Figures 7, 8, 9 and 10. The samples are in various lighting conditions during the day, dawn and early evening, when traveling through urban areas and highway areas around the cities of Quito and Sangolquí.

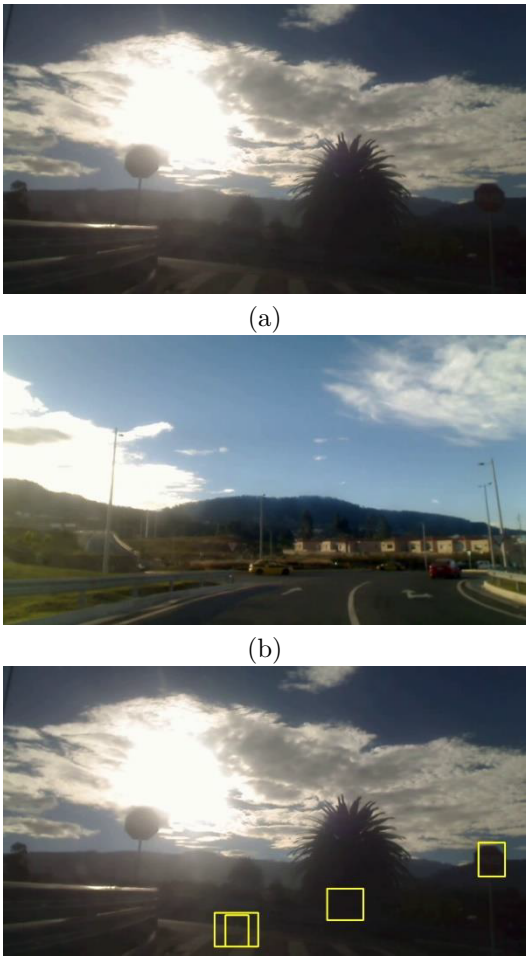

(a)

(b)

(c)

Figure 7. Results of the traffic sign detection system in the case of Stop signs, during a sunny day on a highway; (a) input image, (b) ROI and (c) detections.

(a)

(b)

(c)

Figure 8. Results of the traffic sign detection system in the cases Stop and Give-way signs, during a dark day in an urban area; (a) input image, (b) ROI and (c) detections.

(a)

(b)

(c)

Figure 9. Results of the traffic sign detection system in the case of Speed of 50 sign, during a dark day (at dawn) in urban area; (a) input image, (b) ROI and (c) detections.

(a)

(b)

(c)

Figure 10. Results of the traffic sign detection system in the case of Speed of 100, during a dark day in urban area; (a) input image, (b) ROI and (c) detections.

3.4. Computation times

Table 8 shows the computation time of the global system.

Table 8. Total computation times of the traffic sign detection system in Ecuador in the visible spectrum in the cases of Stop, Give-way signs.

Stage	Average time (ms)
Capture	1,75
Segmentation	28,79
Recognition	14,05
Display	1.75
Total time	46,34

These results are the average values of the processing of images of pixels, distributed as follows: 9999 in sunny, 14744 in normal and 12442 in cloudy.

From these experimental results it can be verified that the computation times, in the cases of segmentation and recognition, are quite short and therefore competitive to be part of applications in real-time systems.

4. Conclusions and future work

In this research work, in the field of driving assistance systems with emphasis on the detection of traffic signs, the following original contributions were made:

- The construction of a new database for the recognition of traffic signs in Ecuador, in the cases of Stop, Give-way and Speed signs. This information is available for the free use of the scientific community.
- The development of a new color segmentation method for the generation of ROI using the *k–NN* classifier together with the $K_m - means$ means clustering algorithm. This implementation efficiently covers the scenarios of normal, sunny and dark lighting during the day. In addition, distance is included as a reference parameter for the ROI preselection. In this way, this proposal reaches a classification rate of 98.7% in the pixels of interest and the background.
- The implementation of a new version of the HOG descriptor consisting of cells of 8×8 pixels, blocks of 2×2 cells with simple overlap and 9 orientations without sign. The classification rate is 99.49 using SVM with a polynomial core.
- The construction of a system to detect traffic signs in Ecuador, specialized in the Stop and Give-way cases. The DET curve indicates that its performance is 96%, so it is competitive regarding the proposals present in the state of the art.
- The construction of a driver assistance system that works in quasi-real time, that is, at 21.58 frames per second, is a system that is easy to install in a vehicle for everyday use.

For the future, this methodology will be extended to all the traffic signs of the prohibition type in Ecuador, where the rest of the speed limit signs for urban areas and highways are located. Finally, it is worth indicating that a method to check and compare the quality of the classifier will be introduced. For this purpose, a method based on ELM is being prepared.

Acknowledgments

The vehicle used for the development of a significant part of this project has been provided by Technologies I&H company, for which gratitude is due. In addition, we thank the anonymous reviewers for their valuable input as they have contributed significantly to the improvement of this manuscript.

References

[1] INEN, *RTE INEN 004-1:2011. Señalización vial. Parte 1. Señalización vertical*, Instituto Ecuatoriano de Normalización Std., 2011. [Online]. Available: https://goo.gl/pSQimH

[2] OMS. (2018) Lesiones causadas por el tránsito. Organizaciíon Mundial de la Salud. [Online]. Available: https://goo.gl/q1Mbuf

[3] K. Schwab, "The global competitiveness report 2015–2016," World Economic Forum, Tech. Rep., 2015. [Online]. Available: https://goo.gl/FvJVkb

[4] ANT. (2017) Siniestros septiembre 2017. Agencia Nacional de Tránsito, Ecuador. [Online]. Available: https://goo.gl/MZ1d75

[5] ——. (2015) Siniestros octubre 2015. Agencia Nacional de Tránsito, Ecuador. [Online]. Available: https://goo.gl/Pc4JfM

[6] B. T. Nguyen, S. J. Ryong, and K. J. Kyu, "Fast traffic sign detection under challenging conditions," in *2014 International Conference on Audio, Language and Image Processing*, July 2014, pp. 749–752. DOI: https://doi.org/10.1109/ICALIP.2014.7\protect \kern +.1667em\relax 009\protect \kern +.1667em\relax 895.

[7] H. Gomez-Moreno, S. Maldonado-Bascon, P. Gil-Jimenez, and S. Lafuente-Arroyo, "Goal evaluation of segmentation algorithms for traffic sign recognition," *IEEE Transactions on Intelligent Transportation Systems*, vol. 11, no. 4, pp. 917–930, 2010. DOI: https://doi.org/10.1109/TITS.2010.2054084.

[8] A. Shaout, D. Colella, and S. Awad, "Advanced driver assistance systems - past, present and future," in *Computer Engineering Conference (ICENCO), 2011 Seventh International*, Dec 2011, pp. 72–82. DOI: https://doi.org/10.1109/ICENCO.2011.6\protect \kern +.1667em\relax 153\protect \kern +.1667em\relax 935.

[9] A. Møgelmose, D. Liu, and M. M. Trivedi, "Detection of u.s. traffic signs," *IEEE Transactions on Intelligent Transportation Systems*, vol. 16, no. 6, pp. 3116–3125, Dec 2015. DOI: https://doi.org/10.1109/TITS.2015.2433019.

[10] S. E. Perez-Perez, S. E. Gonzalez-Reyna, S. E. Ledesma-Orozco, and J. G. Avina-Cervantes, "Principal component analysis for speed limit traffic sign recognition," in *2013 IEEE International Autumn Meeting on Power Electronics and Computing (ROPEC)*, Nov 2013, pp. 1–5. DOI: https://doi.org/10.1109/ROPEC.2013.6\protect \kern +.1667em\relax 702\protect \kern +.1667em\relax 716.

[11] S. Salti, A. Petrelli, F. Tombari, N. Fioraio, and L. D. Stefano, "Traffic sign detection via interest region extraction," *Pattern Recognition*, vol. 48, no. 4, pp. 1039–1049, 2015. DOI: https://doi.org/10.1016/j.patcog.2014.05.017.

[12] H. Li, F. Sun, L. Liu, and L. Wang, "A novel traffic sign detection method via color segmentation and robust shape matching," *Neurocomputing*, vol. 169, pp. 77–88, 2015. DOI: https://doi.org/10.1016/j.neucom.2014.12.111.

[13] T. hastie, R. Tibshirani, and J. Friedman, *The Elements of Statistical Learning: Data Mining, Inference, and Prediction*, S. S. . B. Media, Ed., 2009. [Online]. Available: https://goo.gl/5kPw8C

[14] J. Lillo-Castellano, I. Mora-Jiménez, C. Figuera-Pozuelo, and J. Rojo-Álvarez, "Traffic sign segmentation and classification using statistical learning methods," *Neurocomputing*, vol. 153, pp. 286–299, 2015. DOI: https://doi.org/10.1016/j.neucom.2014.11.026.

[15] T. Chen and S. Lu, "Accurate and efficient traffic sign detection using discriminative adaboost and support vector regression," *IEEE Transactions on Vehicular Technology*, vol. 65, no. 6, pp. 4006–4015, June 2016. DOI: https://doi.org/10.1109/TVT.2015.2500275.

[16] Y. Han, K. Virupakshappa, and E. Oruklu, "Robust traffic sign recognition with feature extraction and k-nn classification methods," in *2015 IEEE International Conference on Electro/Information Technology (EIT)*, May 2015, pp. 484–488. DOI: https://doi.org/10.1109/EIT.2015.7\protect \kern +.1667em\relax 293\protect \kern +.1667em\relax 386.

[17] G. Villalón-Sepúlveda, M. Torres-Torriti, and M. Flores-Calero, "Sistema de detección de señales de tráfico para la localización de intersecciones viales y frenado anticipado," *Revista Iberoamericana de Automática e Informática Industrial RIAI*, vol. 14, no. 2, pp. 152–162, 2017. DOI: https://doi.org/10.1016/j.riai.2016.09.010.

[18] C. Cortes and V. Vapnik, "Support-vector networks," *Machine Learning*, vol. 20, no. 3, pp. 273–297, Sep 1995. DOI: https://doi.org/10.1007/BF00994018.

[19] R. O. Duda, P. E. Hart, and D. G. Stork, *Pattern Classification*, 2nd ed., J. W. . Sons, Ed., 2012. [Online]. Available: https://goo.gl/pvWsE9

[20] N. Cristianini and J. Shawe-Taylor, *An Introduction to Support Vector Machines and Other Kernel-based Learning Methods*. Cambridge University Press, 2000. DOI: https://doi.org/10.1017/CBO9780511801389.

[21] Z. Huang, Y. Yu, and J. Gu, "A novel method for traffic sign recognition based on extreme learning machine," in *Proceeding of the 11th World Congress on Intelligent Control and Automation*, June 2014, pp. 1451–1456. DOI: https://doi.org/10.1109/WCICA.2014.7\protect \kern +.1667em\relax 052\protect \kern +.1667em\relax 932.

[22] J. H. Shi and H. Y. Lin, "A vision system for traffic sign detection and recognition," in *2017 IEEE 26th International Symposium on Industrial Electronics (ISIE)*, June 2017, pp. 1596–1601. DOI: https://doi.org/10.1109/ISIE.2017.8\protect \kern +.1667em\relax 001\protect \kern +.1667em\relax 485.

[23] N. Dalal, "Finding People in Images and Videos," Theses, Institut National Polytechnique de Grenoble - INPG, 2006. [Online]. Available: https://goo.gl/ZZCd7F

[24] H. Bay, A. Ess, T. Tuytelaars, and L. V. Gool, "Speeded-up robust features (SURF)," *Computer Vision and Image Understanding*, vol. 110, no. 3, pp. 346–359, 2008. DOI: https://doi.org/10.1016/j.cviu.2007.09.014.

[25] M. M. Lau, K. H. Lim, and A. A. Gopalai, "Malaysia traffic sign recognition with convolutional neural network," in *2015 IEEE International Conference on Digital Signal Processing (DSP)*, July 2015, pp. 1006–1010. DOI: https://doi.org/10.1109/ICDSP.2015.7\protect \kern +.1667em\relax 252\protect \kern +.1667em\relax 029.

[26] G. P. Martinsanz and J. M. de la Cruz García, *Visión por computador: imágenes digitales y aplicaciones*, R.-M. S. E. y Publicaciones, Ed., 2008. [Online]. Available: https://goo.gl/YDjJG6

[27] Y. Zhu, C. Zhang, D. Zhou, X. Wang, X. Bai, and W. Liu, "Traffic sign detection and recognition using fully convolutional network guided proposals," *Neurocomputing*, vol. 214, pp. 758–766, 2016. DOI: https://doi.org/10.1016/j.neucom.2016.07.009.

[28] Z. Zuo, K. Yu, Q. Zhou, X. Wang, and T. Li, "Traffic signs detection based on faster r-cnn," in *2017 IEEE 37th International Conference on Distributed Computing Systems Workshops (ICDCSW)*, June 2017, pp. 286–288. DOI: https://doi.org/10.1109/ICDCSW.2017.34.

[29] T. Calinski and J. Harabasz, "A dendrite method for cluster analysis," *Communications in Statistics*, vol. 3, no. 1, pp. 1–27, 1974. DOI: https://doi.org/10.1080/03610927408827101.

[30] D. L. Davies and D. W. Bouldin, "A cluster separation measure," *IEEE Transactions on Pattern Analysis and Machine Intelligence*, vol. PAMI-1, no. 2, pp. 224–227, April 1979. DOI: https://doi.org/10.1109/TPAMI.1979.4766909.

[31] T. Robert, W. Guenther, and H. Trevor, "Estimating the number of clusters in a data set via the gap statistic," *Journal of the Royal Statistical Society: Series B (Statistical Methodology)*, vol. 63, no. 2, pp. 411–423. DOI: https://doi.org/10.1111/1467--9868.00\protect \kern +.1667em\relax 293, 2001.

[32] P. J. Rousseeuw, "Silhouettes: A graphical aid to the interpretation and validation of cluster analysis," *Journal of Computational and Applied Mathematics*, vol. 20, pp. 53–65, 1987. DOI: https://doi.org/10.1016/0377-0427(87)90125-7.

[33] T. Fawcett, "Roc graphs: Notes and practical considerations for researchers," Tech. Rep., 2004. [Online]. Available: https://goo.gl/Sr6tFj

[34] N. Dalal and B. Triggs, "Histograms of oriented gradients for human detection," in *2005 IEEE Computer Society Conference on Computer Vision and Pattern Recognition (CVPR'05)*, vol. 1, June 2005, pp. 886–893. DOI: https://doi.org/10.1109/CVPR.2005.177.

[35] R. Kohavi, "A study of cross-validation and bootstrap for accuracy estimation and model selection," in *Proceedings of the 14th International Joint Conference on Artificial Intelligence - Volume 2*, ser. IJCAI'95. San Francisco, CA, USA: Morgan Kaufmann Publishers Inc., 1995, pp. 1137–1143. [Online]. Available: https://goo.gl/j5rXZX

[36] A. Martin, G. Doddington, T. Kamm, M. Ordowski, and M. Przybocki, "The det curve in assessment of detection task performance," 1997, pp. 1895–1898. [Online]. Available: https://goo.gl/nf6MZu

Scientific Paper / Artículo Científico

UNIVERSIDAD POLITÉCNICA SALESIANA ECUADOR
INGENIUS
Revista de Ciencia y Tecnología
https://doi.org/10.17163/ings.n19.2018.10
pISSN: 1390-650X / eISSN: 1390-860X

Design of a Neural Network for the Prediction of the coefficient of Primary Losses in Turbulent Flow Regime

Diseño de una red neuronal para la predicción del coeficiente de pérdidas primarias en régimen de flujo turbulento

Jairo Castillo-Calderón[1,*], Byron Solórzano-Castillo[1], José Moreno-Moreno[2]

Abstract

This investigation is focused on the design of a neural network for the prediction of the friction factor in turbulent flow regime, being this factor indispensable for the calculation of primary losses in closed ducts or pipes. MATLAB®Neural Networks Toolbox is used to design the artificial neural network (ANN), with backpropagation. The database includes 724 points obtained from the Moody diagram. The Reynolds number and the relative roughness of the pipe are the input variables of the ANN, the output variable is the coefficient of friction. The Levenberg-Marquardt algorithm is used for training the ANN by using different topologies, varying the number of hidden layers and the number of neurons that are hidden in each layer. The best result was obtained with a 2-30-30-1 topology, exhibiting a mean squared error (MSE) of 1.75E-8 and a Pearson correlation coefficient R of 0.99999 between the neural network output and the desired output. Furthermore, a descriptive analysis of the variable was performed in the SPSS® software, where the mean relative error obtained was 0.162%, indicating that the designed model is able to generalize with high accuracy.

Keywords: Moody diagram, friction factor, head loss, artificial neural network, backpropagation, turbulent flow.

Resumen

La presente investigación está orientada al diseño de una red neuronal para la predicción del factor de fricción en régimen de flujo turbulento, siendo este indispensable para el cálculo de pérdidas primarias en conductos cerrados o tuberías. Se utiliza Neural Networks Toolbox de MATLAB®para diseñar la red neuronal artificial (RNA), con retropropagación, cuya base de datos comprende 724 puntos obtenidos del diagrama de Moody. Las variables de entrada de la RNA son el número de Reynolds y la rugosidad relativa de la tubería; la variable de salida es el coeficiente de fricción. Utilizando el algoritmo de entrenamiento de Levenberg-Marquardt se entrena la RNA con distintas topologías, variando el número de capas ocultas y el número de neuronas ocultas en cada capa. Con una estructura 2-30-30-1 de la RNA se obtuvo el mejor resultado, exhibiendo un error cuadrático medio (ECM) de 1,75E-8 y un coeficiente de correlación de Pearson R de 0,99999 entre la salida de la red neuronal y la salida deseada. Además, mediante un análisis descriptivo de variable en el *software* SPSS®, se obtiene que el error relativo medio es de 0,162 %, indicando que el modelo diseñado es capaz de generalizar con alta precisión.

Palabras clave: diagrama de Moody, factor de fricción, pérdida de carga, red neuronal artificial, retropropagación, flujo turbulento.

[1,*]Faculty of Energy, Industries and Non-Renewable Natural Resources, Electromechanical Engineering Major, Universidad Nacional de Loja, Ecuador. Author for correspondence ✉: jairocastilloc07@gmail.com.
https://orcid.org/0000-0002-5321-4518, https://orcid.org/0000-0002-0071-2249
[2]Electromechanical Engineering Major, Universidad Nacional de Loja, Ecuador.
https://orcid.org/0000-0002-0205-2635

Received: 13-02-2018, accepted after review: 28-05-2018

Suggested citation: Castillo-Calderón, J.; Solórzano-Castillo, B. y Moreno-Moreno, J. (2018). «Design of a Neural Network for the Prediction of the coefficient of Primary Losses in Turbulent Flow Regime». Ingenius. N.°20, (july-december). pp. 21-27. doi: https://doi.org/10.17163/ings.n20.2018.02.

1. Introduction

The most widely used method to transport fluids from one place to another is to drive them through a pipe system, with circular sections being the most common for this purpose, providing greater structural strength and a greater cross section for the same outer perimeter than any another way [1].

The flow of a fluid in a pipeline is accompanied by a load loss that is accounted for in terms of energy per weight unit of the fluid that flows through it [2].

The primary losses or load losses in a rectilinear conduit of constant section are due to the friction of the fluid against itself and against the walls of the pipe that contains it. On the other hand, secondary losses are load losses caused by elements that modify the direction and speed of the fluid. For both types of loss, part of the energy of the system is converted into thermal energy (heat), which is dissipated through the walls of the pipeline and of devices such as valves and couplings [2,3].

The estimation of the losses of load due to the friction in pipes is an important task in the solution of many practical problems in the different branches of the engineering; hydraulic design and the analysis of water distribution systems are two clear examples.

In the calculation of the pressure losses in pipes, whether the current regime is laminar or turbulent plays a discriminating role [3]. The flow regime depends mainly on the ratio of inertial forces to viscous forces in the fluid, known as Reynolds number (N_R) [4]. Thus, if the is less than 2000 the flow will be laminar and if it is greater than 4000 it will be turbulent [2]. The majority of flows that are found in practice are turbulent [2–4], for this reason the present investigation is developed with this type of flow regime.

Equation 1 proposed by Darcy-Weisbach is valid for the calculation of frictional losses in laminar and turbulent regime in circular and non-circular pipes [2–4].

$$h_L = f \times \frac{L}{D} \times \frac{v^2}{2g} \tag{1}$$

Where:

h_L : loss of energy due to friction (N.m/N).
f : friction factor.
L : length of the flow stream (m).
D : diameter of the pipe (m).
v : average flow speed (m/s).
g : gravitational acceleration (m/s^2).

Equation 2, the implicit relationship known as the Colebrook equation, is universally used to calculate the friction factor in turbulent flow [3,4]. Note that it has an iterative approach.

$$\frac{1}{\sqrt{f}} = -2.0log\left(\frac{\varepsilon/D}{3.7}\right) + \frac{2.51}{N_R\sqrt{f}} \tag{2}$$

Where:

ε/D: relative roughness. It represents the ratio of the average roughness height of the pipe to the diameter of the pipe.

An option for the direct calculation of the turbulent flow friction factor is Equation 3 developed by K. Swamee and K. Jain [2].

$$f = \frac{0.25}{\left[log\left(\frac{\varepsilon/D}{3.7} + \frac{5.74}{N_R^{0.9}}\right)\right]^2} \tag{3}$$

Equations (2) and (3), and others such as that of Nikuradse, Karman and Prandtl, Rouse, Haaland, are obtained experimentally and their use can be cumbersome. Thus, the Moody diagram is one of the most used means to determine the friction factor in turbulent flow [2–4]. This shows the friction factor as a function of the Reynolds number and the relative roughness. The use of the Moody diagram or the aforementioned equations is a traditional means of determining the value of the friction factor when solving problems with manual calculations. However, this can be inefficient. For the automation of the calculations it is necessary to incorporate the equations in a program or spreadsheet to obtain the solution.

This investigation presents an alternative proposal for the prediction of the friction factor using artificial intelligence, specifically an ANN that allows the calculation to be automatic and reliable, thus reducing time and avoiding errors that may occur when using the previously mentioned alternatives.

2. Materials and methods

2.1. ANN design

The multilayer network to be developed has forward connections (feedforward) and employs the backpropagation algorithm which is a generalization of the least squares algorithm. It works through supervised learning and, therefore, it needs a set of training instructions that describe the response that the network should generate from a given input [5].

2.1.1. ANN database

The initialization parameters of the ANN are obtained from a set of 724 data tabulated in Microsoft Excel. These data were acquired using Moody's diagram, that is, through the graphical method that contemplates a sequence of steps based on [2]. The data set considers 43 Reynolds Number values, ($4000 \leq \varepsilon/D \leq 1 \times 10^8$), 20

curves of relative roughness, $(1 \times 10^{-6} \leq \varepsilon/D \leq 0,05)$, and the respective friction factors.

The Reynolds numbers used, shown in Table 1, correspond to those marked on the scale of the abscissas of Figure 1, with the purpose of achieving an exact calculation in the Moody diagram.

The Reynolds number and the relative roughness are the ANN's input variables and the friction factor is the output variable or variable to be predicted. In order to establish an adequate database, only the friction factors that are the consequence of an obvious intersection of any of the 43 Reynolds Numbers in each of the relative roughness curves are considered.

Table 1. Reynolds numbers used

N.°	Value N_R	N.°	Value N_R	N.°	Value N_R
1	4000	16	100000	31	7000000
2	5000	17	200000	32	8000000
3	6000	18	300000	33	9000000
4	7000	19	400000	34	10000000
5	8000	20	500000	35	20000000
6	9000	21	600000	36	30000000
7	10000	22	700000	37	40000000
8	20000	23	800000	38	50000000
9	30000	24	900000	39	60000000
10	40000	25	1000000	40	70000000
11	50000	26	2000000	41	80000000
12	60000	27	3000000	42	90000000
13	70000	28	4000000	43	100000000
14	80000	29	5000000		
15	90000	30	6000000		

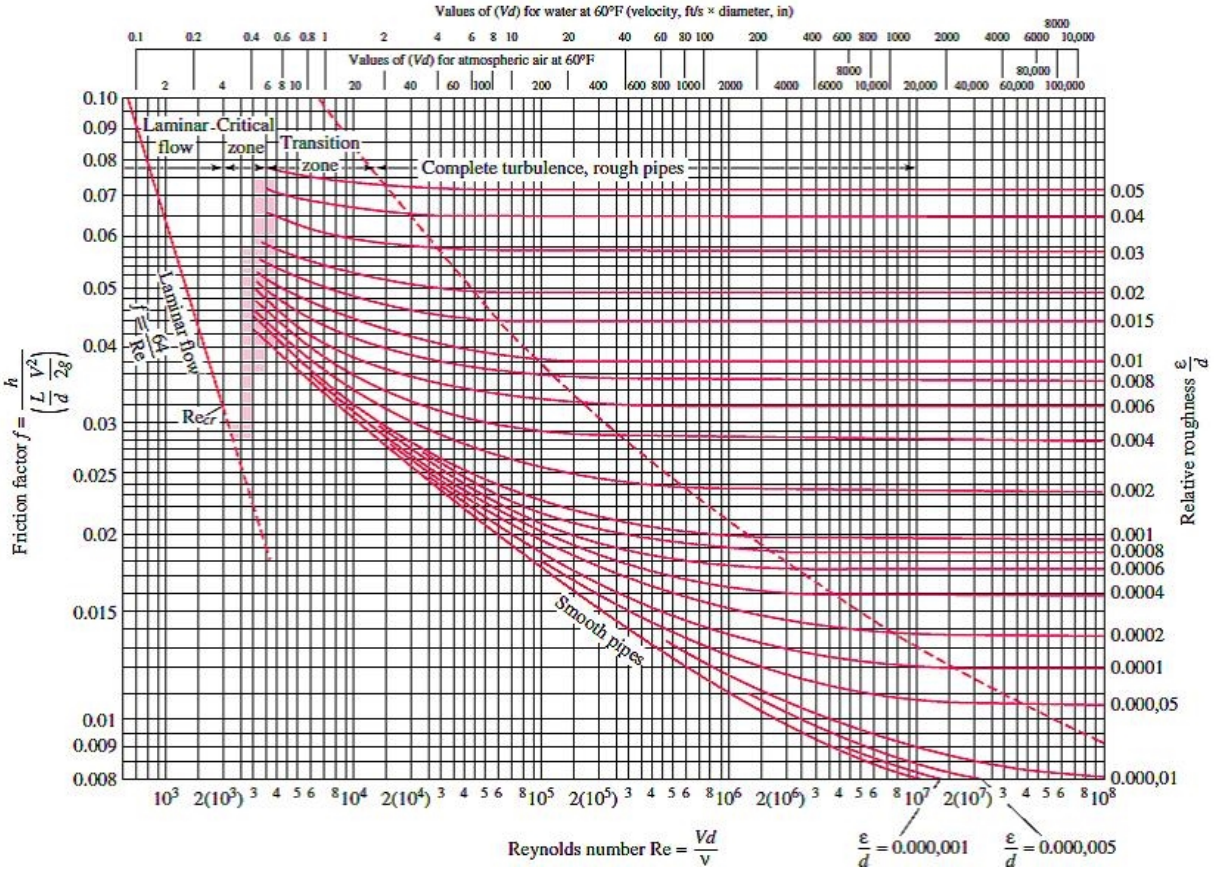

Figure 1. Moody's diagram for the coefficient of friction in smooth and rough wall ducts [6].

2.2. ANN topology

No concrete rules can be given to determine the number of hidden layers and the number of hidden neurons that a network must have to solve a specific problem; the size of the layers, both input and output, is usually determined by the nature of the application [7, 8]. Thus, the problems of the present investigation suggest that the Reynolds number and the relative roughness are the two inputs applied in the first layer and the friction factor, which is the output, is considered in the last layer of the network.

The number of hidden neurons intervenes in the

learning and generalization efficiency of the network; in addition, a single hidden layer is usually sufficient for the convergence of the solution. However, there are occasions when a problem is easier to solve with more than one hidden layer [7, 8].

Therefore, the optimal number of hidden layers and neurons is determined through experimentation.

To be precise, the most appropriate topology of the ANN is selected by testing different configurations by varying the number of hidden layers from one to three and the number of neurons within each hidden layer from 5 to 40 with increments of 5.

2.2.1. ANN Training

The supervised learning of an ANN implies the existence of a training controlled by an external agent so that the inputs produce the desired outputs by strengthening the connections. One way to carry this out is the establishment of previously known synaptic weights [5]. For this reason, the set of input-output pairs is applied to the ANN, that is, examples of inputs and their corresponding outputs [5, 8, 9].

The network is trained with the Levenberg-Marquardt backpropagation algorithm, as it is stable, reliable and facilitates the training of standardized data sets [10–12]. The training is an iterative process and the software, by default, divides the set of 724 data into 3 groups: 70% is comprised by training data, 15% by test data and the remaining 15% by validation data. In each iteration, when using new data from the training set, the backpropagation algorithm allows the output generated from the network to be compared with the desired output and an error is obtained for each of the outputs. As the error propagates backward, from the output layer to the input layer, the synaptic weights of each neuron are modified for each example, so that the network converges to a state that allows all training patterns to be successfully classified [9]. This is to say that the ANN training is carried out by error correction. As the network is trained, it learns to identify different characteristics of the set of inputs, so that when presented with an arbitrary pattern after training, it possesses the ability to generalize, understood as the ease of giving satisfactory outputs to entries not submitted in the training phase [13].

Due to the nature of the input and output data of the multilayer network, the activation or transfer functions must be continuous, and may even be different for each layer, as long as they are differentiable [9–13]. Thus, the tansig activation function is applied in the hidden layers and the purelin activation function in the output layer. These functions are commonly used when working with the backpropagation algorithm.

The ANN learning process stops when the error rate is acceptably small for each of the learned patterns or when the maximum number of iterations of the process has been reached [10], [14], [15]. The performance function used to train the ANN is the mean square error (MSE), denoted by Equation 4 [10–12]. The relative error, reflected arithmetically by Equation 5, is involved in the analysis [10–16].

$$MSE = \frac{1}{n}\sum_{i=1}^{n}(f_{Moody_i} - f_{RNA_i}) \tag{4}$$

$$E_{relativo} = \left(\frac{f_{Moody_i} - f_{RNA}}{f_{Moody}}\right) \times 100 \tag{5}$$

Summarizing the above, Table 2 contains the design characteristics of the ANN applied to the different topologies tested.

Table 2. Design features of the ANN

Characteristic	Description
Database	724
Type of network	Backpropagation
Input variables	N.° Reynolds; relative rug.
Output variable	Coefficient of friction
Training algorithm	Levenberg-Marquardt
Activation function (hidden layers)	*tansig*
Activation function (output layer)	*purelin*
Performance function	MSE (default)
Iterations	1000 (default)

3. Results and discussion

3.1. ANN architecture selection

According to the proposed methodology, a total of 24 architectures are trained, the results of which are shown in Table 3. It is observed that the topologies 2-30-30-1 and 2-25-25-25-1 present better results, since they have an average relative error of 0.1620% and 0.2282%, respectively, and a Pearson correlation coefficient of 0.9999 for both cases. However, the first one is selected because it shows a lower relative error of the predicted values compared to the desired ones and demands a lower computational expenditure. An outline of the structure of the selected ANN is shown in Figure 2. It shows the two external inputs, Reynolds number and relative roughness, applied to the first layer, the 2 hidden layers with 30 neurons each and in the last layer a neuron whose output is the friction factor. Entries are limited only to the flow of information while processing is carried out in the hidden and output layers [5].

Table 3. Results of the different architectures tested

N.° of hidden layers	N.° of neurons in each layer	Acerage relative error (%)	Pearson R correlation coefficient
1	5	0,7422	0,99985
1	10	0,5995	0,99993
1	15	0,4743	0,99994
1	20	0,4707	0,99995
1	25	0,6497	0,99991
1	30	0,447	0,99996
1	35	0,464	0,99994
1	40	0,4227	0,99995
2	5	0,5362	0,99992
2	10	0,4737	0,99996
2	15	0,3641	0,99996
2	20	0,3587	0,99997
2	25	0,2617	0,99998
2	30	0,162	0,99999
2	35	0,3248	0,99996
2	40	0,4675	0,99984
3	5	0,4722	0,99995
3	10	0,4588	0,99995
3	15	0,2591	0,99998
3	20	0,3169	0,99997
3	25	0,2282	0,99999
3	30	0,2936	0,99997
3	35	0,3581	0,9999
3	40	0,3858	0,99994

Using the IBM SPSS Statistics 22® software, a descriptive analysis of the relative error variable is performed for the 724 data of the selected architecture. The histogram of Figure 3 represents the frequency distributions. The results show that the average is 0.1620%, the minimum relative error is 0% and the maximum is 4.2590%.

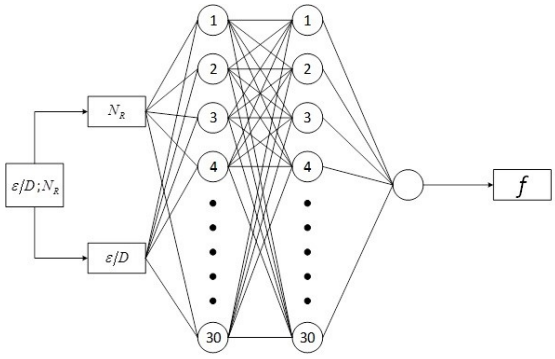

Figure 2. Structure of the designed ANN.

In addition, the standard deviation is 0.327, indicating that the dispersion of the data with respect to the mean is small. The distribution of data shows that there is a considerable predominance of relative error less than 1% in 97% of the total data analyzed. Supporting what is reflected in the histogram, Table 4 summarizes the values of the three quartiles obtained from the statistical analysis. Under Q_1 there are relative errors between the desired output and the network output of less than 0.0313%. Q_2, which is the median value, points out that half of the relative errors are below 0.0720%. Q_3 states that three quarters of the data have a relative error of less than 0.1758%. From Q_3, low relative errors are obtained, however, there are lagged values that are greater than 1%, but these represent only 3% of the total data analyzed. The above shows the quality of approximation of the predicted values of the ANN with respect to those of the Moody diagram.

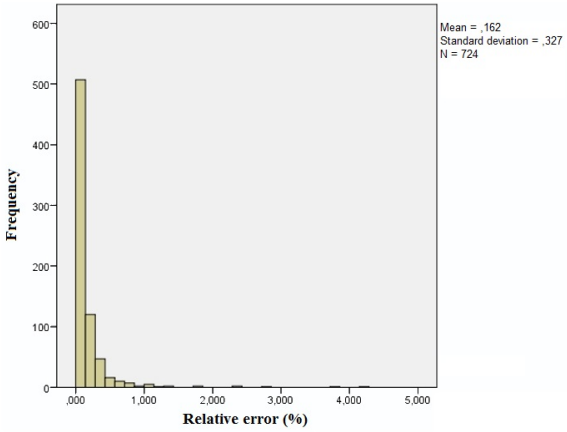

Figure 3. Relative error histogram.

Table 4. Measures of non-central position of the relative error

Statistical parameter	Relative error value
First quartile (Q_1)	0,03%
Second quartile (Q_2)	0,07%
Third quartile (Q_3)	0,18%

3.2. Model performance

The performance of training data sets, tests and validation compared to the desired output is shown in Figure 4. The sample intended for validation is used to measure the degree of generalization of the network, stopping training when it no longer improves, this prevents overfitting [12], understood as a poor performance of the model to predict new values. It is noted that the training process of the ANN with topology 2-30-30-1 is truncated in 91 iterations, because it is when the lowest MSE value of validation is obtained, which is $1,7492 \times 10^{-8}$.

That is, the performance function has been minimized to the maximum and will no longer have a tendency to decrease after 91 iterations. Because the MSE value is very small, closest to zero, the ANN model is able to generalize with great precision.

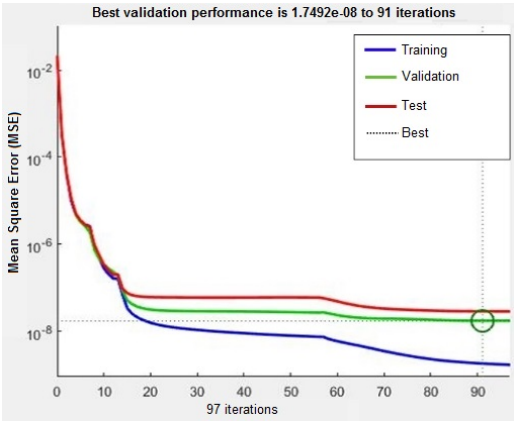

Figure 4. Performance of the ANN training process.

Figure 5 shows the results of the Pearson R correlation coefficient for the designed ANN structure. The line indicates the expected values and the black circles represent the predicted values. The prediction is efficient, and a good performance of the network is observed, since a global index of 0.999999 is obtained indicating a strong and positive linear relationship between the friction factors of the Moody diagram and those granted by the ANN.

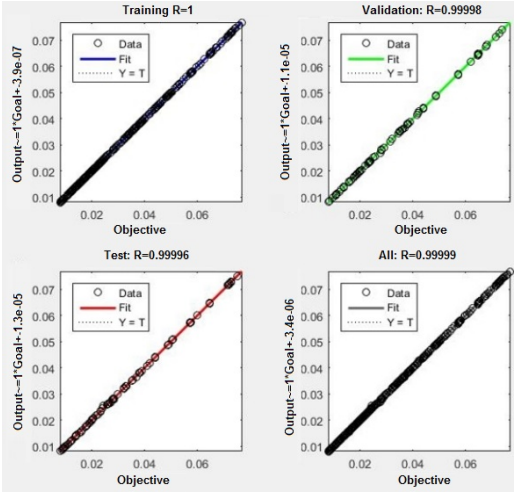

Figure 5. Correlation between expected and predicted values

Several tests are performed with combinations of input pairs that have not been used during training in order to verify the correct performance of the model. Thus, Table 5 details the 36 combinations of input data applied to the ANN and the relative error reached by each of them.

According to Table 5 and Figure 6, the relative error is not distributed equally in the range of input values. In the generated 3D surface graph, the predominance of a relative error lower than 0.5% is observed, corresponding to 24 of the 36 combinations of input pairs applied to the ANN. In addition, there are only 2 relative errors above 1%, concerning the 2 most prominent peaks on the surface, with a maximum of 1.325% for N_R = 1,5E5 y ε/D = 0,006. The results derived from these 32 tests corroborate the correct functioning of the network and its capacity to generalize by presenting inputs different from those used in the training phase.

Table 5. Relative error results for data not considered in training

N_R	ε/D					
	0,01	**0,008**	**0,006**	**0,004**	**0,002**	**0,001**
$4,5 \times 10^{+3}$	0,869	0,282	0,252	0,16	0,344	0,382
$1,5 \times 10^{+4}$	0,452	0,72	0,535	0,178	0,757	0,329
$1,5 \times 10^{+5}$	0,325	0,005	1,325	0,27	1,095	0,25
$1,5 \times 10^{+6}$	0,665	0,541	0,818	0,01	0,147	0,131
$1,5 \times 10^{+7}$	0,387	0,32	0,575	0,134	0,237	0,333
$9,5 \times 10^{+7}$	0,487	0,092	0,712	0,267	0,847	0,02

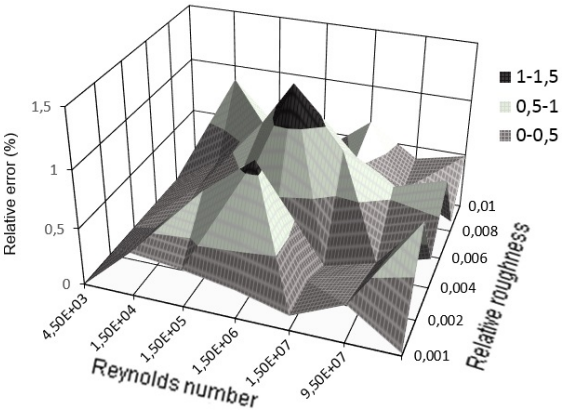

Figure 6. Relative error distribution.

4. Conclusions

The ANN designed in this research represents a reliable and highly accurate alternative to predict the coefficient of primary losses in turbulent flow regime, giving an average relative error of 0.1620% and a Pearson R correlation coefficient of 0.99999 between the values of the Moody diagram and the predicted ones.

The training process was stopped at 91 iterations, reaching an MSE of 1.7492×10^{-8} that indicates the generalization capacity of the proposed ANN.

The results obtained show that the set of 724 data was sufficiently large to allow the ANN, during the training, to be able to learn the relationship between the inputs and outputs applied.

The developed model allows to solve flow problems that involve calculations of the friction factor in an automatic way, taking advantage of the computational speed that the neural networks offer, reducing time and avoiding errors that can be caused when using traditional alternatives.

Referencie

[1] J. R. Calderón Córdova and C. X. Pozo Calva, "Diseño y construcción de un banco de pruebas para pérdidas de carga en tuberías y accesorios con simulación," Tesis de Grado. Universidad Politécnica Salesiana. Ecuador, 2011. [Online]. Available: https://goo.gl/MiF65x

[2] R. L. Mott, *Mecánica de Fluidos*, 2006, ch. Ecuación general de la energía; número de Reynolds, flujo laminar, flujo turbulento y pérdidas de energía debido a la fricción, pp. 197–243. [Online]. Available: https://goo.gl/SkTHPd

[3] C. Mataiz, *Mecánica de fluidos y máquinas hidráulicas*, 1986, ch. Resistencia de superficie: pérdidas primarias en conductos cerrados o tuberías, pp. 203–226. [Online]. Available: https://goo.gl/mW1mkL

[4] Y. A. Cengel and J. M. Cimbala, *Mecánica de fluidos: fundamentos y aplicaciones*, 2006, ch. Flujo en tuberías, pp. 223–342. [Online]. Available: https://goo.gl/DMttmi

[5] P. Ponce Cruz, *Inteligencia Artificial con Aplicaciones a la Ingeniería*, 2011, ch. Inteligencia Artificial, pp. 1–32. [Online]. Available: https://goo.gl/XED1Vo

[6] F. M. White, *Mecánica de Fluidos*, 5$^{\text{th}}$ ed., 2003, ch. Flujo viscoso en conductos, pp. 335–435. [Online]. Available: https://goo.gl/vULEcg

[7] A. Campos Ortiz, "Proceso de distribución aplicando redes neuronales artificiales con supervisión," Master's thesis, Universidad Autónoma de Nuevo León, México, 1998. [Online]. Available: https://goo.gl/io73HZ

[8] J. R. Coutiño Ozuna, "Aplicación de redes neuronales en la discriminación entre fallas y oscilaciones de potencia," Master's thesis, Universidad Autónoma de Nuevo León, 2002. [Online]. Available: https://goo.gl/yKvEFs

[9] N. Peláez Chávez, "Aprendizaje no supervisado y el algoritmo wake-sleep en redes neuronales," Tesis de grado. Universidad Tecnológica de la Mixteca, 2012. [Online]. Available: https://goo.gl/oeygXA

[10] U. Offor and S. Alabi, "Artificial neural network model for friction factor prediction," *Journal of Mechanical Science an Chemical Engineering*, vol. 4, pp. 77–83, 2016. DOI: http://dx.doi.org/10.4236/msce.2016.47011.

[11] M. R. G. Meireles, P. E. M. Almeida, and M. G. Simoes, "A comprehensive review for industrial applicability of artificial neural networks," *IEEE Transactions on Industrial Electronics*, vol. 50, no. 3, pp. 585–601, June 2003. DOI: https://doi.org/10.1109/TIE.2003.812470.

[12] D. Brkić and Ĉojbašić, "Intelligent flow friction estimation," *Computational Intelligence and Neuroscience*, vol. 2016, 2016. DOI: https://doi.org/10.1155/2016/5242596.

[13] J. Hilera and V. Martínez, *Redes neuronales artificiales: fundamentos, modelos y aplicaciones*, 1994, ch. Redes neuronales con conexiones hacia adelante, pp. 101–180. [Online]. Available: https://goo.gl/rovX8y

[14] T. Manning, R. D. Sleator, and P. Walsh, "Biologically inspired intelligent decision making," *Bioengineered*, vol. 5, no. 2, pp. 80–95, 2014. DOI: https://doi.org/10.4161/bioe.26997, pMID: 24335433. [Online]. Available: https://doi.org/10.4161/bioe.26997

[15] R. Yousefian and S. Kamalasadan, "A review of neural network based machine learning approaches for rotor angle stability control," *CoRR*, vol. abs/1701.01214, 2017. [Online]. Available: https://goo.gl/4RYRWs

[16] O. E. Turgut, M. Asker, and M. T. ¸Coban, "A review of non iterative friction factor correlations for the calculation of pressure drop in pipes," *Bitlis Eren University Journal of Science and Technology*, vol. 4, no. 1, pp. 1–8, 2014. DOI: http://dx.doi.org/10.17678/beujst.90203.

Scientific Paper / Artículo Científico

UNIVERSIDAD POLITÉCNICA SALESIANA ECUADOR
INGENIUS
Revista de Ciencia y Tecnología
https://doi.org/10.17163/ings.n20.2018.03
pISSN: 1390-650X / eISSN: 1390-860X

Sustainable Water Consumption of Dwellings In The Cuenca City

Consumo sustentable de agua en viviendas de la ciudad de Cuenca

Eduardo Molina[1], Felipe Quesada[1], Andrea Calle[1], Jessica Ortiz[1,*], Diana Orellana[1]

Abstract

This study proposes and supports the application of 4 criteria for the sustainable management of drinking water inside the dwelling in the city of Cuenca, Ecuador. The criteria determined are: the control of water consumption, the control of leaks, the use of saving devices and water reuse systems. Three levels of assessment are defined for each criterion: standard, best practices and superior practices. For the development of the research, surveys are applied to the population that allow probing the existence and predisposition to incorporate drinking water saving practices in the homes, in addition measurements of water consumption by uses are made in 10 homes for a week, together the official information on the water consumption of the canton Cuenca facilitated by the municipal company of the city is processed, and several standards are analyzed: ISO, INEC and the Ecuadorian Technical Construction Standard, among others. Finally, it concludes with the determination of a percentage of water savings of up to 30%, which can be obtained the application of sustainable practices.

Keywords: Water consumption, water saving strategies, water recycling, water sustainability.

Resumen

El presente estudio propone y sustenta la aplicación de cuatro criterios para la gestión sustentable de agua potable al interior de la vivienda en la ciudad de Cuenca, Ecuador. Los criterios determinados son el control del consumo de agua, el control de fugas, el uso de dispositivos ahorradores y los sistemas de reutilización de agua. Se definen tres niveles de valoración para cada criterio: estándar, mejores prácticas y superiores prácticas. Para el desarrollo de la investigación se aplican encuestas a la población que permiten sondear la existencia y la predisposición de incorporar prácticas de ahorro de agua potable en las viviendas; además, se realizan mediciones del consumo de agua por usos en diez viviendas durante una semana; conjuntamente se procesa la información oficial del consumo de agua del cantón Cuenca facilitado por la empresa municipal de la ciudad y se analizan varias normas: ISO, INEC y la Norma Técnica Ecuatoriana de la Construcción, entre otras. Finalmente, se concluye con la determinación de un porcentaje de ahorro de agua de hasta el 30 %, que se puede obtener con la aplicación de prácticas sustentables.

Palabras clave: Consumo de agua, estrategias de ahorro de agua, reutilización de agua, sustentabilidad del agua.

[1,*]School of Architecture and Urbanism, Universidad de Cuenca, Ecuador.
Author for correspondence ✉: jessicam.ortizf@ucuenca.edu.ec , http://orcid.org/0000-0002-7298-1827
http://orcid.org/0000-0002-6931-0192, http://orcid.org/0000-0003-0762-3772
http://orcid.org/0000-0002-6167-6720, http://orcid.org/0000-0002-4684-6613

Received: 03-05-2018, accepted after review: 12-06-2018

Suggested citation: Molina, E.; Quesada, F.; Calle, A.; Ortiz, J. and Orellana, D. (2018). «Sustainable Water Consumption of Dwellings In The Cuenca City». Ingenius. N.°20, (july-december). pp. 28-38. doi: https://doi.org/10.17163/ings.n20.2018.03.

1. Introducción

Planet Earth is 70% covered by water, of which 98% is salt water and the current technology to make it drinkable is still very restricted due to its high costs. About 2% of fresh water is located in the polar ice caps or aquifers, so only 0.014% is available in the lakes and rivers of the Earth's surface [1].

In the world, drinking water coverage is still a problem both in cities and in rural areas. By the middle of this century, 7,000 million people in 60 countries will suffer water shortages, in the worst case, and at best it will be 2,000 million people in 48 countries. Recent estimates suggest that climate change will be responsible for around 20% of the increase in the global water shortage [2]. One of the alternatives promoted in recent years is a focus on the human right to water. As such, resolution a/res/64/292 of the UN General Assembly explicitly declares «the right to drinking water and sanitation as an essential human right for the full enjoyment of life and all human rights» [3, 4].

Therefore, populations will be favored to the extent that the use of water is minimized and there is a commitment on the part of the citizens to maintain the liquid they now have to satisfy their basic needs and guarantee the supply for future populations. [1]. In this way, the sustainable consumption of water is defined as «the use of water that allows sustaining a society so that it lasts and develops in an indefinite future without altering the integrity of the hydrological cycle and the ecosystems that depend on it» [5, 6].

At the international level, there are several methods of certification for sustainable housing that incorporate indicators for the saving of drinking water, among the most recognized methods are: VERDE NE Residential Offices [7], LEED® Rating System for Homes [8] and the BREEAM ES VIVIENDA Manual [9].

These methods contemplate several strategies such as the detection of leaks by means of historical records, which allows for a comparison between water supplied and water consumed. [10–12]; the installation of saving devices, which can reduce up to 30% of consumption [1], [13]; the use of rainwater, which can be stored for certain household uses [14, 15]; the use of water recycling techniques, which consists of the reutilization of domestic wastewater, allowing, for example, to reload the toilets with gray water [16, 17]; and the implementation of single jet multiple jet meters, in order to control consumption, achieving savings of up to 20% [18, 19].

1.1. Drinking water in the city of Cuenca

According to the World Health Organization, optimal access to water in order to meet all basic consumption and hygiene needs, in order not to cause negative effects on health, should be greater than 100 l/inhabitant/day [20], while the Ecuadorian Construction Standard 2011 establishes that the provision for a house should be between 200 and 350 l/inhabitant/day, reflecting a very wide range, which prevents the existence of consumption control [21].

This lack of control results in increased levels of consumption over time. Such is the case of Cuenca, which, to guarantee the water service for the community, has a catchment of 120 000 m^3 [22] for a population of 524 563 inhabitants [23]. Taking into account that the population projection for the year 2050 will reach 901 499 inhabitants [24], it will be necessary to capture 4610 l/s of water, if current consumption and demand for drinking water is maintained, which is equivalent to a 71.85% increase in catchment.

Obtaining this percentage of new demand puts water resources at risk considering, in addition, that three of the four rivers in the city are currently exploited. In monetary terms the requirement for infrastructure works for 2050 implies an investment of 6865 million dollars [24].

This would cause the provision of drinking water in the city of Cuenca to increase and compare to other Latin American locations, such as Buenos Aires-Argentina where there is a provision of 356 l/inhabitant/day, Sao Paulo-Brazil with 227 l/inhabitant/day, and Santiago de Chile with 203 l/inhabitant/day [25].

Therefore, a sustainable management of water in the homes of Cuenca is necessary in order to reduce these percentages.

With this background, this study raises the possibility of reducing the consumption of drinking water in homes in this city, without affecting the quality or lifestyle of its inhabitants, through the application of sustainable criteria such as incorporating rainwater for certain domestic uses, using sanitary appliances and water recycling techniques.

2. Materials and methods

The methodology of the present investigation is non-experimental and quantitative, and includes two stages:

2.1. Determination of evaluation criteria to reduce the consumption of drinking water

For the determination of criteria, a comparison of four international assessment methods is carried out, where the subject of the sustainable management of drinking water within the home is studied, in order to find convergences between them and establish the criteria that will be considered. The methods analyzed are GEA VERDE NE [7], LEED® for Homes Rating System [8], CASBEE FOR NEW CONSTRUCTION [26] and BREEAM IS HOUSING MANUAL [9].

To determine if the evaluation criteria are feasible and applicable in the local reality of Cuenca, the following selection judgments are established [27]:

1. The evaluation criteria are compatible with the characteristics of the households and/or the city.
2. The evaluation criterion contributes to overcoming the existing problems in the households and/or the city.
3. The application of the evaluation method was feasible.
4. The levels of demand are in line with local conditions.
5. The type of evaluation implemented is based on performance.
6. The evaluation criterion contributes to improving the comfort of the households and/or the conditions of the city.

2.2. Determination of valuation levels

One of the main challenges of the research is to determine the minimum values or standards to be met in each criterion evaluated, which respond to the local reality. The process used in this stage includes the following three sections:

2.2.1. Surveys of 280 homes in the city of Cuenca

A survey is applied that allows the identification of drinking water saving practices and the predisposition of the population to incorporate sustainable strategies. For the survey, a sample of 280 homes distributed in the urban area of Cuenca is taken.

The specific design of statistical sampling is probabilistic, polymetallic and random. The number of selected sectors was based on the number of households in each parish and the distribution by socioeconomic level (A; B; C +; C-; D). The survey of the National Institute of Statistics and Census (INEC) was used to determine the socioeconomic stratum. The sample has a confidence level of 95% and an absolute error of 0.06.

To estimate the size of the sample, the following formula was used:

$$np' = \frac{K^2 \times N \times PQ}{K^2 \times PQ + NE^2}$$

Where:

np' = size of sample to be assessed
K = confidence coefficient
N = size of the universe
PQ = proportion variance
E = maximum permissible error

The survey considers the following:

- Do you use any equipment, device or system to save water?
- For you, what is the importance of a home that saves energy and water; that less resources are consumed during the construction process, or that it causes a minimum impact on the environment?
- Would you be willing to invest in a home with the characteristics of the previous question?

2.2.2. Measurement of water consumption in 10 homes

In order to determine the water consumption through different uses, a specific analysis is carried out in ten homes. The selection criteria of these houses were the geographical dispersion and the variety in the typology of the building. In addition, the limitation of the number of measuring equipment is considered, but mainly the predisposition of the owners to collaborate with the investigation.

For the measurement, water meters, model S120, of the velocimetric type, which consist of a single jet inferential meter, magnetic transmission, direct reading and super dry watchmaking, meet the metrological requirements of classes A and B of the Resolution 246; 2000 of the INMETRO, of the MERCOSUR NM 212 and ISO 4064 standards [28–30].

These meters were installed in the various water outlets (uses): faucets in toilets, kitchens and laundries, showers, water heaters and toilets. Daily consumption is recorded during a whole week to obtain data on the behavior of a family on working days and non-working days.

Finally, a survey is applied, which is based on the one developed by the Ecuadorian Institute of Sanitary Works [31] and is part of the Ecuadorian construction code [32]. In addition, it has been applied in similar investigations [17, 33]. The questions are:

- How many times does a member of the family that lives in the home use the toilet?
- Would you be willing to use rainwater in your home for sanitary, irrigation and cleaning purposes?
- How much money would you be willing to invest monthly in equipment that allows saving and sustainable use of water?

2.2.3. Drinking water consumption data in Cuenca

The city's municipal public company (ETAPA EP) is asked for monthly drinking water consumption forms for all the residential connections to which it provides the service, in order to calculate the arithmetic average of water consumption per existing residential installation.

With these results and with the INEC population and housing census data [34], the arithmetic mean of drinking water consumption per inhabitant in l/inhabitant/day is obtained.

In addition, the monthly water consumption of the residential connections of the ten case studies was requested during a year, in order to assess the measurements obtained in the readings and determine maximum and minimum variations.

Based on the data obtained from the previous points, standards and strategies for sustainable consumption of water in the homes of the city of Cuenca are defined, which help determine the percentages of savings in consumption and costs that can be achieved.

3. Results and discussion

3.1. Determination of evaluation criteria to reduce the consumption of drinking water

Table 1 shows the results of the evaluation of the 6 judgments on the 17 evaluation criteria determined in the international methods. It is observed that not all the evaluation criteria were compatible with the local reality, since in some cases less than 4 selection judgments are met.

Figure 1 shows the four selected criteria: maximum consumption, control of water consumption and leakage, use of saving devices and rainwater reuse systems, which comply with all selection judgments. These are grouped by requirements according to consumption, savings and recycling.

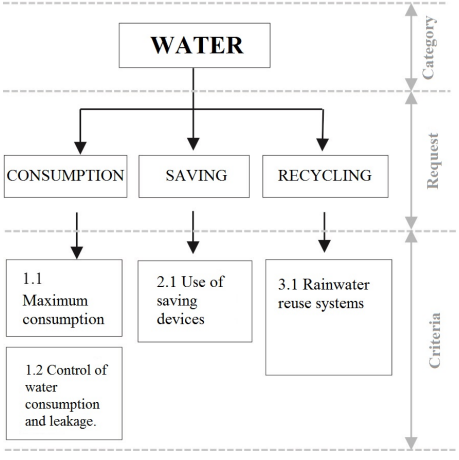

Figure 1. Criterios seleccionados

Table 1. Judgments for the selection of evaluation criteria

Evaluation criteria	Selection judgments 1	2	3	4	5	6
1. Consumption						
BREEAM						
Water meters	x	x	x	x		x
LEED						
Water consumption inside the house	x	x	x			x
GREEN						
Water consumption in sanitary devices	x	x	x	x	x	x
2. Saving						
BREEAM						
Water consumption	x	x	x	x	x	x
Irrigation system	x	x	x	x		x
CASBEE						
Water saved	x	x	x	x	x	x
LEED						
Landscaping	x	x	x	x	x	x
Water savings inside the building	x	x	x	x	x	x
Irrigation system	x	x	x	x	x	x
GREEN						
Water consumption for watering gardens	x	x	x	x	x	x
3. Recycling						
BREAM						
Water recycling	x	x	x	x	x	x
Sustainable water treatment at the site					x	x
Collection of rainwater in artificialized soil	x	x	x	x	x	x
LEED						
Recycle water	x	x	x	x	x	x
VERDE						
Retention of rainwater for reuse	x	x	x	x	x	x
Recovery and reuse of gray water	x	x				x
CASBEE						
Recycling rain water	x	x	x	x	x	x

3.2. Determination of valuation levels

3.2.1. Surveys of 280 homes in the city of Cuenca

The results show that only 24% of households apply a drinking water saving strategy (Table 2).

Table 2. Equipment, devices or systems to save water used at home

Equipment or device	Percentage
Water-saving toilets	6%
Saving devices in the taps	2%
Water-saving washing machine	14%
Water-saving dishwashers	0%
Reuse gray water or rainwater for watering the garden	1%
None	76%
Total	**100%**

Additionally, Table 3 shows that 61% of respondents consider that saving water is important or very important.

Table 3. The importance of a home that saves energy and water; that consumes less resources or causes a minimum impact on the environment for the inhabitants in the city of Cuenca during its construction process

Importance Level	Percentage
Not important	13%
Less important	3%
Indifferent	23%
Important	29%
Very important	32%
Total	**100%**

34% of respondents would be willing to invest in a house with water and energy saving characteristics (Table 4).

Table 4. Would you be willing to invest in a home with the above characteristics?

Provision	Percentage
Yes	34%
No	66%
Total	**100%**

3.2.2. Measurement of water consumption in 10 homes

Results of measurements

The arithmetic mean of the results of the measurements in different uses of the 10 homes is presented in Table 5. It is observed that 54.45% of drinking water consumption is due to sanitary uses, laundry and other uses such as watering gardens, washing yards and cars.

Table 5. Uses of water in homes in the city of Cuenca

Description	Arithmetic media (l)	Percentage %
Total per inhabitant (l/inhabitante/day)	179,508	100
Kitchen	33,531	18,68
Personal hygiene shower	37,386	20,83
Personal hygiene toilets	10,856	6,05
Toilets	50,218	27,98
Laundry and other uses such as watering gardens washing yards and cars	47,518	26,47

Survey results

According to the results of the arithmetic mean applied to the respondents of the ten homes, it is determined that they use the toilet 3.3 times a day (Table 6). This value of perception of use of the toilet is below the actual use, which is 5 times per day on average [35]. As such, this research takes measured data of real use in the households into account.

Table 6. How many times does a member of the family who lives in the household use the toilet?

Household	Daily toilet use
1	3
2	4
3	4
4	4
5	3
6	2
7	5
8	3
9	4
10	1
Arithmetic average	**3,3**

None of the homes surveyed has any system to collect rainwater and 90% would be willing to use rainwater for sanitation, irrigation and cleaning (Table 7. The monthly amount that they would be willing to invest in equipment that allows a sustainable use of water is shown in Table 8.

Table 7. Would you be willing to use rainwater in your home for toilets, irrigation and cleaning purposes?

Availability	Percentage
Sí	90
No	10
Total	**100**

Table 8. Monthly amount that they would be willing to invest in equipment that allows a sustainable use of water

Rank	Percentage
From $0,00 to $10,00	50
From $10,00 to $20,00	30
From $20,00 to $50,00	10
From $50,00 to $100,00	0
More than $100,00	10
Total	**100%**

3.2.3. Drinking water consumption data in Cuenca

Table 9 shows the water consumption of all household connections in Cuenca over a year.

Table 9. Water consumption during 2015 of the households served by ETAPA EP in the city of Cuenca

Month	Total consumption) (m^3	Industrial and commercial consumption (m^3)	Residential consumption (m^3)	Number of residential facilities
dic-15	2 613 187,00	357 176,00	2 256 011,00	104 392,00
nov-15	2 473 961,00	343 162,40	2 130 798,60	104 171,00
oct-15	2 551 035,00	368 922,00	2 182 113,00	104 041,00
sep-15	2 558 923,00	357 506,80	2 201 416,20	103 956,00
ago-15	2 453 018,00	342 898,40	2 110 119,60	103 493,00
jul-15	2 512 488,00	311 477,40	2 201 010,60	105 028,00
jun-15	2 466 598,00	310 049,10	2 156 548,90	104 482,00
may-15	2 556 930,00	308 137,60	2 248 792,40	104 076,00
abr-15	2 774 639,00	274 218,85	2 500 420,15	103 645,00
mar-15	2 657 568,00	257 141,45	2 400 426,55	103 415,00
feb-15	2 752 265,00	260 831,70	2 491 433,30	98 420,00
ene-15	2 760 075,00	261 616,50	2 498 458,50	103 038,00
Total	31 130 687,00	3 753 138,20	27 377 548,80	1 242 157,00
Arithmetic average	2 594 223,92	312 761,52	2 281 462,4	103 513,08

The data shows that the city has an arithmetic mean of 103 513 residential installations. On the other hand, total water consumption is 31 130 687.00 m^3, where residential water consumption represents 27 377 548.80 m3. If the arithmetic mean of the existing facilities is multiplied by 3.73, which corresponds to the average number of inhabitants per household according to the data established by INEC [34], a total of 386 103 people is obtained. Then, if the total residential consumption is divided for the number of people served and transformed into days, an average water consumption of 194.27 l/inhabitant/day is obtained.

In addition, Table 10 shows the variations in water consumption during one year in the ten households. The table shows an arithmetic mean variation of 15.12%, which allows to deduce that, if the variation is greater than this, there may be leaks.

Table 10. Variations of drinking water consumption in housing case studies provided by ETAPA EP

Household	Consumption arithmetic mean (m^3)	Variance	Standard deviation	Variation coefficient in %
1	30,44	23,24	4,82	15,83
2	21,53	62,48	7,9	36,69
3	75,29	96,56	9,83	13,06
4 y 5*	30	10,12	3,18	10,6
6	17,8	1,76	1,33	7,47
7	30,71	21,14	4,6	14,98
8	39,41	23,66	4,86	12,33
9	9,65	2,11	1,45	15,03
10	12,94	1,68	1,3	10,05
Arithmetic average				15,12%

* Houses 4 and 5 share a general meter.

3.2.4. Definition of assessment levels for each evaluation criterion

With the results obtained, three levels of assessment, one basic, one intermediate and one superior, are determined for each of the four evaluation criteria defined in the comparative analysis of international methods, based on Quesada's research (2014) [27].

- **Maximum consumption criterion**

Basic level

The arithmetic mean of drinking water consumption per inhabitant obtained from the measurement of 10 houses is 179.51 l/inhabitant/day (Table 5) and the consumption in the city according to the data of the municipal company during a year is 194.27 l/inhabitant/day. Both numbers are inferior to the Ecuadorian Construction Standard NEC-11 [21], which establishes that household consumption can range between 200 to 350 l/inhabitant/day.

Therefore, given that the values obtained in the case studies and actual consumption are close to 200 l/inhabitant/day, this value is established as a standard for the basic level.

Intermediate level

The surveys carried out in the 280 households show that only 6% use saving toilets (Table 2); the data obtained from the ten households (Table 5) shows that the use of potable water in toilets represents 27.98% of the total consumption.

Therefore, the use of saver toilets with a discharge of 4.8 liters is established as the intermediate level, and considering that a person uses the toilet 5 times a day, it would reflect a consumption of 24 l/inhabitant/day in toilets.

Thus, if the 27.98% consumption by toilets is taken from the total value of 200 l/inhabitant/day, the result is a consumption of 55.96 l compared to the 24 l with the use of a saver toilet, which translates to savings of 31.96 l/inhabitant/day.

The reuse of rainwater adds 40 l in savings (the justification for this data is detailed in the criterion of water reuse), finally obtaining feasible savings of 71.96 l/inhabitant/day. For this reason, a consumption between 160 and 120 l/inhabitant/day is established for the intermediate level.

Superior level

To reach the superior level, it is necessary to demonstrate drinking water consumption of less than 120 l/inhabitant/day per household.

- **Control of water consumption and leakage**

Basic level

It is necessary to establish a leakage control plan, which consists of recording the water consumed, using a meter at the entrance of the household, which enables the generation of a consumption history.

The meter must have the following characteristics: be of multiple jet and comply with the metrological requirements of classes A and B of Resolution 246; 2000 of INMETRO, of MERCOSUR standards NM 212 and ISO 4064. NTE INEN-OIML R 49-1:2009 [29], [36].

Table 10 shows that the arithmetic mean of consumption variation is 15.12%, so it can be said that a variation of more than 15% with respect to the arithmetic average of monthly consumption is an indicator of possible water leaks in the household.

In addition, adequate maintenance must be given to the water facilities, through a plan that indicates the exact place where the pipes are installed. The INEN 1373 standards required for PVC pipe, INEN 2955 and 2956 for thermofusion pipe and other standards for water pipes and fittings must be complied with. Each toilet device must have an angular key or a stopcock, in order to facilitate the maintenance and replacement of the equipment [37].

Therefore, the basic level establishes the use of pipes and sanitary equipment that comply with the aforementioned standards, installed in accordance with technical specifications of each equipment and accessory; in addition, each piece of equipment must have an angular key or a stopcock to facilitate its replacement and maintenance.

The existence of a management plan is also evaluated, which includes:

- a consumption meter that meets the aforementioned characteristics, and
- a monthly record to detect possible leaks.

- **Criteria on the use of saving devices**

Basic level

The basic level is defined in accordance with the stipulations of the local standard NTE INEN 1571: 2011 second revision 2011-07, section 3.1.6.7, for toilets.

The average maximum water consumption per discharge at a pressure of 0.3 MPA should be:

- 6.2 liters per flush for low consumption toilets
- 3.8 liters per flush for low consumption urinals

For saving devices such as faucets and showers with aerators, there is no local standard that establishes an average consumption, so the following evaluation methods are considered:

- Faucets with a maximum flow rate of less than or equal to 5/6 liters at a hydraulic pressure of 0.3 MPa.
- Showers with a maximum flow of less than or equal to 6/9 liters at a hydraulic pressure of 0.3 MPa.

The pressure implemented in the city by ETAPA is continuous service of around 0.5 and 0.7 MPa at the exit of the control meter. From the meter to the supply points, due to the loss of pressure along the path, it can reach the 0.3 MPa that is established for the saving devices.

In the same way, for lack of local regulations on the consumption of water for household appliances, evaluation methods are considered, and a consumption not greater than 40/45 liters per use and for the dishwasher not more than 7/10 liters per use is established for washing machines.

Intermediate level

To reach the intermediate level, in addition to fulfilling the conditions of the basic level, the consumption of water in toilets and urinals must be reduced. The values that are required are taken from the local standard NTE INEN 1571: 2011:

- 4.8 liters per flush for high efficiency toilets
- 1.9 liters per flush for high efficiency urinals

In the case of double-flush toilets, the maximum water consumption should be 4.8 liters per flush on average.

Superior level

For the upper level, it is necessary to comply with the requirements of the intermediate level and demonstrate an improvement in water saving, that is, use devices that have a lower consumption than the ones previously discussed.

- **Criteria for rainwater reuse systems**

Basic level

It is considered that 61% of the people from the 280 households believe in the importance of saving drinking water. In addition, in the ten cases studied, 90% of the owners would be willing to use rainwater in house cleaning, for washing vehicles, and other uses.

Therefore, the basic level contemplates the existence of a rainwater collection system in the household, where the collected water can be used for irrigation, cleaning the house, washing vehicles, and in toilets.

Intermediate level

To determine a maximum consumption range within the intermediate level, the calculation of rainwater supply that could be achieved with the cover of a minimum lot is considered. The formula that is applied is the following:

Supply = 0,8 x effective catchment area x amount of rain [38]

The arithmetic average of constructible area in minimum lots attached to the canton of Cuenca is 71.17 m^2 (Table 11) according to data taken from the ordenance plan [39]. Therefore, a land area land of 120 m^2 is established as a minimum lot, where a continuous building can be located with a frontal and posterior setback of 3 m, since it is the type of implementation

with minimum setbacks in the city. Considering this lot, a roof with a length of eaves of 0.6 m is proposed, respecting the setbacks, with which a total cover area of 85.4 m^2 would be available.

Table 11. Characteristics of minimum lots in sectors of continuous typology, taken from the Ordenance Plan of the Cuenca canton

Minimum front	Minimum area (m^2)	Front setback (m)	Back setback (m)	Buildable area (m^2)
6	75	0	3	57
7	90	3	3	48
7	100	3	3	58
7	120	3	3	78
9	150	5	3	78
9	180	5	3	108
Arithmetic average				**71,17**

Regarding the amount of rainwater, Table 12 shows the month by month arithmetic mean of rainfall in Cuenca. These data correspond to the records from the Directorate of Aviation from the last 30 years [40]. The arithmetic mean of rainfall per year is 869.9 mm, which means that an amount of 869.9 liters of rainwater per year can be captured per square meter of surface area.

Table 12. Arithmetic average of the monthly results of rainfall in mm/m2 in the city of Cuenca from 1977 to 2015. Taken from the General Directorate of Civil Aviation.

Month	Arithmetic average
January	62,4 mm
February	85,9 mm
March	113,7 mm
April	120 mm
May	85,5 mm
June	44,9 mm
July	29,8 mm
August	22,3 mm
September	48,5 mm
October	92,5 mm
November	84,2 mm
December	80,5 mm
Total	**869,9 mm**
Arithmetic average	**72,49 mm**

Applying the formula, a supply of 4.26 m^3 is obtained for the month of January:

$$\begin{aligned} Supply &= 0,8 \times 85,4m^2 \times 62,4mm \\ &= 4,26m^2 \end{aligned}$$

Table 13 shows the amounts of rainwater that could be collected monthly in the partial supply column. The following column shows the accumulated amount per month, and in the last column, the difference in the collection with respect to the previous month is determined. As seen, it is possible to capture a total of 59.45 m3 of rain water per year. If this data is divided for 3.73 inhabitants per household, and it is converted to l/inhabitant/day, it is determined that 43.66 l/inhabitant/day of rainwater can be used. Therefore, a daily rainwater supply of 40 l/inhabitant/day can be established. This number corresponds to 20% of the total water demand of 200 l/inhabitant/day, and represents 4.5 m^3 of water that could be used in toilets, for laundry and for house cleaning.

If the same example of minimum cover is incorporated as a collection area in the laundry yard and garage zones, an area of 21 m^2 of catchment would be increased, so that a total of 55 l/inhabitant/day of rainwater could be incorporated.

Therefore, the intermediate level is defined as the use of between 40 l/inhabitant/day and 55 l/inhabitant/day of rainwater for laundry, irrigation of gardens, household cleaning and toilets.

Superior level

At the superior level, the household should have a rainwater catchment system, which can incorporate an amount greater than 55 l/inhabitant/day for use in laundry, garden irrigation, household cleaning and toilets.

Table 13. Calculation of the catchment volume

Month	Arithmetic mean	Supply (m^3)		Demand (m^3)		Difference (m^3)
	(mm)	Partial	Acumulated	Partial	Acumulated	
January	62,4	4,26	4,26	4,5	4,5	-0,24
February	85,9	5,87	10,13	4,5	9	1,13
March	113,7	7,77	17,9	4,5	13,5	4,4
April	120	8,2	26,1	4,5	18	8,1
May	85,5	5,84	31,94	4,5	22,5	9,44
June	44,9	3,07	35,01	4,5	27	8,01
July	29,8	2,04	37,05	4,5	31,5	5,55
August	22,3	1,52	38,57	4,5	36	2,57
September	48,5	3,31	41,88	4,5	40,5	1,38
October	92,5	6,32	48,2	4,5	45	3,2
November	84,2	5,75	53,95	4,5	49,5	4,45
December	80,5	5,5	59,45	4,5	54	5,45

4. Conclusions

This research demonstrates the possibility of reducing the consumption of drinking water up to 30% in homes in the city of Cuenca, without affecting the quality of life of its inhabitants, through the application of sustainable strategies.

Projecting the percentage of savings in consumption (30%) to the entire city of Cuenca, the current consumption of 27 377 549 m^3 (Table **??**) would be reduced to 19,164,284 m^3, a situation that would ensure that the existing infrastructure provides potable water service for more years than expected, avoiding short-term costs due to new infrastructures and consequent damage to the ecosystem.

Making an economic valuation, a consumption of 200 l/inhabitant/day (basic level) for a house of four inhabitants, equals an average of 24 m^3 at a rate of \$0.60 per m^3 plus \$3.00 charge, resulting in a cost of \$17.40. However, if the requirements of intermediate level of the analyzed criteria are met, consumption would be reduced in the worst case to 140 l/inhabitant/day, with which a family of four members would consume an average of 16.8 m^3, generating a cost of \$9.72, which represents savings of \$7.68 per month, equivalent to 44%.

Finally, the present study could be taken as a reference to establish a reduction of water consumption standards in the local norm, since it was observed that in Cuenca consumption is 194.27 l/inhabitant/day, a value relatively below that established by the national norm. If the savings resulting from the use of efficient toilets is added, taking into account that the use of this type of toilets is more and more common, this would result in an approximate consumption of 162 l/inhabitant/day, a value which is 20% below the national standard.

References

[1] A. A. Bohórquez Panche, K. P. Zabaleta Rodríguez, and A. Chávez Porras, "Programa de ahorro y uso eficiente del agua para la empresa empucol del municipio el colegio, cundinamarca," *Universidad Militar de Nueva Granada*, 1996. [Online]. Available: https://goo.gl/K3cJ8M

[2] UNESCO, "Agua para todos, agua para la vida," Organización de las Naciones Unidas para la Educación, la Ciencia y la Cultura, 2003. [Online]. Available: https://goo.gl/wqfjHN

[3] ONU, "El derecho humano al agua y al saneamiento," Organización de las Naciones Unidas, 2010. [Online]. Available: https://goo.gl/mXL8TG

[4] J. Frausto Ortega, "Abasto del agua en la frontera norte de tamaulipas," *Frontera norte*, vol. 28, no. 55, pp. 153–182, 2016. [Online]. Available: https://goo.gl/NgiVBF

[5] J. Morrison, S. L. Postel, and P. Gleick, "Sustainable use of water in the lower colorado river basin," Pacific Institute, 1996. [Online]. Available: https://goo.gl/Jh4JF7

[6] L. E. Cervera Gómez, "Indicadores de uso sustentable del agua en ciudad juárez, chihuahua," *Estudios fronterizos*, vol. 8, no. 16, pp. 9–41, 2007. [Online]. Available: https://goo.gl/VJDaQo

[7] GBC España, "Residencial oficinas. guía para los evaluadores acreditados. nueva edificación residencial oficinas," 2015. [Online]. Available: https://goo.gl/BPNDBZ

[8] U.S. Green Building Council , "Leed®for homes rating system multifamily mid-rise | october

2010," in *California Version, 2011 Update*, 2011. [Online]. Available: https://goo.gl/nMzXX9

[9] BRE Global Ltd., *Manual BREEAM es vivienda 2011*, BREEAM Vivienda, 2011. [Online]. Available: https://goo.gl/DEDQVF

[10] V. Corral Verdugo, B. S. Fraijo Sing, and C. Tapia Fonllem, "Un registro observacional del consumo individual de agua: Aplicaciones a la investigación de la conducta sustentable," *Revista mexicana de análisis de la conducta*, vol. 34, no. 1, pp. 79–96, 06 2008. [Online]. Available: https://goo.gl/ZmdLuX

[11] M. C. Bustamante Martínez, K. L. Cárdenas Chalá, and J. L. Corredor Rivera, "Formulación del programa de ahorro y uso eficiente de agua para la empresa de servicios públicos del municipio gachetá-cundinamarca„" *Revista Gestión Integral en Ingeniería Neogranadina*, vol. 3, no. 2, 2011. [Online]. Available: https://goo.gl/gEgNey

[12] F. Suárez, J. Santamarta, and A. Suárez, *Hidrología y recursos hídricos en islas y terrenos volcánicos: Métodos, Técnicas y Experiencias en las Islas Canarias*, 05 2013, ch. El transporte hidráulico, pp. 251–263. [Online]. Available: https://goo.gl/pGi92j

[13] P. H. Gleick, D. Haasz, C. Henges-Jeck, V. Srinivasan, K. Kao Cushing, and A. Mann, *Waste Not , Want Not?: The Potential for Urban Water Conservation in California*, E. Pacific Institute for Studies in Development and Security, Eds. Pacific Institute, 2003. [Online]. Available: https://goo.gl/tyXwQk

[14] M. Pacheco Montes, "Avances en la gestión integral del agua lluvia (giall): Contribuciones al consumo sostenible del agua , el caso de lluviatl en méxico," *Revista Internancional de Sostenibilidad Tecnología y Humanismo*, no. 3, pp. 39–57, 2008. [Online]. Available: https://goo.gl/AcsQwi

[15] A. Khastagir and N. Jayasuriya, "Optimal sizing of rain water tanks for domestic water conservation," *Journal of Hydrology*, vol. 381, no. 3, pp. 181–188, 2010. DOI: https://doi.org/10.1016/j.jhydrol.2009.11.040.

[16] J. Gamboa, "Diseño de una instalación sanitaria automática para ahorro de agua en una batería de baño público institucional," Tesis de grado. Universidad Tecnológica de Pereira. Colombia, 2014. [Online]. Available: http://hdl.handle.net/11059/5130

[17] P. J. Kestler Roja, "Uso, reuso y reciclaje del agua residual en una vivienda," Tesis de grado. Universidad Rafael Landívar. Guatemala, 2004. [Online]. Available: https://goo.gl/MfSmFg

[18] D. G. Manco Silva, J. Guerrero Erazo, and A. M. Ocampo Cruz, "Eficiencia en el consumo de agua de uso residencial," *Revista Ingenierías Universidad de Medellín*, vol. 11, no. 21, pp. 23–38, 2012. [Online]. Available: https://goo.gl/zXNm1W

[19] M. A. Reyes Fillo, J. Lara Ávila, and L. Sánchez, "Tecnología de pruebas de medidores de agua de tipo domiciliario en el IMTA," IMTA. Instituto Mexicano de Tecnología del agua., Tech. Rep. 40, 2010. [Online]. Available: https://goo.gl/MA48wP

[20] G. Howard and J. Bartram, "Domestic water quantity, service level and health," WHO. World Health Organization, Tech. Rep., 2003. [Online]. Available: https://goo.gl/5hxpgM

[21] MIDUVI, *Norma Hidrosanitaria NHE agua*, Ministerio de Desarroloo Urbano y Vivienda. Ecuador Std., 2011. [Online]. Available: https://goo.gl/YdmRda

[22] ETAPA EP. (2016) Agua potable. Empresa Pública Municipal de Telecomunicaciones, Agua Potable, Alcantarillado y Saneamiento. Cuenca – Ecuador. [Online]. Available: https://goo.gl/bch4Mt

[23] SENPLADES. (2010) Proyecciones referenciales de población cantonal según años en grupos de edades. Secretaría Nacional de Planificación y Desarrollo. Ecuador. [Online]. Available: https://goo.gl/fzNeRw

[24] B. G. Municipal, *Cuenca. Ciudad sostenible / plan de acción*, Banco Interamericano de Desarrollo. Gobierno Autónomo Descentralizado de la ciudad de Cuenca. Ecuador, 2014. [Online]. Available: https://goo.gl/vQVkVQ

[25] E. Lentini and G. Ferro, *Politicas tarifarias para el logro de los Objetivos de Desarrollo del Milenio y el derecho humano al agua y al saneamiento*, C. C. económica para américa latina y el caribe., Ed. Serie. Recursos Naturales e Infraestructura, 2014. [Online]. Available: https://goo.gl/Kpdxvr

[26] JSBC/IBEC. (2010) Comprehensive assessment system for built environment efficiency (casbee). Japan Sustainable Building Consortium. Institute for Building Environment and Energy Conservation. [Online]. Available: https://goo.gl/V1T4Fg

[27] F. Quesada Molina, "Métodos de evaluación sostenible de la vivienda?: Análisis comparativo

de cinco métodos internacionales," *Revista Habitat Sustentable*, vol. 4, no. 1, pp. 56–67, 2014. [Online]. Available: https://goo.gl/s3evad

[28] Elster, *Medidor Unijato Residencial Agua Caliente*, Elster. Vital Connections, 2010. [Online]. Available: https://goo.gl/KTtA8t

[29] ——. Medidor elster m170. Elster Iberconta. [Online]. Available: https://goo.gl/t71mEX

[30] INEN, *Medidores de agua para agua potable frÍa y agua caliente. Parte 2: MÉtodos de ensayo.*, Instituto Ecuatoriano de Normalización Std., 2016. [Online]. Available: https://goo.gl/7XH2q5

[31] IEOS, *Normas para estudio y diseño de sistemas de agua potable y disposición de aguas residuales para poblaciones mayores a 1000 habitantes.* Instituto ecuatoriano de obras sanitarias., 1992. [Online]. Available: https://goo.gl/vo4k67

[32] ——, *Norma de diseño para sistemas de abastecimiento de agua potable, disposición de escretas y residuos líquidos en el área rural.* Instituto ecuatoriano de obras sanitarias., 2014. [Online]. Available: https://goo.gl/y7kG7w

[33] A. Jiménez Marín and M. Marín Arias, "Diseño de un programa de uso eficiente y ahorro del agua para el acueducto 'Asamun' de la vereda mundo nuevo de la ciudad de Pereira," Tesis de grado. Universidad Tecnológica de Pereira, 2007. [Online]. Available: https://goo.gl/uigpq4

[34] INEC, "Promedio de personas por hogar a nivel nacional," Instituto Nacional de Estadísticas y Censos. Ecuador, Tech. Rep., 2010. [Online]. Available: https://goo.gl/5SXiUT

[35] F. I. Arreguin Cortés, "Uso edficiente del agua," *Ingeniería Hidráulica en México.*, no. 2, pp. 9–22, 1991. [Online]. Available: https://goo.gl/zCmYxz

[36] INEN, *Medidor de agua para agua potable fría y caliente. Parte 1: Requisitos Metrológicos y Técnicos*, Instituto Ecuatoriano de Normalización Std., 2009. [Online]. Available: https://goo.gl/7XH2q5

[37] G. Vázquez Arenas, "Manual de instalaciones de fontanería, evacuación y saneamiento y energía solar en edificación," Universidad Politécnica de Cartagena, 2011. [Online]. Available: https://goo.gl/gA4uSL

[38] I. Adler, G. Carmona, and J. A. Bojalil, "Manual de captación de aguas de lluvia para centros urbanos," El portal del agua desde México, 2013. [Online]. Available: https://goo.gl/zbe3hb

[39] GAD Cuenca, "Reforma, actualización, complementación y codificación de la ordenanza que sanciona el plan de ordenamiento territorial del cantón cuenca: Determinaciones para el uso y ocupación del suelo urbano," 2003. [Online]. Available: https://goo.gl/S7rc4f

[40] DGAC, "Pluviocidad histórico del cantón cuenca," Dirección general de aviavión civil. Cuenca – Ecuador, 2016.

Scientific Paper / Artículo Científico

UNIVERSIDAD POLITÉCNICA SALESIANA ECUADOR
INGENIUS
Revista de Ciencia y Tecnología
https://doi.org/10.17163/ings.n20.2018.04
pISSN: 1390-650X / eISSN: 1390-860X

Prediction of thermal impact reduction in a double wall building

Predicción de la reducción del impacto térmico en un edificio con doble pared

Marcelo Eduardo Berli[1,*], Agustín Brondino[1], José Di Paolo[1]

Abstract

In Santa Fe de la Vera Cruz city, Argentina, a building that includes elements of sustainable architecture, energy efficiency and comfort based on the use of natural resources is being built. Specifically, a double facade design on the front walls is meant to achieve an air chamber that prevents heat transfer from the outside to the inside in summer and vice versa in winter. In this work, a numerical study is presented for the evaluation of the thermal performance of a cavity (air chamber) interposed in a double facade of the building for different climatic conditions, considering two air chambers alternatives: connected and non connected to the outside. Both cases are energetically compared with the standard facade design without chamber. The results show that for summer conditions, a chamber connected to the outside would be the most efficient design, while for winter, the closed cavity is the best saving-energy alternative.

Keywords: computer simulation, energy saving, environment conditioning, sustainable architecture.

Resumen

En la ciudad de Santa Fe de la Vera Cruz, Argentina, se está construyendo un edificio de altura que incluye elementos de arquitectura sustentable, eficiencia energética y confort logrado con la utilización de recursos naturales. Particularmente, un diseño de doble fachada en los frentes que dan al exterior para lograr una cámara de aire que impida la transferencia térmica desde el exterior al interior en verano y al revés en invierno. Este trabajo presenta un estudio numérico de la evaluación del desempeño térmico de la cavidad interpuesta en la doble fachada del edificio, para distintas condiciones climáticas, considerando dos alternativas de diseño: cámara de aire cerrada y cámara de aire conectada con el exterior. Ambos casos se comparan con la situación de inexistencia de la cámara, cuya transferencia de energía térmica se constituye en el caso patrón. Los resultados muestran que para las condiciones de verano, la cavidad con conexión al exterior sería la más recomendable, mientras que para el invierno, la cavidad cerrada es más apta para el ahorro de energía.

Palabras clave: acondicionamiento de ambientes, arquitectura sustentable, ahorro de energía, simulación computacional.

[1,*]PID-UTN AMUTIFE 3457, Research Group in Fluid Mechanics, Universidad Tecnológica Nacional, Santa Fe, Argentina. Autor para correspondencia ✉: mberli@santafe-conicet.gob.ar,
https://orcid.org/xxxx-xxxx-xxxx-xxxx, https://orcid.org/xxxx-xxxx-xxxx-xxxx
https://orcid.org/xxxx-xxxx-xxxx-xxxx

Received: 14-05-2018, accepted after review: 18-06-2018

Suggested citation: Berli, M. E.; Brondino, A. and Di Paolo, J. (2018). «Prediction of thermal impact reduction in a double wall building». Ingenius. N.°20, (july-december). pp. 39-47. doi: https://doi.org/10.17163/ings.n20.2018.04.

1. Introduction

The Jerárquicos Salud mutual society of the city of Santa Fe de la Vera Cruz, Argentina, is building a high-rise administrative building that includes elements of sustainable architecture, is energy efficient and achieves comfort based on the use of the greatest amount of natural resources possible (Figure 1-a). For this purpose, the east, west and southern sides were designed with a double façade that runs from the ground floor to the top floor, which consists of an external and an internal wall of different materials, both separated by a 50 cm thick space of air, as seen in the detail of Figure 1-b. In this way, an air chamber is created that physically separates the external and internal facade and has the objective of achieving thermal insulation between the exterior and the interior of the building. The air chamber of each floor communicates with the chambers of the upper and lower floors by means of circulation holes made in the slab.

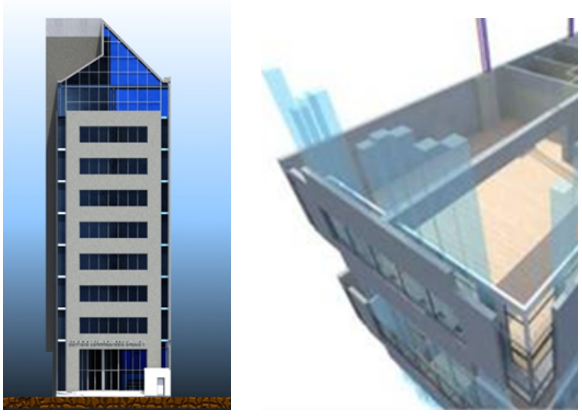

(a) (b)

Figure 1. a) Scheme of the building with double facade. b) View in section and perspective of the double facade.

Because the air chambers of each floor are interconnected, there is a possibility that an air flow can be generated that totally or partially covers the height of the building. This flow would be beneficial from the thermal point of view, especially for the summer periods, since air circulation acts as a barrier that reduces heat transmission from the external side to the internal and transports a significant amount of thermal energy towards the outside of the building, avoiding its entry. The translation in thermal comfort and reduction of the energy consumption in the interior is direct, regulating, in addition, the environmental conditions of the workspaces with greater effectiveness.

However, the potential thermal and energy benefits of the current design, its effective operation and possible modifications required as the work progresses in order to to optimize thermal behavior, are not directly predictable, requiring at this stage experimental and predictive and/or computational tools.

An experimental study of the interconnected air chambers and their thermal performance requires a high investment in materials, time and human resources. On the other hand, the studies carried out by computational simulation yield numerical predictions whose results which help obtain inferences that orient experimentation towards more accurate values. Numerical results guide the design, and the success of their predictive power is based not only on them being based in physical laws, but also on their ability to adapt to new ideas and explore a large number of alternatives.

This work presents the numerical study of the thermal performance of a cavity interposed in the double facade of the building, through computer simulations for different climatic conditions, considering two design alternatives: closed air chamber and air chamber with connection to outside air currents.

The results show that for summer conditions, the design of the cavity implies a significant reduction in thermal energy that would enter the building. Among the alternatives analyzed, the designs of the cavity with connection to the outside would be the most recommended in summer and closed chamber would be the most suitable for winter.

2. Materials and methods

The work is constituted as a computational theoretical work, based on hypotheses about the phenomenon of thermal transfer in the air chamber produced by the double façade. These considerations are summarized in turbulent flow and thermal transfer dominated by convection [1–4] and are listed below:

1) Stationary state because the atmospheric conditions to which the building is exposed vary very slowly during a day, this approach is acceptable and used for the most demanding conditions of the summer and winter seasons.

2) The thermal transfer between the floors occurs only through the circulation holes, assuming that the slabs are perfect insulators. This means that, when calculating the thermal energy that enters each floor, said energy can only come from sources that are connected to the chamber, that is, from the outside and from the air chambers of adjacent floors.

3) There is no contribution of thermal energy by artifacts, people, lights or other sources. This simplification is done to study only the energy savings that result from the existence of the air chamber.

4) The contribution of thermal energy by radiation from the external wall to the internal one is neglected.

5) The moisture content of the air circulating in the cavities is negligible.

6) The air flow in the cavities develops in a turbulent regime. Because the goal is not to have detailed information of the boundary layer in the contact between the walls and the air, a turbulence model of the k-ε type was used, applied in an advanced simulation software.

7) The internal and external walls are assumed to be smooth.

2.1. Definition of the area where the simulations will be carried out

As mentioned in the introduction, this work consists in the study of a physical model that is representative of the cavity whose thermal performance is to be studied. As is known, the availability of computer tools with high computing capacity facilitates the solution of complex problems such as the one addressed in this work. However, since the availability of resources is limited, the size of the problem under study must be reduced in such a way that it is solvable and that, at the same time, ensures the portion studied is representative of the whole problem. In the case of the cavity under study, the simulation of the problem in all of its dimensions is computationally very expensive. For this reason, it is possible to section the problem in a portion whose dimensions contain all the geometric characteristics that condition the air flow in the chamber, so that the behavior of the rest of the cavity can be considered as a repetition of the portion studied. The selection of said portion can be seen in Figure 2-a (transparent prism of orange edges). The prism that delimits the selected area consists of a portion of the chamber corresponding to any floor of the building. If a a photograph of a top view of said chamber was taken, the result would be an image like the one shown in the orange box of Figure 2-b, where the presence of the circulation hole made in the corresponding floor slab and connecting the air chamber with the one of the previous floor can be observed.

As observed in Figure 2-b, the adjacent rectangular section (blue box) and the selected one (orange box) are arranged so as to mirror each other. From a physical point of view, this fact implies a symmetry in the geometry, indicating that the solution of the problem in the orange box section is the same as in its contiguous section (blue box), but mirrored. Mathematically speaking, this means that the derivatives of the variables involved, with respect to the horizontal direction, are null. Thus, the scheme of the two holes in Figure 2-b is repeated with the same positions, each slab dividing the two adjacent floors.

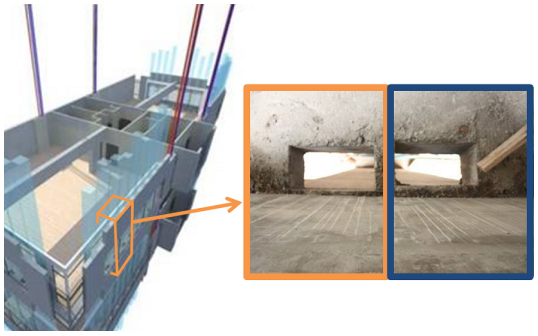

(a) (b)

Figure 2. a) Portion selected for the simulation. b) Circulation holes made in the slab.

As there is a repeated scheme, it is acceptable to solve the problem in the selected portion with standard computational resources. If the interior and exterior wall portions are added to this selection, between which the air chamber and the holes in the slabs are located, the definition of a simulation module is reached, which can be seen in Figure 3. The dimensions and materials of each module are the following:

- External wall: built of concrete, 20 cm thick, 3.45 m high and 70 cm wide.
- Internal wall: built of concrete, 7 cm thick and other dimensions equal to the external wall.
- Air chamber: 50 cm thick and other dimensions equal to the outer wall.
- Holes: 20 cm × 40 cm horizontal section and a thickness (in the slab) of 25 cm.

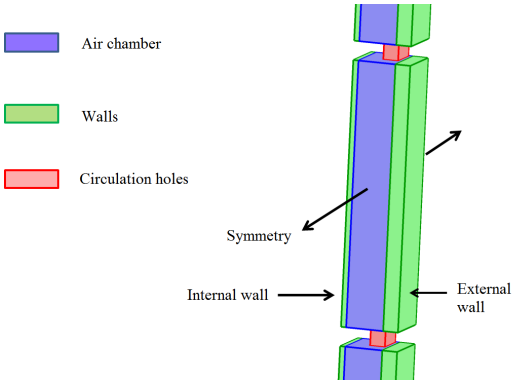

Figure 3. Geometric diagram of the simulation module.

The sum of all the modules through the circulation holes will define the total geometry for the simulation of the problem to be solved. That is, 8 modules like the one in Figure 3, interconnected by the circulation holes.

2.2. Model equations and resolution methodology

The movement of air inside the cavity is mainly due to flotation forces associated with the density gradients that are caused by the difference in temperatures between the walls that generate the cavity. This phenomenon is known as natural convection and its dynamics have been described in previous works by means of the Boussinesq approximation. This approximation considers density variations only in volumetric forces, by means of a linear function with the change in temperature and with validity for incompressible laminar flow and low thermal gradients.

In the simulated cavity, thermal gradients are usually higher than the limits of validity of the Bousinesq approximation [5]. For this reason, and in order to move towards more realistic simulations, a compressible flow model is used in this work, assuming turbulent flow in a stationary state and neglecting the effects of radiation on energy transfer. In this way, the differential equations that describe the flow of natural convection are as follows:

Continuity

$$\nabla \cdot (\rho \mathbf{u}) = 0 \tag{1}$$

Amount of movement

$$\begin{aligned}\rho(\mathbf{u}\cdot\nabla)\mathbf{u} = \nabla\cdot\Big[&-P\mathbf{I} + (\mu+\mu_T)(\nabla\mathbf{u}+(\nabla\mathbf{u})^T)\\ &-\frac{2}{3}(\mu+\mu_T)(\nabla\cdot\mathbf{u})\mathbf{I} - \frac{2}{3}\rho k\mathbf{I}\Big]\\ &+(\rho-\rho_0)\mathbf{g}\end{aligned} \tag{2}$$

Energy

$$\rho C_p \mathbf{u}\cdot\nabla T = \nabla\cdot(k_A\nabla T) \tag{3}$$

where $\mathbf{u}$ is the velocity vector, ρ is air density, $\rho 0$ is air density at ambient temperature (external), P is the modified pressure, g is the acceleration of gravity, μ is air viscosity, μ_T is turbulent viscosity, k is turbulent kinetic energy, C_p is the air's heat capacity, k_A the thermal conductivity of the air and T the temperature.

To describe the turbulent flow, the k-ε model was used, which has been shown to be the most accurate for the calculation of air movement inside rooms in houses and buildings [6]. However, it should be noted that its precision decreases very close to the walls, where models such as the k-ε of low Reynolds number promise a better description of the velocity and temperature profiles [7]. However, this study aims to show the general benefits of the system and not an exact prediction of the values that are calculated near the walls, in which case the description of the k-ε model is very useful for a first estimation and leads to results that require much less computational cost and are more quickly obtained, the latter being desirable in studies required for the decision making of construction companies. Thus, in addition to the conservation equations, the following are added: the equation (4) of turbulent kinetic energy variation and the equation (5) of turbulent dissipation velocity:

$$\rho(\mathbf{u}\cdot\nabla)k = \nabla\cdot\left[\left(\mu+\frac{\mu_T}{\sigma_k}\right)\nabla k\right] + P_k - \rho\epsilon \tag{4}$$

$$\begin{aligned}\rho(\mathbf{u}\cdot\nabla)k =&\nabla\cdot\left[\left(\mu+\frac{\mu_T}{\sigma_\epsilon}\right)\nabla\epsilon\right] + C_{\epsilon 1}\frac{\epsilon}{k}\Big(\mu_T\cdot\\ &\left[\nabla\mathbf{u}:(\nabla\mathbf{u}+(\nabla\mathbf{u})^T) - \frac{2}{3}(\nabla\cdot\mathbf{u}^2)\right]\\ &-\frac{2}{3}\rho k\nabla\cdot\mathbf{u}\Big) - C_{\epsilon 2}\rho\frac{\epsilon^2}{k}\end{aligned} \tag{5}$$

Turbulent viscosity μ_T is defined by Equation (6).

$$\mu_T = C_\mu\rho\frac{k^2}{\epsilon} \tag{6}$$

The parameters of equations (4) to (6) are considered constant, with the following values [5]:

$$\begin{aligned}C_{\epsilon 1} &= 1,44\\ C_{\epsilon 2} &= 1,92\\ C_\mu &= 0,09\\ \sigma_k &= 1\\ \sigma_\epsilon &= 1,3\end{aligned}$$

2.2.1. Condiciones de contorno

Contour conditions

The k-ϵ turbulent flow model used does not solve the profile of velocities against the solid wall but uses wall functions that model the high velocity and temperature gradients that occur in that zone. For this, in addition to the water impermeability condition defined by Equation (7) and the null kinetic energy flow, defined by Equation (8), Equation (9) using a wall function was implemented:

$$\mathbf{u}\cdot\mathbf{n} = 0 \tag{7}$$

$$\nabla k\cdot\mathbf{n} = 0 \tag{8}$$

$$\begin{aligned}\Big[(\mu+\mu_T)(\nabla\mathbf{u}+(\nabla\mathbf{u})^T) - \frac{2}{3}(\mu+\mu_T)(\nabla\cdot\mathbf{u})\mathbf{I}\\ -\frac{2}{3}\rho k\mathbf{I}\Big]\mathbf{n} = -\rho\frac{u_\tau}{\delta_w^+}\mathbf{u}_{tang}\end{aligned} \tag{9}$$

With

$$\epsilon = \rho \frac{C_\mu k^2}{K_v \delta_w^+ \mu}$$

Where $\mathbf{u}_{tang}$ is the tangential velocity, defined as $\mathbf{u}_{tang} = \mathbf{u} - (\mathbf{u} \cdot \mathbf{n})\mathbf{n}$, u_τ is friction speed, K_v is the Von Kármán constant and δ_w^+ is the dimensionless thickness of the wall function. In addition, normal voltage equal to zero was assumed in the inlet and outlet holes, $\tau \cdot \mathbf{u}$, and the pressure at the lower entrance was arbitrarily defined as equal to 0.

Constants in each simulation, the temperatures of the walls that delimit the cavity, and the conditions of symmetry in the cuts that are seen in Figure 3 were considered for the thermal analysis. The temperature of the air entering the cavity is also assumed to be constant and equal to the ambient temperature (T_a).

The differential equations presented, along with their corresponding boundary conditions, are solved numerically using the finite element method with the COMSOL 4.4 commercially licensed software.

2.2.2. Verification of the flow regime

Previous works [1–4, 8, 9] have addressed the analysis of the phenomenon of natural convection in representative air cavities (ceilings, among others) by laminar flow models. However, due to the dimensions of the cavities in this work and the properties of the air, it is reasonable to expect that under normal conditions the flow may be turbulent, which had to be corroborated prior to the selection of the model. For this purpose, the Reynolds number and the Grashof number were used as dimensionless parameters, which were estimated using the physical properties of dry air presented in Table 1. These properties were adopted for normal atmospheric pressure (10^5 Pa) and 30 °C [10], corresponding to the ambient temperature (reference) used in the model.

Table 1. Physical properties of dry air at 30°C and atmospheric pressure

Description	Value
Density (ρ)	1,205 [kg/m^3]
Viscosity (μ)	1,82e-5 [N s/m^3]
Thermal conductivity (k_A)	0,0257 [W/(m K)]
Heat capacity (C_p)	1,005 [kJ/(kg K)]
Coefficient of thermal expansion (β)	3,43e^{-3} [1/K]

The Reynolds number compares the relationship between inertial forces and viscous forces and is defined by the ratio $R_e = \rho U_c L/\mu$, withU_c and L representing the speed and length characteristic to the model. On the other hand, the Grashof number indicates the relationship between the flotation forces and viscous forces, and is defined by the relation $Gr = \rho^2 g \beta \Delta T L^3/\mu^2$, where ΔT is the temperature difference characteristic of the system under study. When the flotation forces are, by comparison, higher than the viscous forces, the regime is considered to be turbulent. The transition between these two regimes for vertical plates is given for a Gr of the order of 10^9 [10].

If the floating flow velocity $U_c = (g\beta\Delta T L)^{1/2}$, the length $L = 3m$ equal to the height of each chamber between two contiguous floors, and the temperature difference between the two walls of the double facade, $\Delta T = 56\ ^\circ C$ are defined as characteristic parameters, the resulting values of $Re \approx 10^6$ and $Gr \approx 10^{11}$ clearly indicate the existence of a turbulent or transition regime, but not laminar. Thus, the results presented in the following section correspond to an air flow inside the cavity that is in a turbulent regime for all the simulated conditions.

3. Results and discussion

The first case demanding study is that of extreme conditions in summer. The section of the external wall in contact with the outside has a temperature of 70 °C, assuming it is exposed to the incidence of the sun in the hours of maximum temperature. On the other hand, the section of the inner wall in contact with the interior of the building has a temperature considered to be pleasant for a working environment, that is, 24 °C. As the objective is to study the thermal performance of the cavity, it is reasonable to first consider the situation of absence of cavity, assuming the external and internal walls are in direct contact, and also suppressing the circulation holes. It should be noted that, in the case of an absence of cavity, both walls are conserved, since having only the external wall would mean that the results would be modified not only by the inclusion of the cavity but also by the addition of another wall, in which case the analysis could not focus only on the existence or absence of the cavity.

3.1. Witness situation: absence of cavity

Figure 4 shows a diagram of the conditions in which the simulation was performed.

Because there are no circulation holes, consideration 2) of section 2 allows for the calculation of the thermal energy transfer of one module independent of the others. Given this situation, a thermal energy input of 204 W/m^2 has been calculated in each module, a value which will be used in the following cases. It should be clarified that, unlike the coming cases, the only thermal transmission mechanism is conduction. For this reason the obtained value can be checked using the Fourier law.

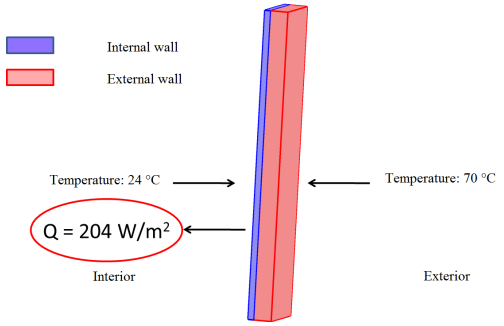

Figure 4. Simulation conditions and thermal energy for absence of cavity.

3.2. Cavity without connection to the exterior

The second case analyzed consists of the air chamber without connection to the outside. That is, although the chambers of all the floors are interconnected through the holes, none of the chambers has any opening that connects them to the external environment of the building. The air will thus be trapped in the chambers and there can only be circulation through the holes. The temperature difference between the external and internal walls generates variations in air density and therefore natural convection [8,9] as shown in Figure 5.

It can be observed that the air in contact with the hottest wall (in red) rises and increases its temperature (the green areas imply a higher temperature than the light blue ones), while in the vicinity of the cold wall (in blue) the air descends and the temperature decreases. In this way, there is a movement of air by the physical phenomenon of natural convection, by which the air transmits thermal energy not only by conduction, but also by convection.

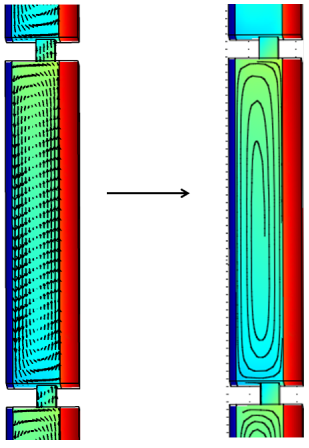

Figure 5. Side view of a module showing air circulation. Left: velocity vectors. Right: current lines.

When quantifying the heat transmitted for this scheme, the resulting value is 51 W/m^2, which means that the reduction of thermal energy that would enter from the outside is 75% with respect to the values of section 3.1.

Given this result, it can be questioned whether the reduction obtained is reasonable. In order to answer this question, it can be assumed that the air trapped in the chamber was stagnant without performing recirculation movements, in which case the energy transferred to the interior would be 2.3 W/m^2 (calculation that can also be performed with Fourier's law), implying a reduction of 99%. These values are in accordance with the fact that air is a poor heat conductor, having a thermal transmission coefficient of 0.025 (W/mK) in comparison, for example, with concrete whose coefficient is 1.5 (W/mK), 60 times higher than that of air. The fact that the reduction is 75% and not 99% is because the movement of the air transfers additional heat by convection.

It should be noted that since there is no connection with the outside, it was found that the air recirculates inside a module and, therefore, there is no flow through the circulation holes, there is no transfer of energy between the modules. This results in the thermal energy flow to the interior being identical in each module. Of course, this is an idealized situation in which all floors are at the same internal temperature and consequently there are no differences in temperatures that could cause a convective movement between the floors.

This result indicates that the mere existence of the air chamber can result in significant energy savings when maintaining a pleasant internal environment.

3.3. Cavity with connection to the outside and natural flow

To simulate the connection of the chambers with the exterior, holes of similar dimensions are assumed to be the circulation holes in the outer walls of the first and last floor modules. That is, section holes of 20 cm by 40 cm and the thickness of the outer wall (20 cm). For the first floor, the hole was designed in the lower lateral part of the first module, as shown in Figure 6-a, while for module 8 the hole was made in the upper lateral part, as shown in 6-b.

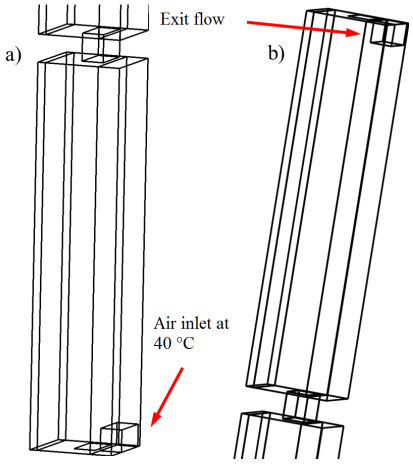

Figure 6. a) Hole that connects the lower module with the exterior. b) Hole that connects the upper module with the exterior.

To carry out the simulation, the same conditions as for case 3.2 were considered, but since in this case there may be air entry from the outside, it is assumed that it is at an elevated summer temperature of 40 °C. The conditions of entry and exit in the first and last module respectively, are indicated in Figure 6, while for the remaining modules the external and internal temperatures are maintained.

The presence of connections with the outside enable a flow that covers all the floors, from the first to the last. Indeed, the results indicate the existence of this flow, as seen in Figure 7. This figure shows, in a side view of the side furthest from the circulation orifice, that the air maintains some recirculation leading to similar effects as in case 3.2, but the side view near the orifice shows the existence of a flow that passes through the cavity from the lower module to the upper one. This circulation would be a way of venting the cavity to avoid the possible stagnation of humidity and the generation of bad odors.

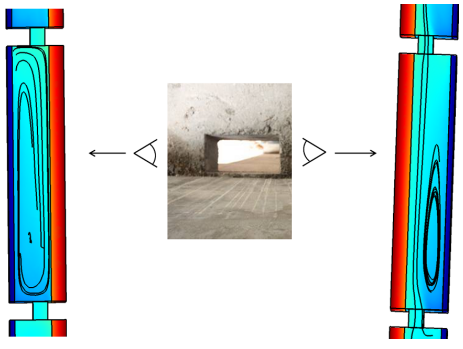

Figure 7. Circulation diagrams by natural convection in the cavities.

As for energy saving, the existence of circulation between the modules modifies the individual performance of each one. The lower modules are benefited since the flow of air from the outside absorbs a certain amount of thermal energy from the hottest wall and transports it by convection to an upper module, so that the higher the modules, the higher amount of energy they receive from the air absorbed from the lower modules.

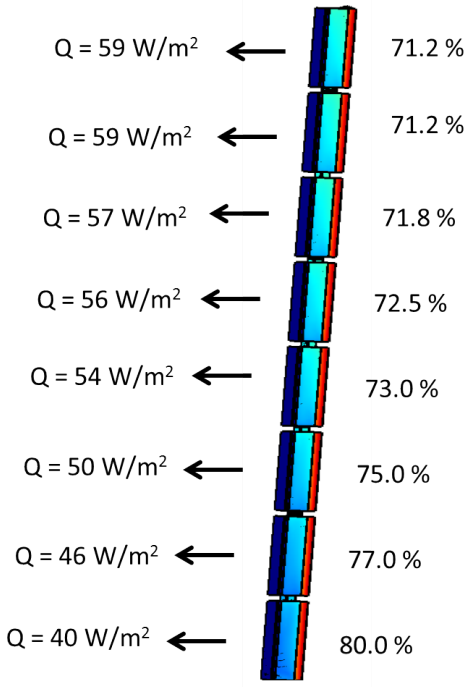

Figure 8. Thermal performance of the 8 modules. The percentages indicate the reduction in the heat transfer of each floor with respect to the situation without an air chamber.

Figure 8 shows the thermal energy transfers and the reduction percentages for each module with respect to case 3.1. It can be observed that the first three modules have a thermal performance equal to or higher than in the case 3.2, however, the savings decrease. Overall, the average reduction between the 8 modules is 74%, very similar to the previous case. In addition, these results can be useful at the time of plotting the occupation of each floor.

4. Simulations for winter conditions

The presence of the cavity, according to the numerical results of this study, shows a very good thermal performance in summer conditions, but it remains to be seen if this behavior is representative of conditions in a winter day. For this purpose, the temperatures of the external wall and of the air were modified, which, in the case of the cavity with connection to the outside, would enter from outside. It should be mentioned that for winter conditions, energy flows outwards, since the situation reverses with respect to summer. In addition, the geometry pattern that arises from subtracting the

cavity to have a comparison reference is maintained. The boundary conditions are as follows:

Internal wall temperature: 24 °C.
External wall temperature: 10 °C.
Ambient air temperature: 10 °C.

This condition would imply a poor incidence of the sun on the external wall and therefore it remains at the same temperature as the outside air.

For the cavity with connection to the outside and natural flow, the results outlined in Figure 9 show that the reduction in energy losses from the interior to the atmosphere is 63%. Although it is an acceptable value, the circulation of air at a lower temperature in contact with the inner wall implies an absorption of thermal energy from the inside. Before this physical fact, the case of closed cavity was analyzed, and the results are schematized in Figure 10. The savings obtained for this second case are 85%, significantly higher than the previous one. It is therefore advisable that, in winter conditions, there is no circulation between the cavities and the exterior.

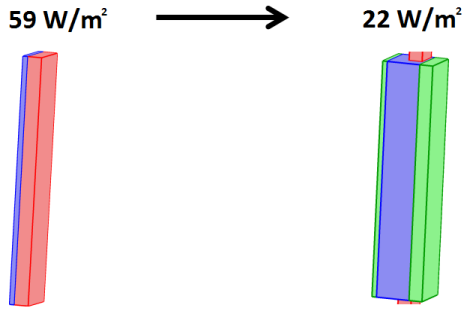

Figure 9. Comparison between absence of cavity and cavity with natural ventilation.

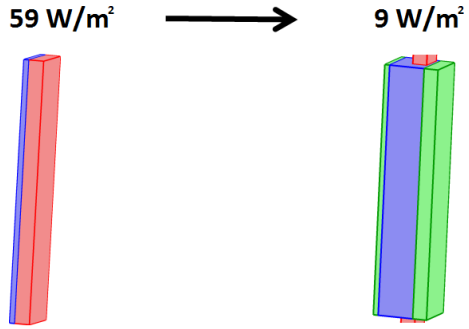

Figure 10. Comparison between absence of cavity and closed cavity.

5. Conclusion

This research presents the numerical study of the thermal performance of a cavity interposed in the double façade designed for the building of the Jerárquicos Salud mutual society in the city of Santa Fe de la Vera Cruz, Argentina. The analysis was made based on computer simulations of different climatic conditions and two design alternatives were considered according to the scheme provided: closed cavity and with connection to the exterior.

The results show that, for summer conditions, the design of the cavity implies a significant reduction in the thermal energy that would enter the building. Both the closed cavity and the cavity connected to the outside are valid alternatives that showed thermal aptitudes for the reduction of transferred energy, with an estimated reduction in summer of around 75% with respect to a design without the cavity. However, the case of the cavity connected to the outside, due to natural ventilation, would be the one selected because it has the possibility of renewing the air trapped in the cavities, reducing the possibility of accumulating humidity and bad odors.

Regardless of the promising predictions for the cavity with natural ventilation for the summer, the results have shown that its thermal performance in winter is inferior with respect to the closed cavity scenario. In the case of natural ventilation in winter, a reduction in thermal energy lost to the exterior of 63% was estimated, while for the design of a closed cavity, this reduction would be of 85%.

The final conclusion of this study based on computational predictions, is that it is suggested to make the orifices of circulation with a system of air flow control, which allows the option to keep the orifices open during the days of higher temperatures and closed during the periods of lower temperatures. Future works with more accurate predictive models near the walls will allow for more precise adjustments in the predictions of this study in terms of the calculated values, while these results can be used conceptually since it is estimated that the accuracy of the heat transfer calculations will not change the trends shown in this work.

Finally, it is worth noting that, according to all the numerical studies carried out, the mere presence of the air chamber shows a remarkable improvement of the thermal performance in terms of energy transfers between the atmosphere and the interior of the building, with the suggestion of the previous paragraph showing the best performance.

References

[1] J. Hirunlabh, S. Wachirapuwadon, N. Pratinthong, and J. Khedari, "New configurations of a roof solar collector maximizing natural ventilation," *Building and Environment*, vol. 36, no. 3, pp. 383–391, 2001. DOI: https://doi.org/10.1016/S0360-1323(00)00016-0.

[2] M. Ciampi, F. Leccese, and G. Tuoni, "Energy analysis of ventilated and microventilated roofs," *Solar Energy*, vol. 79, no. 2, pp. 183–192, 2005. DOI: https://doi.org/10.1016/j.solener.2004.08.014.

[3] H. Asan and L. Namli, "Laminar natural convection in a pitched roof of triangular cross-section: summer day boundary conditions," *Energy and Buildings*, vol. 33, no. 1, pp. 69–73, 2000. DOI: https://doi.org/10.1016/S0378-7788(00)00066-9.

[4] H. F. Oztop, Y. Varol, and A. Koca, "Laminar natural convection heat transfer in a shed roof with or without eave for summer season," *Applied Thermal Engineering*, vol. 27, no. 13, pp. 2252 –2265, 2007. DOI: https://doi.org/10.1016/j.applthermaleng.2007.01.018.

[5] A. Brondino, M. E. Berli, and J. Di Paolo, "Aislación térmica producida por cavidades de aire. análisis de un techo con geometría simplificada y flujo turbulento," in *V Congreso Argentino de Ingeniería Química, Santiago del Estero, Argentina.*, 2016. [Online]. Available: https://goo.gl/2bVmLv

[6] C. Ghiaus, F. Allard, M. Santamouris, C. Georgakis, and F. Nicol, "Urban environment influence on natural ventilation potential," *Building and Environment*, vol. 41, no. 4, pp. 395–406, 2006. DOI: https://doi.org/10.1016/j.buildenv.2005.02.003.

[7] S. Wang, Z. Shen, and L. Gu, "Numerical simulation of buoyancy-driven turbulent ventilation in attic space under winter conditions," *Energy and Buildings*, vol. 47, pp. 360–368, 2012. DOI: https://doi.org/10.1016/j.enbuild.2011.12.012.

[8] M. E. Berli, J. Di Paolo, and F. A. Saita, "Mecánica de fluidos computacional aplicada al diseño térmico pasivo de techos," in *I Congreso Argentino de Ingeniería Mecánica, Bahía Blanca, Argentina*, 2008.

[9] ——, "Heat transfer on a naturally cross-driven ventilated triangular cavity with openings," *Journal of Physics: Conference Series*, vol. 166, no. 1, pp. 1–10, 2009. DOI: http://doi.org/10.1088/1742-6596/166/1/012019. [Online]. Available: http://stacks.iop.org/1742-6596/166/i=1/a=012019

[10] A. Bejan, *Convection Heat Transfer, Fourth Edition*, I. John Wiley & Sons, Ed., 2013. DOI: http://doi.org/10.1002/9781118671627.

Scientific Paper / Artículo Científico

UNIVERSIDAD POLITÉCNICA SALESIANA ECUADOR
INGENIUS
Revista de Ciencia y Tecnología
https://doi.org/10.17163/ings.n20.2018.05
pISSN: 1390-650X / eISSN: 1390-860X

Pedestrian detection at night by using Faster R-CNN y infrared images

Detección de peatones en la noche usando Faster R-CNN e imágenes infrarrojas

Michelle Galarza Bravo[1,*], Marco Flores Calero[2]

Abstract

This paper presents a system for pedestrian detection at nighttime conditions for vehicular safety applications. For this purpose, it analyzes the performance of the Faster R-CNN algorithm for infrared images. The research reveals that Faster R-CNN has problems to detect small scale pedestrians. For this reason, it introduces a new Faster R-CNN architecture focused on multi-scale detection, through two ROI's generators for large size and small size pedestrians, RPNCD and RPNLD respectively. This architecture has been compared with the best Faster R-CNN baseline models, VGG-16 and Resnet 101, which present the best results. The experimental results have been development on CVC-09 and LSIFIR databases, which show improvements specially when detecting pedestrians that are far away, over the DET curve presents the miss rate versus FPPI of 16% and over the Precision vs Recall the AP of 89.85% for pedestrian class and the mAP of 90% over LSIFIR and CVC-09 test sets.

Keywords: pedestrian, infrared, Faster R-CNN, RPN, multi-scale, nighttime.

Resumen

En este artículo se presenta un sistema de detección de peatones en la noche, para aplicaciones en seguridad vehicular. Para este desarrollo se ha analizado el desempeño del algoritmo Faster R-CNN con imágenes en el infrarrojo lejano. Por lo que se constató que presenta inconvenientes a la hora de detectar peatones a larga distancia. En consecuencia, se presenta una nueva arquitectura Faster R-CNN dedicada a la detección en múltiples escalas, mediante dos generadores de regiones de interés (ROI) dedicados a peatones a corta y larga distancia, denominados RPNCD y RPNLD respectivamente. Esta arquitectura ha sido comparada con los modelos para Faster R-CNN que han presentado los mejores resultados, como son VGG-16 y Resnet 101. Los resultados experimentales se han desarrollado sobre las bases de datos CVC-09 y LSIFIR, los cuales demostraron mejoras, especialmente en la detección de peatones a larga distancia, presentando una tasa de error versus FPPI de 16 % y sobre la curva Precisión vs. Recall un AP de 89,85 % para la clase peatón y un mAP de 90 % sobre el conjunto de pruebas de las bases de datos LSIFIR y CVC-09.

Palabras clave: peatón, infrarrojo, Faster R-CNN, RPN, múltiples escalas, noche.

[1,*]Electronic, Automation and Control Engineering Major, Universidad de las Fuerzas Armadas ESPE Sanglquí – Ecuador. Autor para correspondencia ✉: magalarza@espe.edu.ec, https://orcid.org/0000-0001-8401-1871
[2]Department of Electrics and Electronics, Universidad de las Fuerzas Armadas ESPE, Sangolquí – Ecuador. https://orcid.org/0000-0001-7507-3325

Received: 02-05-2018, accepted after review: 18-06-2018

Suggested citation: Galarza Bravo, M. and Flores Calero, M. (2018). «Pedestrian detection at night by using Faster R-CNN y infrared images». Ingenius. N.°20, (jjuly-december). pp. 48-57. doi: https://doi.org/10.17163/ings.n20.2018.05.

1. Introduction

Pedestrian detection systems (PDS) are one of the most important technological components that have emerged in recent years with the development of mobile robotics applied to the automotive sector and other similar technologies aimed at vehicular safety [1], which need to operate with high quality standards and have a high efficiency and accuracy, because their goal is to protect human life by preventing collisions from happening [2].

Several reports worldwide indicate that traffic accidents generate high material and human costs [3], where pedestrians have a high accident rate, reaching up to 22% [4]. In the case of Ecuador, road accidents represent more than 10% of deaths due to traffic accidents [5]. Therefore, the detection of pedestrians is a subject of active and challenging research due to the complexity of the road scene, which constantly changes due to several factors. For instance, atmospheric conditions contribute to a low visibility and a permanent change of illumination, occlusions generate incomplete information of the human form, distance impairs the quality of the visual information [1, 6, 7]. At night these mishaps are magnified due to dark environments [1, 2, 8, 9].

On the other hand, due to the recent success of Deep Learning techniques [10, 11], the main objective of this work is to implement a method for the detection of pedestrians at night using visual information in the far infrared and the convolutional neural networks, specifically the architectures of the Faster R-CNN type [9, 11–15] to obtain a competitive system that generates cutting-edge results comparable to those in previous works. Therefore, a new Faster R-CNN architecture is presented at multiple scales, which is evaluated under the test sets of the CVC-09 [16] and LSIFIR [17] databases. The results show improvements especially when detecting pedestrians which are at a distance.

The document is organized as follows. The second section presents the methods and materials used, detailing the previous work carried out in the PDS field, especially deep-learning techniques. Additionally, the proposed design of the new Faster R-CNN architecture for the generation of regions of interest, classification and detection of pedestrians during the night is described, followed by the experimental evaluation for different configurations of the proposed model. Subsequently, in the results and discussion section, the values obtained with respect to the detection quality are displayed on the databases destined to the development of PDS at night. Finally, the last section is devoted to conclusions, recommendations and future work that can be done to improve this proposal.

2. Methods and materials

2.1. Previous works

Currently, there are multiple specialized investigations in the detection of pedestrians at night [1, 2, 7–9, 15, 18–30]. To carry out this process, generally, the work is divided into two parts. The first consists in the generation of ROI, and the second in the classification into pedestrians or background. In this way, it is possible to keep the person located while they remain in the scene.

2.1.1. Generation of ROI over images in the far infrared

For the generation of ROI on infrared images there are several methods, the most popular are: sliding windows [18] that exhaustively search over the whole image in several scales, which means the method requires many computational resources and makes it ineffective for real-time applications. To overcome these drawbacks, new proposals have been created, for example, segmentation by movement, proposed by Chen et al. [19] where regions of local interest are identified using PCA and Fuzzy techniques. Kim and Lee [21] have developed a method that combines image segments instead of thresholds and the low frequencies of far infrared images. Ge et al. [22] have proposed an adaptive segmentation method consisting of two thresholds, one specialized for locating bright areas and another for low contrast areas. Chun et al. [31] apply edge detection to obtain a faster ROI generator.

At present, there are more sophisticated methods that use models of convolutional neural networks and their variants for the generation of new proposals [1, 9, 12, 18]. Thus, the detection of heat points in multispectral resolution using IFCNN (Illumination Fully Connected Neural Network) has been proposed by Guan et al. [8] Vijay et al. [20] add a convolutional neuronal network to the work of Chen et al. [19], for classification. Kim et al. [23] have used cameras in the visible spectrum to detect pedestrians at night using CNN. Other alternatives include the Region Proposal Network or RPN, which is initially focused on locating the ROI by means of a combination of exhaustive search and sliding windows, in three orientations and three scales (9 reference boxes) for each sliding window. Each initial proposal is used to train a completely convolutional network to generate the predictions of the bounding box and the probability scores [12].

2.1.2. Classification of pedestrians on images in the far infrared

The methods developed for the classification can be grouped into two categories: the models based on the manual generation of characteristics [24, 25, 32], and

the models of automatic learning of characteristics using deep learning techniques (DL) [8, 11, 33–38].

In the first case, different manual methods of generating characteristics are used together with a classification algorithm, some examples include: HOG + SVM [26,27], HOG + Adaboost [28], HOG + LUV [39], Haar + Adaboost [29], Haar + HOG and SVM [30]. The second category includes convolutional neural networks (CNN) [2,8,11,34,38], with their different architectures, such as R-CNN [40], Fast R-CNN [41] and Faster R-CNN [12, 15].

The Fast R-CNN architecture [12, 15] essentially decreases the computational load with respect to CNN, and for this reason the detection time of the R-CNN layer [41] decreases. Consequently, Fast R-CNN together with selective search presents a better detection quality. However, both methods require an external ROI generator and have problems when detecting small objects that, in the context of pedestrians, involve long distances [41, 42].

To remedy these drawbacks, Faster R-CNN [12,15] has been added, including a ROI generator based on fully connected RPN layers which share the feature maps generated by the convolutional network with Fast R-CNN [15]. Therefore, very deep networks can be implemented because the total image passes only once through the CNN stage [15].

Therefore, Faster R-CNN is being widely used to construct PDS [1, 9, 42]. For example, in [1] Faster R-CNN has been used for pedestrian detection in multiple spectra, initially Faster R-CNN has been trained with only color and infrared images, Faster RCNN-C and Faster RCNN-T respectively, using a new model of neural network for training. Subsequently, features have been combined in different stages, creating Early Fusion, Halfway Fusion, Late Fusion and Score Fusion models. Additionally, Wang et al. [9], with reference to Liang et al. [41], combine RPN + BDT to build a pedestrian detection system in multiple spectra. However, it is considered that Faster RCNN does not work very well for the detection of pedestrians, because the feature maps do not present enough information for long-distance pedestrians. For this reason, Feris et al. [43] have proposed a subnetwork for the generation of ROI in multiple scales together with a subnet for the classification based on Fast R-CNN.

2.2. Pedestrian detection system at night

Figure 1 shows the proposed scheme for the development of the PDS at night, using images taken with infrared illumination and as a Faster R-CNN base architecture together with the VGG16 model [44] where some detailed changes have been developed below.

2.2.1. Generation of ROI over images in the far infrared

Because the original architecture of Faster RCNN [12,15] presents detection problems in the case of pedestrians that are in the distance, the architecture developed in Feris et al is taken into account. [43] Therefore, it has been decided to place two independent region proposal networks (RPN), which have different characteristics, as detailed in Table 2. In both cases, with an approach directed to pedestrians at short distance (RPNCD) and long distance (RPNLD). As shown in Figure 2, RPNLD is powered by the characteristics that are provided by the conv4_3 layer of VGG16 [44], because the grouping networks can discriminate pedestrians that are in the distance, where the more abundant feature maps are beneficial for detecting pedestrians over long distances [6]. Regarding RPNCD, like the original architecture of Faster R-CNN [12], it is fed by the characteristics delivered by the conv5_3 layer, since it extracts the most representative characteristics present in the image. For this reason, it provides excellent results for pedestrians at short distance.

2.2.2. Classification of ROI over images in the far infrared

For the classification stage, the architecture presented in Figure 3 is proposed. As in [43], the option of increasing the resolution of feature maps by applying deconvolution is considered in order to provide better information to the ROI grouping layer. Therefore, the Fast R-CNN part receives the characteristics extracted by the conv4_3 layer of VGG16 [44] as direct input, its deconvolution and the ROI generated by RPNCD and RPNLD as a whole.

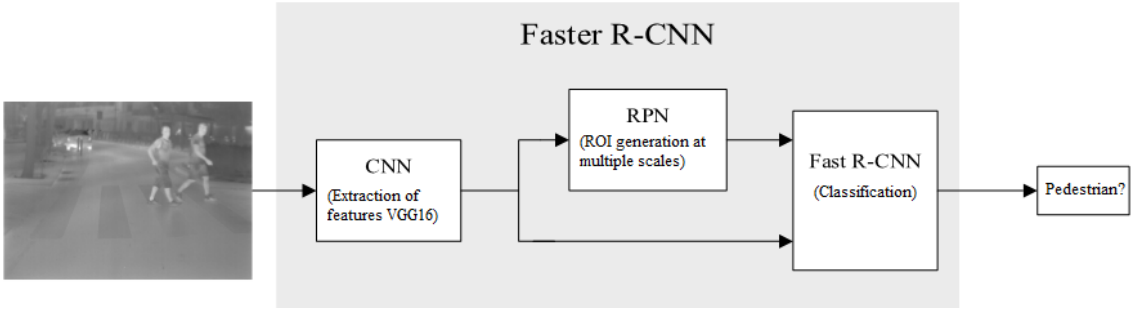

Figure 1. Schematic of the pedestrian detection system at night using Faster R-CNN and images in the far infrared.

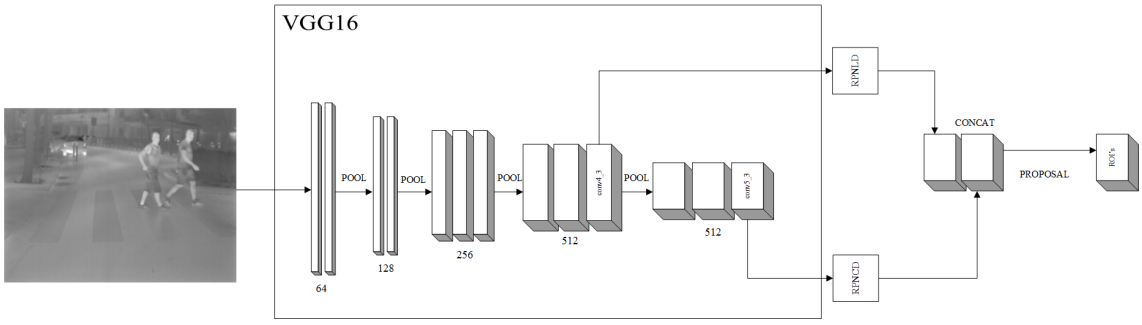

Figure 2. Multiscale RPN architecture based on the VGG16 network [2]. This is the subnetwork responsible for the ROI generation stage.

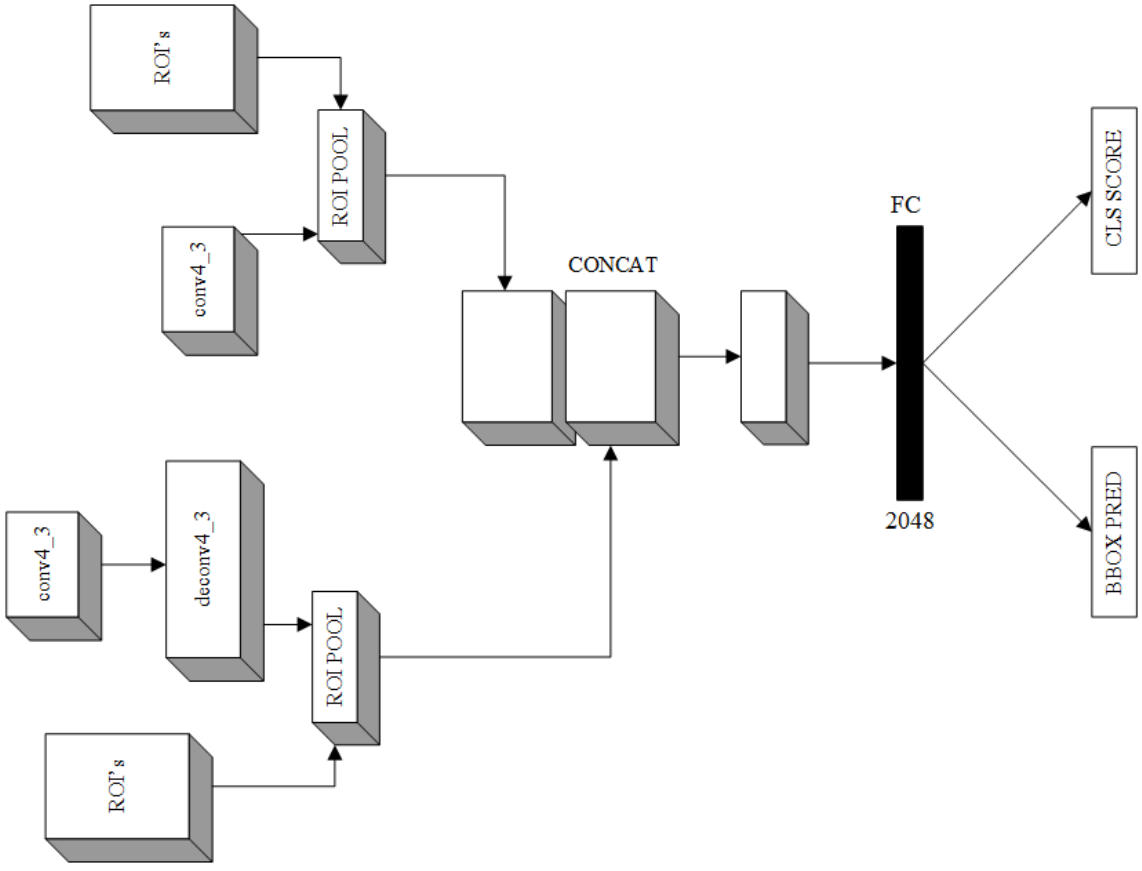

Figure 3. MS-CNN classification architecture [41]. This subnet is intended for the classification stage.

2.2.3. Technical details of the implementation

The learning of the proposed architecture has been developed from the CVC-09 [16] and LSIFIR [17] databases as detailed below:

1. CVC-09 database [16]: It is one of the most used bases for the detection of pedestrians at night. In this case, it was used for the training and testing of the proposal, and later for its validation. Table 1 describes the training and test sets. This database is tagged with pedestrians present in the scene B_{gt}.

Table 1. Content of the CVC-09 database at night

	Positives	**Negatives**
Training	2200	1002
Test	2283	–

However, in the case of long distances the database presents inconsistencies that have been corrected. Thus, a set of images has been re-labeled to correct these drawbacks and to debug labeling errors.

1. The LSI Far Infrared Pedestrian Dataset database (LSIFIR) [16]: It is another important database for the development of algorithms for pedestrian detection at night. Table 2 describes the training and test sets, with their respective sizes. In this case, like CVC-09, it was used for the training, validation and testing of the proposal.

Table 2. Content of the LSIFIR database. The value in parentheses represents the number of frames that contain pedestrians

	Clasification	**Detection**
Training	43391 (10209)	2936 (3225)
Test	2205 (5945)	5788 (3279)

In order to train the network, the algorithm initially re-scales the shortest part of the input image to 600 pixels. Regarding the training of the network, this is done through the approximate joint training methodology proposed by Ren et al. [12]. In addition, the weights of each layer belonging to the network are initialized by means of the pre-trained model VGG16, and then fine-tuned by means of the Minchart Stochastic Gradient Descent [45] and the recent Adam optimization algorithm [46] with hyperparameters detailed in Table 3.

As for the RPN, they work independently. Therefore, their training is also independent. The proposals generated by each of them are combined and then labeled using the NMS (Non Maximum Supression) algorithm, where if the IoU (Intersection over Union) index, given by Equation (1), is greater than 0.6, it is a pedestrian, if it is less than 0.3, is labeled as a non-pedestrian, and in case of not fulfilling any of the two conditions, said proposals are excluded from the training.

Immediately after, in the classification stage, NMS is again applied to reduce detection redundancies, applying a threshold of 0.6, where each detection greater than the threshold is labeled as a pedestrian, otherwise a non-pedestrian.

$$IoU = \frac{Area(B_{det} \cap B_{gt})}{Area(B_{det} \cup B_{gt})} \tag{1}$$

Where B_{gt} is the intersection and B_{det} the union, between the actual bounding box annotated in the database CVC-09 [16] or LSIFIR [17] and the result of the bounding box predicted by our model.

Table 3. Training parameters for the proposed model for pedestrian detection at night

Parameter	**Value**
Learning rate	0,001
Momentum	0,9
RMSProp	0,999
Weight loss	0,0005
Epsilon	10^{-8}
Images by batch	2

2.2.4. Experimental evaluation

To arrive at the proposed model, multiple experiments have been developed, as can be seen in Tables 4 and 5, where the ROI generation subnet and the effects caused by the configuration of the different scales and aspect ratios of RPNCD and RPNLD are analyzed.

For the experiments, the CVC-09 training sets have been used together with LSIFIR for the learning stage of the network and the test sets for the evaluation.

Additionally, the classification subnetwork and the effects caused by deconvolution were analyzed. In Table 5, the results show that applying this strategy allows for an increase in the resolution of the characteristic maps, which causes an increase in the MPA of approximately 6%.

Table 4. Configuration parameters of RPN reference boxes for pedestrians at short and long distance. Results of the ROI generation subnet

Parameter	RPNCD	RPNLD	mAP (%)	fps
Scale	64, 128, 256	128, 256, 512	86	10
Aspect R.	1:8, 1:4, 1:2	1:1, 1:2, 2:1		
Scale	64, 128, 256	64, 128, 256	85,6	10
Aspect R.	1:8, 1:4, 1:2	1:1, 1:2, 2:1		
Scale	32, 64, 128	128, 256, 512	84,5	10
Aspect R.	1:8, 1:4, 1:2	1:1, 1:2, 2:1		

Table 5. Results obtained by applying deconvolution to the classification subnet

Parameter	RPNCD	RPNLD	mAP (%)	fps
Scale	64, 128, 256	128, 256, 512	89,9	5
Aspect R.	1:8, 1:4, 1:2	1:1, 1:2, 2:1		
Scale	64, 128, 256	64, 128, 256	87,8	5
Aspect R.	1:8, 1:4, 1:2	1:1, 1:2, 2:1		
Scale	32, 64, 128	128, 256, 512	86,8	5
Aspect R.	1:8, 1:4, 1:2	1:1, 1:2, 2:1		

3. Results and discussion

Regarding the evaluation of the effectiveness of the proposal, two of the databases representing the reference point were used, aimed at the development of pedestrian detection systems at night using infrared illumination.

3.1. Evaluation protocol

To evaluate the proposed system, the Mean Average Precision (mAP) metrics is proposed, which allows for the measurement of the accuracy of the detector, so that the average accuracy of each detection is calculated for different values of the recall index [12].

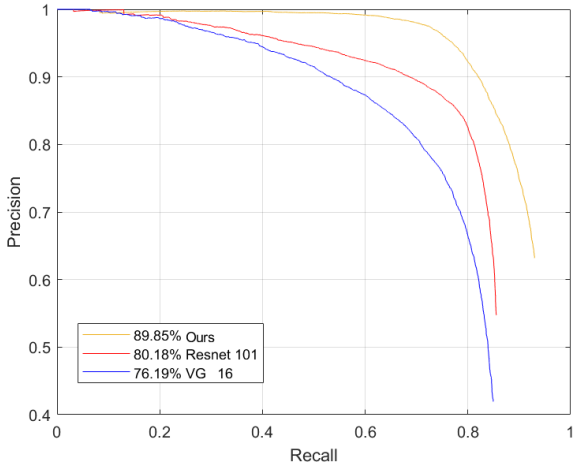

Figure 4. Curve, Precision vs. Recall of the results obtained for different Faster R-CNN network architectures for the pedestrian class, on the combination of the test sets of the CVC-09 and LSIFIR databases.

Additionally, the standard protocol proposed by Dollár et al. [47], that is, the curves that relate the average error rate (miss rate) versus false positives per image (FPPI) will be used in the range of 10^{-2} to 10^{0} FPPI, which is an indicator of specialized accuracy in vehicular topics for pedestrian detection.

3.2. Discussion of results

In Figure 4 are presented the experiments carried out on the test sets of the CVC-09 [16] and LSIFIR [17] databases for different Faster R-CNN network architectures are presented in Table 6. The results have been obtained under the same computational conditions, where it can be observed that this new proposal reaches an MPA of 94.6% in the validation stage, which shows that the learning is superior to that of other proposals. However, it has the disadvantage of requiring a greater computational effort.

Table 6. Results of the tests and validation of the CVC-09 database. Mean average precision (mAP) and image processing per second (fps)

	Validation	Test	
Model	mAP (%)	mAP (%)	fps
VGG16	83,4	76,4	14
Resnet 101	86,1	80,2	8
Ours	94,6	89,9	5

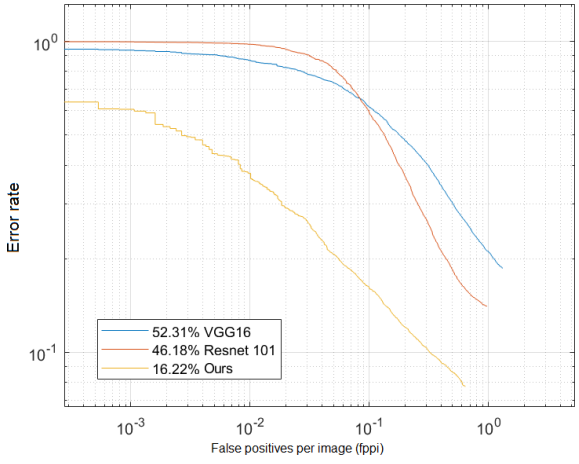

Figure 5. Curves of the average error rates versus FPPI for the different Faster R-CNN network architectures on the combination of the test sets of the CVC-09 and LSIFIR databases.

Thus, it can be seen in Figure 5 that the results of the original models of Faster R-CNN and other models presented by other investigations have been surpassed, as detailed in Table 7.

Table 7. Comparison of average error rates of pedestrian detection systems at night under the CVC-09 and LSIFIR databases

Model	Error rate (%) en 10^{-2}
Latent-SVM HOPE [1]	25,1
Fuzzy C-means CNN [20]	65,4
Ours	16,22

3.3. Processing time

For the experimental evaluation, a computer composed of a GPU with the operating system Linux 16.04, an Nvidia Geforce GTX 1080 Ti card, with 11 GB GDDR5X 352 memory was used. The training time was approximately 5 hours. The average detection time is 170 milliseconds, on images of 640×480 pixels; that is, the system processes 5 images per second.

4. Conclusions and recommendations

4.1. Conclusions

This work presented a method of detecting pedestrians at night using modern artificial intelligence techniques. The following contributions were made:

Figure 6. Examples selected with the results obtained on the combination of the test sets of the LSIFIR and CVC-09 databases, during the night.

- Development of a new DL architecture based on Faster R-CNN together with the VGG16 model for the detection of pedestrians at night using images in the far infrared. The multi-scale RPN network presented better detection specifically for long-distance pedestrians, as shown in Figure 6. Compared to the original RPN architecture, the of RPNCD and RPNLD architecture produced better results. The new architecture increased the mAP from 76.4 to 86%. Additionally, a significant contribution was presented when applying deconvolution to the classification subnet, with the mAP increasing from 86 to 89.9%. However, the deconvolution added in the classification stage increases the computational load. As a result, the network processing is reduced from 10 frames to 5 frames per second.
- Comparison of the performance of the original Faster R-CNN architecture together with the VGG16 and Resnet 101 models, on the CVC-09 and LSIFIR databases, obtaining better results in mAP 9.7% for Resnet 101 and 13.5% for VGG16 Regarding the average error rate, a difference of 29.96% was obtained for Resnet 101 and 36.09% for VGG16.
- Regarding detection, the proposed model demonstrates superior performance with respect to Olmeda et al. [44] and John et al. [14], where the average error rate is reduced by 8.88% with respect to [44] and 49.18% with respect to [14].
- The processing time is 5 frames per second, which makes this proposal a viable method for real-time applications, aimed at vehicular safety.

4.2. Recommendations and future work

To improve the performance of this system it is necessary to include the following recommendations:

- Optimize the proposed algorithm to work in real time, that is, so it is able to process at least 25 frames per second.
- Include a set of features based on multiple spectra for better performance during the day and night.

Acknowledgments

The authors wish to express their thanks to the researchers who have made the databases of pedestrians in the infrared possible, since without this information

it would have been very difficult to develop this research. In addition, the authors wish to acknowledge the anonymous reviewers who contribute their work for the improvement of this document.

References

[1] D. König, M. Adam, C. Jarvers, G. Layher, H. Neumann, and M. Teutsch, "Fully convolutional region proposal networks for multispectral person detection," in *2017 IEEE Conference on Computer Vision and Pattern Recognition Workshops (CVPRW)*, July 2017. DOI: https://doi.org/10.1109/CVPRW.2017.36, pp. 243–250.

[2] D. Olmeda, C. Premebida, U. Nunes, J. M. Armingol, and A. de la Escalera, "Pedestrian detection in far infrared images," *Integrated Computer-Aided Engineering*, vol. 20, no. 4, pp. 347–360, 2013. [Online]. Available: https://goo.gl/Rss9Qp

[3] WHO. (2004) World report on road traffic injury prevention. World Health Organization. [Online]. Available: https://goo.gl/PBhixd

[4] ANT. (2017) Siniestros octubre 2016. Agencia Nacional de Tránsito. Ecuador. [Online]. Available: https://goo.gl/GoXFX5

[5] ——. (2016) Siniestyros agosto 2017. Agencia Nacional de Tránsito. Ecuador. [Online]. Available: https://goo.gl/GoXFX5

[6] J. Li, X. Liang, S. Shen, T. Xu, and S. Yan, "Scale-aware fast R-CNN for pedestrian detection," *CoRR*, 2015. [Online]. Available: https://goo.gl/27CMsz

[7] J. Yan, X. Zhang, Z. Lei, S. Liao, and S. Z. Li, "Robust multi-resolution pedestrian detection in traffic scenes," in *IEEE Conference on Computer Vision and Pattern Recognition*, June 2013. DOI: https://doi.org/10.1109/CVPR.2013.390, pp. 3033–3040.

[8] D. Guan, Y. Cao, J. Liang, Y. Cao, and M. Y. Yang, "Fusion of multispectral data through illumination-aware deep neural networks for pedestrian detection," *CoRR*, 2018. [Online]. Available: https://goo.gl/AAWJFp

[9] J. Liu, S. Zhang, S. Wang, and D. N. Metaxas, "Multispectral deep neural networks for pedestrian detection," *CoRR*, 2016. [Online]. Available: https://goo.gl/Czc6Jg

[10] Y. Guo, Y. Liu, A. Oerlemans, S. Lao, S. Wu, and M. S. Lew, "Deep learning for visual understanding: A review," *Neurocomputing*, vol. 187, pp. 27–48, 2016. DOI: https://doi.org/10.1016/j.neucom.2015.09.116, recent Developments on Deep Big Vision.

[11] L. Deng and D. Yu, "Deep learning: Methods and applications," *Foundations and Trends in Signal Processing*, vol. 7, no. 3–4, pp. 197–387, 2014. DOI: http://dx.doi.org/10.1561/2000000039. [Online]. Available: http://dx.doi.org/10.1561/2000000039

[12] S. Ren, K. He, R. Girshick, and J. Sun, "Faster r-cnn: Towards real-time object detection with region proposal networks," in *Advances in Neural Information Processing Systems 28*. Curran Associates, Inc., 2015, pp. 91–99. [Online]. Available: https://goo.gl/5i64rm

[13] C. Ertler, H. Posseger, M. Optiz, and H. Bischof, "Pedestrian detection in rgb-d images from an elevated viewpoint," in *22nd Computer Vision Winter Workshop*, 2017. [Online]. Available: https://goo.gl/L4wB1e

[14] C. C. Pham and J. W. Jeon, "Robust object proposals re-ranking for object detection in autonomous driving using convolutional neural networks," *Signal Processing: Image Communication*, vol. 53, pp. 110–122, 2017. DOI: https://doi.org/10.1016/j.image.2017.02.007.

[15] X. Zhang, G. Chen, K. Saruta, and Y. Terata, "Deep convolutional neural networks for all-day pedestrian detection," in *Information Science and Applications 2017*, K. Kim and N. Joukov, Eds. Singapore: Springer Singapore, 2017. DOI: https://doi.org/10.1007/978-981-10-4154-9_21, pp. 171–178.

[16] Elektra, *CVC-09: FIR Sequence Pedestrian Dataset*, ElektraAutonomous Vehicle developed by CVC & UAB & UPC, 2016. [Online]. Available: https://goo.gl/NhYuZ2

[17] D. Olmeda, C. Premebida, U. Nunes, J. Armingol, and A. de la Escalera., "Lsi far infrared pedestrian dataset," Universidad Carlos III de Madrid. España, 2013. [Online]. Available: https://goo.gl/pJTGvj

[18] D. Heo, E. Lee, and B. Chul Ko, "Pedestrian detection at night using deep neural networks y saliency maps," *Journal of Imaging Science and Technology*, vol. 61, no. 6, pp. 60 403–1–60 403–9, 2017. DOI: https://doi.org/10.2352/J.ImagingSci.Technol.2017.61.6.060403.

[19] C. Bingwen, W. Wenwei, and Q. Qianqing, "Robust multi-stage approach for the detection of moving target from infrared imagery," *Optical Engineering*, vol. 51, no. 6, 2012. DOI: https://doi.org/10.1117/1.OE.51.6.067006.

[20] V. John, S. Mita, Z. Liu, and B. Qi, "Pedestrian detection in thermal images using adaptive fuzzy c-means clustering and convolutional neural networks," in *2015 14th IAPR International Conference on Machine Vision Applications (MVA)*, May 2015. DOI: https://doi.org/10.1109/MVA.2015.7153177, pp. 246–249.

[21] D. Kim and K. Lee, "Segment-based region of interest generation for pedestrian detection in far-infrared images," *Infrared Physics & Technology*, vol. 61, pp. 120–128, 2013. DOI: https://doi.org/10.1016/j.infrared.2013.08.001.

[22] J. Ge, Y. Luo, and G. Tei, "Real-time pedestrian detection and tracking at nighttime for driver-assistance systems," *IEEE Transactions on Intelligent Transportation Systems*, vol. 10, no. 2, pp. 283–298, June 2009. DOI: https://doi.org/10.1109/TITS.2009.2018961.

[23] J. H. Kim, H. G. Hong, and K. R. Park, "Convolutional neural network-based human detection in nighttime images using visible light camera sensors," *Sensors*, vol. 17, no. 5, pp. 1–26, 2017. DOI: https://doi.org/10.3390/s17051065.

[24] B. Qi, V. John, Z. Liu, and S. Mita, "Pedestrian detection from thermal images with a scattered difference of directional gradients feature descriptor," in *17th International IEEE Conference on Intelligent Transportation Systems (ITSC)*, Oct 2014. DOI: https://doi.org/10.1109/ITSC.2014.6958024, pp. 2168–2173.

[25] M. R. Jeong, J. Y. Kwak, J. E. Son, B. Ko, and J. Y. Nam, "Fast pedestrian detection using a night vision system for safety driving," in *2014 11th International Conference on Computer Graphics, Imaging and Visualization*, Aug 2014. DOI: https://doi.org/10.1109/CGiV.2014.25, pp. 69–72.

[26] J. Kim, J. Baek, and E. Kim, "A novel on-road vehicle detection method using πhog," *IEEE Transactions on Intelligent Transportation Systems*, vol. 16, no. 6, pp. 3414–3429, Dec 2015. DOI: https://doi.org/10.1109/TITS.2015.2465296.

[27] K. Piniarski, P. Pawlowski, and A. D. abrowski, "Pedestrian detection by video processing in automotive night vision system," in *2014 Signal Processing: Algorithms, Architectures, Arrangements, and Applications (SPA)*, Sept 2014, pp. 104–109. [Online]. Available: https://goo.gl/uxnD6X

[28] S. L. Chang, F. T. Yang, W. P. Wu, Y. A. Cho, and S. W. Chen, "Nighttime pedestrian detection using thermal imaging based on hog feature," in *Proceedings 2011 International Conference on System Science and Engineering*, June 2011. DOI: https://doi.org/10.1109/ICSSE.2011.5961992, pp. 694–698.

[29] H. Sun, C. Wang, and B. Wang, "Night vision pedestrian detection using a forward-looking infrared camera," in *2011 International Workshop on Multi-Platform/Multi-Sensor Remote Sensing and Mapping*, Jan 2011. DOI: https://doi.org/10.1109/M2RSM.2011.5697384, pp. 1–4.

[30] P. Govardhan and U. C. Pati, "Nir image based pedestrian detection in night vision with cascade classification and validation," in *2014 IEEE International Conference on Advanced Communications, Control and Computing Technologies*, May 2014. DOI: https://doi.org/10.1109/ICACCCT.2014.7019339, pp. 1435–1438.

[31] Y. Chun-he and D. Cai-Fang, "Research of the method of quickly finding the pedestrian area of interest," *Journal of Electrical and Electronic Engineering*, vol. 5, no. 5, pp. 180–185, 2017. DOI: http://doi.org/10.11648/j.jeee.20170505.14.

[32] J. Baek, J. Kim, and E. Kim, "Fast and efficient pedestrian detection via the cascade implementation of an additive kernel support vector machine," *IEEE Transactions on Intelligent Transportation Systems*, vol. 18, no. 4, pp. 902–916, April 2017. DOI. https://doi.org/10.1109/TITS.2016.2594816.

[33] Y. Guo, Y. Liu, A. Oerlemans, S. Lao, S. Wu, and M. S. Lew, "Deep learning for visual understanding: A review," *Neurocomputing*, vol. 187, pp. 27–48, 2016. DOI: https://doi.org/10.1016/j.neucom.2015.09.116.

[34] H. A. Perlin and H. S. Lopes, "Extracting human attributes using a convolutional neural network approach," *Pattern Recognition Letters*, vol. 68, pp. 250–259, 2015. DOI: https://doi.org/10.1016/j.patrec.2015.07.012.

[35] P. Sermanet, K. Kavukcuoglu, S. Chintala, and Y. Lecun, "Pedestrian detection with unsupervised multi-stage feature learning," in *2013 IEEE Conference on Computer Vision and Pattern Recognition*, June 2013. DOI: https://doi.org/10.1109/CVPR.2013.465, pp. 3626–3633.

[36] D. Ribeiro, J. C. Nascimento, A. Bernardino, and G. Carneiro, "Improving the performance of pedestrian detectors using convolutional learning," *Pattern Recognition*, vol. 61, pp. 641–649, 2017. DOI: https://doi.org/10.1016/j.patcog.2016.05.027.

[37] P. Sermanet, D. Eigen, X. Zhang, M. Mathieu, R. Fergus, and Y. Lecun, "Overfeat: Integrated

recognition, localization and detection using convolutional networks," 12 2013. [Online]. Available: https://goo.gl/zNNUCd

[38] D. Tomè, F. Monti, L. Baroffio, L. Bondi, M. Tagliasacchi, and S. Tubaro, "Deep convolutional neural networks for pedestrian detection," *Signal Processing: Image Communication*, vol. 47, pp. 482–489, 2016. DOI: https://doi.org/10.1016/j.image.2016.05.007.

[39] J. Cao, Y. Pang, and X. Li, "Learning multilayer channel features for pedestrian detection," *IEEE Transactions on Image Processing*, vol. 26, no. 7, pp. 3210–3220, July 2017. DOI: https://doi.org/10.1109/TIP.2017.2694224.

[40] R. Girshick, J. Donahue, T. Darrell, and J. Malik, "Rich feature hierarchies for accurate object detection and semantic segmentation," in *2014 IEEE Conference on Computer Vision and Pattern Recognition*, June 2014. DOI: https://doi.org/10.1109/CVPR.2014.81, pp. 580–587.

[41] R. Girshick, "Fast r-cnn," in *2015 IEEE International Conference on Computer Vision (ICCV)*, Dec 2015. DOI: https://doi.org/10.1109/ICCV.2015.169, pp. 1440–1448.

[42] L. Zhang, L. Lin, X. Liang, and K. He, "Is faster r-cnn doing well for pedestrian detection?" in *Computer Vision – ECCV 2016*, B. Leibe, J. Matas, N. Sebe, and M. Welling, Eds. Cham: Springer International Publishing, 2016. DOI: https://doi.org/10.1007/978-3-319-46475-6_28, pp. 443–457.

[43] Z. Cai, Q. Fan, R. Feris, and N. Vasconcelos, "A unified multi-scale deep convolutional neural network for fast object detection," 2016. [Online]. Available: https://goo.gl/Y4XNZv

[44] K. Simonyan and A. Zisserman, "Very deep convolutional networks for large-scale image recognition," in *International Conference on Learning Representations*, 2014. [Online]. Available: https://goo.gl/98akRT

[45] J. Konečný, J. Liu, P. Richtárik, and M. Takáč, "Mini-batch semi-stochastic gradient descent in the proximal setting," *IEEE Journal of Selected Topics in Signal Processing*, vol. 10, no. 2, pp. 242–255, March 2016. DOI: https://doi.org/10.1109/JSTSP.2015.2505682.

[46] D. P. Kingma and J. Ba, "Adam: a method for stochastic optimization," in *ICLR 2015*, 2015. [Online]. Available: https://goo.gl/so1Da8

[47] P. Dollar, C. Wojek, B. Schiele, and P. Perona, "Pedestrian detection: An evaluation of the state of the art," *IEEE Transactions on Pattern Analysis and Machine Intelligence*, vol. 34, no. 4, pp. 743–761, April 2012. DOI: https://doi.org/10.1109/TPAMI.2011.155.

[48] K. He, X. Zhang, S. Ren, and J. Sun, "Deep residual learning for image recognition," in *IEEE Conference on Computer Vision and Pattern Recognition (CVPR)*, June 2016. DOI: https://doi.org/10.1109/CVPR.2016.90, pp. 770–778.

Scientific Paper / Artículo Científico

UNIVERSIDAD POLITÉCNICA SALESIANA ECUADOR
INGENIUS
Revista de Ciencia y Tecnología
https://doi.org/10.17163/ings.n20.2018.06
pISSN: 1390-650X / eISSN: 1390-860X

A Technical Study of Solar and Biogas Energy Usage in Electric Vehicles in Ilhabela, Brazil

Estudio técnico del uso de energía solar y biogás en vehículos eléctricos en Ilhabela-Brasil

Raul Pereira Micena[1,*], Omar R. Llerena P.[1],
Wendell de Queiróz Lamas[2], José Luz Silveira[1]

Abstract

Currently, Hybrid Power Systems (HPS) provide an excellent opportunity for generation of electricity. This paper presents the study of a hybrid system considering two energy sources (solar - biogas) available in the Ilhabela island in the state of São Paulo – Brazil. This system will supply electricity to electric vehicles. The study is based on the calculation of the energy demand of the electric vehicles on the island. Then the capacity of biogas production in Ilhabela is determined. Subsequently, in order to know the energy produced and the amount of biogas needed by the microturbine, an energy analysis of this plant is carried out. Lastly, the energy needed to be generated with the photovoltaic plant is calculated. The results show that, considering a market insertion index of 4% of electric vehicles, the average energy demand is 46.327 kWh/month. On the other hand, the amount of biogas produced on the island is twice what is needed to generate 16.200 kWh/month. Finally, the solar plant will produce 30.127 kWh/month.

Keywords: Biogas, Electric Vehicles, Solar Energy, Ilhabela.

Resumen

Actualmente, los sistemas híbridos de generación de energía se han mostrado como una excelente oportunidad para la generación de electricidad. En este trabajo se presenta el estudio de uno de estos sistemas considerando dos fuentes de energía disponibles (solar – biogás) en la isla Ilhabela en el estado de San Pablo – Brasil, con miras a dotar de energía a vehículos eléctricos. Este estudio se basa primeramente en el cálculo de la demanda de energía de los vehículos eléctricos en esta isla. Luego se determina la capacidad de producción de biogás en Ilhabela. Posteriormente se efectúa un análisis energético de la planta con una microturbina a biogás para conocer la energía producida y la demanda de biogás. Como último paso, se calcula la cantidad de energía necesaria a ser generada con la planta fotovoltaica. Los resultados muestran que, considerando un índice de inserción de mercado del 4 % de los vehículos eléctricos, la demanda energética media es de 46 327 kWh/mes. Por otro lado, la capacidad de producción de biogás en la isla es dos veces mayor a la necesaria para generar 16 200 kWh/mes. Finalmente, la planta fotovoltaica producirá 30 127 kWh/mes.

Palabras clave: biogás, vehículos eléctricos, energía solar, Ilhabela.

[1,*]Energy Systems Optimization Laboratory (LOSE) / Research Institute in Bioenergy (IPBEN) – UNESP. Brazil. Author for correspondence ✉: raul.micena@unesp.br, https://orcid.org/0000-0003-0486-4108 https://orcid.org/0000-0003-2115-4036, https://orcid.org/0000-0002-7588-0335

[2]Department of Basic Sciences and Environments. Escola de Engenharia de Lorena. Universidade de São Paulo (USP). Brasil. http://orcid.org/0000-0003-2764-5725

Received: 14-05-2018, accepted after review: 25-06-2018

Suggested citation: Micena, R. P.; Llerena, O. R.; de Queiróz Lamas, W. and Silveira, J. L. (2018). «A Technical Study of Solar and Biogas Energy Usage in Electric Vehicles in Ilhabela, Brazil». Ingenius. N.°20, (july-december). pp. 58-69. doi: https://doi.org/10.17163/ings.n20.2018.06.

1. Introduction

Energy is considered a fundamental input in productive activities, having an important role in the development process of humanity. Access to modern forms of energy, particularly to electricity, brings a series of social benefits that improve the quality of life of the population [1].

One of the sectors with the highest energy consumption is transportation. In 2014, this sector worldwide was responsible for 28% of global energy demand and 23% of global CO_2 emissions, which come from the consumption of fossil fuels. In relation to the use of oil, this sector consumed 65% of the final global demand [2].

On the other hand, in a scenario of growing concern about climate change, less polluting alternatives are sought for the transport of people and cargo. In this sense, electric vehicles (EV) are being widely disseminated. According to the projections of Bloomberg New Energy Finance [3], in 2040 more than half of the new cars sold in the world will be electric. Unlike combustion vehicles, EVs do not emit greenhouse gases during operation.

However, the energy that feeds their electric motors can originate from different sources of energy, some of them highly polluting, such as coal and oil, making the adoption of EVs less effective as a measure to reduce greenhouse gas emissions. From the perspective of a full cycle analysis, the electricity available to charge the batteries must be generated from renewable or clean sources so that these vehicles have zero emissions [4].

In this sense, hybrid power generation systems or HPGSs are a good alternative. According to Thibaud et al. [5], these types of systems use more than one energy source to supply a variety of different loads. Typically, these systems work in isolation taking advantage of the renewable resources available on site, but they can also be used in conjunction with conventional sources of power generation.

According to Justo Roberts, when sized correctly, HPGSs present technical, economic and environmental advantages in relation to systems using a single renewable source or traditional systems [6].

This article proposes the technical analysis and sizing of a HPGS (solar-biogas) for application on the Ilhabela-SP-Brazil island, considering energy potentials currently available on the island and that are not being exploited. The goal of the proposed system is to generate charging stations for a specific fleet of electric vehicles. For this study, different degrees of EV penetration are considered in relation to the current fleet of automobiles.

For a structured analysis of this proposal, a bibliographic review of battery EVs (BEVs) and their relation to renewable energy sources is carried out. Afterwards, the methodology describes the technical analysis and sizing of the system step by step. Finally, the results are analyzed and discussed and the conclusions about the analysis developed are obtained.

1.1. Electric vehicles with battery

Briefly, a battery electric vehicle (BEV) can be described as a vehicle whose wheels are driven by an electric motor, which in turn is powered by electric current stored in a battery bank. Its main components can be seen in Figure 1.

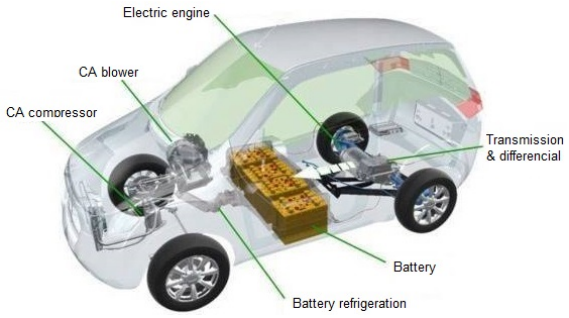

Figure 1. Basic components of an electric vehicle [7].

The charge of a BEV's batteries is largely obtained through the use of a conventional residential electrical outlet. However, the high recharge periods and the need to perform loads faster and more frequently, resulted in the advent of public charging stations [8]. These stations can be independent or connected to a network of stations with state-of-the-art devices [9].

1.2. Use of renewable energy sources in the BEV

The literature is quite diverse in terms of integration between EVs and renewable energy sources [10–12]. The models that study this integration tend mainly to measure the capacity of relationship between them, as well as the impacts on the performance of the electric network [13]. Up next are some applications using biogas and photovoltaic solar energy.

1.2.1. Use of biogas in BEV

Biomass energy differs from other renewable sources, such as solar and wind, by the fact that it can be easily stored and consumed when necessary. Biofuels, such as ethanol produced from sugarcane, are the most common form of biomass used in vehicles.

This fuel is burned directly in internal combustion engines (ICE). However, electricity from biofuels tends to provide a higher return on investment compared to use in final processes such as the one mentioned above [14].

Several recent studies indicate that the use of bioelectricity in a vehicle is more effective than the conversion of biomass into biofuels. Schmidt et al. [8]

evaluated the production and use of various types of biofuels in Austria, compared to bioelectricity. The results indicate that emissions of greenhouse gases, the effects of land use and the required amount of biomass stocks are reduced compared to using EV biofuels.

On the other hand, Campbell et al. [15] conclude that the gross average production, in kilometers traveled per hectare of biomass production, is 112% higher for bioelectricity than for biofuels. In addition, the net average compensation of greenhouse gases for the switchgrass production (grass of the genus Panicum L.) is 108% greater in bioelectricity than that of biofuels [13].

1.2.2. Use of photovoltaic energy in BEV

Over the years, several methods of charging BEV using photovoltaic panels (PVs) have been proposed. The most prominent is the combination between PV and the electricity grid. In this way, they use photovoltaic energy whenever possible, but switch to the grid when photovoltaic energy is insufficient or not available [16].

The connection to the network of BEV charging stations, together with photovoltaic solar energy, allow a greater interaction between the EV and the network, enabling the flow of energy from the vehicle to the network, with a technology called vehicle-to -grid (V2G) [17]. Thanks to being connected to the network, the photovoltaic generation does not necessarily have to occur in the same physical space of the charging station, since the energy can be transported through the distribution systems.

Another approach is to use the PV system outside the power grid. This system is known as PV-standalone [18]. This approach requires the use of batteries for the storage of the energy generated during periods with high solar radiation. The use of batteries in this type of systems raises the costs of both initial investment and maintenance.

1.3. Photovoltaic solar energy (PV)

Solar energy is the largest source of renewable energy available in nature, originating in the radiation coming from the fusion reactions of the hydrogen and helium nuclei inside the Sun.

On the other hand, photovoltaic systems are characterized by high reliability and low maintenance, as their high initial cost is often compensated by the low operational cost. Through the PV effect, the solar cells contained in the panels convert solar energy directly into renewable, safe and non-polluting electricity [19].

The basic component of solar energy is the photovoltaic cell. This is composed of two layers of semiconductor material. The layers, one of type N, with excess of electrons and another of type P, with deficit of electrons, are joined, forming a PN junction. When there is the incidence of photons coming from sunlight, the electrons acquire energy, and then, with the presence of an external conductor, the migration of the electrons generates an electric current. If the cell does not suffer from solar incidence, electrons and gaps remain trapped behind that barrier [20]. Figure 2 shows the operation of the PV panel.

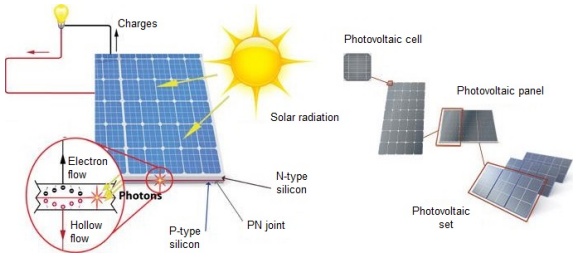

Figure 2. Operation of the PV panel [18].

In the industrialization process, the photovoltaic cells are interconnected in series-parallel arrays forming the PV modules (Figure 2). The most used PV modules are based on poly or monocrystalline technology [21]. But recently, fine films are becoming popular, especially for large installations [22].

Generally, in photovoltaic installations the modules are organized in series circuits, in order to reach the necessary DC voltage. To obtain a higher power, several chains are connected in parallel. The behavior of a PV system under different intensities of solar irradiation and temperature can be understood by examining its characteristic currents of current-voltage (IV) and voltage-power (PV).

There will always be a single point of operation in which the power will be maximum, that is, the point of maximum power (PMP) at a certain temperature and irradiation. The PMP is not fixed; it varies continuously according to temperature and solar irradiation. Because of this dynamic, a tracker to find the point of maximum power is necessary to ensure that the maximum power of the array of PV panels is always extracted (Figure 3) [16].

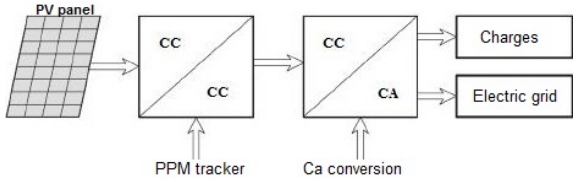

Figure 3. Block diagram of a PV system showing its main components, including the PPM [23].

1.4. Solar energy in Brazil

According to Pereira et al. [24], the annual average of global irradiation presents a good uniformity in Brazil.

The averages are relatively high throughout the territory. The values of incident global solar radiation in any region of the Brazilian territory vary between 1500 and 2500 kWh/m^2/year, and are higher than in most European countries, such as Germany (900-1250 kWh/m^2/year), France (900-1650 kWh/m^2/year) and Spain (1200-1850 kWh/m^2/year), places where solar energy projects are widely used.

Despite the favorable conditions for the development of this type of technology, in Brazil it is still incipient [25]. According to the Ministry of Mines and Energy (MME) [26], at the end of 2016, Brazil had 24 MW of installed power in centralized photovoltaic power plants. However, such power is not yet enough to place Brazil among the twenty world leaders in the production of this type of energy, all of them with an installed capacity exceeding 1 GW [27].

Despite the low installed power in large photovoltaic power plants, Brazil has managed to emerge in the use of solar energy thanks to distributed generation, these being the main promoters for the use of this technology.

The regulation, elaborated in 2012 by the ANEEL (National Electric Energy Agency) through Normative Resolution N.° 482 and perfected in 2016, brings important incentives to the installation of small-sized power plants based on renewable sources, such as solar and wind energy. As part of this regulation, the Electric Power Compensation System was instituted, which allows the accumulation of generation surpluses in relation to consumption, thus generating credits that can be used within a period of five years [28].

The number of distributed power generation connections at micro scale (up to 75 kW of installed power) and mini (greater than 75 kW and less than 5 MW) is on the rise in Brazil, reaching 10 561 connections registered in 2017, against just four in 2012, with an installed capacity of 114.7 MW, with solar energy responsible for 70% of this total [29].

2. Materials and methods

2.1. Profile of Ilhabela Island

Located on the coast of the state of São Paulo (see Figure 4), Ilhabela is an island populated by 32 197 inhabitants. With a total area of 347.5 km^2; 85% of the territory of the island corresponds to units of environmental conservation. The remaining 15% corresponds to areas suitable for urbanization. Its road structure is installed along the entire coast, connecting the central part of the city with the most remote neighborhoods. This island has a fleet of 17,449 vehicles, of which 7041 are automobiles [30].

Figure 4. Location of Ilhabela, on the coast of the state of San Pablo [31].

Because it does not have its own large-scale electric power generation, electricity in the municipality of Ilhabela is supplied by means of submarine cables, which transmit the energy from the continent to the island. In this way, if the demand for electricity on the island grows considerably, the supply will have to be reinforced, either through the expansion of the submarine cable network, or through the introduction of power generation plants. The latter is one of the proposals of this work, since it proposes the use of photovoltaic solar energy in conjunction with a biogas thermoelectric plant, which would be installed on the island.

According to the Municipal Plan of Ilhabela, currently, 6.5% of the urban population of the municipality has its sewage collected, being thrown directly into the sea without an effective treatment, with a simple removal of coarse waste. A system of wastewater treatment stations is in the implementation phase, and projections are that, by 2025, 3,795,000 m^3 of waste will be produced and, by 2030, 4 345,000 m^3 [32].

According to Lamas, methane (CH_4) present in biogas produced from the anaerobic treatment of sewage waste, is approximately 21 times more damaging to the atmosphere than carbon dioxide (CO_2) [33]. Therefore, the energy use of biogas becomes interesting, since it reconciles the generation of renewable energy and environmental sanitation.

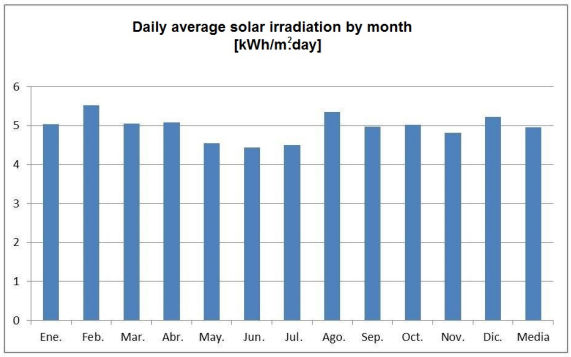

Figure 5. Monthly average daily solar irradiation (kWh/m^2/day) on Ilhabela Island

On the other hand, according to the data obtained from the Sérgio S. de Brito Solar and Wind Energy

Reference Center (CRESESB, in Portuguese) [34], Ilhabela has a solar irradiation pattern with intensity variation depending on the season. February is the month with the highest average solar radiation (5.56 kWh/m^3/day) and June the month with the lowest average, with only 3.92 kWh/m^3/day. Figure 5 shows the daily-monthly solar radiation.

2.2. Energy consumption of a BEV

In this study, BEV performance is analyzed in terms of the fuel consumption rate (TCE). That is, the TCE is calculated as the ratio between the power consumed and the distance traveled [35]. Equation 1 is used for this calculation.

$$TCE = \frac{Energy\ consumed\ (kWh)}{Distance\ travelled\ (km)} \quad (1)$$

The lower the TCE, the better the energy efficiency. The autonomy of the BEV is calculated with Equation 2.

$$Auto = \frac{Energy\ fully\ charged\ BEV\ (kWh)}{TCE\ (kWh/km)} \quad (2)$$

The average distance traveled by a vehicle in Brazil is similar to the one verified in the state of Louisiana (USA), estimated at 35 km/day [36].

According to the projection of the Energy Research Company (EPE, acronym in Portuguese) [37], EVs will represent 1.7% of the national fleet by 2025, and 4.5% by 2030.

The calculation of electrical consumption per km in a BEV fleet can be calculated with Equation 3 [38].

$$CelEVB = P_M \times n \times D \times TCE \quad (3)$$

Where:

PM – market penetration of the BEV;
n – total number of cars in the fleet considered;
D – average distance traveled by a BEV in the period of one day;
TCE – electric consumption rate per km.

2.3. Energy analysis of the biogas plant

The environmental peculiarities of the place where this project is intended to start require that the use of biomass produces the least possible impact. Thus, gas microturbine technology offers solutions with low NO_x emission rates, which represents a great impact for the greenhouse effect. The manufacturer of the Capstone 30 microturbine guarantees an NO_x emission rate of less than 9 ppm in exhaust gases. Thus, the environmental advantage obtained with the use of this technology is evident, since compared to the technology of conventional internal combustion generating groups (Otto cycle), these have an emission of 3000 ppm, [39].

For this study, the Capstone 30 microturbine is selected, a model already used in other works with biogas from wastewater from San Pablo – Brazil [40] and in cogeneration processes [41]. The characteristics of this turbine are presented in Table 1.

Table 1. Characteristics of the CAPSTONE C30 microturbine [39]

Model	C30
Power (kW)	30
Efficiency (%)	26
Exhaust gas flow (kg/s)	0,31
Exhaust temperature (°C)	275
Heat Rate (MJ/kWh)	13,8

2.3.1. Biogas composition

The biogas generated from the anaerobic digestion of biomass from wastewater has the composition presented in Table 2 [40].

Table 2. Composition of biogas

Component	Volume (%)	PCI (kJ/kg)
CH_4	66,5	50
CO_2	30,5	-
$O_2 + N_2$	0,5	-
H_2O	2,5	-
Total	100	22,2

2.3.2. Biogas production

According to França Junior [42], the average rate of biogas generation is 170.9 m^3 per 1000 m^3 of treated waste. Therefore, it is possible to calculate the biogas values that can be obtained for the wastewater treatment station (ETE) of Ilhabela with Equation 4.

$$m_{biogas} = tx_{biogas} \times m_{residue} \quad (4)$$

Where:

m_{biogas} – volume of biogas generated [m^3/year];
tx_{biogas} – average rate of biogas generation (0,1079 m^3 biogas/m^3 residue);
$m_{residue}$ – volume of treated waste [m^3/year].

With the result of equation 4, the flow values in [kg/s] can be obtained with Equation 5.

$$m_{bio} = \frac{m_{biogas} \times \gamma_{biogas}}{31\ 104\ 000(s/año)} \quad (5)$$

Where:

m_{bio} – biogas flow [kg/s];

m_{biogas} – volume of biogas generated [m^{3}year];
γ_{biogas} – specific mass of biogas with composition 65 % CH_4 y 35 % CO_2 (1,1518 kg/Nm^3) [43].

2.3.3. Energy analysis

The methodology adopted for the energy analysis of the biogas plant is that used by Llerena [44]. This analysis is detailed below step by step.

2.3.4. Control volume of the Brayton cycle

In Figure 6, the gas cycle is observed. This cycle has a compressor, a combustion chamber, the turbine and the heat exchanger.

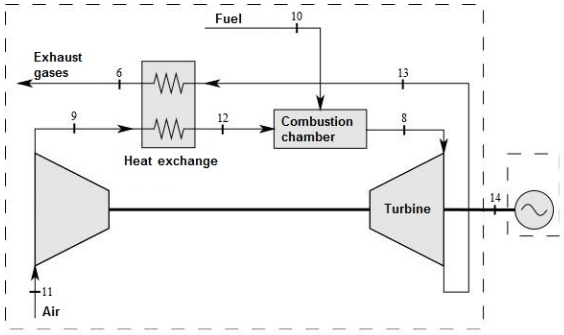

Figure 6. Control volume of the Brayton cycle [41].

In this study the ISO conditions of the microturbine of the GTW Handbook are maintained [45]. Considering that the efficiency of the electric generator is 95%, the power is obtained in point 14 with Equation 6:

$$\dot{W}_{14} = \frac{P_{generator}}{\eta_{generator}} \tag{6}$$

Where:
P – electric power in the generator [kW].

Now, the biogas flow is calculated with Equation 7:

$$HR \cdot P = PCI_{biogas} \cdot m_{biogas} \tag{7}$$

Where:
HR – Heat Rate [MJ/kWh];
P – power at the turbine output [kW];
PCI – lower calorific value of biogas [kJ/kg];
M – biogas flow [kg/s].

With the flows of the biogas and the exhaust gases, the air flow is calculated with Equation 8:

$$\dot{m}_{11} = \dot{m}_6 - \dot{m}_{biogas} \tag{8}$$

2.3.5. Compressor control volume

According to Çengel and Boles [46] the compressors have an isentropic efficiency that varies between 80 and 90%. In this study, the highest efficiency was used.

Point 9

The air flow at the compressor outlet is equal to the air flow at the compressor inlet, so we have Equation 9:

$$\dot{m}_9 = \dot{m}_{11} \tag{9}$$

According to the GTW Handbook [45], the pressure ratio is 4:1. With this data, the pressure in point 9 is calculated. For this, Equations 10 and 11 were used:

Pressure in point 9:

$$P_9 = P_{11} \cdot Rp \tag{10}$$

Relative pressure in point 9:

$$Pr_9 = P_{11}\frac{P_9}{P_{11}} \tag{11}$$

With Equation 12, the enthalpy is obtained at point 9 [44].

$$h_9 = \frac{h_{9s} - h_{11}}{\eta_{cpmp}} + h_{11} \tag{12}$$

Point 12

According to Carvalho [47], there is a 3% loss in the outlet pressure in the heat exchanger. According to the same author, in the case of temperature, there is a difference of 324 °C. Thus, the pressure and temperature at point 12 are calculated with Equations 13 and 14, respectively.

Pressure in point 9:

$$P_{12} = P_9 - (P_9 \cdot 0,03) \tag{13}$$

Temperature at point 9:

$$T_{12} = T_9 + \Delta T \tag{14}$$

To calculate the air flow at point 12, Equation 15 was used.

$$\dot{m}_{12} = \dot{m}_9 \tag{15}$$

2.3.6. Control volume of the combustion chamber

Point 8

The flow of the exhaust gases at point 6 is equal to the flow of gases at the outlet in the combustion chamber. Thus, Equation 16 was used to calculate the gas flow at point 8.

$$\dot{m}_8 = \dot{m}_6 \tag{16}$$

According to Carvalho [47] there is a pressure loss of 3% in the combustion chamber. Thus, Equation 17 was used to calculate the output pressure of the CC.

$$P_8 = P_{12} - (P_{12} \cdot 0,03) \tag{17}$$

According to Saravanamuttoo et al. [48], the CC can have an efficiency of 99%. Now, with the law of conservation of energy we have Equation 18

$$\dot{m}_8 \cdot \dot{h}_8 = \dot{m}_{12} \cdot \dot{h}_{12} + (PCI_{biogas} \cdot \dot{m}_{biogas}) \cdot \eta_{CC} \tag{18}$$

2.3.7. Turbine control volume

Point 13

For calculating pressures in the turbine, the same air ratio as the compressor was considered. Thus, the relative pressure at point 13 is calculated with Equation 19:

$$Pr_{13} = Pr_8 \frac{P_{13}}{P_8} \tag{19}$$

The energy balance is calculated with Equation 20:

$$(h_8 - h_{13a}) \cdot \dot{m}_8 = \dot{W}_{14} + \frac{(h_9 - h_{11}) \cdot \dot{m}_{11}}{\eta_{comp}} \tag{20}$$

The efficiency of the turbine is calculated with Equation 21.

$$\eta_{turbine} = \frac{\dot{W}_{generator}}{PCI_{biogas} \cdot \dot{m}_{biogas}} \tag{21}$$

2.4. Sizing of the PV system

2.4.1. Calculation of the necessary photovoltaic power

Through the calculation of the nominal power (generated from solar radiation) necessary to meet the average daily consumption of the loads, and with the data of the energy supplied by the biogas plant, the area of the solar panels to be installed can be estimated.

This calculation shows, approximately, the capacity of the system dimensioned to meet the demand, supplying energy in equal quantity to that requested by the loads (EV Fleet).

Through the application of Equation 22, the nominal installed power required to meet the demand is determined [49]:

$$P_{FV} = \frac{E}{n_V n_R HSP} S_f \tag{22}$$

Where:

E – energy demand requested by the load;
S_f – safety factor for resistive and thermal losses in photovoltaic cells, with an adopted value of 1.15;
n_v *and* n_R – efficiencies of system components;
HSP – Peak-Sun-Hours.

The average daily solar irradiation can be referred to in terms of "peak sun hours" (HSP). This value refers to the equivalent number of daily hours that a given region should undergo (1 kW/m^2) to receive the same amount of solar energy. Thus, the number of HSP is numerically equal to that of the average solar irradiation (kWh/m^2.dia). With this value it is possible to estimate the total area to be occupied by the photovoltaic modules. In this way, through the division of installed power by the efficiency of the modules, the resulting area is found [46]. Equation 23.

$$A_{total} = \frac{P_{FV}}{E_{ff}} \tag{23}$$

Where:

A_{total} – area of the modules (m^2);
PFV – average power required (kW);
Eff – efficiency of the modules(%).

2.4.2. Costs of photovoltaic solar energy

In Brazil, the total installation cost is composed of the following elements: PV modules (43%), inverters (24%), physical structure and protections (16%) and installation (17%) [50].

According to data from the Greener report [51], the average price of installed kW of photovoltaic solar energy in Brazil in 2017 was between 8 R$/kW, for smaller systems, and 4.62 R$/kW for major systems. Other values are in accordance with Table 3.

Table 3. Prices [45]

Power (kW)	2	4	8	12	30	50	75	150
Price (R$/W)	8	6,84	5,95	5,65	5,26	5,1	5,01	4,62

3. Results and discussion

3.1. Analysis of energy consumption

Taking into account the fleet of 7041 automobiles, and based on the projection of the EPE. By means of the calculation of the TCE and with Equation 3, the monthly energy consumption of the EV fleet can be calculated, according to their degree of market penetration. The results are presented in Table 4.

Table 4. Consumption of electric power of the BEV in relation to market penetration

BEV market penetration	N. of electric vehicles	Average energy consumption (kWh/month)
4%	282	46 327,21
2%	141	23 163,60

From Table 4 it can be seen that a higher EV penetration means a higher energy demand. This increase also represents a more powerful photovoltaic solar plant and consequently a larger installation area will be necessary.

3.2. Energy analysis of the biogas plant

The results of the energy analysis of the microturbine using biogas are shown in Table 5.

Table 5. Summary of the energy analysis

Point	T [°C]	P[kPa]	Flow [kg/s]	h [kJ/kg]
6	275	101,32	0,31	490
8	831,9	393	0,31	1167,15
9	184,3	405,3	0,3041	459,67
10	25	101,32	0,0059	-
11	25	101,32	0,3041	298,6
12	508	393,24	0,304	801,9
13	594,6	96,25	0,31	825,77

According to Table 5, the microturbine needs a flow rate of 0.0059 kg/s of biogas to provide its nominal power of 30 kW. With Equations 4 and 5, and with the flow projections of 3 795 000 m^3 /year in 2025 and 4 345 000 m^3/year in 2030 in the Ilhabela sewerage system, a production capacity of 0,0152 kg/s in 2025 and 0.0174 kg/s of biogas in 2030 is reached, with both values above the consumption need of the microturbine, making this type of energy feasible from the technical point of view.

Thus, with the biogas plant operating 18 hours a day, at full capacity (30 kW) at times when there is no solar irradiation, there is an average generation of 16 200 kWh/month. With this monthly energy value, and with the energy consumption of the BEV fleet, according to Table 6, the need for additional generation of energy by the photovoltaic system was calculated (it is considered that this system will work the remaining 6 hours).

Table 6. Energy to be served by the PV system, given the operation regime of the biogas plant

BEV market penetration	Energy biogas (kWh/month)	Energy of the PV solar system (kWh/month)
4%	16 200,00	30 127,21
2%	16 200,00	6963,6

With the information presented in the previous table, the PV systems suitable for the energy supply in the two scenarios were sized.

3.3. Analysis of the sizing of the photovoltaic plant

By means of Equation 22, the photovoltaic power needed to supply the additional energy demand was calculated to supplement the energy already provided by the biogas system. Because it is an island, with a tourist and ecological vocation, the area occupied by photovoltaic generation is a very important factor for the implementation of this technology. With Equation 23, and adopting an efficiency of 15% in the PV modules, typical in models of polycrystalline silicon technology available in the market, the total area of installation of the modules was calculated. The results are presented in Table 7.

Table 7. Power and area occupied by dimensioned PV systems

BEV market penetration	Power (kW)	Installed area (m^2)
4%	305,20	2 034,69
2%	70,54	470,30

For the same generation capacity in the biogas system (30 kW), the area occupied by the PV system grew by more than four times. Taking into account the environmental impact caused by the occupation of relevant portions of the area by the PV system, and the possibility of distributed generation, the application of this technology leads to a choice between the construction of a larger photovoltaic plant or a larger number of small plants, suitable for residential-sized facilities.

3.4. Analysis of installation costs

The cost of the biogas generator system with the Capstone 30 microturbine, was already used in similar works by Coelho [40], where a value of R$ 8568.62 per installed kW was reached. Thus, the investment in a complete 30 kW system with this type of technology would cost R$ 257,058.60.

In relation to the photovoltaic plant, considering the two options (centralized and distributed), and with the current costs of the market, the investment for the installation of this PV system were also calculated. Adding these two costs, the total costs of the HPGS was obtained, which are presented in Table 8.

Table 8. Total investment for the HPGS

% VEB	Distributed PV		Centralized PV	
	R$	Config.	R$	Config.
4%	2 344 647	77 x 4 kW	1 667 096	2 x 150 kW
2%	739 583	18 x 4 kW	610 487	1 x 70 kW

4. Conclusions

Due to the peculiarities of being an island, its tourist and ecological potential, renewable sources of energy are the ideal solution for current and future energy demands of Ilhabela, which will have to occur at some point due to the challenges imposed by the advent of BEV.

It is concluded that the installation of the biogas plant is technically feasible, since the capacity of biogas production on the island will be 0.0152 kg/s in 2025 and 0.0174 kg/s in 2030, that is, twice as much as what is necessary for the plant to work at its maximum capacity (0.0059 kg/s). The biogas plant will have a production of 16 200 kWh/month.

From the photovoltaic plant it is concluded that, if the fleet of electric vehicles is doubled, and the generation capacity of the biogas system is maintained (16 200 kWh/month), the installed power of the supplementary PV system will increase by more than four times its capacity, as well as its installation area. It is also concluded that the adoption of centralized PV systems led to a 28.9% reduction in total investment in a more long-term scenario. In the scenario for 2025, with 2% market penetration of the BEV, the option for the centralized PV system led to a 17.5% reduction in the total cost of installing the HPGS. These differences in capital cost per watt installed between the larger and smaller systems are due to the scale gains in the PV equipment market.

Finally, if on the one hand, centralized photovoltaic generation has a lower cost of installation, on the other, distributed generation is a better promoter of social development, by moving local labor and favoring small businesses, in addition to the benefit of the compensation of energy generated by users of residential distributed generation, with significant reduction in electricity expenses.

References

[1] K. Reiche, A. Covarrubias, and E. Martinot, "Expanding electricity access to remote areas: Off-grid rural electrification in developing countries," *WorldPower2000*, pp. 52–60, 2000. [Online]. Available: https://goo.gl/4d6m7k

[2] T. Hirota, "Task 17 pv for transport draft task workplan for 2018-2020," Waseda University, Tech. Rep., 2017. [Online]. Available: https://goo.gl/jDegU4

[3] Bloomberg New Energy Finance, "Electric vehicle outlook 2017," Bloomberg Finance L.P, Tech. Rep., 2017. [Online]. Available: https://goo.gl/BNtKZe

[4] A. Poullikkas, "Sustainable options for electric vehicle technologies," *Renewable and Sustainable Energy Reviews*, vol. 41, pp. 1277–1287, 2015. DOI: https://doi.org/10.1016/j.rser.2014.09.016.

[5] J. J. Roberts, S. Thibaud, and P. O. Prado, "Proyecto de un sistema híbrido de generación con energías renovables para un establecimiento rural aislado," in *XI Latin-American Congress on Electricity Generation and Transmission "Bioenergy for Electricity Generation" and "Ecological Issues in Power Plants", At São José dos Campos, Brazil*, 2015. [Online]. Available: https://goo.gl/omxcph

[6] A. Cassula, P. O. Prado, J. L. Silveira, and J. J. Roberts, *Energía: Investigaciones en América del Sur,*, 1st ed. Editorial de la Universidad del Sur, 2017, ch. Dimensionamiento de Sistemas Híbridos de Generación de Energía, pp. 109–136. [Online]. Available: https://goo.gl/yBQo3y

[7] T. Wilberforce, Z. El-Hassan, F. Khatib, A. A. Makky, A. Baroutaji, J. G. Carton, and A. G. Olabi, "Developments of electric cars and fuel cell hydrogen electric cars," *International Journal of Hydrogen Energy*, vol. 42, no. 40, pp. 25 695–25 734, 2017. DOI: https://doi.org/10.1016/j.ijhydene.2017.07.054.

[8] V. Gass, J. Schmidt, and E. Schmid, "Analysis of alternative policy instruments to promote electric vehicles in austria," *Renewable Energy*, vol. 61, pp. 96–101, 2014. DOI: https://doi.org/10.1016/j.renene.2012.08.012.

[9] E. Talebizadeh, M. Rashidinejad, and A. Abdollahi, "Evaluation of plug-in electric vehicles impact on cost-based unit commitment," *Journal of Power Sources*, vol. 248, pp. 545–552, 2014. DOI: https://doi.org/10.1016/j.jpowsour.2013.09.009.

[10] K. Seddig, P. Jochem, and W. Fichtner, "Integrating renewable energy sources by electric vehicle fleets under uncertainty," *Energy*, vol. 141, pp. 2145–2153, 2017. DOI: https://doi.org/10.1016/j.energy.2017.11.140.

[11] M. Honarmand, A. Zakariazadeh, and S. Jadid, "Integrated scheduling of renewable generation and electric vehicles parking lot in a smart microgrid," *Energy Conversion and Management*, vol. 86, pp. 745–755, 2014. DOI: https://doi.org/10.1016/j.enconman.2014.06.044.

[12] W. Liu, W. Hu, H. Lund, and Z. Chen, "Electric vehicles and large-scale integration of wind power – the case of inner mongolia in china," *Applied Energy*, vol. 104, pp. 445–456, 2013. DOI: https://doi.org/10.1016/j.apenergy.2012.11.003.

[13] D. B. Richardson, "Electric vehicles and the electric grid: A review of modeling approaches, impacts, and renewable energy integration," *Renewable and Sustainable Energy Reviews*, vol. 19, pp. 247–254, 2013. DOI: https://doi.org/10.1016/j.rser.2012.11.042. [Online]. Available: http://www.sciencedirect.com/science/article/pii/S1364032112006557

[14] L. D. D. Harvey, *Energy and the New Reality 2: Carbon-free Energy Supply*, Earthscan, Ed., 2010. [Online]. Available: https://goo.gl/RzPzu4

[15] J. E. Campbell, D. B. Lobell, and C. B. Field, "Greater transportation energy and ghg offsets from bioelectricity than ethanol," *Science*, vol. 324, no. 5930, pp. 1055–1057, 2009. DOI: http://doi.org/10.1126/science.1168885.

[16] A. R. Bhatti, Z. Salam, M. J. B. A. Aziz, K. P. Yee, and R. H. Ashique, "Electric vehicles charging using photovoltaic: Status and technological review," *Renewable and Sustainable Energy Reviews*, vol. 54, pp. 34–47, 2016. DOI: https://doi.org/10.1016/j.rser.2015.09.091.

[17] F. Mwasilu, J. J. Justo, E.-K. Kim, T. D. Do, and J.-W. Jung, "Electric vehicles and smart grid interaction: A review on vehicle to grid and renewable energy sources integration," *Renewable and Sustainable Energy Reviews*, vol. 34, pp. 501–516, 2014. DOI: https://doi.org/10.1016/j.rser.2014.03.031.

[18] S. J. Chiang, H. J. Shieh, and M. C. Chen, "Modeling and control of pv charger system with sepic converter," *IEEE Transactions on Industrial Electronics*, vol. 56, no. 11, pp. 4344–4353, Nov 2009. DOI: https://doi.org/10.1109/TIE.2008.2005144.

[19] J. L. Silveira, C. E. Tuna, and W. de Queiroz Lamas, "The need of subsidy for the implementation of photovoltaic solar energy as supporting of decentralized electrical power generation in brazil," *Renewable and Sustainable Energy Reviews*, vol. 20, pp. 133–141, 2013. DOI: https://doi.org/10.1016/j.rser.2012.11.054.

[20] M. G. Villalva and J. R. Gazoli, *Energía solar fotovoltaica: conceitos e aplicações*, ERICA, Ed., 2012. [Online]. Available: https://goo.gl/CJKrDF

[21] M. Benaouadj, A. Aboubou, M. Becherif, M. Y. Ayad, and M. Bahri, "Recharging of batteries/-supercapacitors hybrid source for electric vehicles application using photovoltaic energy in a stand-alone point," in *2012 First International Conference on Renewable Energies and Vehicular Technology*, March 2012. DOI: https://doi.org/10.1109/REVET.2012.6195264, pp. 161–166.

[22] J.-H. Song, Y.-S. An, S.-G. Kim, S.-J. Lee, J.-H. Yoon, and Y.-K. Choung, "Power output analysis of transparent thin-film module in building integrated photovoltaic system (bipv)," *Energy and Buildings*, vol. 40, no. 11, pp. 2067–2075, 2008. DOI: https://doi.org/10.1016/j.enbuild.2008.05.013.

[23] N. Altin and T. Yildirimoglu, "Labview/matlab based simulator for grid connected pv system," in *4th International Conference on Power Engineering, Energy and Electrical Drives*, May 2013. DOI: https://doi.org/10.1109/PowerEng.2013.6635804, pp. 1316–1321.

[24] E. B. Pereira, F. R. Martins, S. L. de Abreu, and R. Rüther, *Atlas Brasileiro de Energia Solar*. SWERA, 2017. [Online]. Available: https://goo.gl/8Sr1tG

[25] CCEE. (2015) 3° leilão de fontes alternativas (3° lfa). Camara de Comercialização de Energia Elétrica. [Online]. Available: https://goo.gl/Sy8iWg

[26] MME, *Boletim mensal de monitoramento do setor elétrico*, Ministério de Minas e Energia, 2017.

[27] R. L. Nascimento, "Energia solar no brasil: situação e perspectivas," Camara dos Deputados. Brasil., Tech. Rep., 2017. [Online]. Available: https://goo.gl/gmSddm

[28] ANEEL, *Resolução normativa n. 687, Altera a Resolução Normativa n 482, Módulos 1 e 3 dos Procedimentos de Distribuição - PRODIST*, Agencia Nacional de Energia Elétrica. Brasil Std., 2017. [Online]. Available: https://goo.gl/T6PiFn

[29] ——, *Nota Técnica n. 0056/2017-SRD/ANEEL, Atualização das projeções de consumidores residenciais e comerciais com microgeração solar fotovoltaicos no horizonte 2017-2024*, Agencia Nacional de Energia Elétrica. Brasil Std., 2017. [Online]. Available: https://goo.gl/uq4L3i

[30] IBGE, *Conheça cidades e estados do brasil*, Instituto Brasileiro de Geografia e Estatística, 2017. [Online]. Available: https://goo.gl/nCPqGJ

[31] Itapemar Hotel. (2017) Mapa de bolso - ilhabela. [Online]. Available: https://goo.gl/zW4mFS

[32] P. M. de Ilhabela, *Plano Municipal Integrado de Saneamiento Básico*, Governo do Estado de São Paulo, 2015. [Online]. Available: https://goo.gl/4WVGst

[33] W. Q. Lamas, "Análise termoeconômica de uma mini-estação de tratamento de esgoto com auto-suficiência energética," Ph.D. dissertation, Universidade Estadual Paulista, Faculdade de Engenharia de Guaratinguetá, 2007. [Online]. Available: https://goo.gl/8jqqJu

[34] CRESESB. (2018) Potencial solar - sundata v 3.0. Centro de referência para energia solar e eólica Sérgio Brito. [Online]. Available: https://goo.gl/Ae2cUG

[35] G. M. Fetene, S. Kaplan, S. L. Mabit, A. F. Jensen, and C. G. Prato, "Harnessing big data for estimating the energy consumption and driving range of electric vehicles," *Transportation Research Part D: Transport and Environment*, vol. 54, pp. 1–11, 2017. DOI: https://doi.org/10.1016/j.trd.2017.04.013.

[36] R. Baran and L. F. L. Legey, "The introduction of electric vehicles in brazil: Impacts on oil and electricity consumption," *Technological Forecasting and Social Change*, vol. 80, no. 5, pp. 907–917, 2013. DOI: https://doi.org/10.1016/j.techfore.2012.10.024.

[37] J. B. Soares, "Matriz elétrica brasileira e matriz elétrica brasileira e as rei's," in *Empresa de Pesquisa Energética, Ministério de Minas e Energia*, 2016. [Online]. Available: https://goo.gl/q5GnBS

[38] E. F. Choma and C. M. L. Ugaya, "Environmental impact assessment of increasing electric vehicles in the brazilian fleet," *Journal of Cleaner Production*, vol. 152, pp. 497–507, 2017. DOI: https://doi.org/10.1016/j.jclepro.2015.07.091.

[39] V. Pecora, "Implantação de uma unidade demonstrativa de geração de energia elétrica a partir do biogás de tratamento do esgoto residencial da usp," Master's thesis, Universide de São Paulo (Instituto de Eletrotécnica e Energia). Brasil, 2006. [Online]. Available: https://goo.gl/n35Ysr

[40] S. T. Coelho, S. M. S. G. Velazquez, O. S. Martins, and F. C. de Abreu, "Sewage biogas convertion into eletricity," in *Anais do 6. Encontro de Energia no Meio Rural, 2006, Campinas (SP, Brasil)*, 2006. [Online]. Available: https://goo.gl/X6LWYt

[41] J. C. Galarza, O. Llerena, and J. L. Silveira, "Thermodynamic and economic analysis of cogeneration system applied in biodiesel production," in *XI Latin-American congress electricity generation and transmission - CLAGTEE 2015*, 2015. [Online]. Available: https://goo.gl/9KuUc6

[42] A. T. França Junior, "Análise do aproveitamento energético do biogás producido numa estação de tratamento de esgoto. 2008," Master's thesis, Universidade Estadual Paulista (UNESP). Brasil, 2008. [Online]. Available: https://goo.gl/yAA3zq

[43] D. F. da Costa, "Geração de energia elétrica a partir do biogás do tratamento de esgoto. 2006," Master's thesis, Escola Politécnica, Universidade de São Paulo. Brasil, 2006. [Online]. Available: https://goo.gl/U8u5qM

[44] O. Llerena, "Análisis energético, exergético y económico de un sistema de cogeneración: Caso para una planta azucarera de san pablo," *INGENIUS*, no. 19, pp. 29–39, 2018.
textscdoi: https://doi.org/10.17163/ings.n19.2018.03. 2018.

[45] GTW. (2012) 2012 gtw handbook. Gas Turbine World. PequotPublishing Inc. [Online]. Available: https://goo.gl/qmjxen

[46] Y. Cengel and M. Boles, *Termodinámica*, M. G. Hill., Ed., 2015. [Online]. Available: https://goo.gl/XCTYQU

[47] H. M. de Carvalho, "Desenvolvimento matemático para avaliação de desempenho de turbinas a gás de um eixo," Master's thesis, Universidade Federal de Itajubá. Brasil, 2006. [Online]. Available: https://goo.gl/cSeUzQ

[48] H. I. H. Saravanamuttoo, G. F. Crichton Rogers, and H. Cohen, *Gas Turbine Theory*, P. Hall, Ed., 2001. [Online]. Available: https://goo.gl/smXkp6

[49] M. M. Mahmoud and I. H. Ibrik, "Techno-economic feasibility of energy supply of remote villages in palestine by pv-systems, diesel generators and electric grid," *Renewable and Sustainable Energy Reviews*, vol. 10, no. 2, pp. 128–138, 2006. DOI: https://doi.org/10.1016/j.rser.2004.09.001.

[50] D. I. Marinoski, I. T. Salamoni, and R. Ruther, "Pré-dimensionamento de sistema solar fotovoltaico:estudo de caso do edifício sede do crea-sc," in *I Conferêcia Latino-Americana De Construção Sustentável X Encontro Nacional de Tecnologia do Ambiente Construído. São Paulo. ANTAC*, 2004. [Online]. Available: https://goo.gl/QxnFCa

[51] Greener. (2017) Em 12 meses, preço dos sistemas fotovoltaicos cai 24%. Greener. Pesquisa, Estrategia, Inovação. [Online]. Available: https://goo.gl/iLbso8

Scientific Paper / Artículo Científico

UNIVERSIDAD POLITÉCNICA SALESIANA ECUADOR
INGENIUS
Revista de Ciencia y Tecnología
https://doi.org/10.17163/ings.n20.2018.07
pISSN: 1390-650X / eISSN: 1390-860X

Equivalent elastic modulus for prediction of deformations in joints

Módulos elásticos equivalentes para predicción de deformaciones en articulaciones

Franco Marinelli[1], Brenda A. Weiss[1,*], Marcelo E. Berli[1], José Di Paolo[1]

Abstract

When studying human joints contact mechanics, surface deformations are relevant as they enable a lubrication flow channel that reduces wear. In order to determine the validity of different methods to predict surface displacements, these were applied to the dry and static contact of healthy and prosthetic joints, both for knee and hip joints. Three equivalent elastic modulus for a simplified column model were evaluated: elastic modulus for a layer solid, elastic modulus for a semi-infinite solid (or Winkler elastic modulus) and elastic modulus for a corrected semi-infinite solid. A hertzian load was considered for all cases. The results were compared with the solution of the elasticity equations by means of the finite element method (FEM). The results for the Young´s modulus, corresponding to a material as a layer, are those that best approximate the FEM prediction. It is also shown that the Young´s module derived from the semi-infinite approximation are inappropriate. Likewise, this work allowed the training of an undergraduate student in Computational Mechanics.

Keywords: finite element, hip joint, knee joint, lineal contact, lubrication, punctual contact.

Resumen

En el estudio de la mecánica de contacto de las articulaciones humanas, la deformación de las superficies en contacto es fundamental porque posibilita un canal por el que fluye el lubricante reduciendo el desgaste. Para determinar la validez de las predicciones de los desplazamientos de estas superficies a partir de distintos métodos, estos se aplican al estudio del contacto seco y estático de articulaciones de rodilla y de cadera, sanas y protésicas. Aplicando una carga hertziana, se evaluaron tres módulos elásticos equivalentes en un modelo simplificado de columna: el correspondiente a un sólido de pequeño espesor, el correspondiente a un sólido semiinfinito o de Winkler y el correspondiente a un sólido semiinfinito corregido. Los resultados se contrastaron con la solución obtenida resolviendo numéricamente las ecuaciones de elasticidad mediante el método de elementos finitos (MEF). Los resultados para el módulo de Young correspondiente a un material de pequeño espesor, son los que mejor se aproximan a los obtenidos por el MEF. Se demuestra también, que los módulos de Young derivados de la aproximación de sólido semiinfinito son inapropiados. Asimismo, con este trabajo se ha entrenado un becario en las artes de la Mecánica Computacional.

Palabras clave: cadera, contacto lineal, contacto puntual, elementos finitos, lubricación, rodilla.

[1,*]Computational Biomechanics Group, Faculty of Engineering, Universidad Nacional de Entre Ríos, Argentina. Author for correspondence ✉: bweiss@ingenieria.uner.edu.ar.
https://orcid.org/0000-0001-5919-9614, https://orcid.org/0000-0002-0514-1756,
https://orcid.org/0000-0001-9404-6787, https://orcid.org/0000-0002-6964-1864.

Received: 21-05-2018, accepted after review: 14-06-2018

Suggested citation: Marinelli, F.; Weiss, B.; Berli, M. y Di Paolo, J. (2018). «Equivalent elastic modulus for prediction of deformations in joints». Ingenius. N.°20, (july-december). pp. 70-82. doi: https://doi.org/10.17163/ings.n20.2018.07.

1. Introduction

The human knee and hip joints allow relative movement between the bones that compose them, femur and tibia in the first case, hip and femur in the second.

Wear is the main factor limiting the useful life of knee and hip implants [1], and given the need for more durable prostheses evidenced in the increase in revision arthroplasties projected for the year 2030 [2, 3], the study of the mechanics of joint contact becomes highly important.

Both in healthy and prosthetic joints, joint surfaces are lubricated by synovial fluid and the lubrication regime depends, among other factors, on the deformation suffered by the joint surfaces in contact.

Numerous studies of lubricated contact in human joints express the displacements suffered by joint surfaces by means of approximate models that simplify the system of equations, reducing the computational effort to solve them [4, 5]. These models are valid for low rigidity linear elastic and layer materials, in which the dimension in the direction of the load is at least an order of magnitude less than the other dimensions [6]. In this case, the displacement at a point on the surface of the solid is assimilated to that of an isolated column (not connected to its surroundings) of a material that has elastic properties expressed through an elastic or Young's modulus, called an equivalent.

Three equivalent Young's modulus can be mentioned, which can be included in the column displacement models and which are analyzed and compared in this work: the equivalent Young's modulus that arises from considering a layer solid [6], and two Young's modulus named Winkler [7] and corrected semi-infinite (SIC) both derived from considering a semi-infinite solid.

In this work, representative cases of healthy and prosthetic joints are evaluated, applying the three mentioned elastic modulus, and the results obtained are compared with those provided by the solution of the elastic problem in the material, through the resolution of the differential linear elasticity equation, using numerical calculation based on the finite element method (FEM). This solution is assumed as the exact solution [8].

Although the joints of the knee and hip, healthy and prosthetic, are lubricated by synovial fluid, they are usually considered as a dry and static contact [9,10], displaying, in some cases, pressure profiles which are practically identical as those obtained from elastohydrodynamic models [11]. Therefore, in this work a Hertzian load is applied in all cases.

All contact problems are inherently non-linear since the contact area depends, in a non-linear way, on the load [9, 12]. In the present work, a cylinder-on-plane geometry (CoP, linear contact situation) equivalent to the knee and a geometry of the sphere-on-plane type (SoP, point contact situation) equivalent to the hip is considered [13–15].

This article is the product of training activities in the arts of Computational Mechanics of an advanced student of the Bioengineering major, as a research initiation fellow for the main project in which this work is inscribed.

2. Materials and methods

2.1. CoP model

The knee joint, both natural and prosthetic, can be physically abstracted as a full cylindrical body in linear contact with a hollow cylindrical body. In such an abstraction, the curvature in the medial-lateral direction of the elements in contact (tibial and femoral components) is neglected. Additionally, when the contact region is small compared to the radius of the cylinders, the contact between two rollers can be represented by the contact of an equivalent roller and a plane. The equivalent cylinder (see Figure 1) has the combined curvature of the cylinders considered initially, that is, in this case the radius R' is obtained from the radii of the femoral condyle (or femoral component, R_2) and the radius of the tibial plate (or tibial component, R_1). Figure 1b shows the equivalent representation and the system of coordinate axes, with the x axis coinciding with the anterior-posterior direction (and movement of the knee), the y- axis coinciding with the direction of application of the load and the z axis with the medial-lateral direction.

The fundamental reason for this geometrical approximation is the possibility of proposing a flow model in Cartesian coordinates for the elastic problem and also in the case of lubricated contact [16, 17]. This description is simpler to solve, not only analytically in some cases, but also numerically.

The linear contact produces a state of flat deformations independent of the medial-lateral direction. In this work, H is defined as the length of a knee joint in this direction (see Table 1).

According to the above, the knee joint can be modeled as a non-deformable cylinder on a flat solid of low rigidity as shown in Figure 1b. The thickness of the flat solid will represent the joint thickness of the natural cartilages in a healthy joint (see section 2.5). In the case of the prosthetic joint, the deformable material is ultra high molecular weight polyethylene (UHMWPE), which has a modulus of elasticity of 100 times less than that of the femoral component, since it is usually made of a medical grade stainless titanium or steel alloy (AISI 316L among others).

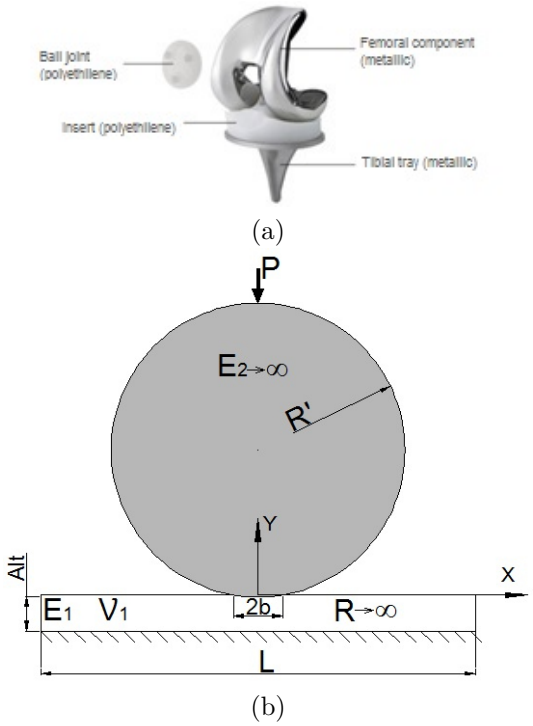

Figure 1. (a) Total knee prosthesis [18].
(b) Equivalent representation in a CoP contact.

Table 1. Parameters used for the simulation of knee joints

	Description	Value
F	Load	2,352 x 103[N]
H	Material width assumed in the direction of the cylinder axis	0,03 [m]
R_1	Radius of the femoral condyle	0,033 [m]
R_2	Radius of the tibial plate	0,045 [m]
R'	Equivalent radius	0,1237 [m]
v_1	Poisson's ratio	0,4
P	Load per unit length	78,400 x103 [N/m]

2.1.1. Hertzian load

The hertzian load acting on dry contact in Figure 1b [16] follows a semi-ellipse distribution for the specific load per unit area, as shown in Equation (1):

$$q(x) = \frac{q0}{b}\sqrt{b^2 - +x^2} \tag{1}$$

Where q_0 is the maximum specific load per unit area, acting in the center of the contact, that is, in the center of the segment of length 2b, and is given by:

$$q_0 = \left[\frac{P(R_1 + R')}{\pi^2(R_1R')(k_1 + k_2)}\right]^{\frac{1}{2}} \tag{2}$$

P is the load per unit length in the direction of the cylinder axis. The value of P is given by the relation between the total load F on the contact and the length of the cylinder H:

$$P = \frac{F}{H} \tag{3}$$

The term $\frac{(R_1+R')}{(R_1R')}$ it is taken as $\frac{1}{R'}$ for tending R_1 to infinity. The constants k_i of Equation 2 contain the properties of the linear elastic material: Young's modulus and Poisson's ratio. Given the parameters in Figure 1b, k_2 is null, therefore:

$$k_1 = \frac{1 - v_1^2}{\pi E_1} \tag{4}$$

Finally, the load q0 is defined by:

$$q_0 = \left[\frac{P}{\pi^2 R' k_1}\right]^{\frac{1}{2}} \tag{5}$$

The half-width b of the contact is given by:

$$b = \sqrt{\frac{4P(k_1 + k_2R_1R')}{R_1 + R'}} \tag{6}$$

and taking into account the previous considerations

$$b = \sqrt{4Pk_1R'} \tag{7}$$

where the radius R' [16] is given by:

$$R' = \frac{R_1R_2}{R_2 - R_1} \tag{8}$$

2.2. SoP model

The hip or coxofemoral joint can be physically abstracted as a full spherical body in point contact with a hollow spherical body as shown in Figure 2a. This geometric model is usually called a ball-in-socket type and is characterized by the radius of the femoral head (convex spherical surface), the radius of the acetabulum (concave spherical surface), and the space between both surfaces (clearence c*). The equations that govern this model are expressed in spherical coordinates, therefore, they require a 3-dimensional analysis [11].

An equivalent model, which allows for the expression of the governing equations in Cartesian coordinates—and for the simplification of its resolution by converting it into a problem in 2 dimensions—, is the so-called "ball-on-plane" as shown in Figure 2b [19].

Both a healthy hip joint and a prosthetic joint can be modeled geometrically as a sphere on a deformable plane. This approach is valid when it comes to small contact regions compared to the radius of the spherical surfaces. The equivalent sphere has a R' radius which is obtained from the radius of the femoral head (R_2) and the inner radius of the acetabulum (R_1), so that the sphere in contact with the plane possesses the combined curvature of the spheres of Figure 2a.

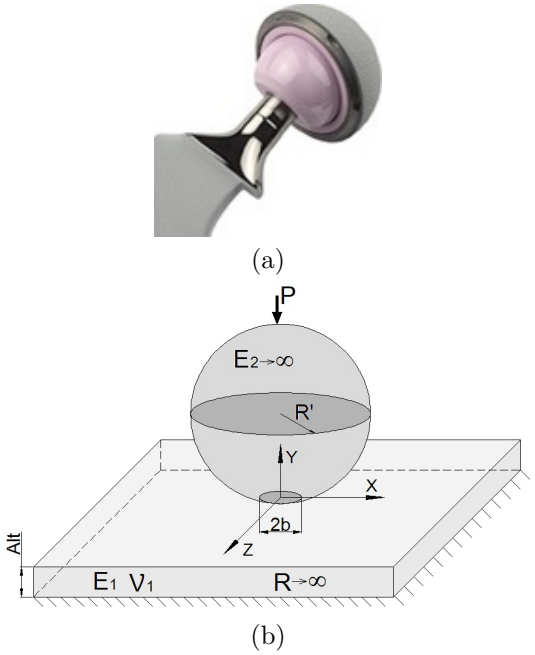

Figure 2. The geometry has polar symmetry. (a) Total hip prosthesis [18]. The femoral head and acetabulum are highlighted in pink. (b) Equivalent representation in a SoP contact.

Table 2. Parameters used for the simulation of hip joints

	Healthy joint	**Prosthetic joint**
P	2,352 x 103 [N]	2,352 x 103 [N]
$R1$	0,021 [m]	0,018 [m]
$c*$	400 [µm]	80 [mm]
R'	1,07 [m]	4,1[µm]
n	0,4	0,4
E	10 [MPa]	1 [GPa]

2.2.1. Estimation of the load

For the determination of the charge on the dry contact surface, the hertzian model was used for a sphere on a plane.

$$q(r) = \frac{q_0}{b}\sqrt{b^2 - r^2} \tag{9}$$

Where q_o is the maximum load per unit area, acting in the center of the circular contact surface of radius b.

$$q_0 = \frac{3}{2}\frac{P}{b^2\pi} \tag{10}$$

P, in this case, is the total charge exerted on the sphere. The radius b, is given by:

$$b = \sqrt[3]{\frac{3PR'}{4K}} \tag{11}$$

K being

$$K = \left(\frac{1 - v_1^2}{E_1} + \frac{1 - v_1^2}{E_2}\right) \tag{12}$$

Since E_2 is 2 orders of magnitude greater than E_1, it could be assumed that E_2 tends to infinity, so K becomes:

$$K = \left(\frac{1 - v_1^2}{E_1}\right)^{-1} \tag{13}$$

2.3. Equivalent elastic modulus

2.3.1. Column model for layer material (PE)

This model is based on the assumption that the deformable material is composed of columns of cross section to the load (see Figure 3) with differential size. Each column is in lateral contact with columns of the same characteristics, the tangential forces between them being negligible [6].

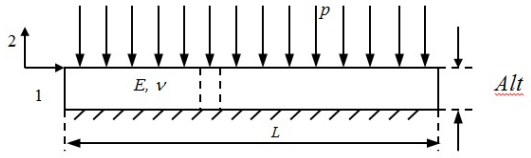

Figure 3. Layer solid subject to a compression in the direction of the layer.

Assuming the solid is a linear elastic, the relationship between tensions (T) and deformations (E) is given by Hooke's law which, in terms of the constants of Lamé (μ and λ) and in indexical notation, is expressed:

$$T_{i,k} = 2\mu E_{i,k} + \lambda E_{j,j}\delta_{i,k} \tag{14}$$

where $\delta_{i,k}$ is the Kronecker delta and E and T are the tensors of deformations and tensions, respectively. If it is assumed that the material considered is linear elastic, of low stiffness and layer, loaded to compression in the direction of its thickness (direction y or 2 in indexes), then, the normal tension in the direction y is much greater than the others, which can therefore be neglected. Likewise, deformations other than the relative shortening in the y direction are negligible. Hooke's law is:

$$T_{y,y} = (2\mu + \lambda)E_{y,y} \tag{15}$$

which is equivalent to Hooke's law for a single column of elastic modulus $(2\mu + \lambda)$, then (see Figure 1b):

$$E_{y,y} = -\frac{d}{Alt} \tag{16}$$

$$T_{y,y} = -p \tag{17}$$

Where p is the normal tension of the surfaces in contact, d is the surface displacement and Alt is the thickness of the low rigidity material.

$$p = (2\mu + \lambda)\frac{d}{Alt} = E_c^{''}\frac{d}{Alt} \tag{18}$$

Where $E_c^{''}$ is the equivalent elastic modulus, which in terms of Young's modulus (E_1) and Poisson's ratio (v_1) of the tibial component is expressed:

$$E_c^{''} = \frac{E_1(1-v_1)}{(1+v_1)(1-2v_1)} \tag{19}$$

2.3.2. Winkler equivalent elastic modulus (W) and corrected semi-infinite solid (SIC)

The Winkler equivalent module arises from the case of a solid limited by a plane and with infinite depth in the direction normal to that plane. In this normal direction, a distributed contact load acts on the plane, which produces displacements at every point of the solid. The elastic problem is described by a potential function from which the tensions and, by virtue of Hooke's law, the displacements at each point are obtained. The potential function or function of Airy, has one expression for linear contact and another for point contact.

For a load distribution, both for the case of linear contact [16] and point contact [17], the combined displacements of the surfaces that delimit two different solids in contact, are equivalent to twice the displacement of a solid with a «reduced» or «equivalent» elastic modulus, which links the elastic properties of both solids:

$$\frac{1}{E'} = \frac{1}{2}\left[\frac{1-v_1^2}{E_1} + \frac{1-v_1^2}{E_2}\right] \tag{20}$$

In the particular case in which both solids in contact are equal, the equivalent modulus E' takes the expression (21) and it is called Winkler:

$$E_w^{'} = \frac{E_1}{1-v_1^2} \tag{21}$$

The Winkler modulus is therefore applicable only in the case of natural joints, where both surfaces correspond to the articular cartilage and has been used in scientific publications [7].

As previously discussed, in the case of prosthetic joints, the modulus of elasticity of the femoral component (E_2) is 2 orders of magnitude greater than E_1, therefore the modulus of elasticity obtained from Equation (20) is.

$$E_{SIC}^{'} \approx \frac{2E_1}{1-v_1^2} = 2E_w^{'} \tag{22}$$

$E_{SIC}^{'}$ is identified as elastic modulus of corrected semi-infinite solid (SIC) since it is another particular case of Equation (20).

Note that $E_W^{'}$ y $E_{SIC}^{'}$ are less than $E_C^{''}$ for all values of E and v that are considered. Hence, one of the objectives of this work is to determine the validity of using $E_W^{'}$, $E_C^{''}$ and $E_{SIC}^{'}$ in a specific application.

2.4. Displacement models

To determine the displacement suffered by the surfaces in each case to be analyzed, expression (18) was used, for which the contact pressure is the specific load per unit area q of the hertzian contact. In the case of the knee prosthesis, the load varies longitudinally with the coordinate transverse to the axis of the cylinder (Equation 1), while for the hip joint, the load varies radially (Equation 9). Thus, the displacements in each case are:

$$d(x) = \frac{Alt}{E_i^{''}}q(x) \tag{23}$$

$$d(r) = \frac{Alt}{E_i^{''}}q(r) \tag{24}$$

Where d is the displacement of the surface and $E_i^{''}$ is the equivalent elastic modulus, which is varied for the analysis between those obtained for: material of layer ($E_C^{''}$), semi-infinite or Winkler solid ($E_W^{'}$) and corrected semi-infinite solid ($E_{SIC}^{'}$).

2.5. Parameters for the simulation of knee joints

In the case of knee joints, the parameters shown in Table 1 were used.

It is usually considered that the average maximum strength that a lower limb joint supports is approximately three times the person's body weight in most daily activities such as walking, climbing stairs and standing on one leg [20, 21]. Considering a person with a body mass (MC) of 80 kg, the total load F on the contact area will be 2352 [N] ($F = MC[kg] \times 3 \times 9,8[m/s^2]$). The load per unit length P is calculated according to Equation (3), assuming that the cylinder length H is 0.03 [m].

For the healthy joint, the modulus of elasticity of the articular cartilage is 10 MPa [22], and for the case of the prosthetic joint, it is 1 GPa for the UHMWPE [19]. Both cartilage and UHMWPE have a Poisson's ratio of 0.4.

For this simulation, three thicknesses are used for the deformable material: 1,2, 2 and 2,5 mm for the joint thickness of both layers of cartilage [23] and 8, 10 and 12 mm for the case of the prosthetic joint made of UHMWPE [24].

2.6. Hip joint

In the case of hip joints, the parameters shown in Table 2 were used.

As in the case of the knee joint, a person with a body mass (MC) of 80 kg is considered and the total load borne by the joint is approximately 3 times the body weight of the person [25].

It should be clarified that the constant c* is the difference between the radius of the acetabulum and the radius of the femoral head ($R_2 - R_1$).

For this simulation, three thicknesses are used for the deformable material: 1,2, 2 and 2,5 mm for the joint thickness of both layers of cartilage and 8, 10 and 12 mm for the case of the prosthetic joint made of UHMWPE.

2.7. Obtaining results through FEM

The calculation by finite elements is done using the Structural Mechanics module of the COMSOL Multiphysics 5.3 licensed software. The analyzed geometries were discretized with Lagrangequadratic elements, tetrahedral for the volumes and triangular for the surfaces. In any case and in the corresponding geometries, the linear elasticity differential equation and the compatibility equations, preloaded in the Structural Mechanics module were solved using the MUMPS direct solver, available in COMSOL Multiphysics. The boundary conditions used are described below.

For the knee joint, the simulation is carried out in a 2D domain (indicated in gray in Figure 4) since the load does not vary in the direction of the axis of the cylinder. The boundary conditions are established as follows: the edges L_1, L_3, L_4 and L_5 are defined as tension-free, L_6 is fixed, that is, with zero displacements, and at the edge L_2 the acting tension is the specific hertzian charge q(x) defined in Equation (1) (Figure 4). It should be noted that the used domain is larger than the sector of interest (the one limited by L_2), because the high Poisson's ratio of the simulated materials makes them act almost as incompressible, deforming in the opposite direction at some points in sections L_1 and L_3. Therefore, a larger domain allows the simulation to comply with the imposed boundary conditions.

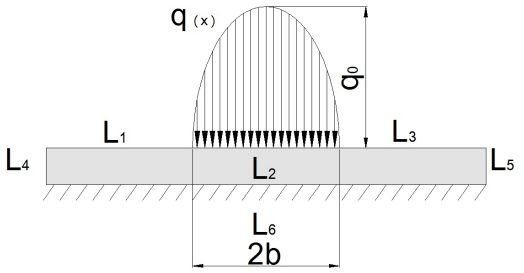

Figure 4. Scheme of the domain for knee joint where the elastic problem is solved through the FEM. The edges are presented where different edge conditions are applied.

In the case of the hip joint, the simulation is performed in a 3D domain (indicated in gray in Figure 5) because the load varies radially.

For this case the base of the prism representing the deformable material was fixed and the rest of the faces are free of tensions, except the central circle, of diameter 2b, where the load is exerted. There, the acting tension is the specific hertzian charge q (r) defined in Equation (9)..

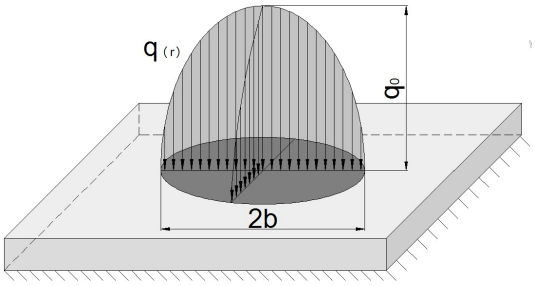

Figure 5. Scheme of the domain for hip joint where the elastic problem is solved through the FEM.

3. Results and discussion

3.1. Knee joint

For the case of the healthy joint, where two layers of thin material are assumed to cover the femoral condyles and the tibial plate, the results of displacement of the surfaces in contact are shown in Figure 6. It should be noted that the total displacements of both coatings are equal to one of only two times the thickness (see Equation 23). Therefore, the results shown in Figure 6 correspond to a solid with the thickness of two cartilages.

It is worth highlighting the positive displacements predicted by the FEM solution taken as accurate shown in Figure 6, due to the quasi-incompressibility of the assumed material due to the high value of Poisson's ratio, as discussed in item 2.6.

While the simplified model with the Winkler equivalent elastic modulus estimates displacements exces-

sively greater than that those given by the FEM solution, the calculations using the corrected elastic modulus of semi-infinite solid underestimates them for the analyzed cases. The results for the simplified model with the equivalent elastic modulus corresponding to the layer solid are the ones that have better approximation with respect to the values thrown by the FEM solution, in Figure 6 the curves for PE and FEM are superimposed.

In Table 3, the maximum displacements obtained for each equivalent elastic modulus and the value obtained by the FEM solution are shown. Table 4 shows the percentage differences corresponding to Table 3, always with respect to the FEM solution.

Figure 7 shows the results obtained for the case of the knee prosthesis. Table 5 shows the maximum displacements for each equivalent elastic modulus and those obtained through FEM. Table 6 shows the corresponding percentage difference.

The overestimation of the displacements when the Winkler equivalent Young's modulus is used in the case of the prosthesis is notewhorthy. This is because this modulus of elasticity corresponds to a particular case of the equivalent modulus of elasticity for a semi-infinite solid in which both surfaces in contact have the same mechanical properties, which does not happen in prosthetic joints. However, the validity of the Winkler modulus applied to healthy joints (Figure 6) can also be questioned since it assumes a semi-infinite solid and not a thin layer as it actually the case with natural cartilages.

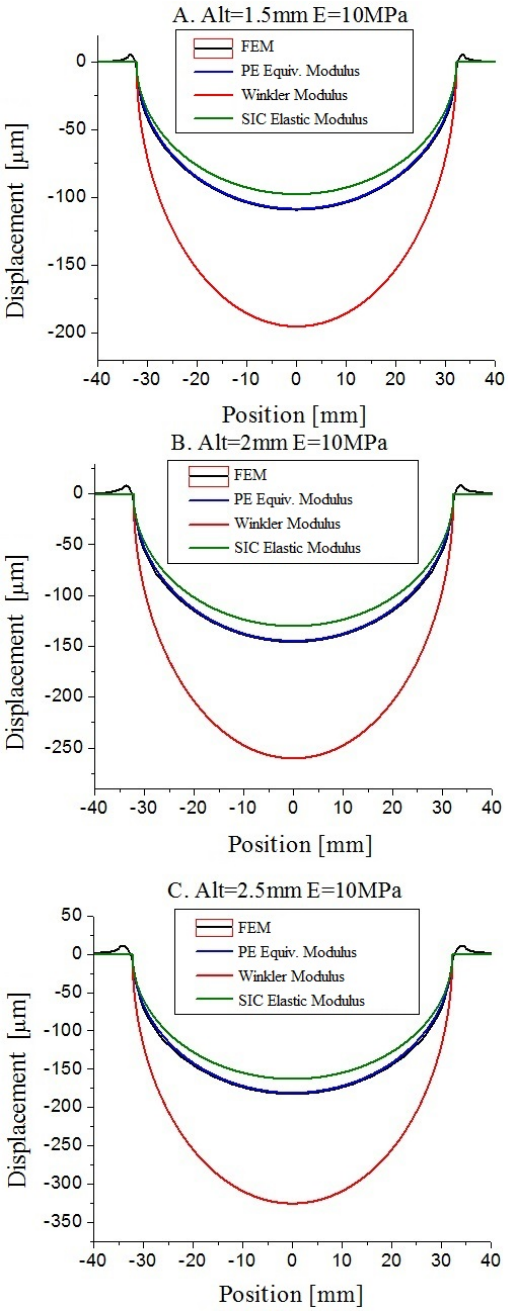

Figure 6. Comparison of the displacement curves of the surfaces in contact obtained for each equivalent elastic module, in contrast to the solution obtained by the FEM in the case of a healthy joint.

Table 3. Maximum displacement obtained by the FEM and for the simplified model with each equivalent elastic modulus considered for the natural knee joint

	Maximum displacement [µm]			
Alt [mm]	**MEF**	**PE**	**W**	**SIC**
1,5	109	108	196	98
2	145	144	260	130
2,5	182	181	326	163

Table 4. Percentage difference of PE, W and SIC results compared to that obtained by FEM for natural knee joints

	Percentage difference [%]		
Alt [mm]	**PE**	**W**	**SIC**
1,5	-0,91	79	-10,1
2	-0,69	79,3	-10,3
2,5	-0,55	78,6	-10,4

Table 5. Maximum displacement obtained by FEM and for the simplified model with each equivalent elastic modulus considered in knee prosthesis

	Maximum displacement [µm]			
Alt [mm]	**MEF**	**PE**	**W**	**SIC**
8	68	58	104	52
10	80	72	130	65
12	92	87	156	78

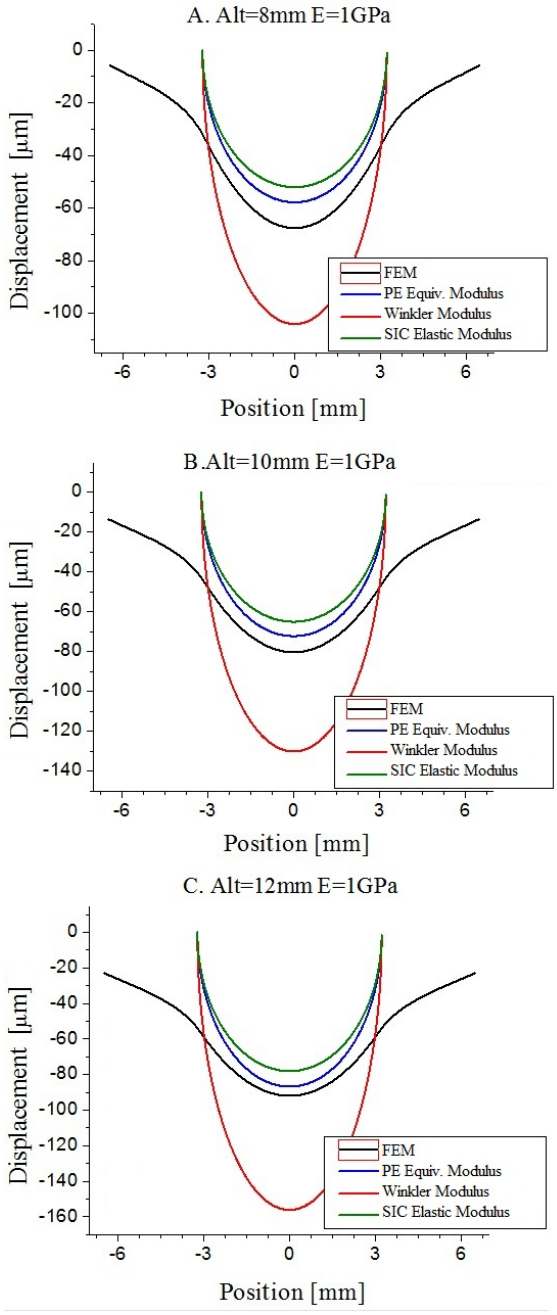

Figure 7. Comparison of the displacement curves of the surfaces in contact obtained for each equivalent elastic module, in contrast to the solution obtained by the FEM in the case of a prosthetic joint.

The comparison of the results of Figures 6 and 7 also reveal the impoverishment of the approximation of layer solid when the elastic modulus of the material and the thickness of the material increase. It is worth noting that UHMWPE's Young's modulus is 100 times greater than that corresponding to natural cartilages.

Table 6. Percentage difference of PE, W and SIC results compared to those obtained by FEM in knee prosthesis

	Percentage difference [%]		
Alt [mm]	**PE**	**W**	**SIC**
8	-14,7	53	-23,6
10	-10	62,5	-18,75
12	-5,43	70	-15,21

3.2. Hip joint

For a healthy hip joint, where two coatings of equal thickness are assumed for which the displacements are added, the surfaces of Figures 8 to 10 were obtained. Table 7 shows the maximum displacements obtained by the simplified model and the different equivalent Young's modules considered, together with the results obtained by the FEM. Table 8 shows the percentage difference of the results of the simplified model with respect to those obtained by the FEM.

Figures 8, 9 and 10 show that for the simplified model, for the cases of layer material and corrected semi-infinite solid, the results have a good approximation to those obtained by the FEM. In the case of the equivalent elastic Winkler modulus, it is shown that the displacement is highly overestimated. This is seen more clearly in Table 8 where, for the layer material, the approximate error is 5% by default with respect to that estimated by the FEM, for the corrected semi-finite material the error is close to 15%, also by default, while for the Winkler elastic modulus the displacement values are overestimated with a very high error, which exceeds 70% (Table 9).

Table 7. Maximum displacement obtained by FEM and for the simplified natural hip joint model with each equivalent elastic modulus considered

	Maximum displacement [µm]			
Alt [mm]	**MEF**	**PE**	**W**	**SIC**
1,5	27,36	26,05	46,89	23,44
2	36,51	34,73	62,52	31,26
2,5	45,69	43,42	78,15	39,07

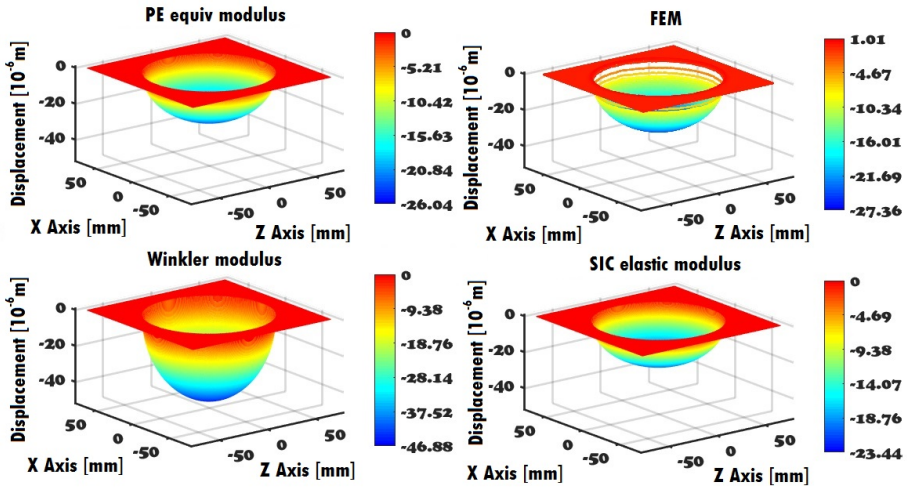

Figure 8. Displacement surfaces obtained for each equivalent Young's modulus and that correspond to the FEM, for healthy natural joint. Alt = 1.5 mm. E = 10 MPa.

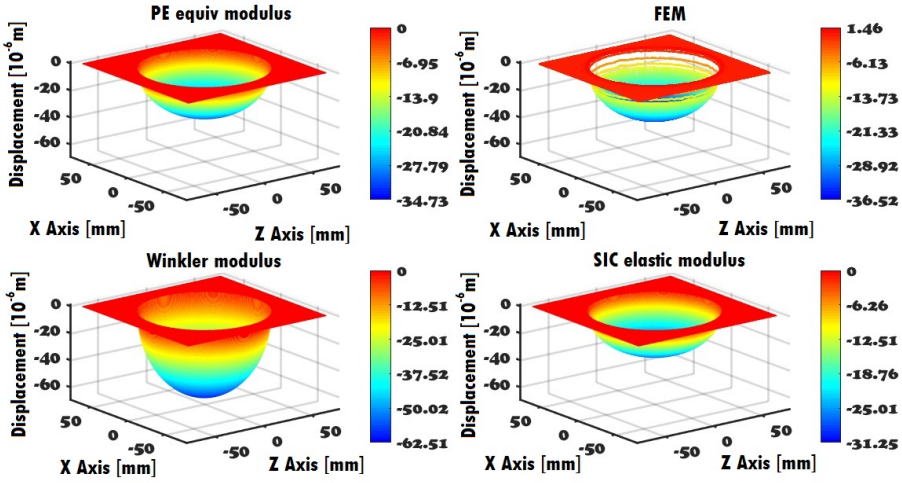

Figure 9. Displacement surfaces obtained for each equivalent Young's modulus and that correspond to the FEM, for healthy natural joint. Alt = 2 mm. E = 10 MPa.

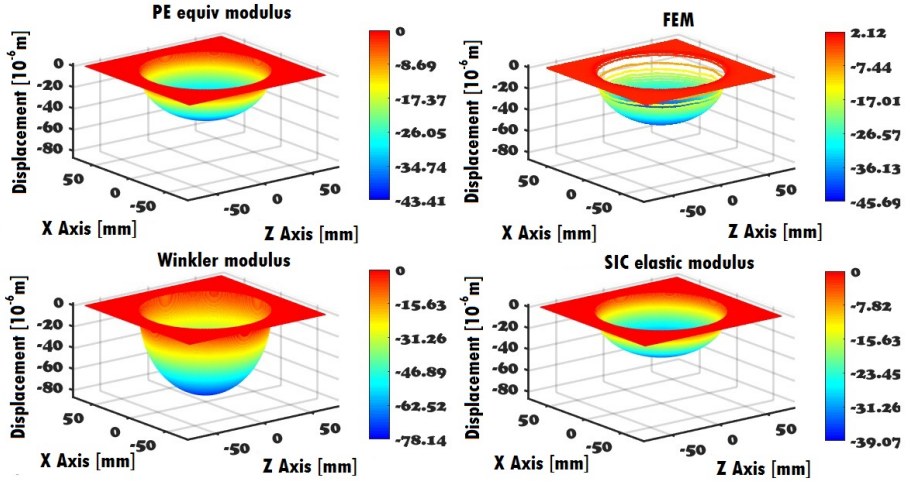

Figure 10. Displacement surfaces obtained for each equivalent Young's modulus and that correspond to the FEM, for healthy natural joint. Alt = 2.5 mm. E = 10 MPa.

Table 8. Percentage difference of PE, W and SIC results compared to those obtained by FEM for natural hip joint

Alt [mm]	Percentage difference [%]		
	PE	W	SIC
1,5	-4,78	71,39	-14,31
2	-4,87	71,23	-14,39
2,5	-4,97	71,05	-14,48

Table 9. Maximum displacement obtained by FEM and for each equivalent elastic modulus considered for the case of prosthetic joint

Alt [mm]	Maximum displacement [mm]			
	MEF	PE	W	SIC
8	15,37	12,69	22,85	11,42
10	20,11	15,87	28,56	14,28
12	24,82	19,04	34,27	17,14

Figures 11 to 13 show the results corresponding to hip prostheses. In this case, discussions for healthy hip articulation are also valid, except that the difference or percentage error relationships are different. Comparing the maximum displacements that occur in the center of the contact, it is observed that for the layer and corrected semi-infinite materials the results of the simplified model differ around 20% and 30%, respectively, by default with respect to that obtained through the FEM. For the Winkler's equivalent elastic modulus, on the other hand, an error of 38% and 48% is presented (Table 10). This is due to the fact that with the increase of the thickness of the solid, the approximation of semi-infinite solid is improved, while the SIC and the layer approach worsen. In addition, the PE approach, as in the case of the knee, is worsened by the increase in the elastic modulus between the natural cartilage and the UHMWPE of the prosthetic joint.

Table 10. Percentage difference of the PE, W and SIC results with respect to that obtained by the FEM for the case of prosthetic joint

Alt [mm]	Percentage difference [%]		
	PE	W	SIC
8	-17,42	48,65	-25,68
10	-21,1	42,02	-28,99
12	-23,28	38,09	-30,96

4. Conclusions

An analysis of deformations has been presented from the calculation of displacements of the surfaces of two solids in charged contact, to evaluate the relevance of using simplified models when constructing contact models. The study was motivated by human joints, where the displacement of surfaces in contact is fundamental to enable a lubrication flow that acts to minimize wear.

For the prediction of the displacements, three equivalent Young's modulus were evaluated in a simplified column model: for a layer solid, for a semi-infinite or Winkler solid, and for a corrected semi-infinite solid.

The results obtained for the Young equivalent module corresponding to a material of layer, are those that better approximate those obtained by the FEM in both geometries considered: linear contact (equivalent to the knee) and point contact (equivalent to the hip). However, the percentage differences with respect to the FEM solution vary in each case and for each material analyzed: natural cartilage (less than 5% in the hip and less than 1% in the knee) or UHMWPE in the prosthetic joint (less than 23, 3% in the hip and less than 15% in the knee). These differences in all cases are by default, which would not be a problem in itself since underestimation puts the analysis on the safe side.

It was demonstrated that the equivalent Young modules derived from the semi-infinite solid approximation, such as the Winkler modulus and the SIC modulus, are inappropriate due to the excessive overestimation of the calculated displacements obtained when considering the first (greater than 38% and reaching the 70% in several cases) and the underestimation of the displacements when considering the second (higher than 10% and reaching 30% in some cases). This, by virtue of what was said in the previous paragraph, puts the analysis at risk for the Winkler's case since, in complete lubrication models, there is a risk of predicting separations between the surfaces in contact that are greater than what would actually occur.

Finally, the work was very useful for the training in the arts of Computational Mechanics of an advanced student of the Bioengineering major, in their role as a research fellow at Universidad Nacional de Entre Ríos, Argentina.

Acknowledgements

To Universidad Nacional de Entre Ríos for financing through PID 6162 and to CONICET for funding through a doctoral grant.

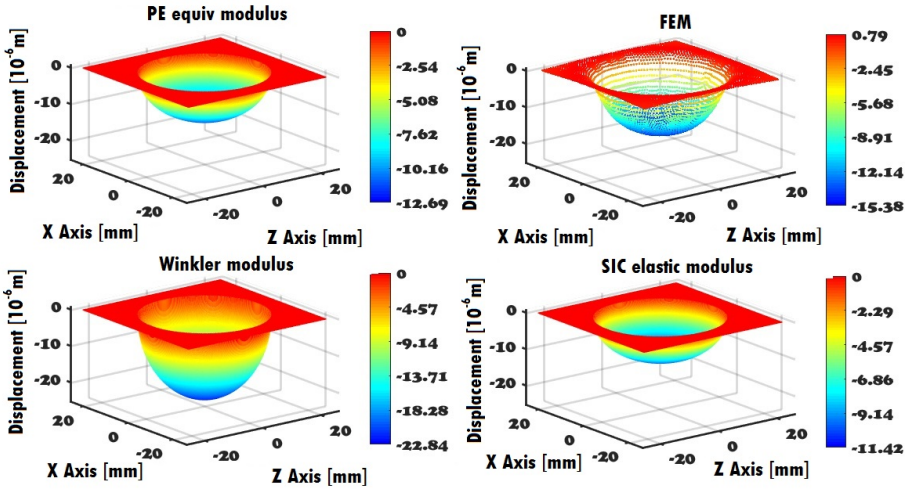

Figure 11. Displacement surfaces obtained for each equivalent Young's modulus and that correspond to the FEM, for prosthetic articulation. Alt = 8 mm. E = 1 GPa.

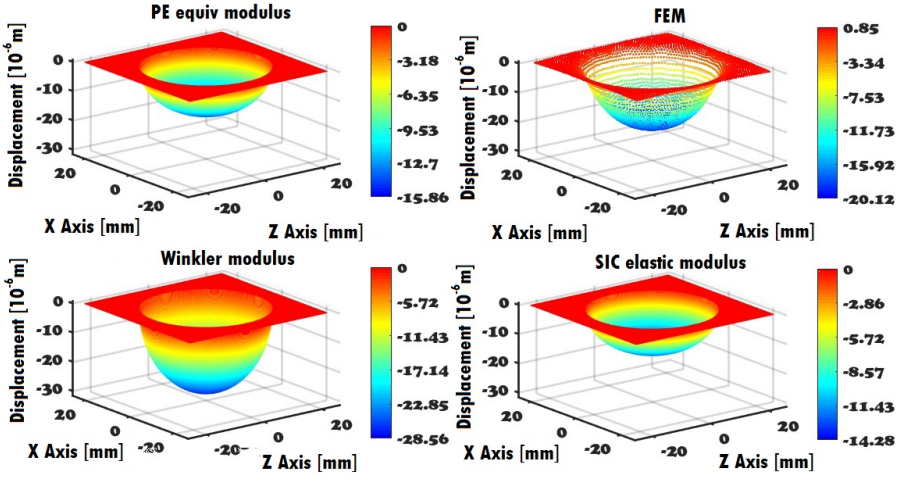

Figure 12. Displacement surfaces obtained for each equivalent Young's modulus and that correspond to the FEM, for prosthetic articulation. Alt = 10 mm. E = 1 GPa.

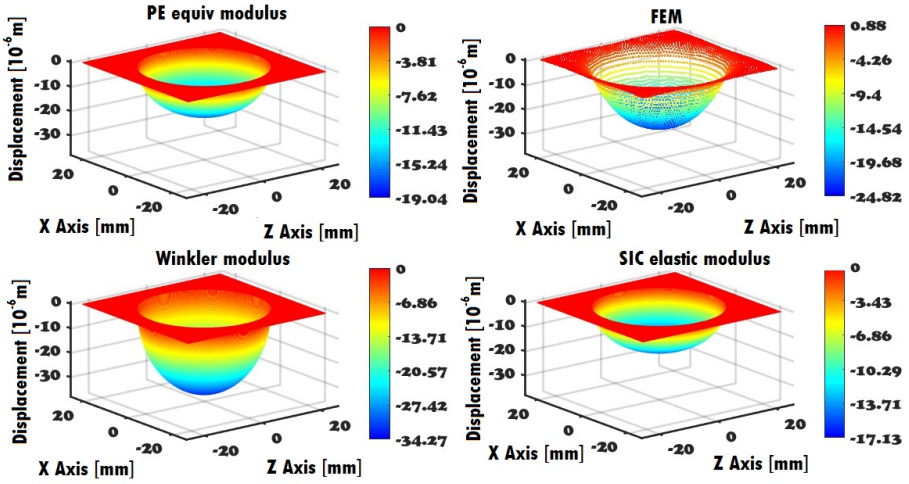

Figure 13. Displacement surfaces obtained for each equivalent Young's modulus and that correspond to the FEM, for prosthetic articulation. Alt = 12 mm. E = 1 GPa.

References

[1] K. J. Bozic and M. D. Ries, "Wear and osteolysis in total hip arthroplasty," *Seminars in Arthroplasty*, vol. 16, no. 2, pp. 142–152, 2005, cOMPLICATIONS AFTER TOTAL HIP ARTHROPLASTY.

[2] R. Pivec, A. J. Johnson, S. C. Mears, and M. A. Mont, "Hip arthroplasty," *The Lancet*, vol. 380, no. 9855, pp. 1768–1777, 2012.

[3] S. Kurtz, K. Ong, E. Lau, F. Mowat, and M. Halpern, "Projections of primary and revision hip and knee arthroplasty in the united states from 2005 to 2030," *The Journal of bone and joint surgery*, vol. 89, pp. 780–785, 04 2007. [Online]. Available: https://goo.gl/1qXADn

[4] Y. Su, P. Yang, Z. Fu, Z. Jin, and C. Wang, "Time-dependent elastohydrodynamic lubrication analysis of total knee replacement under walking conditions," *Computer Methods in Biomechanics and Biomedical Engineering*, vol. 14, no. 6, pp. 539–548, 2011.

[5] M. Mongkolwongrojn, K. Wongseedakaew, and F. E. Kennedy, "Transient elastohydrodynamic lubrication in artificial knee joint with non-newtonian fluids," *Tribology International*, vol. 43, no. 5, pp. 1017–1026, 2010, special Issue on Second International Conference on Advanced Tribology (iCAT2008).

[6] J. Di Paolo, D. M. Campana, S. Ubal, and M. E. Berli, "Flujos de lubricación en canales elásticos. una experiencia didáctica en clases de mecánica del continuo para bioingeniería," in *VI Congreso Argentino de Enseñanza en Ingeniería (VI CAEDI)*, 2008. [Online]. Available: https://goo.gl/LLLpNC

[7] M. Yousfi, "Etude biomécanique de l'articulation du genou humain. caractérisation mécanique et modélisation de l'ecoulement du fluide synovial en ecrasement lors d'un cycle de marche," Master's thesis, Université du 20 Août 1955 Skikda, 2014. [Online]. Available: https://goo.gl/GQJmsr

[8] T. J. R. Hugues, *The Finite Element Method: Linear Static and Dynamic Finite Element Analysis*, C. Corporation, Ed., 2012. [Online]. Available: https://goo.gl/ktCM6S

[9] K. V. Nemade and V. K. Tripathi, "A mathematical model to calculate contact stresses in artificial human hip joint," *International Journal of Engineering Research and Development*, vol. 6, no. 12, pp. 119–123, 2013. [Online]. Available: https://goo.gl/FyQQpX

[10] F. Li, H. Chen, and K. Mao, "Computational simulation analysis for torus radius of edge contact in hip prostheses," *Acta of bioengineering and biomechanics*, vol. 17, no. 3, pp. 67–73, 2015. [Online]. Available: https://goo.gl/8AJ7nz

[11] Q. Meng, F. Liu, J. Fisher, and Z. Jin, "Contact mechanics and lubrication analyses of ceramic-on-metal total hip replacements," *Tribology International*, vol. 63, pp. 51–60, 2013, the International Conference on BioTribology 2011.

[12] J. Armas Sánchez, "Análisis de la fractura por contacto mecánico y su solución por análisis numérico," Master's thesis, Instituto Politécnico Nacional. México, 2015. [Online]. Available: https://goo.gl/LnEdPf

[13] J. Di Paolo and M. E. Berli, "Numerical analysis of the effects of material parameters on the lubrication mechanism for knee prosthesis," *Computer Methods in Biomechanics and Biomedical Engineering*, vol. 9, no. 2, pp. 79–89, 2006, pMID: 16880159.

[14] M. E. Berli, D. M. Campana, S. Ubal, and J. Di Paolo, "Lubrication model of a knee prosthesis, with non newtonian fluid and porous rough material," *Latin American applied research*, vol. 39, no. 2, pp. 105–111, 2009. [Online]. Available: https://goo.gl/aKL9Ky

[15] B. A. Weiss, M. E. Berli, S. Ubal, and J. Di Paolo, "umerical solution of a 2d lubrication model with sommerfeld boundary conditions for hip prostheses," in *VI Latin American Congress on Biomedical Engineering CLAIB, Paraná, Argentina 29, 30 & 31 October*, vol. 49, 2014.

[16] D. Dowson and G. R. Higginson, *Elasto-Hydrodinamic Lubrication.* Pergamon Press, 1977. [Online]. Available: https://goo.gl/NV522s

[17] H. P. Evans and W. Snidle, "The elastohydrodynamic lubrication of point contacts at heavy loads," *Proceedings of the Royal Society of London A: Mathematical, Physical and Engineering Sciences*, vol. 382, no. 1782, pp. 183–199, 1982.

[18] MBA. (2017) More power in your hands. MBA Surgical Empowerment. [Online]. Available: https://goo.gl/aPngur

[19] F. Mattei, Land Di Puccio, B. Piccigallo, and E. Ciulli, "Lubrication and wear modelling of artificial hip joints: A review," *Tribology International*, vol. 44, no. 5, pp. 532–549, 2011, special Issue: ECOTRIB 2009.

[20] I. Kutzner, B. Heinlein, F. Graichen, A. Bender, A. Rohlmann, A. Halder, A. Beier, and G. Bergmann, "Loading of the knee joint during activities of daily living measured in vivo in five subjects," *Journal of Biomechanics*, vol. 43, no. 11, pp. 2164–2173, 2010.

[21] A. Sharma, "A method to calculate the femoro-polyethylene contact pressures in total knee arthroplasty in vivo," Master's thesis, University of Tennessee, United States, 2005. [Online]. Available: https://goo.gl/QucK2c

[22] J. S. Jurvelin, M. D. Buschmann, and E. B. Hunziker, "Mechanical anisotropy of the human knee articular cartilage in compression," *Proceedings of the Institution of Mechanical Engineers, Part H: Journal of Engineering in Medicine*, vol. 217, no. 3, pp. 215–219, 2003, pMID: 12807162.

[23] D. E. T. Shepherd and B. B. Seedhom, "Thickness of human articular cartilage in joints of the lower limb," *Annals of the Rheumatic Diseases*, vol. 58, no. 1, pp. 27–34, 1999.

[24] H. Oonishi, H. Iwaki, N. Kin, S. Kushitani, N. Murata, S. Wakitani, and K. Imoto, "The effects of polyethylene cup thickness on wear of total hip prostheses," *Journal of Materials Science: Materials in Medicine*, vol. 9, no. 8, pp. 475–478, 1998.

[25] G. Bergmann, G. Deuretzbacher, M. Heller, F. Graichen, A. Rohlmann, J. Strauss, and G. N. Duda, "Hip contact forces and gait patterns from routine activities," *Journal of Biomechanics*, vol. 34, no. 7, pp. 859–871, 2001.

Scientific Paper / Artículo Científico

UNIVERSIDAD POLITÉCNICA SALESIANA ECUADOR
INGENIUS
Revista de Ciencia y Tecnología
https://doi.org/10.17163/ings.n20.2018.08
pISSN: 1390-650X / eISSN: 1390-860X

Multi-criteria Methods Applied in the Selection of a Brake Disc Material

Métodos multicriterio aplicados en la selección de un material para discos de freno

Mario Chérrez-Troya[1,*], Javier Martínez-Gómez[1,2], Diana Peralta-Zurita[1], Edilberto Antonio Llanes-Cedeño[1]

Abstract

The selection of material for an automotive component is a complex process, because it involves an exploration of the main criteria according to the properties required by the component to be designed. The purpose of this study is to evaluate an alternative material in the manufacture of a brake disc in light SUV type vehicles, using multi-criteria methods; five candidate materials are taken into consideration for the desired application (Ti_6Al_4V, $Al_{10}Si$ C, AISI 304L, ASTM A 536 and ASTM A48). The multi-criteria methods (MCDM) used are: VIKOR - multidisciplinary optimization and compromise solution; ELECTRE I - elimination and options that reflect reality; COPRAS - proportional complex evaluation; ARAS - additive ratio evaluation; MOORA - multi-objective optimization based on radius analysis and the ENTROPIA method used for the weighting of criteria. It is concluded that the best alternative is the ASTM A536 material according to the COPRAS, ELECTRE I, and ARAS methods due to its low density, a high elastic limit and a good resistance to compression; the second option is ASTM A48 according to VIKOR and MOORA.

Keywords: brake disc, multi-criteria methods, MCDM.

Resumen

La selección de material para un componente automotor es un proceso complejo, porque implica una exploración de los principales criterios de acuerdo con las propiedades exigidas por el componente a diseñar. El presente estudio tiene como objetivo evaluar un material alterno en la fabricación de un disco de freno en vehículos livianos tipo SUV, a partir de los métodos multicriterio; para lo cual se toman en consideración cinco materiales candidatos para la aplicación deseada (Ti_6Al_4V, $Al_{10}Si$ C, AISI 304L, ASTM A 536 y ASTM A48). Los métodos multicriterio (MCDM) empleados son: VIKOR – la optimización multidisciplinar y solución de compromiso; ELECTRE I – eliminación y opciones que reflejan la realidad; COPRAS – evaluación compleja proporcional; ARAS – evaluación de relación de aditivos; MOORA – optimización multiobjetivo basado en el análisis de radios y el método ENTROPÍA que se emplea para la ponderación de los criterios. Se obtiene que la mejor alternativa es el material ASTM A536 según los métodos COPRAS, ELECTRE I, y ARAS por su baja densidad, un alto límite elástico y una buena resistencia a la compresión; en segunda opción es el ASTM A48 según VIKOR y MOORA.

Palabras clave: disco de freno, métodos multicriterio, MCDM.

[1,*]Materials Research Group, Universidad Internacional SEK, Quito – Ecuador.
Author for correspondence ✉: mcherrez.mdm@uisek.edu.ec
https://orcid.org/0000-0001-7628-9793, https://orcid.org/0000-0001-8807-7595
https://orcid.org/0000-0002-9523-0743, https://orcid.org/0000-0001-6739-7661
[2]National Institute of Energy Efficiency and Renewable Energy, INER, Quito – Ecuador

Received: 14-05-2018, accepted after review: 25-06-2018

Suggested citation: Chérrez-Troya, M.; Martínez-Gómez, J.; Peralta-Zurita, D. and Llanes-Cedeño, E. A. (2018). «Multi-criteria Methods Applied in the Selection of a Brake Disc Material». Ingenius. N.°20, (july-december). pp. 83-94. doi: https://doi.org/10.17163/ings.n20.2018.08.

1. Introduction

In the development of the automotive industry, brakes are one of the main safety devices, therefore, the materials to be selected must have the appropriate physical and mechanical properties for optimum performance of the brake disc.

The formation of thermal cracks in the materials used in brake discs depends on thermal fatigue or very severe thermal stresses, produced by the variation of temperature during braking and environmental operating conditions [1]. During braking, the kinetic and potential energy is converted into thermal energy, therefore, it is necessary to know the temperature and thermal stress in braking [2]. It is necessary to investigate the use of new materials that improve braking efficiency and provide greater stability and safety to the vehicle [3]. It is important to select a lightweight alternative material to cast iron which to reduce fuel consumption, depending on its specific weight [4].

The Hierarchical Analytical Process method is used for the environmental evaluation in the selection of composite materials for automotive components, because the available data are difficult to quantify and the characteristics to be evaluated are intangible in an analytical model [5] A systematic and efficient approach to the selection of materials is necessary in order to select the best alternative for a specific engineering application [6]. Multicriteria methods such as COPRAS (Complex Proportional Assessment), VIKOR (from Serbian: VIseKriterijumska Optimizacija I Kompromisno Resenje,: Multicriteria Optimization and Compromise Solution), ELECTRE I (Elimination and Choice Expressing the Reality), ARAS (additive ratio assessment), MOORA (multi-objective optimization on the basis of ratio analysis) and ENTROPIA which is used to calculate the weight of each criterion, have proven to be adequate methods to validate the selection of materials [5, 6].

In the last 3 years the demand in Ecuador for SUVs of the Chevrolet brand has increased by 7%, with the Suzuki Grand Vitara Sz 2.0 being the fifth most sold vehicle in the country, according to the Association of Automotive Companies of Ecuador [7]. Taking into account that Ecuador is encouraging the inclusion of national products, it is important to select an existing material in the country for the manufacture of the brake disc along with the cost/benefit analysis. The objective of this study is to evaluate an alternative material in the manufacture of a brake disc in light SUV type vehicles, through the COPRAS, VIKOR, ELECTRE I, ARAS, MOORA and ENTROPIA multicriteria methods.

2. Materials and methods

2.1. Definition of the problem

Different types of alloys for the design and manufacture of brake discs in the automotive industry have been developed, because they must meet extremely high parameters, as this device works at high degrees of wear and temperature.

Gray cast iron discs have better wear resistance than alloy or Ti compounds, however, the addition of hard particles to a Ti based compound can substantially improve wear resistance [8]. The analysis of the mechanical properties between an aluminum alloy, cast iron, titanium alloy, ceramic materials and compounds resulted in the most appropriate material for the manufacture of a brake disc to an aluminum alloy [9]. An alternative to metals are composite materials such as high-strength fiber glass, which has greater wear resistance and lighter weight [10].

Thermal conductivity is among the important properties that the selected material must have. A high value allows heat to be dissipated quickly and a high thermal expansion coefficient allows a good thermal expansion when exposing the brake disc to a temperature variation.

In addition a good elastic limit, Young's modulus and a Poisson's coefficient will allow to support high tensions without suffering permanent deformations in the disk. A high value of resistance to compression, traction and Brinell hardness, will prevent the material from fracturing due to the forces produced by the jaws at the time of braking. To reduce the consumption of the vehicle it is necessary to reduce the weight of the vehicle, for this reason the brake disc must have a low density. It is important to carry out a cost-benefit analysis of the selected material.

Taking all these criteria into account, the candidate materials for the manufacture of brake discs in Ecuador are the following: Ti_6Al_4V (titanium alloy, number 1), $Al_{10}Si$ C (aluminum alloy or Duralcan, number 2), AISI 304L (stainless steel, number 3), ASTM A536 (nodular gray cast iron, number 4) and ASTM A48 (pearl gray cast iron, number 5).

2.2. Multi-criteria methods. Pondering criteria

The multicriteria methods used are COPRAS, VIKOR, ELECTRE I, ARAS and MOORA. The calculation of the weights of each criterion is done through the Entropy method, in order to have objective results since it assumes that a criterion has greater weight when there is greater diversity in the evaluation of each alternative.

2.2.1. Entropy method

Entropy measures the uncertainty in the information formulated using the theory of probability. It indicates that a broad distribution represents more uncertainty than a distribution with pronounced peaks. The Entropy method is calculated in the following steps [11]:

Step 1: Construction of the decision matrix.

$$r = \begin{bmatrix} r_{11} & r_{12} & \cdots & r_{1n} \\ r_{21} & r_{22} & \cdots & r_{2n} \\ \vdots & \vdots & \ddots & \vdots \\ r_{m1} & r_{m2} & \cdots & r_{mn} \end{bmatrix}$$

Step 2: Calculation of the normalized decision matrix P_{ij}, the objective of normalization is to obtain values without dimensions of different criteria to make comparisons between them [11]. It is calculated using equation (1).

$$P_{ij} = \frac{x_{ij}}{\sum_{i=1}^{m} x_{ij}} \tag{1}$$

Step 3: Calculation of entropy E_j, by means of equation (2)

$$E_j = -k \left(\sum_{i=1}^{m} p_{ij} ln(p_{ij}) \right) \qquad t = 1, 2, 3, \ldots, n. \tag{2}$$

Where $k = \frac{1}{ln\ m}$ it is a constant that guarantees $0 \leq Ej \leq 1$ and m is the number of alternatives.

Step 4: Calculation of criterion diversity D_j, equation (3) allows this parameter to be calculated.

$$D_j = 1 - E_j \tag{3}$$

Step 5: Calculation of the normalized weight of each criterion W_j, by means of equation (4).

$$W_j = \frac{D_j}{\sum_{i=1}^{m} D_j} \tag{4}$$

2.2.2. COPRAS method

The COPRAS method selects the best decision alternatives considering the ideal and worst-ideal solutions, in a classification and step-by-step evaluation of the alternatives in terms of their importance and degree of utility. The algorithm of the COPRAS method consists of the following steps [12]:

Step 1: Calculation of the normalized decision matrix x_{ij}^*, through equation (5).

$$x_{ij}^* = \frac{x_{ij}}{\sum_{i=1}^{m} x_{ij}} \tag{5}$$

Step 2: Determine the weighted normalized decision matrix D_{ij}, according to equation (6).

$$D_{ij} = x_{ij}^* \cdot w_j = \begin{bmatrix} w_1 r_{11} & w_2 r_{12} & \cdots & w_n r_{1n} \\ w_1 r_{21} & w_2 r_{22} & \cdots & w_n r_{2n} \\ \vdots & \vdots & \ddots & \vdots \\ w_1 r_{m1} & w_2 r_{m2} & \cdots & w_n r_{mn} \end{bmatrix} \tag{6}$$

Where x_{ij}^* is the normalized performance value of i_{th} alternatives in j_{th} criteria and w_j is the weight associated to the j_{th} criteria.

Step 3: The sums S_{i+} and S_{i-} of the weighted normalized values are calculated for both the beneficial and non-beneficial criteria, respectively. These sums S_{i+} and S_{i-} are calculated by means of equations (7) and (8) respectively.

$$Si_{i+} = \sum_{k=1}^{k} D_{ij} \tag{7}$$

$$Si_{i-} = \sum_{k=1}^{k} D_{ij} \tag{8}$$

Step 4: Determine the relative importance of the alternatives Q_i through equation (9).

$$Q_i = S_i + \frac{\sum_{j=1}^{m} S_{i-}}{S_{i-} \sum_{j=1}^{m} \frac{1}{S_{i-}}} \tag{9}$$

The relative importance Q_i of an alternative shows the degree of satisfaction achieved by this alternative.

Step 5: Calculation of the yield index Pi of each alternative, using the following equation (10).

$$P_1 = \frac{Q_i}{Q_{max}} \times 100 \tag{10}$$

Where Q_{max} is the maximum value of relative importance. The value of the performance index P_i is used to obtain a complete classification of the candidate alternatives.

2.2.3. VIKOR method

The basic concept of VIKOR is to first define the ideal positive and negative solutions. The positive ideal solution indicates the alternative with the highest value (score of 100) while the ideal negative solution indicates the alternative with the lowest value (score of 0). The VIKOR commitment algorithm has the following steps [13]:

Step 1: Define the initial decision matrix X_{ij}.

$$X_{ij} = \begin{bmatrix} x_{11} & x_{12} & \cdots & x_{1n} \\ x_{21} & x_{22} & \cdots & x_{2n} \\ \vdots & \vdots & \ddots & \vdots \\ x_{m1} & x_{m2} & \cdots & x_{mn} \end{bmatrix}$$

Step 2: Calculation of the normalized initial decision matrix f_{ij}, using equation (11).

$$f_{ij} = \frac{x_{ij}}{\sqrt{\sum_{i=1}^{m} x_{ij}^2}} \tag{11}$$

Step 3: Determine the best f_i^* and the worst f_i^- value of all the criteria functions of each alternative. By means of equations (12) and (13) respectively.

$$\begin{aligned} f_i^* &= max_j \ f_{ij} \\ i &= 1, 2, 3, \ldots, m \end{aligned} \tag{12}$$

$$\begin{aligned} f_i^- &= min_j \ f_{ij} \\ i &= 1, 2, 3, \ldots, m \end{aligned} \tag{13}$$

Step 4: Calculation of the distance from each value to the positive ideal solution S_i and the distance from each value to the ideal negative solution R_i, by means of equation (14) and (15) respectively.

$$S_i = \sum_{j}^{n} W_i \frac{f_i^* - f_{ij}}{f_i^* - f_i^-} \tag{14}$$

$$R_i = Max_j \frac{W_i f_i^* - f_{ij}}{f_i^* - f_i^-} \tag{15}$$

Step 5: Calculation of the values I_i, para $i = 1, \ldots, I$ is defined by equation (16).

$$I_i = v \left[\frac{s_i - s^*}{s^- - s^*} \right] + (1 - v) \left[\frac{R_i - R^*}{R^- - R^*} \right] \tag{16}$$

Where $S^* = Min\ S_i$, $S^- = Max\ S_i$, $R^* = Min\ R_i$, $R^- = Max\ R_i$, and v is a weighting reference ($v > 0.5$). $\frac{(R_i - R^*)}{(R^- - R^*)}$, represents the distance of the ideal negative solution of i_{th} values.

Step 6: The ranking is determined, the highest value is the best alternative

2.2.4. ELECTRE I Method

The ELECTRE I method has the ability to handle discrete quantitative and qualitative criteria and provides a complete order of alternatives. The limitation is replaced by the concordance and discordance of the matrix index. The procedure of the ELECTRE I method is as follows [14]:

Step 1: Define the initial decision matrix r_{ij}.

$$r_{ij} = \begin{bmatrix} r_{11} & r_{12} & \cdots & r_{1n} \\ r_{21} & r_{22} & \cdots & r_{2n} \\ \vdots & \vdots & \ddots & \vdots \\ r_{m1} & r_{m2} & \cdots & r_{mn} \end{bmatrix}$$

Step 2: Normalization of the decision matrix, this process will allow transforming different scales and units among several common criteria that allow comparisons accross criteria, according to equation (17).

$$R_{ij} = \frac{r_{ij}}{\sqrt{\sum_{i=1}^{m} {r_{ij}}^2}} \tag{17}$$

PStep 3: Construction of the normalized weighted decision matrix V_{ij}. For which the normalized decision matrix R_{ij} is multiplied with its respective weight, expressed in equation (18).

$$V_{ij} = W_i \times R_{ij} \tag{18}$$

$$V_{ij} = \begin{bmatrix} W_1 r_{11} & W_2 r_{12} & \cdots & W_n r_{1n} \\ W_2 r_{21} & W_2 r_{22} & \cdots & W_n r_{2n} \\ \vdots & \vdots & \ddots & \vdots \\ W_n r_{m1} & W_n r_{m2} & \cdots & W_n r_{mn} \end{bmatrix}$$

Step 4: Calculation of the intervals of agreement (C_{ab}) and disagreement (D_{ab}), that is, C_{ab} indicates the most preferable alternative and D_{ab} indicates the least preferable alternative. Equations (19) and (20) are used respectively.

$$C_{ab} = \{j | x_{aj} \geq x_{bj}\} \tag{19}$$

$$D_{ab} = \{j | x_{aj} \leq x_{bj}\} = j - C_{ab} \tag{20}$$

Step 5: Determination of the agreement interval matrix C_{ab}, which is obtained by adding the weights to the weights associated with the criteria in which the alternative i is better than the alternative j or vice versa; in case of a tie, half of the weight is assigned to each of the alternatives according to equation (21).

$$C_{ab} = \sum_{j=C_{ab}} W_j \tag{21}$$

Step 6: Determination of the discordance index matrix D_{ab}, which is calculated as the largest difference between the criteria for which the alternatives i is dominated by the j, then dividing by the greater difference in absolute value between the results obtained by the alternative i and j, according to equation (22).

$$D_{ab} = \frac{\left(\begin{smallmatrix} max \\ j \in D_{ab} \end{smallmatrix}\right) |V_{aj} - V_{bj}|}{\left(\begin{smallmatrix} max \\ j \in J, m, n \in I \end{smallmatrix}\right) |V_{mj} - V_{nj}|} \tag{22}$$

Step 7: Calculation of the maximum threshold $\bar{c}$ for the concordance index and the maximum threshold $\bar{d}$ for the discordance index, by means of equations (23) and (24) respectively.

$$\bar{c} = \sum_{a=1}^{m} \sum_{b}^{m} \frac{c(a, b)}{m(m-1)} \tag{23}$$

$$\bar{d} = \sum_{a=1}^{m} \sum_{b}^{m} \frac{c(a,b)}{m(m-1)} \tag{24}$$

Step 8: Calculation of the dominant concordance matrix. Once the concordance indexes and the minimum agreement threshold have been determined, the dominant agreement matrix is calculated with the following condition:

$$cd_{ij} \begin{cases} e(a,b) = 1 & \text{si } c(a,b) \geq \bar{c} \\ e(a,b) = 0 & \text{si } c(a,b) < \bar{c} \end{cases}$$

Step 9: Calculation of the dominant discordant matrix. In the same way as the previous one, the values of the matrix of dominant discordance are obtained from the matrix of discordance index and the maximum threshold of discordance $\bar{d}$. By the following condition.

$$dd_{ij} \begin{cases} f(a,b) = 1 & \text{si } d(a,b) \geq \bar{d} \\ f(a,b) = 0 & \text{si } d(a,b) < \bar{d} \end{cases}$$

Step 10: Calculation of the upper and lower net value C_a and D_a, by means of equations (25) and (26) respectively.

$$C_a = \sum_{b=1}^{n} c_{(a,b)} - \sum_{b=1}^{n} c_{(b,a)} \tag{25}$$

$$D_a = \sum_{b=1}^{n} d_{(a,b)} - \sum_{b=1}^{n} d_{(b,a)} \tag{26}$$

Where C_a is the sum of the competitive superiority number of all the alternatives and D_a is used to determine the inferiority number by classifying the alternatives.

2.2.5. ARAS method

The ARAS method determines the complex relative efficiency of a feasible alternative that is directly proportional to the relative effect of the values and weights of the main criteria considered. Based on the theory of utility and the quantitative method. The steps of this method are the following [15].

Step 1: Conformation of the decision matrix X_{ij},

$$X_{ij} = \begin{bmatrix} x_{11} & x_{12} & \cdots & x_{1n} \\ x_{21} & x_{22} & \cdots & x_{2n} \\ \vdots & \vdots & \ddots & \vdots \\ x_{m1} & x_{m2} & \cdots & x_{mn} \end{bmatrix}$$

Step 2: Calculation of the normalized decision matrix ($\overline{X_{ij}}$), taking into account the beneficial values calculated with equation (27).

$$\overline{X_{ij}} = \frac{x_{ij}}{\sum_{i=0}^{m} X_{ij}} \tag{27}$$

$$\bar{X}_{ij} = \begin{bmatrix} \bar{x}_{11} & \bar{x}_{12} & \cdots & \bar{x}_{1n} \\ \bar{x}_{21} & \bar{x}_{22} & \cdots & \bar{x}_{2n} \\ \vdots & \vdots & \ddots & \vdots \\ \bar{x}_{m1} & \bar{x}_{m2} & \cdots & \bar{x}_{mn} \end{bmatrix}$$

The non-beneficial criteria are calculated by means of equation (28).

$$X_{ij} = \frac{1}{X_{ij}^{*}}; \overline{X_{ij}} = \frac{x_{ij}}{\sum_{i=0}^{X_{ij}}} \tag{28}$$

Step 3: Calculation of the weighted normalized decision matrix is done with equation (29).

$$\hat{X}_{ij} = \bar{X}_{ij} \times W_j \tag{29}$$

$$\hat{X}_{ij} = \begin{bmatrix} \hat{x}_{11} & \hat{x}_{12} & \cdots & \hat{x}_{1n} \\ \hat{x}_{21} & \hat{x}_{22} & \cdots & \hat{x}_{2n} \\ \vdots & \vdots & \ddots & \vdots \\ \hat{x}_{m1} & \hat{x}_{m2} & \cdots & \hat{x}_{mn} \end{bmatrix}$$

The weight values W_j are determined by the Entropy method.

Where W_j is the criterion weight j and $\bar{X}_{ij}$ it is the standardized classification of each criterion.

Step 4: Calculation of the optimization function S_i using equation (30).

$$S_i = \sum_{j=1}^{n} \hat{X}_{ij} \tag{30}$$

Where S_i is the value of the optimization function of the alternative i. This calculation has a directly proportional relationship with the process of the values X_{ij} and weights W_j of the criteria investigated and their relative influence on the final result.

Step 5: Calculation of the degree of utility. This degree is determined by comparing the variant that is under analysis with the best S_o, according to equation (31).

$$K_i = \frac{s_i}{s_o} \tag{31}$$

Where S_i and So are the values of the optimization function. These values range from 0% to 100%, therefore the alternative with the highest K_i is the best of the alternatives analyzed.

2.2.6. MOORA method

The MOORA method begins from reference points. These references will be the highest evaluation of the radius vector of alternatives with respect to each criterion, whether maximum or minimum. The steps of this method are described as follows [16].

Step 1: Determination of the initial decision matrix X_{ij}.

$$X_{ij} = \begin{bmatrix} x_{11} & x_{12} & \cdots & x_{1n} \\ x_{21} & x_{22} & \cdots & x_{2n} \\ \vdots & \vdots & \ddots & \vdots \\ x_{m1} & x_{m2} & \cdots & x_{mn} \end{bmatrix}$$

Step 2: Calculation of the radius matrix of the form $X_{ij} = [(\overline{x_{ij}})]$ to normalize the initial decision matrix, equation (32) is used.

$$\overline{X_{ij}} = \frac{x_{ij}}{\sqrt{\sum_{i=1}^{m} x_{ij}^2}} \tag{32}$$

Step 3: The weight vector of the criteria is defined.

$$W = |W_1 \quad W_2 \quad W_3 \quad \ldots \quad W_n|$$

Step 4: Calculation of the matrix normalized by weights. It is weighted by multiplying the standardized deduction matrix by the weights of each criterion.

Step 5: The aggregation function is determined to evaluate each alternative $S(x_i)$, using equation (33).

$$S(x_i) = \sum_{i=1}^{h} \overline{X_{ij}} - \sum_{i=h+1}^{h} \overline{X_{ij}} \tag{33}$$

Where $i = 1, 2, 3, \ldots, h$ corresponds to the criteria cataloged as a maximum; $i = h+1, h+2, \ldots n$ corresponds to the criteria cataloged as a minimum.

Step 6: The preference ranking is determined. The best alternative is the one with the highest $S(x_i)$ value.

3. Results and discussion

3.1. Application of the entropy method

The candidate materials and the criteria under analysis are shown in Table 1. The properties of the alternatives are: density (A), price (B), Young's modulus (C), elastic limit (D), Poisson's radius (E), tensile strength (F), compressive strength (G), Brinell hardness (H), thermal conductivity (I) and coefficient of thermal expansion (J). The Entropy method is applied for the weighting criteria, in order to obtain objective weights at the time of the evaluation, since it is based on defined mathematical models; unlike the AHP method that is based on expert criteria applied by [14].

Table 2 shows the normalized decision matrix of the Entropy method, which is calculated according to equation (1). The values of the entropy E_j of each variable, the diversity of criteria (D_j) and the normalized weights of each criterion (W_j) are indicated in Table 3, according to equations (2), (3) and (4) respectively.

Table 1. Evaluation matrix

Material	Density (kg/m^3)	Price (USD/kg)	Young's modulus (GPa)	Elastic limit (MPa)	Poisson's radius Poisson	Tensile strength (MPa)	Compression resistance (MPa)	Brinell hardness (HV)	Thermal conductivity (W/m°C)	Coefficient of thermal expansion (µstrain/°C)
	A	B	C	D	E	F	G	H	I	J
Ti_6Al_4V	4430	27.5	115	898	0.349	620	848	347	8.91	9.1
$Al_{10}SiC$	2770	8.29	88	358	0.32	372	358	118	148	18
AISI 304L	7980	4.53	205	310	0.275	620	310	210	16	18
ASTM A536	7150	0.67	173	339	0.28	500	351	217	41	12.5
ASTM A48	7200	0.67	120	149	0.265	250	170	252	46	13

Table 2. Normalized decision matrix P_{ij}

A	B	C	D	E	F	G	H	I	J
0.150	0.660	0.164	0.437	0.234	0.262	0.416	0.303	0.034	0.128
0.093	0.199	0.125	0.174	0.214	0.157	0.175	0.103	0.569	0.255
0.270	0.108	0.292	0.150	0.184	0.262	0.152	0.183	0.061	0.255
0.242	0.016	0.246	0.165	0.188	0.211	0.172	0.189	0.157	0.177
0.243	0.016	0.171	0.072	0.178	0.105	0.083	0.220	0.177	0.184

Table 3. Calculation E_i, D_j and W_j according to the Entropy method

Criteria	E_i	D_j	W_j
A	0.961	0.038	0.038
B	0.602	0.397	0.399
C	0.971	0.028	0.028
D	0.894	0.105	0.106
E	0.996	0.003	0.003
F	0.969	0.030	0.031
G	0.911	0.088	0.088
H	0.966	0.033	0.033
I	0.749	0.250	0.251
J	0.981	0.018	0.019

3.2. COPRAS

The normalized decision matrix (x^*_{ij}), is calculated with equation (5), while the normalized matrix by weight (D_{ij}) is calculated according to equation (6) represented in Table 4. The sum of the weighted normalized values (S_{i+}), (S_{i-}) the relative importance (Q_i) shows the degree of satisfaction of an alternative and the performance index (P_i) that determines the ranking of candidate materials for the manufacture of a brake disc, are calculated with equations (7), (8), (9) and (10) respectively and all these calculations are indicated in Table 5, where the best material is 4 (ASTM A536) due to the selection of the best decision alternatives related to Young's modulus (C), elastic limit (D), Poisson radius (E), tensile-compression resistance (F and G), hardness (H) and thermal conductivity (I).

Table 4. Standard decision matrix of weights D_{ij} of the COPRAS method

Material	**A**	**B**	**C**	**D**	**E**	**F**	**G**	**H**	**I**	**J**
1	0.005	0.263	0.004	0.046	0.0008	0.008	0.037	0.010	0.008	0.002
2	0.003	0.079	0.003	0.018	0.0007	0.004	0.015	0.003	0.143	0.004
3	0.010	0.043	0.008	0.016	0.0006	0.008	0.013	0.006	0.015	0.004
4	0.009	0.006	0.007	0.017	0.0007	0.006	0.015	0.006	0.039	0.003
5	0.009	0.006	0.004	0.007	0.0006	0.003	0.007	0.007	0.044	0.003

Table 5. Calculation S_{i+}, S_{i-}, Q_i, P_i and COPRAS Ranking

Material	S_{i+}	S_{i-}	Q_i	P_i	**Ranking**
1	0.118	0.269	0.128	47.68	4
2	0.195	0.083	0.227	84.65	3
3	0.073	0.053	0.123	45.93	5
4	0.096	0.015	0.269	100.0	1
5	0.079	0.015	0.251	93.35	2

3.3. VIKOR

The normalized initial decision matrix f_{ij} is presented in Table 6, these values are obtained by means of equation (11). The best and worst value is determined with equations (12) and (13) respectively, which is shown in Table 7. The values of the distance from each value to the positive solution (S_i), is calculated according to equation (14), is indicated in Table 8 and the distance to the ideal negative solution (R_i), is calculated with the equation (15), which is shown in Table 9. The value of (I_i) is obtained by equation (16), the highest value of (I_i) determines the best material in this case is an ASTM A48 (number 5). These values are indicated in Table 10, due to their low density (A), low Poisson radius (E) and high Brinell hardness (H).

Table 6. Normalized decision matrix F_{ij} with the VIKOR method

Material	A	B	C	D	E	F	G	H	I	J
1	0.318	0.945	0.351	0.831	0.521	0.561	0.810	0.645	0.055	0.280
2	0.198	0.284	0.268	0.331	0.477	0.336	0.342	0.219	0.917	0.553
3	0.573	0.155	0.625	0.286	0.410	0.561	0.296	0.390	0.099	0.553
4	0.513	0.023	0.528	0.313	0.418	0.452	0.335	0.403	0.254	0.384
5	0.517	0.023	0.366	0.137	0.395	0.226	0.162	0.468	0.285	0.400

Table 7. Ideal and non-ideal solution according to VIKOR

	A	B	C	D	E	F	G	H	I	J
fi*	0.573	0.945	0.625	0.831	0.521	0.561	0.810	0.645	0.917	0.553
fi-	0.198	0.023	0.268	0.137	0.395	0.0226	0.162	0.219	0.055	0.280

Table 8. Calculations S_i, S_{imax} and S_{imin}

Material	S_i	S_{imax}	S_{imin}
1	0.319		
2	0.548		
3	0.757	0.864	0.319
4	0.795		
5	0.864		

Table 9. Calculations R_i, R_{imax} and R_{imin}

Material	R_{i+}	R_{imax}	R_{i-}	R_{imin}
1	0.251		0.000	
2	0.285		0.000	
3	0.341	0.399	0.000	0.000
4	0.399		0.002	
5	0.399		0.003	

Table 10. Calculations of I_i for v =0.5 and VIKOR Ranking

Material	Ii	***Ranking***
1	0.315	5
2	0.568	4
3	0.830	3
4	0.936	2
5	1.000	1

3.4. ELECTRE I

The data of the initial decision matrix is tabulated in Table 1 and the weighted standard decision matrix (V_{ij}) is obtained using equation (18), said values are indicated in Table 11. The matrix of concordance intervals (C_{ab}), is calculated according to equation (19) and is shown in Table 12. By means of equation (20) the matrix values of discordance intervals (D_{ab}) are calculated, which are tabulated in Table 13. The maximum threshold ($\bar{c}$) for the concordance index, is determined with equation (23) and the dominant concordance

matrix (cd_{ij}) is represented in Table 14. While the maximum threshold for the discordance index ($\bar{d}$), is calculated according to equation (24), tabulated in Table 15 and the jarring matrix (dd_{ij}) is shown in Table 16. Finally, the upper and lower net value (C_a) and (C_b), is obtained according to equations (25) and (26) respectively, these values are indicated in Table 17. The material with the best score is ASTM A536. The materials with the best score are the $Al_{10}SiC$ (number 2) and the ASTM A536 (number 4), with thermal conductivity (I), elastic limit (D) and tensile-compression resistance (F and G) as determining factors.

Table 11. Weighted normalized decision matrix V_{ij} according to ELECTRE I

Material	A	B	C	D	E	F	G	H	I	J
1	0.026	0.021	0.009	0.088	0.001	0.017	0.071	0.021	0.013	0.005
2	0.030	0.285	0.007	0.035	0.001	0.010	0.030	0.007	0.231	0.010
3	0.016	0.337	0.017	0.030	0.001	0.017	0.026	0.013	0.025	0.010
4	0.018	0.390	0.015	0.033	0.001	0.014	0.029	0.013	0.064	0.007
5	0.018	0.390	0.010	0.014	0.001	0.007	0.014	0.015	0.071	0.007

Table 12. Interval concordance matrix C_{ab}

	Alt. 1	Alt. 2	Alt. 3	Alt. 4	Alt. 5
Alt. 1	0.000	0.291	0.285	0.301	0.301
Alt. 2	0.708	0.000	0.498	0.507	0.539
Alt. 3	0.714	0.501	0.000	0.078	0.275
Alt. 4	0.698	0.492	0.921	0.000	0.496
Alt. 5	0.698	0.461	0.724	0.504	0.000

Table 13. Array of discrepancy intervals D_{ab}

	Alt. 1	Alt. 2	Alt. 3	Alt. 4	Alt. 5
Alt. 1	0.000	0.201	0.183	0.149	0.199
Alt. 2	1.000	0.000	1.000	1.000	1.000
Alt. 3	1.000	0.250	0.000	0.063	0.337
Alt. 4	1.000	0.626	1.000	0.000	1.000
Alt. 5	1.000	0.656	1.000	0.418	0.000

Table 14. Dominant concordance matrix cd_{ij} and concordance threshold $\bar{c}$

	Alt. 1	Alt. 2	Alt. 3	Alt. 4	Alt. 5	$\bar{c}$
Alt. 1	0.000	0.000	0.000	0.000	0.000	
Alt. 2	1.000	0.000	0.000	1.000	1.000	
Alt. 3	1.000	1.000	0.000	0.000	0.000	0.5
Alt. 4	1.000	0.000	1.000	0.000	0.000	
Alt. 5	1.000	0.000	1.000	1.000	0.000	

Table 15. Dominant disagreement matrix dd_{ij} and discordance threshold $\bar{d}$

	Alt. 1	Alt. 2	Alt. 3	Alt.4	Alt. 5	$\bar{d}$
Alt. 1	1.000	1.000	1.000	1.000	1.000	
Alt. 2	0.000	1.000	0.000	0.000	0.000	
Alt. 3	0.000	1.000	1.000	1.000	1.000	0.654
Alt. 4	0.000	1.000	0.000	1.000	0.000	
Alt. 5	0.000	0.000	0.000	1.000	1.000	

Table 16. Matrix of aggregate dominance (concordance-discordant) acd_{ij}

	Alt. 1	**Alt. 2**	**Alt. 3**	**Alt.4**	**Alt. 5**
Alt. 1	0.000	0.000	0.000	0.000	0.000
Alt. 2	0.000	0.000	0.000	0.000	0.000
Alt. 3	0.000	1.000	0.000	0.000	0.000
Alt. 4	0.000	0.000	0.000	0.000	0.000
Alt. 5	0.000	0.000	0.000	1.000	0.000

Table 17. Calculation of the upper and lower net value D_{ai} and ELECTRE I Ranking

Materiales	C_{ai}	D_{ai}	***Ranking***
1	0.0000	0.000	2
2	10.000	–1.000	1
3	–1.0000	1.000	3
4	10.000	–1.000	1
5	–1.0000	1.000	3

3.5. ARAS

According to equation (27) the normalized decision matrix is calculated ($\bar{X}_{ij}$), taking into account the calculation of the non-beneficial values by means of equation (28). Subsequently, the decision matrix normalized by weight ($\hat{X}_{ij}$) is defined by equation (29), whose values are presented in Table 18. Using equation (30) to calculate the values of the optimization function (S_i) of each of the alternatives, the degree of utility (K_i) is calculated by means of equation (31), which determines the ranking of the alternatives for the application under study. These values are shown in Table 19, showing that the material ASTM A536 (number 4) is the best as a result of the relative effect of the values of thermal conductivity, yield strength and compressive strength.

Table 18. Weighted normalized decision matrix $\hat{X}_{ij}$, of the ARAS method

Material	**A***	**B***	**C**	**D**	**E**	**F**	**G**	**H**	**I**	**J**
1	0.008	0.004	0.004	0.046	0.0008	0.008	0.037	0.010	0.008	0.002
2	0.014	0.014	0.003	0.018	0.0007	0.004	0.015	0.003	0.143	0.004
3	0.004	0.026	0.008	0.016	0.0006	0.008	0.013	0.006	0.015	0.004
4	0.005	0.177	0.007	0.017	0.0007	0.006	0.015	0.006	0.039	0.003
5	0.005	0.177	0.004	0.007	0.0006	0.003	0.007	0.007	0.044	0.003

Table 19. Calculations S_i, K_i and Ranking

Material	S_i	K_i	***Ranking***
1	0.131	0.470	4
2	0.223	0.800	3
3	0.104	0.373	5
4	0.279	1.000	1
5	0.261	0.9383	2

3.6. MOORA

The decision matrix ($\overline{X_{ij}}$) is obtained according to equation (32). Table 20 shows the weighted normalized decision matrix. Then we obtain the aggregation function S(xi) that evaluates each alternative by means of equation (33), and this calculation also determines the preference ranking of each alternative. The values are shown in Table 21, showing that the material Al_{10} Si C (number 2) is the best because its thermal conductivity (I) and coefficient of thermal expansion (J) are high compared to the rest of the materials experienced.

Table 20. Weighted normalized decision matrix $\hat{X}_{ij}$, by the MOORA method

Material	A	B	C	D	E	F	G	H	I	J
1	0.012	0.377	0.009	0.088	0.001	0.017	0.071	0.021	0.013	0.005
2	0.007	0.113	0.007	0.035	0.001	0.010	0.030	0.007	0.231	0.010
3	0.022	0.062	0.017	0.030	0.001	0.017	0.026	0.013	0.025	0.010
4	0.019	0.009	0.015	0.033	0.001	0.014	0.029	0.013	0.064	0.007
5	0.019	0.009	0.010	0.014	0.001	0.007	0.014	0.015	0.071	0.007

Table 21. Aggregation function S(xi) and Ranking MOORA

Material	S(xi)	*Ranking*
1	–0.159	5
2	0.212	1
3	0.057	4
4	0.149	2
5	0.113	3

3.7. EVALUATION OF THE MCDM

The MCDM has the task of classifying a finite number of decision alternatives, each of which is explicitly described in terms of different decision criteria that must be taken into account simultaneously. For this reason, these methods are used in the selection of the material for the construction of a brake disc.

Figure 1 shows the ranking of all MCDM methods, with the observation that the COPRAS and ARAS method have the same ranking values, so their curves overlap.

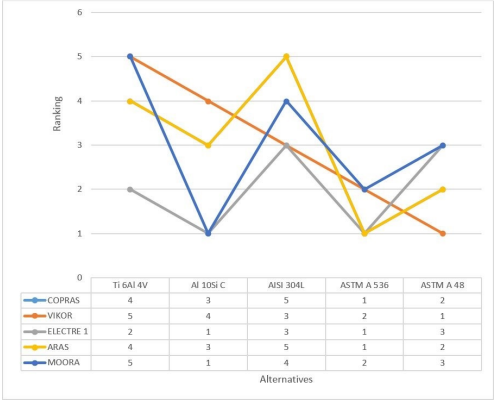

Figure 1. Ranking of the alternatives according to the MCDM methods

The best material in the COPRAS, ELECTRE I, and ARAS methods is ASTM A536, because of its low density (A), high elastic limit (D) and good compressive strength (G), the MOORA and VIKOR method place it as a second alternative. The second best option evaluated is the Al 10Si C and the ASTM A48 by the criteria of ELECTRE I, MOORA and VIKOR, since it has good thermal conductivity (I), low density (A) and an accessible price (B). These results are aligned with the materials used in the study conducted by Maleque, Dyuti, & Rahman [9]. In addition, Kharate & Chaudhari [17] study the effect of material properties on the noise and performance of the brake disc by the FEM and EMA approach, for which they experiment with gray cast iron, ceramic coal and steel, obtaining as a result that the gray cast iron has a natural frequency lower than the rest of the materials tested.

4. Conclusions

The MCDM methods used in this investigation allowed the selection of a material for the manufacture of a brake disc, incorporating quantitative and qualitative criteria. The weighting of the properties of the candidate materials for the construction of a brake disc was obtained by the ENTHROPY method. According to the COPRAS, ELECTRE I and ARAS methods, the

best material is ASTM A536, with better thermal and mechanical properties. A second option according to the criteria of ELECTRE I, MOORA and VIKOR are the $Al_{10}Si$ C and the ASTM A48. The MCDM techniques allow solving complex problems, which adapt to any type of need and apply to different areas of engineering.

References

[1] SENAE. Página principal. Servicio nacional de aduana del Ecuador. [Online]. Available: https://goo.gl/X4Jk9k

[2] H. Sakamoto and K. Hirakawa, "Fracture analysis and material improvement of brake discs," *JSME International Journal Series A Solid Mechanics and Material Engineering*, vol. 48, no. 4, pp. 458–464, 2005. DOI: https://doi.org/10.1299/jsmea.48.458.

[3] P. Hwang and X. Wu, "Investigation of temperature and thermal stress in ventilated disc brake based on 3d thermo-mechanical coupling model," *Journal of Mechanical Science and Technology*, vol. 24, no. 1, pp. 81–84, Jan 2010. DOI: https://doi.org/10.1007/s12206-009-1116-7.

[4] V. Thilak, R. Krishnaraj, M. Sakthivel, K. Kanthavel, M. D. Marudachalam, and R. P. G, "Transient thermal and structural analysis of the rotor disc of disc brake," *International Journal of Scientific & Engineering Research*, vol. 2, no. 8, pp. 1–4, 2011. [Online]. Available: https://goo.gl/1X9m8t

[5] F. Bagnoli, F. Dolce, and M. Bernabei, "Thermal fatigue cracks of fire fighting vehicles gray iron brake discs," *Engineering Failure Analysis*, vol. 16, no. 1, pp. 152–163, 2009. DOI: https://doi.org/10.1016/j.engfailanal.2008.01.009.

[6] B. A. Ali, S. Sapuan, E. Zainudin, and M. Othman, "Implementation of the expert decision system for environmental assessment in composite materials selection for automotive components," *Journal of Cleaner Production*, vol. 107, pp. 557–567, 2015. DOI: https://doi.org/10.1016/j.jclepro.2015.05.084.

[7] P. Chatterjee and S. Chakraborty, "Material selection using preferential ranking methods," *Materials & Design*, vol. 35, pp. 384–393, 2012. DOI: https://doi.org/10.1016/j.matdes.2011.09.027.

[8] P. J. Blau, B. C. Jolly, J. Qu, W. H. Peter, and C. A. Blue, "Tribological investigation of titanium-based materials for brakes," *Wear*, vol. 263, no. 7, pp. 1202–1211, 2007. DOI: https://doi.org/10.1016/j.wear.2006.12.015.

[9] M. Maleque, S. Dyuti, and M. M. Rahman, "Material selection method in design of automotive brake disc," in *Proceedings of the World Congress on Engineering 2010 Vol III*, 06 2010. [Online]. Available: https://goo.gl/7q9dpc

[10] A. Bahrami, N. Soltani, M. Pech-Canul, and C. A. Gutiérrez, "Development of metal-matrix composites from industrial/agricultural waste materials and their derivatives," *Critical Reviews in Environmental Science and Technology*, vol. 46, no. 2, pp. 143–208, 2016. DOI: https://doi.org/10.1080/10643389.2015.1077067.

[11] A. Jahan, F. Mustapha, S. M. Sapuan, M. Y. Ismail, and M. Bahraminasab, "A framework for weighting of criteria in ranking stage of material selection process," *The International Journal of Advanced Manufacturing Technology*, vol. 58, no. 1, pp. 411–420, Jan 2012. DOI: https://doi.org/10.1007/s00170-011-3366-7.

[12] N. Kundakci and A. Işik., "Integration of macbeth and copras methods to select air compressor for a textile company," *Decision Science Letters*, vol. 5, no. 3, pp. 381–394, 2016. DOI: http://dx.doi.org/10.5267/j.dsl.2016.2.003.

[13] R. J. Girubha and S. Vinodh, "Application of fuzzy vikor and environmental impact analysis for material selection of an automotive component," *Materials & Design*, vol. 37, pp. 478–486, 2012. DOI: https://doi.org/10.1016/j.matdes.2012.01.022.

[14] L. Anojkumar, M. Ilangkumaran, and V. Sasirekha, "Comparative analysis of mcdm methods for pipe material selection in sugar industry," *Expert Systems with Applications*, vol. 41, no. 6, pp. 2964–2980, 2014. DOI: https://doi.org/10.1016/j.eswa.2013.10.028.

[15] E. K. Zavadskas and Z. Turskis, "A new additive ratio assessment (aras) method in multicriteria decision–making," *Ukio Technologinis ir Ekonominis Vystymas*, vol. 16, no. 2, pp. 159–172, 2010. DOI: http://doi.org/10.3846/tede.2010.10.

[16] B. Mallick, B. Sarkar, and S. Das, "Application of the moora method for multi-criteria inventory classification," *Indian Science Cruiser*, vol. 31, no. 6, pp. 15–21, 12 2017. DOI: http://doi.org/10.24906/isc/2017/v31/i6/166459.

[17] N. Kharate and S. Chaudhari, "Effect of material properties on disc brake squeal and performance using fem and ema approach." *Materials Today: Proceedings*, vol. 5, no. 2, Part 1, pp. 4986–4994, 2018. DOI: https://doi.org/10.1016/j.matpr.2017.12.076.

Scientific Paper / Artículo Científico

UNIVERSIDAD POLITÉCNICA SALESIANA ECUADOR
INGENIUS
Revista de Ciencia y Tecnología
https://doi.org/10.17163/ings.n20.2018.09
pISSN: 1390-650X / eISSN: 1390-860X

Kinematic and dinamic study of the suspension system of an electric single seater competition Formula Student

Estudio cinemático y dinámico del sistema de suspensión de un monoplaza de competencia eléctrico Formula Student

Christian Arévalo[1,*], Ayrton Medina[1], Juan Valladolid[1]

Abstract

The level of competitiveness generated by Formula Student has led to a series of studies and technological advances in order to improve the performance of single-seaters, so that their operation is successful according to the requirements of the competition. This document details the study of the suspension system of an electric Formula Student single-seater. This study involves an analysis of the kinematics and dynamics of the suspension system in which an analytical determination of movement, loads and vibrations is carried out by means of simulation software and mathematical calculations. The aim of the study is to evaluate the performance of the suspension according to the regulations of the competition, to establish parameters that improve the suspension system and at the same time the performance of the car in terms of comfort and safety.

Keywords: Single seater, Suspension, Dynamics, Kinematics.

Resumen

El nivel de competitividad que genera la Formula Student ha desencadenado en una serie de estudios y avances tecnológicos con el fin de mejorar cada vez más el rendimiento de los monoplazas para que se desenvuelvan con éxito ante las exigencias de la competencia. En este documento se detalla el estudio del sistema de suspensión de un monoplaza de competencia eléctrico Formula Student. Este estudio involucra un análisis de la cinemática y dinámica del sistema de suspensión en el cual se realiza una determinación analítica del movimiento, cargas y vibraciones por medio de software de simulación y de cálculos matemáticos. Con el estudio se busca evaluar el rendimiento de la suspensión en función del reglamento de la competencia, con el fin de establecer parámetros que mejoren el sistema de suspensión y a la vez el desempeño del monoplaza en términos de confort y seguridad.

Palabras clave: monoplaza, suspensión, dinámica, cinemática.

[1,*]Transport Engineering Research Group (GIIT), Automotive Mechanical Engineering Major, Universidad Politécnica Salesiana, Cuenca – Ecuador. Author for correspondence ✉: carevalom@est.ups.edu.ec.
https://orcid.org/0000-0002-2906-3553, https://orcid.org/0000-0002-9172-7568,
https://orcid.org/0000-0002-3506-2522.

Received: 13-04-2018, accepted after review: 19-06-2018

Suggested citation: Arévalo, C.; Medina, A. and Valladolid, J. (2018). «Kinematic and dinamic study of the suspension system of an electric single seater competition Formula Student». Ingenius. N.°20, (july-december). pp. 95-106. doi: https://doi.org/10.17163/ings.n20.2018.09.

1. Introduction

Formula Student is a student competition organized by the SAE (Society of Automotive Engineers) whose main objective is to promote the best training of young engineers [1], challenging university students to design, build and test the performance of a formula type vehicle that successfully meets the tests stipulated in the respective regulations [2], to then compete with other students around the world.

The technological advances and the level of competitiveness generated by Formula Student have motivated the UPS Racing Team of Universidad Politécnica Salesiana to develop two single-seater cars. The first one was a combustion car for the 2014 competition in the UK, while the second was an electric vehicle for the UK Formula Student Electric competition in 2017.

According to the results of last year [3], in the dynamic events the electric car has had problems with some mechanical and electrical systems; among the mechanical difficulties is the lack of adjustments in the settings and the suspension damping, as well as a failure located in a member of the lower control arm of the rear suspension.

Considering that the suspension plays a very important role in the performance of the vehicles in terms of safety and comfort, there is a need to carry out studies of the suspension that allow for improvements either in the development or in the design, so that the car can be competitive.

The main suspension design in competition is the deformable parallelogram (doublé A-arm or double wishbone), which can have three forms of spring-damper assembly activation, which are: direct, by means of a push-rod, or pull rod [4]. These suspension systems are simple in design, easy to adjust, resistant, have good adaptability and can be light if they are made with composite materials, which is why they are widely used by Formula 1 and Formula Student cars [5].

The suspension must incorporate a good kinematic design to keep the tire as perpendicular as possible to the pavement, to maintain optimal cushioning and adequate elasticity rates to keep the tire on the ground at all times. In addition, the components must be resistant so that they do not fail under static and dynamic loads [6–9].

The objective of this work is to carry out the dynamic and kinematic study of the suspension system of the Formula Student electric vehicle, by means of kinematic simulation programs and mathematical calculations, to determine the performance of the suspension and to establish improvements or solutions to the problems that arise during the study.

2. Materials and methods

2.1. Study vehicle

The vehicle used to study the suspension is a Formula Student electric competition car, as shown in Figure 1.

Figure 1. Formula Student electric single-seater

The dimensions of the car are shown in Table **??**.

Table 1. Dimensions of the electric single-seater

Especification	Dimension
Front track width	1200 mm
Rear track width	1180 mm
Wheelbase	1600 mm
Weight with pilot	345 kgf
Front weight distribution	45%
Back weight distribution	55%
Height of center of gravity	300 mm

2.2. Suspension system characteristics

The characteristics of the suspension system are shown in Table 2.

Table 2. Suspension system characteristics

Specification	Detail
Type of suspension system (Front/rear)	Deformable parallelogram
Activation system spring - shock absorber (Front/rear)	Push-rod
Stabilizer bar (Front/rear)	Sprat type
Shock absorbers (Front/rear)	Ohlins TTX25
Rigidity of the spring (front/front) (N/mm)	150/200
Total length of the boat/bounce suspension (mm)	30/30
Material	Carbon fiber and aluminum 7075 T6
Tires	19.5 x 7.5-10 (Hoosier), R25
Rims	7 in x 10 in (Braid), offset: +35

2.3. eometric parameters

The coordinates of the connection points of each element of the suspension are as shown in Table 3. The connection points, in addition to allowing the definition of geometric parameters of the suspension, are necessary for the kinematics simulation program and for the 3D calculation of the forces in the members of the suspension.

Table 3. Coordinates of the connection points of the suspension's elements

Pts.	Front suspension			Rear suspension		
	X(mm)	Y(mm)	Z(mm)	X(mm)	Y(mm)	Z(mm)
P1	1443,9	212	227,59	15	250	203,59
P2	1732	212	227,59	335	250	203,59
P3	1730	520	218,83	148,83	555	219
P5	1446,6	256	377,59	15	290	347,59
P4	1732	256	377,59	335	290	347,59
P5	1760	520	400,83	171,17	529	401
P6	1710	480,74	244,78	148,83	513	241,8
P8	1710	295,72	509,03	148,83	308	628,68
P9	1790	520	218,83	220	549,14	259,83
P10	1750	190	227,59	220	258,5	234,2
P11	1710	61,21	534,99	148,83	70,51	660,02
P12	1710	238,98	534,99	148,83	245,98	660,2
P13	1760	520	310	160	541,98	310
P14	1760	590	310	160	600	310
P15	1699	238,38	468,88	159,83	245,98	596,42
P16	1721	238,38	468,88	137,83	245,98	596,42

Figure 2 shows the location of the connection points of the suspension elements.

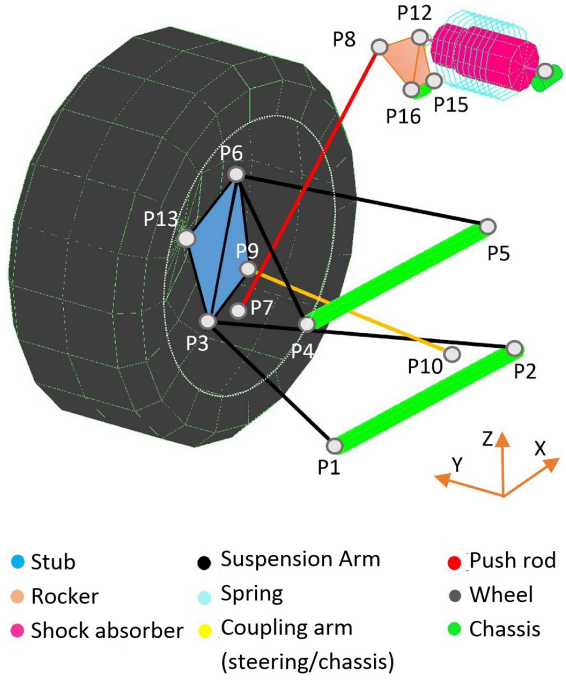

Figure 2. Location of the connection points of the suspension elements.

Table 4 shows the geometric parameters based on wheel dimensions, track gauge, wheelbase and the coordinates of the suspension connection points according to [6, 7].

Table 4. Geometric parameters of the suspension system

Parameter	Front suspension	Rear suspension
Height of the balancing center (mm)	44,84	70,02
Angle of advance (°)	7	9
Output angle (°)	8,13	0
Angle of fall (°)	0	0
Mechanical Trail (mm)	28,32	70,02
Scrub radius (mm)	24,56	0
Anti-sinking / (%) Anti-lifting	0	0

An analysis is made of the results of the FSAE TIRE TEST CONSORTIUM [10], referring to the Hoosier® tire 19.5 x 7.5-10, which is used in the study car. The analysis is carried out in order to determine the range of acceptable angles of fall, the behavior of the tire and a prediction of the maximum forces it can withstand. Figure 3 shows that the maximum lateral force is presented for an angle of fall of –1° to –1.3°, while the maximum longitudinal force is made for a fall of 0°. The tire does not suffer a sharp drop in grip after reaching the maximum peak, so an effective fall range of 1 to -3° can be set.

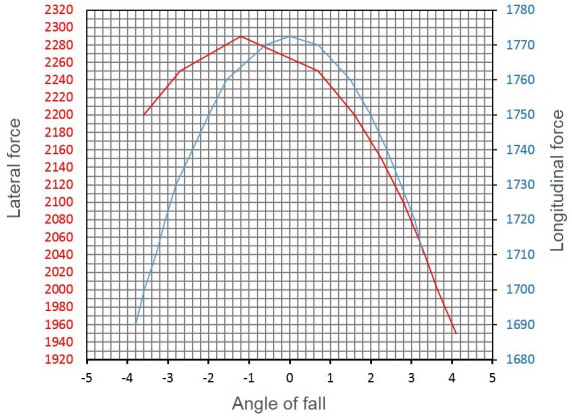

Figure 3. Angle of fall at different lateral and longitudinal forces, for a normal weight of 1000 N.

3. Results and kinematic analysis

Using Lotus Suspension Analisys, a kinematic analysis of the suspension system is performed. The program allows the user to know the behavior of the suspension with the geometry established on various stages in the track, such as bounce and rebound, roll and direction turn [11]. The parameters that are analyzed are those that characterize the behavior of the suspension [12], such as:

- Balancing center
- Angle of fall
- Angle of advance
- Toe (convergence/divergence)

For the simulation, the dimensions of the car and the coordinates of the connection points of each element of the suspension are inserted into the program. Lotus creates a three-dimensional model of the type of suspension to be analyzed as shown in Figure 4.

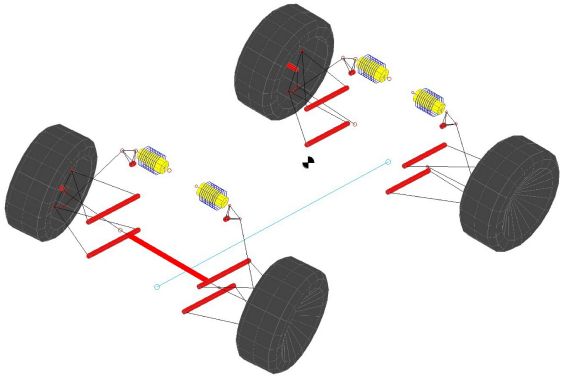

Figure 4. Simulated suspension system in Lotus Suspension Analysis.

The elevation or bounce of the suspension in the vertical direction is analyzed, which tries to simulate the passage of the car over a bump or obstacle of 30 mm in height. For this analysis, only the right wheel of the front and rear axle is considered, because the left wheels display a similar behavior.

Figure 5 shows that the front wheels in a bouncing situation have a maximum negative fall gain of -1.13°, and in rebound a maximum positive fall of 0.9°. The rear wheels in the bouncing situation have a maximum negative fall gain of -1.63°, and in rebound a maximum positive fall of 1.41°. The behavior of the angle of fall is favorable according to [13], because when the vehicle passes through a curve, the most loaded wheel will have a negative fall gain and the discharged wheel a positive fall gain, improving the lateral grip and its traction simultaneously. In order to achieve maximum performance of the tire and reduce the positive angle of fall, a static angle of fall for the front and rear wheels of -1° and -1.5° respectively can be established. Having a static fall, wheels with maximum compression approach a negative fall of -2.6°, staying within an effective range of 1° and -3°, according to the analysis of the tires. According to the recommendation of Carroll Smith [9], the static fall adjustment can be reduced by improving the grip of the tire in both curved and straight trajectories.

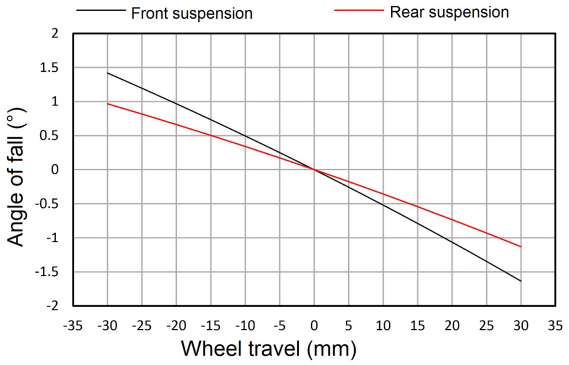

Figure 5. Variations of the angle of fall with wheel bounce and rebound.

According to Figure 6, the forward advancing angle becomes positive with the wheel bounce and negative with the rebound, while the rear advancing angle has a positive orientation in both bounce and rebound. The angle of advance contributes to the gain of the angle of fall during a turn. According to the results, during curves the angle of advance will cause the external wheel to have a negative fall gain and the fall of the internal wheel to trend to be positive.

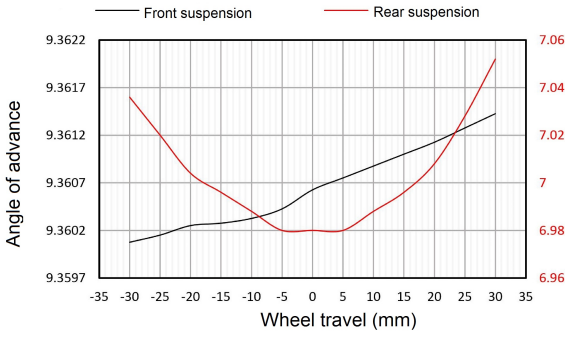

Figure 6. Variations of the angle of advance with wheel bounce and rebound.

Figure 7 shows that the maximum vertical travel of the center of balance with the bounce and rebound is 80.344 mm and 86.4 mm for the front and rear suspension respectively. The center of balance is maintained at all times above the ground plane, something very desirable according to [14]. The height of the center of balance to the center of gravity and the anti-roll effect of the elastic elements allow the angle of roll of the chassis to be 1° at a lateral acceleration of 1 G, without considering the deformation of the tires.

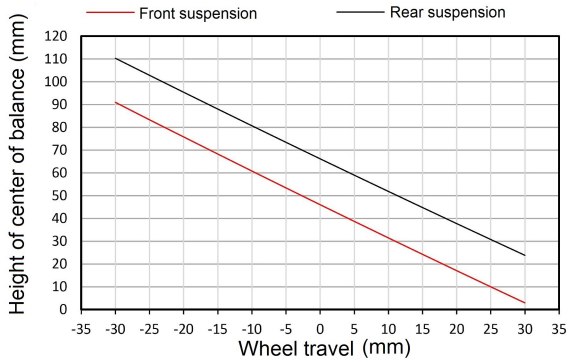

Figure 7. Variations of the height of the center of balance with bounce and rebound of the wheel.

The maximum rear toe is 0.1393 degrees with wheel rebound and maximum forward toe is 0.0328 degrees with wheel bounce, as shown in Figure 8. A slightly positive toe reduces rolling resistance and a negative toe improves maneuverability in curves, however, excessive toe increases tire wear. The low values are due to the fact that the bump steer effect is null, which has been achieved with a correct geometry of the steering rods.

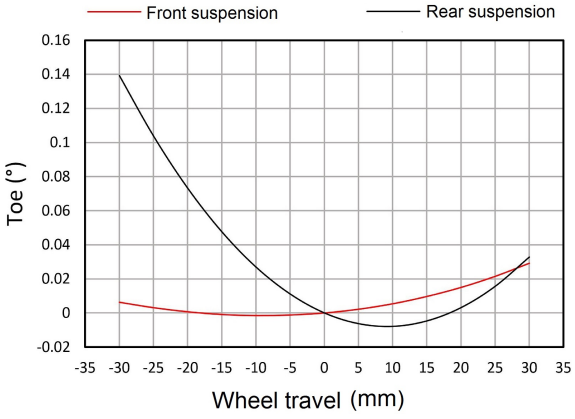

Figure 8. Toe variations with bounce and rebound of the wheel.

The passage of the car through a curve is simulated, which causes the suspension to tilt due to centrifugal acceleration. The lateral force is translated into a roll angle of the chassis. According to Figure 9, when the rolling of the chassis is positive the wheel is external to the curve and if it is negative the wheel is internal to the curve. With a rolling of 3° of the chassis, the maximum angle of fall for the external and internal wheel of the front axle is 1.28 and -1.52 degrees respectively, while in the rear axle the maximum angle of fall is 1,83° for the outer wheel and -2,01 for the inner wheel. Depending on the results, the wheels outside the curve have a negative fall gain, allowing for an improvement in tire grip.

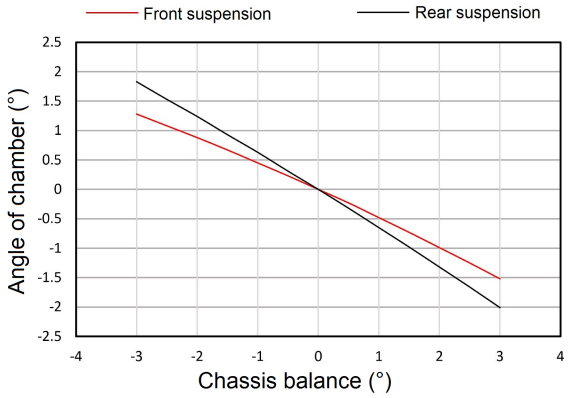

Figure 9. Variations of the angle of fall with rolling of the chassis.

Figure 10 shows that the rear and front swing centers have a lateral travel of 186.44 mm and 119.05 mm respectively, with a maximum rolling of the chassis of 3°. Considering the effect in the reduction of the rolling of the elastic elements (springs and stabilizer bar), as well as a lateral acceleration of 1 G; the chassis will have 1° of roll, where the lateral migration of the balancing center will be 63.57 mm/G and 40.25 mm/G in the front and rear suspension respectively.

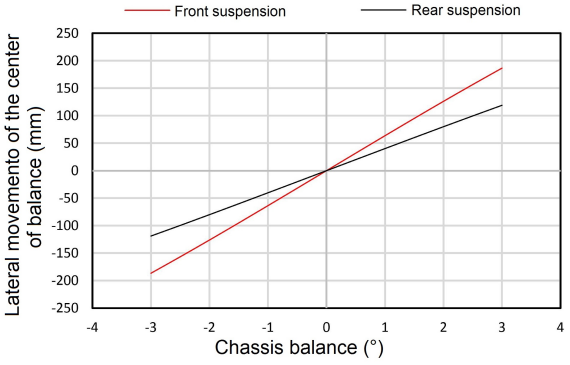

Figure 10. Lateral movement of the center of rolling with rolling of the chassis.

Figure 11 shows the behavior of the right front wheel with the turn of the direction. When the wheel is internal to the curve and with the maximum angle of rotation has a negative fall of -2.75°. If the wheel is external to the curve, a positive fall of 5.33° is generated with the maximum turn.

4. Results and dynamic analysis

The calculations of the forces generated in the members of the suspension system are performed when the vehicle is subjected to different dynamic load scenarios. It is important to consider as many scenarios as possible because the forces generated will vary for each member depending on the load case. Five different load scenarios are established to which the vehicle is subjected in a typical road environment [15].

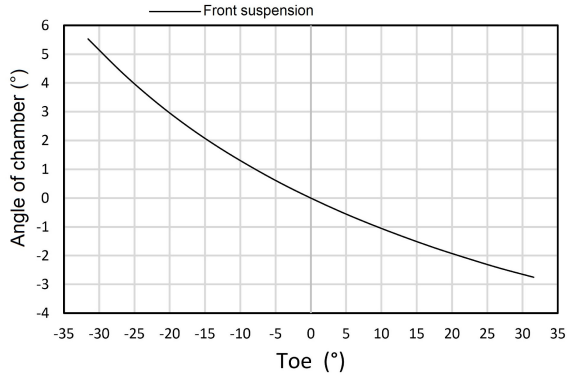

Figure 11. Variations of the angle of fall with the turn of the direction.

- Linear acceleration
- Linear braking
- Passing through curve
- Acceleration in curve
- Curved braking
- Passing through obstacle

For each load scenario, the forces generated in the referential system are calculated, X in longitudinal direction to the vehicle, Z in perpendicular direction to the ground and Y in the direction transverse to the vehicle. The forces that are generated in the tire patch in the X and Z directions due to acceleration and braking as shown in Figure 12, are defined by equations 1-6:

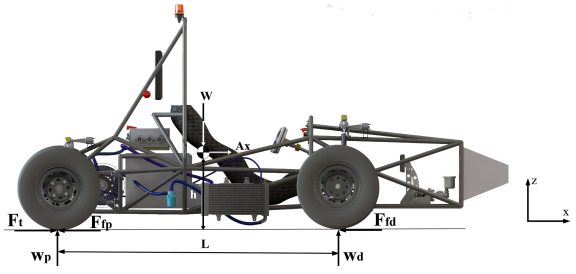

Figure 12. Forces present in the tire patch during acceleration and braking.

$$Ax = \frac{v_f - v_o}{t} \tag{1}$$

$$Ft = \frac{\frac{\mu \times W \times b}{L}}{1 - \frac{h}{L} \times \mu} \tag{2}$$

$$Ffp = \mu \times \left(W_e - \frac{W \times Ax \times h}{l} \right) \tag{3}$$

$$Ffd = \mu \times \left(W_e - \frac{W \times Ax \times h}{l} \right) \tag{4}$$

$$Wd = W_{ed} + \frac{W \times Ax \times h}{l} \tag{5}$$

$$Wp = W_{ep} - \frac{W \times Ax \times h}{l} \tag{6}$$

Where:

Ax = longitudinal acceleration (m/s^2)
v_o = initial speed (m/s)
v_f = final speed (m/s)
Ft = tensile force (N)
W = weight of the vehicle (N)
l = wheelbase (m)
h = height of the center of gravity (m)
μ = coefficient of adhesion
Wed = static weight on the front axle (N)
Wep = static weight on the rear axle (N)
Wd = dynamic weight on the front axle (N)
Wp = dynamic weight on the rear axle (N)
Ffd = braking force on the front axle (N)
Ffp = braking force on the rear axle (N)
b = distance from the axle posterior to the center of gravity (m)

The forces that are generated in the tire patch in the Y and Z directions due to the curve path as shown in Figure 13, are determined by equations 7, 8, 9.

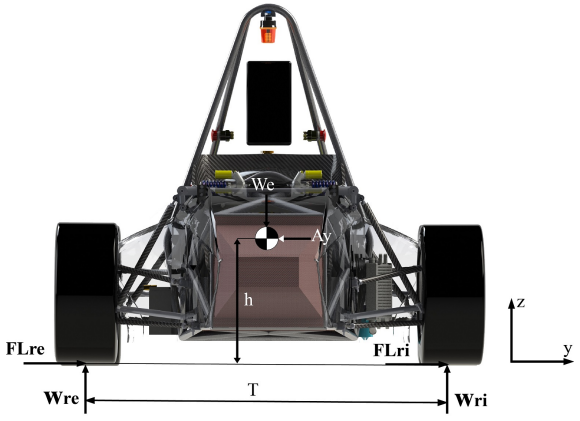

Figure 13. Forces present in the tire patch on the curve.

$$Fl = \frac{m \times v^2}{4 \times r} \tag{7}$$

$$w_{re} = \frac{W_e}{2} + \frac{W_e \times Ay \times h}{T} \tag{8}$$

$$Wp = W_{ep} - \frac{W \times Ax \times h}{l} \tag{9}$$

Where:

m = mass of the vehicle (kg)
v = vehicle speed (m/s)
r = radius of curvature (m)
Ay =lateral acceleration (m)
W_e= static weight on the axle (N)

W_{re}= dynamic weight on the outer wheel (N)
W_{ri}= dynamic weight on the inner wheel (N)
T = track width (m)
h = height of the center of gravity (m)

The forces generated in the tire patch in the Z direction due to passing through an obstacle are determined by equation 10:

$$F_{eje} = 0,2 m_{axis} \times a_z \tag{10}$$

Where:
F_{axis} = force on the shaft (N)
a_z =vertical acceleration (m/s^2)
m_{axis} = mass of the axis (kg)

With the established load scenarios, we proceed to determine the forces that are generated in the suspension members. In the front and rear suspension there are a total of six members, where two members are the upper control arm (BCS), two members of the lower control arm (BCI), one of the push-rod (PR) and one of the coupling arm (BA). For this analysis it is assumed that the load acts on the center of the wheel. The wheel center is considered to be the base of the rigid body and point (0,0,0) as shown in Figures 14 and 15.

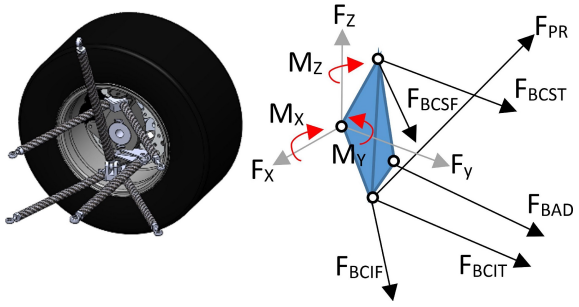

Figure 14. Free body diagram of the forces in the members of the front suspension.

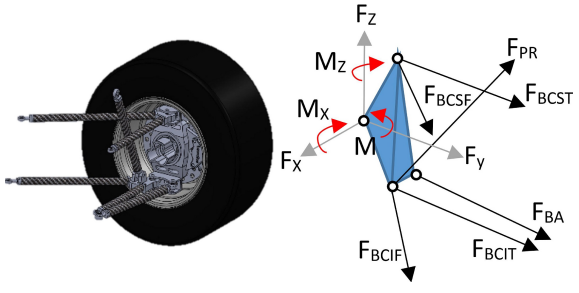

Figure 15. Free body diagram of the forces in the members of the rear suspension.

A system of vectors and matrices is used to determine how these forces are distributed along each of the suspension elements [16].

With a balance of forces and moments with respect to the X, Y and Z coordinate axes of the wheel center, six equations are determined. The system of equations is solved by the following expression:

$$\begin{aligned} [A]x &= B \\ x &= [A]^{-1}B \end{aligned} \tag{11}$$

x represents the unknown force in each of the suspension members.

$$x = \begin{pmatrix} F_{PR} \\ F_{BCSF} \\ F_{BCST} \\ F_{BCIF} \\ F_{UCST} \\ F_{BA/BAD} \end{pmatrix} \tag{12}$$

B represents the forces and moments in X, Y and Z generated in the center of the tire patch and resolved on the center of the wheel.

$$B = \begin{pmatrix} F_x \\ F_y \\ F_z \\ Mx \\ My \\ Mz \end{pmatrix} \tag{13}$$

The matrix A is determined by the unit vectors obtained from the sum of forces and momentsin the X, Y and Z directions of each member. The force vector ($\overrightarrow{F}$) is equal to the product point between the unit vector (u) and the magnitude of the force ($|F|$), as shown in equation 15. The moment ($\overrightarrow{M}$) is equal to the cross product between the force vector ($\overrightarrow{F}$) and the moment arm vector ($\overrightarrow{r}$), as can be seen in equation 15.

$$\begin{aligned} \overrightarrow{F} &= |F| \times \overrightarrow{u} \\ \overrightarrow{M} &= \overrightarrow{F} \times \overrightarrow{r} \end{aligned} \tag{14}$$

$$\overrightarrow{M} = |F| \times \overrightarrow{u} \times \overrightarrow{r} \tag{15}$$

$$[A] = \begin{bmatrix} u_{PRx} & u_{BCSFx} & u_{BCSTx} & \cdots \\ u_{PRy} & u_{BCSFy} & u_{BCSTy} & \cdots \\ u_{PRz} & u_{BCSFz} & u_{BCSTz} & \cdots \\ (u_z r_y - u_y r_z)_{PR} & (u_z r_y - u_y r_z)_{BCSF} & (u_z r_y - u_y r_z)_{BCST} & \cdots \\ (u_z r_x - u_x r_z)_{PR} & (u_z r_x - u_x r_z)_{BCSF} & (u_z r_x - u_x r_z)_{BCST} & \cdots \\ (u_y r_x - u_x r_y)_{PR} & (u_y r_x - u_x r_y)_{BCSF} & (u_y r_x - u_x r_y)_{BCST} & \cdots \end{bmatrix}$$

$$\begin{bmatrix} \cdots & u_{BCIFx} & u_{BCITx} & u_{BAx} \\ \cdots & u_{BCIFy} & u_{BCITy} & u_{BAy} \\ \cdots & u_{BCIFz} & u_{BCITz} & u_{BAz} \\ \cdots & (u_z r_y - u_y r_z)_{BCIF} & (u_z r_y - u_y r_z)_{BCIT} & (u_z r_y - u_y r_z)_{BA} \\ \cdots & (u_z r_x - u_x r_z)_{BCIF} & (u_z r_x - u_x r_z)_{BCIT} & (u_z r_x - u_x r_z)_{BA} \\ \cdots & (u_y r_x - u_x r_y)_{BCIF} & (u_y r_x - u_x r_y)_{BCIT} & (u_y r_x - u_x r_y)_{BA} \end{bmatrix} \quad (16)$$

Tables 5 and 6 show the maximum forces of tension and compression in the members of the suspension system, as a result of the different load scenarios. The maximum tensile forces in the members of the suspension arms are –4313 N and –5131 N in the front and rear respectively, and the maximum compression forces are 4165 N and 5119 N. The front and rear push-rods work only in compression where the forces are 5358 N and 8544 N for the front and rear respectively.

Table 5. Results of the forces on the members of the front suspension

Load scenarios	Forces on the members of the front suspension					
	FPR	**FBCSF**	**FBCST**	**FBCIF**	**FBCIT**	**FBAD**
Acceleration (N)	487	109	82	–272	–178	–58
Braking (N)	1149	4162	–2726	–2021	3350	–2623
Curve (N)	1092	–1160	–1459	1063	957	825
Acceleration and curve (N)	296	–1339	–1594	1508	1248	918
Braking and curve (N)	2495	1013	4165	146	–4313	–1109
Step through obstacle (N)	5358	1203	906	–2990	–1954	–629
Maximum force (N)	5358	4162	4165	–2290	–4313	–2623

Table 6. Results of the forces in the members of the rear suspension

Load scenarios	Forces in the members of the rear suspension					
	FPR	**FBCSF**	**FBCST**	**FBCIF**	**FBCIT**	**FBAD**
Acceleration (N)	1494	–3942	2874	4775	–5131	–776
Brakimg (N)	754	2582	–1333	-2437	988	482
Curve (N)	2239	998	–2225	–155	1297	-625
Acceleration and curve (N)	2090	–3168	238	5119	–2503	52
Braking and curve (N)	956	–1772	-949	3553	–153	–268
Step through obstacle (N)	8544	1646	1986	–2593	–2915	521
Maximum force (N)	8544	–3942	2874	5119	–5131	776

Compression and tensile tests are performed to determine if the limbs support the maximum calculated loads. In the tensile test, the bond strength between the aluminum grafts and the carbon fiber tube is measured [17]. The graft is an aluminum element glued with a high resistance adhesive to the carbon fiber tube, allowing the anchoring to the chassis or to the spindle by means of ball joints. The tubes are of two external diameters, 18.1 mm and 21.3 mm with a thickness of 1.15 mm. The larger diameter tube is used for the push-rod and the coupling arms. The smaller diameter tube is used for the suspension arms.

Table 7. Results of the compression and tensile tests of the members of the suspension

Tube diameter (mm)	Traction force (KN)	Fuerza Compression force (KN)
18,1	2,9	13,59
21,3	8,93	13,88

According to the results of Table 7, it can be said that the members of the suspension arms could fail in tension, since according to the tensile test, the maximum joint force is 2.9 KN, and the maximum tension force in one member of the suspension arm is –5.13 KN. In the case of compression, the members are subject to buckling, therefore, it is necessary to perform a calculation of critical buckling (P_{cr}) and safety factor (F_s), defined by equations 18 and 19. The calculation will make it possible to more accurately predict a case of compression failure [18].

$$P_{cr} = \frac{C\pi^2 El}{l^2} \quad (17)$$

$$F_s = \frac{P_{cr}}{c} \quad (18)$$

Where:

C = condition constant of articulated ends
P = axial force (N/m^2)
E= modulus of material elasticity (N/m^2)
I= moment of inertia (m^4)
l = length of the bar (m)

According to the results of Table 8, the members of the suspension arms, push-rod and coupling arm would

not fail due to buckling effects since, according to the calculation, they have safety factors greater than 2 and support higher compression forces than 13 KN.

Table 8. Results of the calculation of critical buckling and safety factor of suspension members working by compression

Tube diameter (mm)	Buckling critical (N)	Axial force (N)	Security factor
18,1	14 181,35	5119	2,77
21,3	18 769,27	8544	2,19

Since one of the most important tasks of the suspension system is to absorb the irregularities of the road without losing traction in the tires, the vast majority of cars are equipped with shock absorbers and springs to fulfill this purpose. In this section, through a model of 2 degrees of freedom of the suspension system of ¼ of the vehicle [19], the analysis of the frequencies of the suspension is made, generating an interaction between the road and the vehicle. Figure 16 shows the model of the suspension of a quarter of the vehicle with 2 degrees of freedom, which includes the elastic constant of the tire, as well as the non-suspended mass. The position of the suspended mass is X_1, the non-suspended mass is X_2 and X_0 serves to model the unevenness of the terrain.

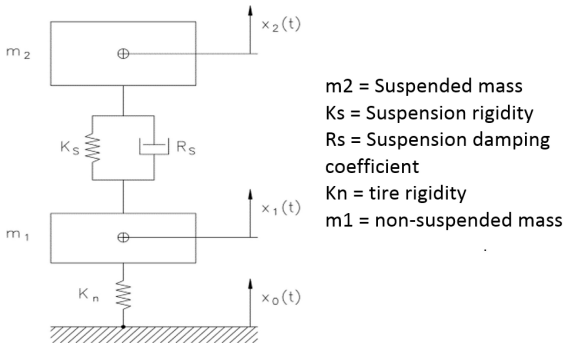

Figure 16. Full model of a quarter of a vehicle [11].

The transfer function of 2 degrees of freedom is given by the following expression:

$$\frac{x_2(s)}{x_0(s)} = \frac{R_s \cdot K_n \cdot s \cdot K_s \cdot K_n}{(m_1 \cdot s^2 + R_s \cdot s + K_s + K_n)(m_2 \cdot s^2 + R_s \cdot s + K_s) - (R_s \cdot s - K_s)^2} \tag{19}$$

With the defined modeling, the necessary initial parameters are established to allow the study to be carried out, as shown in Table 9.

Table 9. Parameters of the model of a quarter of a vehicle

Parameter	Front suspension	Rear suspension
m2: suspended mass (kg)	61,1	74,75
Ks: suspension rigidity (N/m)	26 220,47	34 960,62
Rs: suspension damping coefficient (Ns/m)	.....	.....
Kn: tire stiffness (N/m)	102 917,699	132 322,756
m1: mass not suspended (kg)	10,9	13,25
MR: motion ratio	1,3	1,4
Kw: wheel stiffness (N/m)	15515,071	17837,051
fm2: natural frequency of the suspended mass (Hz).	2,36	2,3
fm1: natural frequency of the unsuspended mass (Hz)	16,62	16,81
Ccr: critical damping coefficient (Ns/m)	2487,28	3233,274

The force developed by a shock absorber (F_a) is represented by the equation:

$$F_d = R_s \cdot v_p \tag{20}$$

Where:

R_s= damping coefficient [Ns/m]

v_p= speed on the piston of the shock absorber [m/s]

Using mathematical Matlab software, the transmissibility of the suspension system is analyzed at different damping coefficients for high and low speed provided by the TTX 25 damper [20]. By means of equation 23 and the graph in Figure 17, the slopes or damping coefficients for the different damper settings are determined as shown in Table 10.

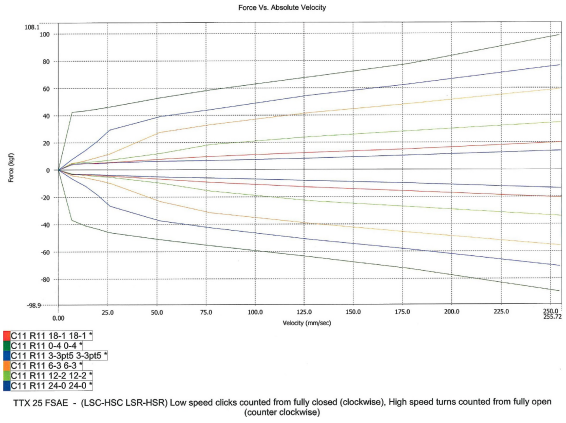

Figure 17. Damping coefficients for different shock absorber settings [21]

To maximize the traction area, the lowest possible transmissibility is required. The graphics of Figures 18 and 19 show the response of the second-degree model of the front and rear suspension. It can be seen that if the damping factor is increased at low input frequencies, the transmissibility is reduced to the maximum, which means that the tire will not lose traction. After the point of intersection, the low damping factors result

in a lower transmissibility, attenuating movement in the chassis [22].

Table 10. Damping coefficients for different shock absorber settings

Adjustment of the shock absorber	Low speeds slope [KN*s/m]	High speeds slope [N*s/m]
C11 R11 0-4	52,788	2223
C11 R11 3-3pt5	11,77	1962
C11 R11 6-3	5,282	1831
C11 R11 12-2	2,354	882,9
C11 R11 18-1	3,678	689,1
C11 R11 24-0	3,678	567,5

According to the transmissibility analysis, a high damping factor is necessary (ξ) at low speeds and a low value for high speeds in the shock absorber. The TTX25 shock absorber, for the front suspension, needs a very close value of $\xi = 0,73$, which is achieved with setting C11 R11 6-3 for low speed. For high speeds the setting C11 R11 24.0 provides un $\xi = 0,22$. In the rear suspension a value of $\xi = 0,68$ is required, which is achieved with the C11 R11 0-4 setting for low speed. For high speeds the setting C11 R11 18.1 provides un $\xi = 0,22$.

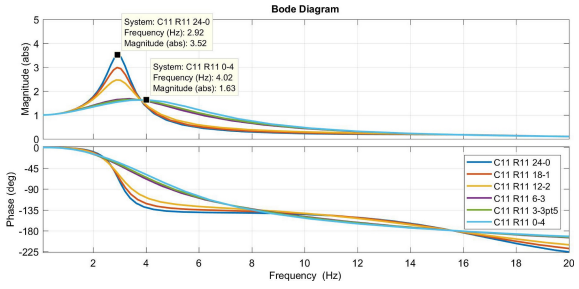

Figure 18. Transmissibility of the second-degree model of the front suspension.

As the system moves both compression and extension, according to [23] it is better to have a damping factor lower than compression and greater than extension in relation to the desired value in order to avoid resonance in the system (see Figure 20).

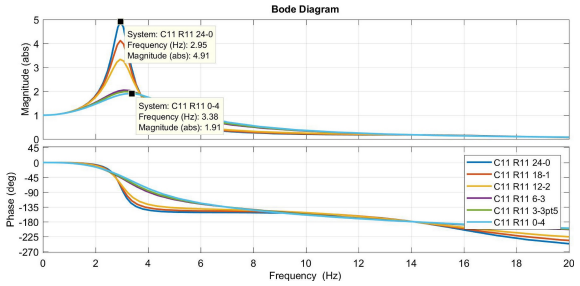

Figure 19. Transmissibility of the second-degree model of the rear suspension.

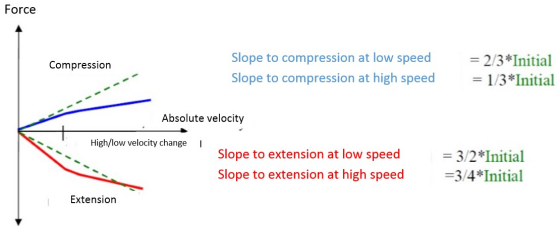

Figure 20. Slope adjustment for high speeds and low speeds. [23]

According to the analysis made, the use of double the compression damping factor for extension is determined. In this way, it is possible to achieve a good grip of the wheel, a lower transmissibility and better maneuverability. The calibrations that meet these requirements are shown in Tables 11 and 12.

Table 11. Damping factor of the front suspension

Adjustment of shock absorberr	Compression		Extension	
	Low speed	High speed	Low speed	High speed
C11 R11 12-2	0,92	0,34	.....	.....
C11 R11 6-3	.....	.....	2,08	0,72

Table 12. Factor de amortiguamiento de la suspensión posterior

Adjustment of shock absorberr	Compression		Extension	
	Low speed	High speed	Low speed	High speed
C11 R11 12-2	0,72	0,27	.....	.....
C11 R11 6-3	.....	.....	1,63	0,56

Figures 21 and 22 show the system response of the front and rear suspension respectively in front of a vertical displacement as input. It can be seen that the calibrations of the low speed damping factor in compression attenuate oscillations in the shortest time possible with respect to other calibrations.

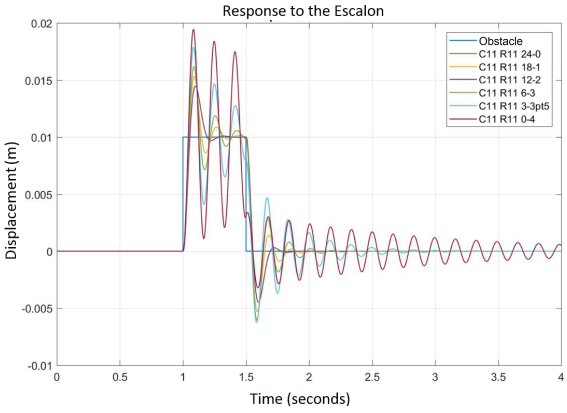

Figure 21. Response of the front suspension system to a vertical displacement as input.

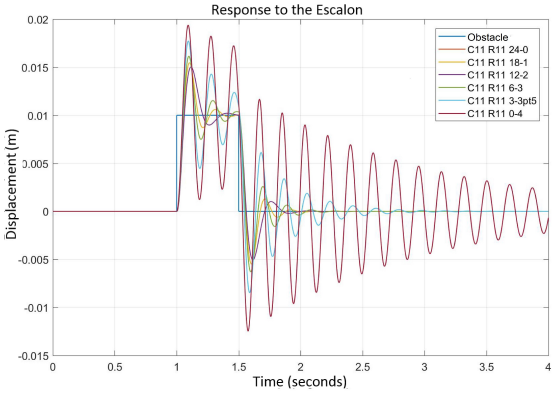

Figure 22. Response of the rear suspension system to a vertical displacement as input.

5. Conclusions

This research helps to have a broader view of the suspension systems used by FSAE competition vehicles. With the study of the kinematics, the behavior of the suspension of the car was determined under different scenarios on the track, such as passing through a curve or an obstacle. Depending on the results, it can be said that the configuration provided for the single-seater's suspension allows a good directional control of the vehicle (null bump steer effect) and an adequate negative fall gain of the wheel with the travel of the suspension or rolling of the chassis, giving a good lateral grip to the tires. However, with the turn of the steering there is a gain of excessive positive fall in the front wheels, which would affect the lateral grip in very tight corners. With the appropriate adjustments in the angles of advance, exit, static fall and convergence, the required or optimal conditions of vehicle stability and steering could be ensured, allowing greater accelerations, better braking and faster cornering steps. According to the study of the forces in the members of the suspension with dynamic loads, it was determined that the suspension arms subjected to stress loads can fail in critical cases, the problem is in the strength of the joints between the aluminum grafts. With the second-degree model of a quarter of a vehicle and with the help of Matlab, a transmissibility analysis was carried out that allowed defining the characteristics that the shock absorber must have to guarantee maximum contact area, which produces greater traction.

References

[1] IMechE. Formula student. Institution of Mechanical Engineers. [Online]. Available: https://goo.gl/Mkjf9n

[2] S. International. (2017) Formula sae rules. [Online]. Available: https://goo.gl/pSeNqe

[3] Formula Studente Germany. (2017) Formula student electric - world ranking list. Mazur Events+Media. [Online]. Available: https://goo.gl/2Q75AE

[4] A. Staniforth, *Competition Car Suspension: Design, Construction, Tuning*, Haynes, Ed., 1999. [Online]. Available: https://goo.gl/2jhg7s

[5] Rapid-Racer. (2016) Suspension. [Online]. Available: https://goo.gl/5Dpwjr

[6] W. F. Milliken and D. L. ;illiken, *Race Car Vehicle Dynamics*, S. International, Ed., 1995. [Online]. Available: https://goo.gl/iuhFqJ

[7] T. Pashley, *How to Build Motorcycle-engined Racing Cars*, V. P. Ltd, Ed., 2008. [Online]. Available: https://goo.gl/XdxRGM

[8] M. Royce and S. Royec, *Learn & Compete: A Primer for Formula SAE, Formula Student and Forumula Hybrid Teams*, R. Graphic, Ed., 2012. [Online]. Available: https://goo.gl/9rxtrG

[9] C. Smith, *Tune to Win*, C. S. Consulting, Ed., 1978. [Online]. Available: https://goo.gl/KaTkxq

[10] Milliken Research. (2018) Formula sae tire test consortium. Milliken Research Associates Incorporated. [Online]. Available: https://goo.gl/ErGrP5

[11] G. P. Pillajo Quijia, "Estudio cinemático del comportamiento de la suspensión de un prototipo de formula sae student eléctrico del equipo upm racing," Master's thesis, Universidad Politécnica de Madrid. España, 2012. [Online]. Available: https://goo.gl/aTb5mt

[12] P. De la fuente aguilera, "Análisis de la suspensión del vehículo monoplaza eléctrico UPM-03e del equipo UPM racing," Universidad Politécnica de Madrid. España., 2016. [Online]. Available: https://goo.gl/PvvCV3

[13] S. Juvanteny Gimenez, "Estudio y diseño del sistema de suspensión para un prototipo de fórmula sae," Tesis de grado. Universidad Politécnica de Cataluña. España, 2015. [Online]. Available: https://goo.gl/q93zhh

[14] E. I. Efler herranz, "Diseño de la suspensión trasera de un vehículo formula student," Tesis de grado. Universidad Politécnica de Madrid. España, 2016. [Online]. Available: https://goo.gl/YkgNnv

[15] E. D. Flickinger, "Design and analysis of formula sae car suspension members," Master's thesis, California State University, Northridge. EEUU, 2014. [Online]. Available: https://goo.gl/tcUw5g

[16] L. Borg, "An approach to using finite element models to predict suspension member loads in a formula sae vehicle," Master's thesis, Virginia Polytechnic Institute and State University. USA, 2009. [Online]. Available: https://goo.gl/i8bV4B

[17] A. C. Cobi, "Design of a carbon fiber suspension system for fsae applications," Bachelor thesis. Massachusetts Institute of Technology. USA, 2012. [Online]. Available: https://goo.gl/h1tQU3

[18] R. G. Budynas and J. K. Nisbett, *Diseño en ingeniería mecánica de Shigley*, 9th ed., M. Mc Graw-HILL, Ed., 2012. [Online]. Available: https://goo.gl/dumukn

[19] F. Aparicio Izquierdo, *Teoría de los vehículos automóviles*, E. T. S. d. I. I. Universidad Politécnica de Madrid, Ed., 1995. [Online]. Available: https://goo.gl/M2EHoy

[20] J. Hurel, E. Teran, F. Flores, and B. Flores, "Modelo físico y matemático del sistema de suspensión de un cuarto de vehículo," in *15th LACCEI International Multi-Conference for Engineering, Education, and Technology. USA*, 2017. [Online]. Available: https://goo.gl/7yrFEK

[21] ´OHLINS. (2017) Ttx25 mkii,. ´OHLINS. Advanced Suspension Technology. [Online]. Available: https://goo.gl/Kra2dB

[22] A. Espejel Arroyo, "Rediseño de un sistema de suspensión para un auto de competencia mediante adams/car y matlab," Tesis de grado. Universidad Nacional Autónoma de México, 2015. [Online]. Available: https://goo.gl/sTxBg9

[23] M. Giariffa and S. Brisson, "Tech tip: Spring & dampers, episode four. a new understanding," OPTIMUMG. Vehicle dynamics solutions, Tech. Rep., 2017. [Online]. Available: https://goo.gl/kVkg6o

Scientific Paper / Artículo Científico

UNIVERSIDAD POLITÉCNICA SALESIANA ECUADOR
INGENIUS
Revista de Ciencia y Tecnología
https://doi.org/10.17163/ings.n20.2018.10
pISSN: 1390-650X / eISSN: 1390-860X

Access System Using an RFiD Card and Face Verification

Sistema de acceso usando una tarjeta RFiD y verificación de rostro

José Ignacio Vega-Luna[1,*], Francisco Javier Sánchez-Rangel[1], Gerardo Salgado-Guzmán[1], Mario Alberto Lagos-Acosta[1]

Abstract

This paper presents the development of an access system to a data center using a RFiD card and verification of the user's face. The system consists of three input modules and a central module. The objective was to design a system to transmit, from each input module to the central module, the universal unique identifier of the RFiD card or UUID for its acronym in English and the user's face image to consult in a MySQL database and in a directory of photographs if the user can access the corresponding area of the input module. Each input module consists of a Raspberry Pi 3 B+ card, an RFiD card reader, a video camera and a liquid crystal display or LCD for its acronym in English. The central module is composed of the same elements as the input modules and has a touch screen used in the user interface instead of an LCD screen. The communication between the nodes is WiFi, achieving a precision of 99.2% in the verification of the face and a response time of 180 ms using 310 trained photographs.

Keywords: Face verification, MySQL, Raspberry Pi 3 B+, RFiD, touchscreen, video camera.

Resumen

En este trabajo se presenta el desarrollo de un prototipo de sistema de acceso a un centro de datos usando como identificación una tarjeta de radio frecuencia o RFiD y verificación del rostro del usuario. El sistema se compone de tres módulos de entrada y un módulo central. El objetivo fue diseñar un sistema para transmitir, desde cada módulo de entrada al módulo central, el identificador único universal de la tarjeta RFiD o UUID y la imagen del rostro del usuario para consultar en una base de datos MySQL y en un directorio de fotografías si el usuario puede acceder al área correspondiente del módulo de entrada. Cada módulo de entrada consta de una tarjeta Raspberry Pi 3 B+, un lector de tarjetas RFiD, una cámara de video y una pantalla de cristal líquido o LCD. El módulo central se compone de los mismos elementos que los módulos de entrada y cuenta con una pantalla táctil usada en la interfaz de usuario en lugar de una pantalla LCD. La comunicación entre los nodos es wifi, logrando una precisión del 99,2 % en la verificación del rostro y un tiempo de respuesta de 180 ms usando 310 fotografías entrenadas.

Palabras clave: cámara de video, MySQL, pantalla táctil, Raspberry Pi 3 B+, verificación de rostro, RFiD.

[1,*]Digital Systems Area, Department of Electronics, Universidad Autónoma Metropolitana-Azcapotzalco Cd. de México, Méxivo. Author for correspondence ✉: vlji@correo.azc.uam.mx.
https://orcid.org/0000-0002-4226-2936, https://orcid.org/0000-0002-4182-5856,
https://orcid.org/0000-0002-0581-7410, https://orcid.org/0000-0003-0455-007X.

Received: 14-05-2018, accepted after review: 21-06-2018

Suggested citation: Vega-Luna, J. I.; Sánchez-Rangel, F. J.; Salgado-Guzmán, G. and Lagos-Acosta, M. A. (2018). «Access System Using an RFiD Card and Face Verification». Ingenius. N.°20, (july-december). pp. 107-116. doi: https://doi.org/10.17163/ings.n20.2018.10.

1. Introduction

Data processing centers (DPC), also called data centers, are facilities that concentrate resources and equipment necessary for the processing and storage of information, as well as telecommunications equipment for companies and organizations. In data centers, different devices are used to access facilities, including electromagnetic locks, turnstiles, video cameras, motion detectors, identification cards, biometric systems and keyboards to enter a password, among others. Commonly, data centers are divided into sections called bunkers and are periodically audited in order to be certified. An important point that audits consider is the procedures and techniques used in security and access to facilities [1]. Currently there are different solutions for the identification of people to control the access to the bunkers of a data center. Some biometric solutions are based on the recognition of a person's fingerprints, face, hand geometry, iris, retina pattern, voice and signature [2].

This work presents the requirement of a data center operator company. The objective was to have an access system that uses a RFiD card and verification of the user's face to activate the actuator of the access door of the bunker the user is trying to access. Access must have two levels of security. The established requirements were to have a reliable system, easy to locate and use. The use of RFiD cards was required because they are cheap and easy to use. The maximum distance from the bunker farthest to the monitoring office is 65 meters, and 35 meters with line of sight to the wifi access point. The proposed solution consisted of a system composed of three input modules and a central module. The data center has three bunkers in whose entrance doors an input module was installed. The central module was installed in the data center monitoring office. The input modules are responsible for reading the information stored in the RFiD card, capturing the photograph of the user's face, and transmitting the information of the card and JPEG file with the photograph to the central module for validation, using Wi-Fi technology.

An Ethernet segment was not used to transmit the user identification information to the monitoring office so as not to install additional wiring or modify the existing one. Once the information is received, the central module checks the user database to see if the UUID of the RFiD card is authorized to enter the bunker associated with the input module, verifies that the user's face is the one registered in the photograph directory, and registers the date and time of entry request in the database. If both of the above conditions are met, the central module transmits the command to the input module to activate the corresponding door actuator. The input modules and the central module were implemented using a Raspberry Pi 3 B+ card with Raspbian operating system as the basis. The main reason for using the Raspberry Pi card was because there is a large number of applications and libraries developed by the open source community that are easy to install, configure and use in Raspbian [3]. In the system presented here, the use of an RFiD card was implemented as the first security mechanism and the NFC/RFiD 532 device was used to read cards. The technology of near field communication, NFC, arose from the combination of RFiD technology and smart cards. It allows the identification and characterization of people or objects without physical contact using radio waves transmitted by a label. RFiD technology allows the exchange of information between objects located close to each other. The communication with NFC is safer than other technologies since the transmitter and receiver are closely coupled, with a maximum proximity of 10 centimeters, without the need to run an application. In recent years, NFC technology has been used in several ways with mobile phones, on the Internet of Things or IoT and in the field of sensors [4].

Although it was initially decided to use RFiD cards, alternative technologies were explored for the identification of users, including technologies such as rapid response codes or QR and the iBeacon system. QR codes are an improvement to bar codes, they store information in dot matrixes or barcodes in a two-dimensional way [5]. When a mobile device reads a QR code it executes an application to perform a specific action. In the development of this work a combination of RFiD technology and QR codes could be used, but it would be a slightly more expensive and slower system, since in addition to using a method of printing the QR code on RFiD cards, these could not be reused. On the other hand, iBeacon is a protocol used in indoor positioning systems, or IPS, patented by Apple Inc. It is based on low-cost transmitters and low power consumption that indicate their presence to a device with iOS operating system and some devices with Android operating system [6]. There are transmitter providers, called beacons, compatible with iBeacon. Beacons use Bluetooth technology transmitters with low power consumption or BLE for short, or Bluetooth 4.0, which transmit their UUID to mobile electronic devices, allowing a mobile phone or tablet to perform an action or application based on the location of the beacon upon receiving identification, or following up with clients or users of beacons. The iBeacon system is used in mobile commerce, where an application, running on a mobile phone, can find the location of a product associated with a beacon inside a store or a beacon can send offers or promotions to the mobile phone. In other applications, beacons transmit information about nearby stores and restaurants to the mobile phone, as well as waiting times or distribution of points of interest messages according to the phone's location. The iBeacon technology differs from others,

such as NFC/RFiD, in that the transmission made by the beacon is one-way and requires that an application be run on iOS or Android. It could have been an option to use iBeacon in the development of this work, which would imply using a beacon as the user's identifier and an iOS device at each access point to the data center, which would increase the complexity of use, installation and cost of the system [7].

With the explosion of services based on the Internet, or Internet of Things, RFiD technology continues to be used in different developments and applications of identification, including supply chain [8], health care, object localization, home automation, security systems and product delivery in restaurants [9]. Work has been done on access systems to Arduino-based facilities, RFiD cards and MySQL databases. The difference with respect to the presented here is that a Raspberry card of more recent technology and lower cost than Arduino is used [10]. Additionally, the works that have been developed use Ethernet communication to the database and in this work Wi-Fi wireless technology was used, whose implementation is non-intrusive to the data center facilities [11]. Similarly, work has been carried out on access systems for homes, offices, and even vehicles, which use smartphones to emulate NFC cards and NFC PN532 readers [12] such as the one used in this work. In these systems the user must carry a smart phone to identify himself, which is not feasible nor is it an option in the data centers due to the cost and the fact that sometimes the users are visitors. Various works have also been carried out using QR codes or a combination of these with RFiD cards to control access to facilities, for location and navigation systems [13] and for product identification [14] and medical images. Access systems to data centers have even been created combining QR codes and watermarks [15]. The use of QR codes provides a higher level of security than RFiD cards, but the cost of implementation and operation of these systems is high, since once a card with a QR code is used it can not be used for another user and the hardware for printing and reading QR codes is more expensive than an NFC reader. Other works recently carried out for identification, location and access control integrate iBeacon and wifi [16] or Bluetooth LE technologies. These systems have the limitation of using devices with iOS or Android operating system, which makes them more expensive than the one developed in this work.

The verification of the person's face is used as the second security mechanism. Facial recognition began to be used in the 60s. It was a semi-automatic process in which an operator identified the features of the person in two or more photographs and calculated the distances to reference points to compare them with each other. The technological advances of computing in recent years have created an explosion of algorithms, techniques and non-intrusive applications of automated facial recognition that run on a computer to identify a person in a digital image. Taking the image of an unknown person, a profile with the same face in a set of known images must be found, also called training images. This is done with one of two purposes: 1) Verification or authentication of faces, comparing an image of a person's face with another image. The application confirms or denies the identity of the face, the objective is to ensure that the person is who they say they are; and 2) identification or recognition of faces, comparing the image of an unknown face with the images of known faces stored in a database to determine someone's identity. Facial recognition is an area that integrates the following technologies: image processing, computer vision, pattern recognition, neural networks and machine learning [17]. The procedure used by facial recognition systems generally consists of five phases:

- Registration phase, the image of the face of the person to be identified is captured using a camera or a video camera.
- Phase of the image processing, the face alignment is carried out based on some geometric properties and an independent image of the illumination and color range of the original image is obtained.
- Phase of extraction of biometric information, facial characteristics are obtained as a biometric pattern.
- Comparison phase, the biometric pattern compares the pattern of faces stored in the database. It is a 1:N comparison where the percentage of similarity of the person to be identified is determined with respect to the photographs stored in the database.
- Decision making phase, using a matrix of similarities, the person that was found with the highest percentage of similarity of the database is identified using an established range.

In recent times, the use of facial recognition systems has experienced a boom in different types of applications, used to authenticate the owners of mobile devices, in the detection of sleepy or tired drivers, in human trafficking, in risk analysis and in situations in places with a high concentration of people [18]. Microsoft applies facial recognition to access a Windows computer [19], while Apple is trying to have a mechanism in which iOS users can automatically share photos with tagged friends. Facebook and Google have engaged in a war on the design and use of facial recognition algorithms to tag friends and find photos of a person. They aim to achieve the perfect algorithm, recognizing faces much better than the human being. Google introduced, in 2015, the facial recognition

system called FaceNet, with an accuracy of 99.63%, recognizing photos on Google+ [20]. This system uses machine learning, generating a map in a compact Euclidean space from the image of a human face, where the distances correspond directly to the measure of similarity of the face. With this space, the tasks of verification and recognition of an image can be easily performed using standard techniques such as FaceNet vector embeddings. The FaceNet system uses a deep convolutional neuronal network trained with more than 260 million face images. The authors of FaceNet indicate that they have developed the state of the art of facial recognition methods using only 128 bytes for each face and more than 13,000 face images of the Internet to verify if two images are the same person, while the system of recognition YouTube Faces achieves 95.12%. The technology used by Facebook for facial recognition is called DeepFace, it was developed by the Israeli company face.com and released in 2013 [21]. The creators of DeepFace indicate that they can achieve an accuracy of 97.25% when comparing two faces.

In recent years, facial recognition has been used in access systems in data centers. Reliable systems with an acceptable percentage of accuracy can be achieved without using algorithms as sophisticated as those developed by companies such as Google and Facebook, which are proprietary and patented algorithms. There are many open source algorithms that can be used in the operating system of a small, low-cost and powerful computer like the Raspberry Pi 3 B + card. One of these algorithms is the histogram of oriented gradients or HOG, called the HOG algorithm [22]. This algorithm was developed in 2005, it is one of the most advanced and it is continuously improved to optimize it and achieve greater precision. A HOG is a feature descriptor used in computer vision and image processing for the detection of objects. This counts the occurrences of gradient orientation in defined parts of an image. The descriptors can be used as input data or features for a machine learning algorithm. There are open source libraries that implement the phases of a facial recognition system with the HOG algorithm and deep machine learning, which are easy to install and use, significantly reducing the program code [23]. One of these libraries is Face_Recognition and is the one used in this work to verify the face of users. This library uses a trained neural network and is based on dlib, the state of the art tool in face recognition built with deep learning. The authors of Face_Recognition indicate that its accuracy is 99.38% and provides several functions with which you can perform some actions such as finding faces in a photograph, determining the location of the reference points of a face, manipulating the facial features of a face, biometrically coding a face, comparing two coded faces, recognizing faces in real time video and recognizing faces located in a photograph using a directory of photographs of people getting the name of each person. In order to use the Face_Recognition library, the following tools must be installed in Raspian: Python library for picamera (python3-picamera), dlib v19.6 and OpenCV.

On the other hand, a great variety of access systems to data centers has been made through biometric devices. Some of these systems carry out facial recognition using a desktop computer to implement the recognition process [24] and wired communication between the computer and the video camera [25] or webcam. They are efficient, but their cost and size is greater than the one developed in this paper. Other systems of this type are based on reading the iris of the eye [26] using a reader installed in the access door or by means of the user's smartphone. These systems are more secure than those of RFiD cards, QR codes, fingerprint reading or 2D facial recognition, but the cost of the reader is much higher.

2. Materials and methods

The methodology used in the design of this system consisted of dividing it into two components: the input modules and the central module. Subsequently, the system was implemented by choosing the appropriate elements and the lowest cost according to the established requirements. The functional block diagram of the system is shown in Figure 1.

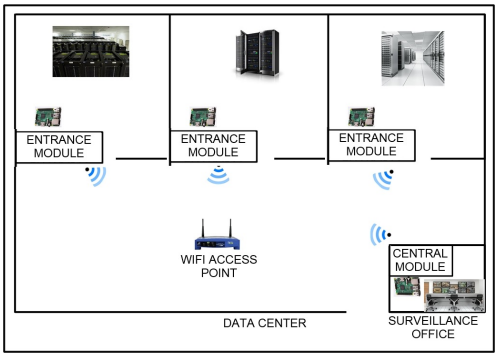

Figure 1. Functional block diagram of the access system

2.1. The input modules

Three input modules were built, all with the same architecture as the one shown in Figure 2. The main functions of these modules are the following: continuously explore if a card is found under the reach of the RFiD reader and read the UUID, capture the image of the face of the person trying to access, transmit the information read from the card and the photograph of the person in a JPEG file to the central module, and wait for the response from the central module to allow or deny access to the user. Each input module

consists of: a Raspberry Pi 3 B + card, an RFiD card reader, a video camera, a 2x16 LCD screen and an output interface.

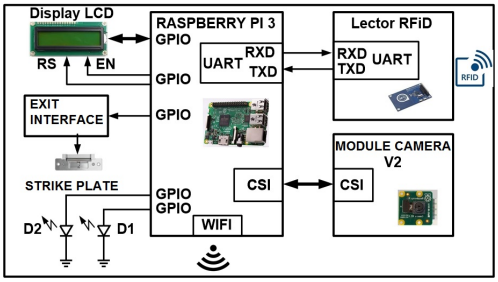

Figure 2. Block diagram of the input modules

The Raspberry Pi 3 B + card used in this module has the following hardware resources: 1 GB of RAM, 40 GPIO terminals, serial interface for camera, or CSI, DSI port for touch screen, Gigabit Ethernet port, SD memory slot and a Wi-Fi interface. The RFiD card reader used is the NFC/RFiD PN532 device. This reader is one of the most used in applications that use NFC technology, cards and RFiD tags of 13.56 MHz, since its main integrated circuit is embedded in many smartphones. It can write RFiD cards and labels type 1 to 4 and integrate an antenna whose range is 10 centimeters.

There is a large number of open source tools to make applications with the NFC/RFiD PN532. One of these tools is the libnfc library. In both the input modules and the central module, the RFiD reader was connected to the UART port of the Raspberry Pi and version 1.7.0 of the libnfc library was downloaded. Before installing and configuring libnfc, in the core of the Raspberry Pi operating system, the UART was disabled as a console port using the paspi-config tool and editing the /boot/config.txt file. Next, the libnfc library was installed and built using the following commands: sudo make clean and sudo make install all, which created the corresponding drivers, documentation files, binaries and executables. The input modules also contain a camera module for Raspberry V2 connected to the CSI interface of the Raspberry Pi 3 B+. This camera module has a high-resolution Sony IMX219 sensor of 8 megapixels. It allows the capture of photographs with a maximum resolution of 3238 x 2464 and high definition video.

There are open source libraries to use the camera and manipulate photos and video that can be invoked from Raspbian or from a program in Python. The camera can be controlled using the raspinstall command. However, in this work the Python python-picamera library was used in case that, in the future, it is necessary to modify the capture characteristics of photographs or video in the system. The camera of the input modules was enabled through Raspbian's raspi-config tool and later the python-picamera library was installed using the command: sudo apt-get install python3-picamera. Once the above was done, the camera.capture function ('file.jpg') could be used to capture an image in a JPEG file. The program that runs on the capture nodes was made in Phyton 3.6 and performs the following actions: configures timers, the UART port, Wi-Fi interface, GPIO terminals and peripheral devices, RFiD reader, video camera and LCD screen, display the message that tells the user to place the RFiD card in the reader on the LCD screen, and then enters a continuous cycle where the RFiD reader scans every 0.5 seconds by executing the nfc-pool_8c function.

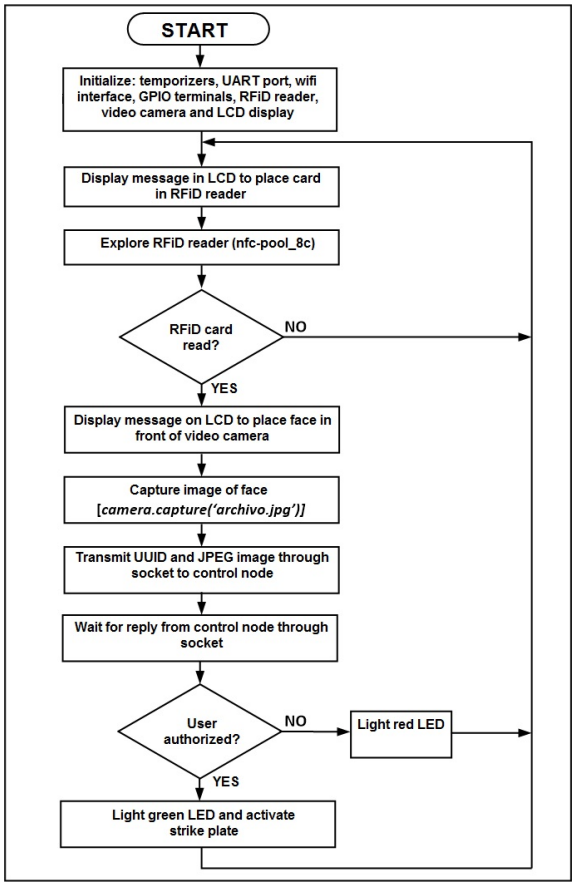

Figure 3. Flow diagram of the program of the input modules

The communication between the input and the control modules was carried out using message exchange with sockets under the client-server scheme. The input modules are the clients and the control module is the server. When the reader detects a card, it displays a message on the LCD screen asking the user to stand in front of the video camera and captures the image of the person's face in a JPEG file. Subsequently, the program transmits the UUID of the RFiD card and the JPEG file to the central module through a socket. Once the above is done, the program waits for the response of the central module in the socket. If the an-

swer indicates that the user is authorized to enter, the input module activates the actuator of the access door, through the interface connected to a GPIO terminal of the Raspberry card, and turns on a green LED (D1), connected to another GPIO terminal, for 3 seconds. If the user is not authorized, it lights a red LED (D2) intermittently for 5 seconds. Figure 3 shows the flow diagram of the program.

To be able to use sockets from Python, the corresponding library must be installed by executing the following command: sudo apt-get install socket. The output interface that controls the input gate actuator was connected to a GPIO terminal on the Raspberry card as shown in Figure 4.

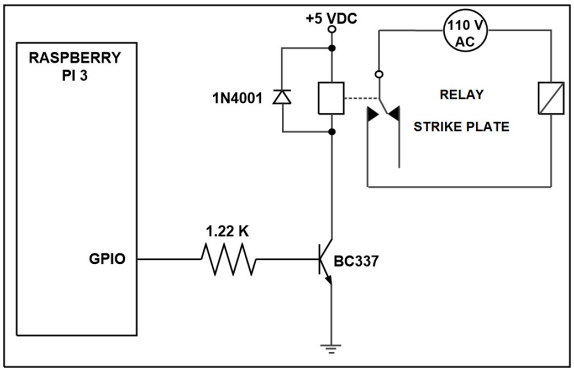

Figure 4. Entrance door actuator exit interface.

2.2. The central module

The central module consists of the following components: a Raspberry Pi 3 B+ card, an RFiD card reader, a video camera and a 3.5" Pi+TFT touch screen. Figure 5 shows the block diagram of the architecture of the central module.

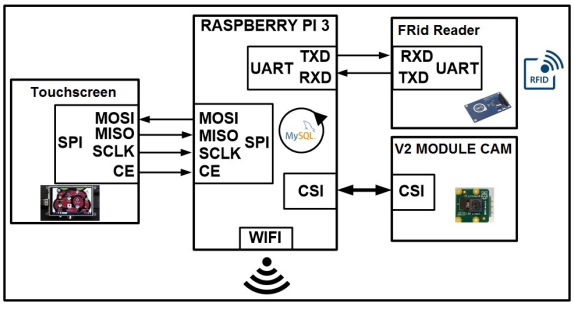

Figure 5. Block diagram of the central module.

The programming of the central module was carried out in Phyton 3.6 and it is divided into three parts: the main program, the communication routine with the input modules and the routine of the user interface. The main program configures timers, the UART port, the Wi-Fi interface and peripheral devices, RFiD reader, video camera and touch screen and invokes the two routines of the system, as indicated in the flow diagram in Figure 6.

In this module a database was created, managed with MySQL, which stores the information of authorized users to access the bunkers and a directory with the photographs of the face of previous users.

The communication routine with the input modules executes a program in the background that performs the following functions: 1) Create a socketthrough which it receives from the input modules the UUID and the JPEG file. 2) Access the MySQL database to determine if the user is authorized to enter the corresponding area. 3) Invokes the routine that verifies that the user's face is in the photo directory. 4) Update the user record in the MySQL database with date and time of entry. 5) Transmit the message to the input module to activate the door actuator or deny entry. 6) Update the log of access attempts by storing the JPEG file.

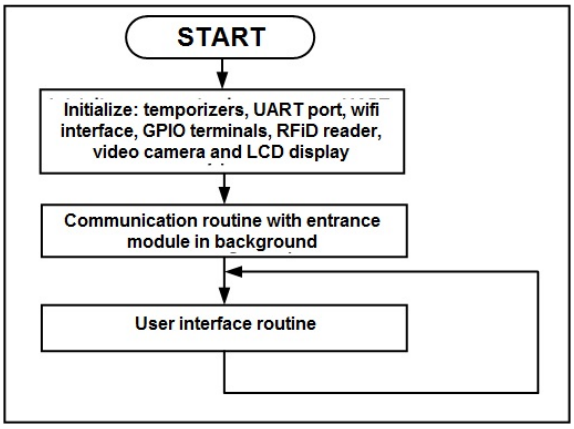

Figure 6. Flow chart of the main program of the central module.

Figure 7 shows the flow diagram of this routine. Both the database and the directory of coded and trained photographs reside in the Raspberry Pi 16 GB SD card. A table containing user records was created in the database. Each record stores the UUID of the assigned RFiD card, number of doors to which it has access, name, company and user email. To create the database and user table the following tasks were carried out:

1.- Installation of the MySQL server and client, as well as the Python API to access MySQL.

2.- Creation of the database executing the following commands: mysql -u root -p, mysql> CREATE DATABASE RFID_DB; CREATE TABLE users_tbl (id INT NOT NULL PRIMARY KEY AUTO_INCREMENT, UUID VARCHAR(20), doors VARCHAR(20), name VARCHAR(20), last name VARCHAR(30), company VARCHAR(20), email VARCHAR(30)).

Once the database was created, the program in Python was made to access it. Python uses an object or data structure, called a cursor, to access the data in the table. This object allows operations to create, read, update and remove records in the database. The program executes the following general actions:

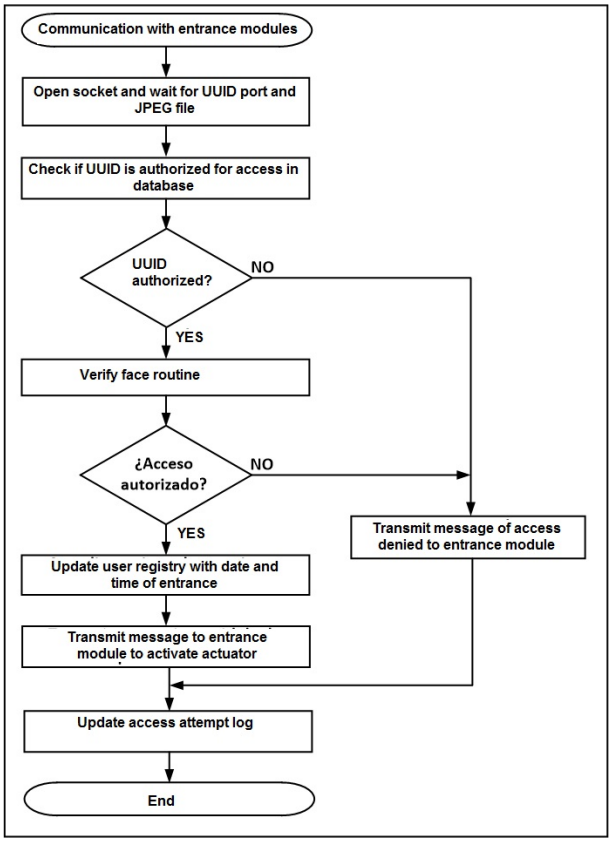

Figure 7. Flow diagram of communications with the input modules

1.- Import the Python API for MySQL: import MySQLdb.

2.- Make the connection to the database: db = MySQLdb.connect ("localhost", "root", "password", "RFID_DB").

3.- Define the cursor object: cursor = db.cursor ().

4.- Wait for the option selected by the user in the graphic interface.

5.- Depending on the option, define one of the following SQL query's: cursor.execute ("INSERT INTO users-tbl"), cursor.execute ("SELECT * FROM users_tbl"), cursor.execute ("UPDATE users_tbl SET") or cursor.execute ("DELETE FROM users_tbl WHERE")

6.- Execute the query: db.commit ().

In the photo directory, the name of each file corresponds to the name of the user registered in the MySQL database. The routine that checks if the user's face is in the photo directory performs the following actions: loads the image of the face received from an input module in a buffer using the face_recognition.load_image_file function, encodes and learns to recognize the stored image in the buffer using the function face_recognition.face_encodings and enters a cycle where it compares the encoded image of the buffer with each image of the directory of coded photographs. The cycle ends when it finds equivalence between the two images analyzed or when it explored the entire directory without finding equivalence. The comparison is made through the function face_recognition.compare_faces, which obtains, if successful, the name of the user of the photograph. If the name obtained is equal to the name read from the user's record in the database, it returns to the routine that invoked it authorizing access to the user, as shown in the flow diagram in Figure 8. It was considered that the image received from the input module contains only one face, otherwise the face_recognition.face_locations function would have to be used to find the faces in the image and code them individually.

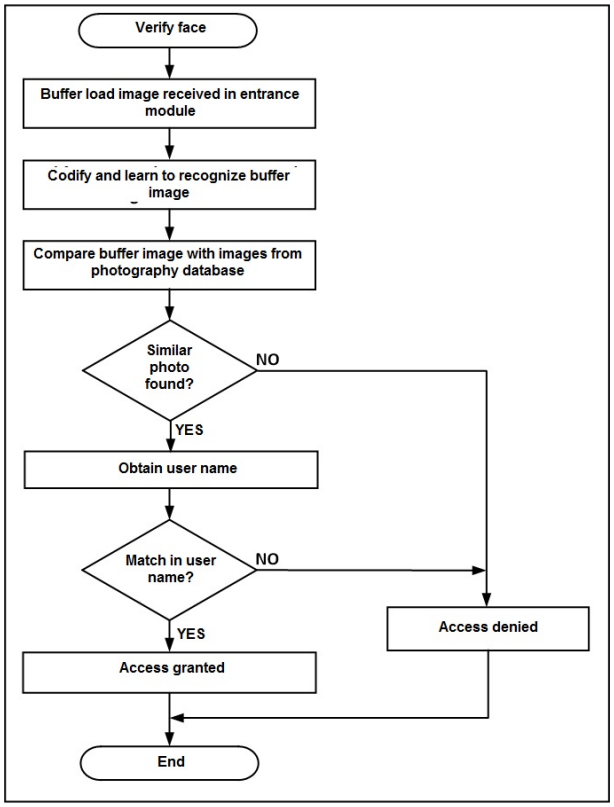

Figure 8. Flow diagram of the face verification routine

The routine that implements the graphical user interface, allows for access and management of the

database using the touch screen. The screen used in the central module is the 3.5" Pi+TFT device which has a resolution of 480 x 320 and was connected to the SPI port of the Raspberry Pi card. In the user interface, the administrator can perform the following operations: uploads, deletions and changes of users, as well as showing the registered users and the log of access attempts. The RFiD card reader and the validation module camera are used when registering or making changes to a user's registry. The user interface was made using pygame. The pygame tool is a set of libraries that can be used in a Python program for the implementation of videogames, multimedia programs and graphical user interfaces, since it allows to display text, images and sounds on a touch screen and control the position of the cursor. This tool is installed by default with the Raspbian version for Raspberry Pi. The IP address of the Wi-Fi interface of each input module is fixed and is used by the central module to determine the door number which the user is trying to access.

3. Results and discussion

Four groups of tests were carried out. The first group aimed to measure the RFiD reader's reach for the input modules. By placing 50 cards in the module reader, it was determined that the range is 14 centimeters, a little more than indicated in the manufacturer's specifications. The second group of tests aimed to store the photographs of 50 users in the central module's directory and train the neural network. The average size of each photograph was 110 KB. The third group of tests aimed to determine the accuracy of the face verification system of users registered in the database. This group of tests was carried out in several phases. In the first phase, the directory of trained photographs stored 50 faces. In each subsequent phase, 20 photographs were added, leading to a total of 310. In each phase, 40 different faces were verified. With some faces, the recognition was not successful despite it being registered in the central module. The number of unsuccessful matches led, as a consequence, to an accuracy of 96.3% in the first phase, which increased as the number of photographs trained increased until reaching 99.2% as shown in the graph in Figure 9.

The fourth group of tests aimed to measure the response time of the system. To carry out these tests in each of the phases of the previous test group, the face capture time of a person registered in the database and the time until the central module received a response were both recorded in a file in the input module once the authorized person was verified. The response time in the first phase was 132 ms on average. It increased to 180 ms in the last phase, an almost imperceptible change for the user, as indicated in the graph in Figure 10. The photographs of the directory of the central module were taken with enough ambient light, from the front, without glasses, poses or objects preventing a clear view of the face. It is recommended that when registering new users, several photographs of the face are captured using different expressions, allowing the system to be more tolerant and in order to improve both accuracy and response time. The implementation of this work did not require installing additional wiring for data transmission or modifying the existing one. The central module is installed in a data center control office, this makes it more practical than the commercially available alternatives that use wired communication. The cost of the system is $350.00 USD, lower than existing commercial alternatives, which cost $1700.00 USD on average.

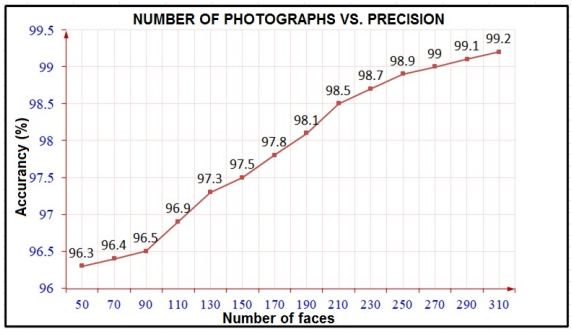

Figure 9. Accuracy of the system with different amounts of faces included in training

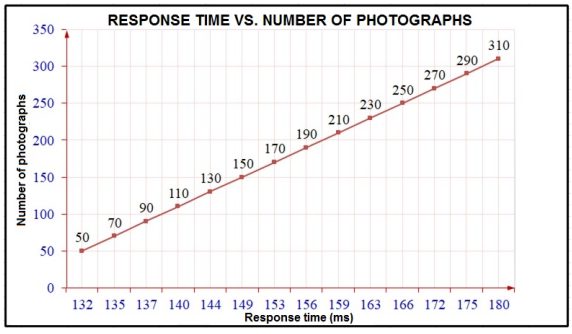

Figure 10. System response time

4. Conclusions

The result of this work was an access system with a double safety mechanism which is more robust than those commercially available that use only one mechanism. It was built using the latest technology and low-cost components, open source software and communication via WiFi, which does not impact the data center facilities, resulting in a practical application that meets the established requirements. The reading range of RFiD cards achieved was 14 centimeters. In

face verification, 99.2% accuracy and 180 ms response time were achieved using 310 trained photographs.

Future works

With the percentage of accuracy and response time achieved, the data center requested a second version that incorporates the following features: 1) Incorporate a web server to the central module and a touch screen in the input modules so that the administrator can access the user database and photo directory from any input module and 2) Incorporate a fingerprint reader in all modules to have an additional level of security. These functionalities are feasible to perform with the current architecture of the system modules.

Acknowledgements

We appreciate the support provided by the Electronics Department at Universidad Autónoma Metropolitana-Azcapotzalco.

References

[1] M. V. M. Lima, R. M. F. Lima, and F. A. A. Lins, "A multi-perspective methodology for evaluating the security maturity of data centers," in *2017 IEEE International Conference on Systems, Man, and Cybernetics (SMC)*, Oct 2017. DOI: https://doi.org/10.1109/SMC.2017.8122775, pp. 1196–1201.

[2] M. Levy and J. O. Hallstrom, "A new approach to data center infrastructure monitoring and management (dcimm)," in *2017 IEEE 7th Annual Computing and Communication Workshop and Conference (CCWC)*, Jan 2017. textscdoi: https://doi.org/10.1109/CCWC.2017.7868412, pp. 1–6.

[3] I. B. Mustaffa and S. F. B. M. Khairul, "Identification of fruit size and maturity through fruit images using opencv-python and rasberry pi," in *2017 International Conference on Robotics, Automation and Sciences (ICORAS)*, Nov 2017. DOI: https://doi.org/10.1109/ICORAS.2017.8308068, pp. 1–3.

[4] J. Mihal'ov and M. Hulič, "Nfc/rfid technology using raspberry pi as platform used in smart home project," in *2017 IEEE 14th International Scientific Conference on Informatics*, Nov 2017. DOI: https://doi.org/10.1109/INFORMATICS.2017.8327257, pp. 259–264.

[5] N. Goel, A. Sharma, and S. Goswami, "A way to secure a qr code: Sqr," in *2017 International Conference on Computing, Communication and Automation (ICCCA)*, May 2017. DOI: https://doi.org/10.1109/CCAA.2017.8229850, pp. 494–497.

[6] S. Menon, A. George, N. Mathew, V. Vivek, and J. John, "Smart workplace – using ibeacon," in *2017 International Conference on Networks Advances in Computational Technologies (NetACT)*, July 2017. DOI: https://doi.org/10.1109/NETACT.2017.8076803, pp. 396–400.

[7] X. Li, D. Xu, X. Wang, and R. Muhammad, "Design and implementation of indoor positioning system based on ibeacon," in *2016 International Conference on Audio, Language and Image Processing (ICALIP)*, July 2016. DOI: https://doi.org/10.1109/ICALIP.2016.7846648, pp. 126–130.

[8] M. Chamekh, S. E. Asmi, M. Hamdi, and T. H. Kim, "Context aware middleware for rfid based pharmaceutical supply chain," in *2017 13th International Wireless Communications and Mobile Computing Conference (IWCMC)*, June 2017. DOI: https://doi.org/10.1109/IWCMC.2017.7986576, pp. 1915–1920.

[9] K. B. Eric and W. H. Ya, "Iot based smart restaurant system using rfid," in *4th International Conference on Smart and Sustainable City (ICSSC 2017)*, June 2017. DOI: https://doi.org/10.1049/cp.2017.0123, pp. 1–6.

[10] M. Andriansyah, M. Subali, I. Purwanto, S. A. Irianto, and R. A. Pramono, "e-ktp as the basis of home security system using arduino uno," in *2017 4th International Conference on Computer Applications and Information Processing Technology (CAIPT)*, Aug 2017. DOI: https://doi.org/10.1109/CAIPT.2017.8320693, pp. 1–5.

[11] S. Nath, P. Banerjee, R. N. Biswas, S. K. Mitra, and M. K. Naskar, "Arduino based door unlocking system with real time control," in *2016 2nd International Conference on Contemporary Computing and Informatics (IC3I)*, Dec 2016. DOI: https://doi.org/10.1109/IC3I.2016.7917989, pp. 358–362.

[12] J. Cui, D. She, J. Ma, Q. Wu, and J. Liu, "A new logistics distribution scheme based on nfc," in *2015 International Conference on Network and Information Systems for Computers*, Jan 2015. DOI: https://doi.org/10.1109/ICNISC.2015.48, pp. 492–495.

[13] W. Xiao-Long, W. Chun-Fu, L. Guo-Dong, and C. Qing-Xie, "A robot navigation method based on rfid and qr code in the warehouse," in *2017 Chinese Automation Congress (CAC)*, Oct 2017. DOI: https://doi.org/10.1109/CAC.2017.8244199, pp. 7837–7840.

[14] H. Keni, M. Earle, and M. Min, "Product authentication using hash chains and printed qr codes," in *2017 14th IEEE Annual Consumer Communications Networking Conference (CCNC)*, Jan 2017. DOI: https://doi.org/10.1109/CCNC.2017.7983126, pp. 319–324.

[15] P. Pramkeaw, T. Ganokratanaa, and S. Phatchuay, "Integration of watermarking and qr code for authentication of data center," in *2016 12th International Conference on Signal-Image Technology Internet-Based Systems (SITIS)*, Nov 2016. DOI: https://doi.org/10.1109/SITIS.2016.111, pp. 669–672.

[16] H. Zou, Z. Chen, H. Jiang, L. Xie, and C. Spanos, "Accurate indoor localization and tracking using mobile phone inertial sensors, wifi and ibeacon," in *2017 IEEE International Symposium on Inertial Sensors and Systems (INERTIAL)*, March 2017. DOI: https://doi.org/10.1109/ISISS.2017.7935650, pp. 1–4.

[17] Z. Yu, F. Liu, R. Liao, Y. Wang, H. Feng, and X. Zhu, "Improvement of face recognition algorithm based on neural network," in *2018 10th International Conference on Measuring Technology and Mechatronics Automation (ICMTMA)*, Feb 2018. DOI: https://doi.org/10.1109/ICMTMA.2018.00062, pp. 229–234.

[18] N. Mokoena, H. D. Tsague, and A. Helberg, "2d methods for pose invariant face recognition," in *2016 International Conference on Computational Science and Computational Intelligence (CSCI)*, Dec 2016. DOI: https://doi.org/10.1109/CSCI.2016.0163, pp. 841–846.

[19] D. Goldman. (2015) Microsoft will let you unlock windows 10 with your face. CNN tech. [Online]. Available: https://goo.gl/tgo8pM

[20] F. Schroff, D. Kalenichenko, and J. Philbin, "Facenet: A unified embedding for face recognition and clustering," in *2015 IEEE Conference on Computer Vision and Pattern Recognition (CVPR)*, June 2015. DOI: https://doi.org/10.1109/CVPR.2015.7298682, pp. 815–823.

[21] S. Srisuk and S. Ongkittikul, "Robust face recognition based on weighted deepface," in *2017 International Electrical Engineering Congress (iEECON)*, March 2017. DOI: https://doi.org/10.1109/IEECON.2017.8075885, pp. 1–4.

[22] M. Wiglasz and L. Sekanina, "Evolutionary approximation of gradient orientation module in hog-based human detection system," in *2017 IEEE Global Conference on Signal and Information Processing (GlobalSIP)*, Nov 2017. DOI: https://doi.org/10.1109/GlobalSIP.2017.8309171, pp. 1300–1304.

[23] J. Zeng, X. Zhao, C. Qin, and Z. Lin, "Single sample per person face recognition based on deep convolutional neural network," in *2017 3rd IEEE International Conference on Computer and Communications (ICCC)*, Dec 2017. DOI: https://doi.org/10.1109/CompComm.2017.8322819, pp. 1647–1651.

[24] X. Chen, L. Qing, X. He, J. Su, and Y. Peng, "From eyes to face synthesis: a new approach for human-centered smart surveillance," *IEEE Access*, vol. 6, pp. 14 567–14 575, 2018. DOI: https://doi.org/10.1109/ACCESS.2018.2803787.

[25] A. H. M. Amin, N. M. Ahmad, and A. M. M. Ali, "Decentralized face recognition scheme for distributed video surveillance in iot-cloud infrastructure," in *2016 IEEE Region 10 Symposium (TENSYMP)*, May 2016. DOI: https://doi.org/10.1109/TENCONSpring.2016.7519389, pp. 119–124.

[26] Ş. Karahan and Y. S. Akgül, "Eye detection by using deep learning," in *2016 24th Signal Processing and Communication Application Conference (SIU)*, May 2016. DOI: https://doi.org/10.1109/SIU.2016.7496197, pp. 2145–2148.

UNIVERSIDAD POLITÉCNICA SALESIANA ECUADOR
INGENIUS
Revista de Ciencia y Tecnología
pISSN: 1390-650X / eISSN: 1390-860X

Guidelines for publication in Ingenius Journal

1. General Information

Ingenius is a scientific publication of the *Universidad Politécnica Salesiana* of Ecuador, published since January 2007, with a fixed biannual periodicity, specialized in Mechanical Engineering, Electrical Engineering, Electronics, Computer Science and its integration in what is now known as Mechatronics; these lines of action strengthen areas such as automation, control, robotics, among others..

It is a scientific journal, which uses the peer-review system, under double-blind review methodology, according to the publication standards of the Institute of Electrical and Electronics Engineers (IEEE). Compliance with this system allows authors to guarantee an objective, impartial and transparent review process, which facilitates the publication of their inclusion in reference databases, repositories and international indexing.

Ingenius is indexed in the directory and selective catalog of the Regional Online Information System for Scientific Journals of Latin America, the Caribbean, Spain and Portugal (Latindex), in the Directory of Journals of Open Access DOAJ, In the Information Matrix for the Analysis of Journals, MIAR, In the Ibero-American Network of Innovation and Scientific Knowledge, REDIB and in repositories, libraries and specialized catalogs of Latin America.

The journal is published in a double version: printed (ISSN: 1390-650X) and digital (e-ISSN: 1390-860X), in Spanish, each work being identified with a DOI (Digital Object Identifier System. The articles sent to Ingenius magazine must comply with the following criteria:

2. Scope and policy

2.1. Theme

Original contributions in Mechanical Engineering, Electrical and Electronic Engineering, Computer Science and its integration in what is now known as Mechatronics, as well as related areas: Automation, Control, Domotics, Robotics in their different fields of action and all those related disciplines with the same central theme.

All the work carried out by national or foreign researchers may be published once they meet the required scientific quality criteria.

2.2. Contributions

Ingenius Journal preferably publishes articles related to empirical research, and also reports of technological development, proposals for models and innovations, products for the elaboration of graduate and postgraduate thesis that contribute to the field of science and technology, as well as select revisions of literature. (state-of-the-art).

- **Research:** 5,000 to 6,500 words of text, including title, abstracts, descriptors, charts and references.
- **Reports:** 5,000 to 6,500 words of text, including title, abstracts, charts and references.
- **Reviews:** 6,000 to 7,000 words of text, including charts and references. Current, selective and justified references, would be specially valued from among 40 works

The Ingenius Journal publishes original and unpublished works written in Spanish and English, they may not have been published

through any printed or electronic media, nor be in the process of arbitration or publication.

Every article will be subjected to a rigorous arbitration process; the evaluation of the article will be made according to criteria of originality, relevance, relevance, contributions, scientific rigor and compliance with established editorial guidelines.

Being an arbitrated publication, the Editorial Board approves its publication based on the concept of specialized pairs. The reception of a document does not imply commitment of publication.

It is essential to present a letter of presentation and grant of rights which can be downloaded from: <
urlhttps://goo.gl/ZNkMRD>.

Contributions must be exclusively sent and through the OJS (Open Journal Sys-tem) <`https://goo.gl/JF7dWT`>. In which all authors must previously register as a user. For any consultation of the procedure you should contact:

<revistaingenius@ups.edu.ec>,
<jcalle@ups.edu.ec> ó
<mquinde@ups.edu.ec>.

3. Presentation and structure of the manuscripts

For those works that are empirical investigations, the manuscripts will follow the IMRDC structure (Introduction, Materials and Methods, Results and Discussion and Conclusions), being optional the Notes and Supports. Those papers that, on the contrary, deal with reports, studies, proposals and reviews may be more flexible in their epigraphs, particularly in material and methods, analysis, results, discussion and conclusions. In all typologies of works, references are mandatory.

Articles may be written on Microsoft Word (.doc or .docx) or LaTeX(.tex). The template to be used can be downloaded from the journal's website, a, <`https://goo.gl/gtCg6m`>, while for LaTeX in <`https://goo.gl/hrHzzQ`>, it is necessary that the file be anonymised in Properties of File, so that the author(s) ID is not displayed.

Figures, Graphs and/or Illustrations, as well as Charts shall be numbered sequentially including an explanatory description for each. The equations included in the article must also be numbered; the figures, charts and equations must be cited in the text.

Use space after point, commas and question marks.

Use "enter" at the end of each paragraph and title heading. Do not use .enter.anywhere else, let the word processor program automatically break the lines.

Do not center headings or subheadings as they should be aligned to the left.

Charts must be created in the same program used for the document body, but must be stored in a separate file. Use tabs, not spaces, to create columns. Remember that the final size of printed pages will be 21 x 28 cm, so the tables must be designed to fit the final print space.

3.1. Structure of the manuscripts

3.1.1. Presentation and cover letter

1. **Título (español) / Title (inglés):** Concise but informative, in Spanish on the front line and in English on the second, when the article is written in Spanish and vice versa if it is written in English.
2. **Authors and affiliations:** Full name and surname of each author, organized by order of priority and their institutional affiliation with reference to the end of the first sheet, where it must include:

Dependency to which belongs within the institution, Institution to which he/she belongs, country, ORCID. A maximum of 5 authors will be accepted, although there may be exceptions justified by the complexity and extent of the topic.

3. **Abstract (Spanish) / Abstract (English):** It will have a maximum extension of 230 words, first in Spanish and then in English. : 1) Justification of the topic; 2) Objectives; 3) Methodology and sample; 4) Main results; 5) Main conclusions.
4. **Keywords (Spanish) / Keywords (English):** 6 descriptors must be presented for each language version directly related to the subject of the work. The use of the key words set out in UNESCO's Thesaurus will be positively valued.
5. **Presentation (Cover Letter):** A statement that the manuscript is an original contribution, not submission or evaluation process in another journal, with the confirmation of the signatory authors, acceptance (if applicable) of formal changes in the manuscript according to the guidelines and partial assignment of rights to the publisher, according to the format established in: <https://goo.gl/ZNkMRD>

3.1.2. Manuscript

1. **Título (español) / Title (inglés):** Concise but informative, in Spanish on the front line and in English on the second, when the article is written in Spanish and vice versa if it is written in English.
2. **Authors and affiliations:** Full name and surname of each author, organized by order of priority and their institutional affiliation with reference to the end of the first sheet, where it must include: Dependency to which belongs within the institution, Institution to which he/she belongs, country, ORCID. A maximum of 5 authors will be accepted, although there may be exceptions justified by the complexity and extent of the topic.
3. **Abstract (Spanish) / Abstract (English):** It will have a maximum extension of 230 words, first in Spanish and then in English. : 1) Justification of the topic; 2) Objectives; 3) Methodology and sample; 4) Main results; 5) Main conclusions.
4. **Keywords (Spanish) / Keywords (English):** 6 descriptors must be presented for each language version directly related to the subject of the work. The use of the key words set out in UNESCO's Thesaurus will be positively valued.
5. **Introduction:** It should include the problem statement, context of the problem, justification, rationale and purpose of the study, using bibliographical citations, as well as the most significant and current literature on the topic at national and international level.
6. **Material and methods:** It must be written so that the reader can easily understand the development of the research. If applicable, it will describe the methodology, the sample and the form of sampling, as well as the type of statistical analysis used. If it is an original methodology, it is necessary to explain the reasons that led to its use and to describe its possible limitations.
7. **Analysis and results:** It will try to highlight the most important observations, describing, without making value judgments, the material and methods used. They will appear in a logical sequence in the text and the essential charts and figures avoiding the duplication of data.
8. **Discussion and Conclusions:** It will summarize the most important findings,

relating the observations themselves to relevant studies, indicating contributions and limitations, without adding data already mentioned in other sections. It should also include deductions and lines for future research.

9. **Supports and acknowledgments (optional):** The Council Science Editors recommends the author (s) to specify the source of funding for the research. Priority will be given to projects supported by national and international competitive projects.
10. **The notes (optional):** will go, only if necessary, at the end of the article (before the references). They must be manually annotated, since the system of footnotes or the end of Word is not recognized by the layout systems. The numbers of notes are placed in superscript, both in the text and in the final note. The numbers of notes are placed in superscript, both in the text and in the final note. No notes are allowed that collect simple bibliographic citations (without comments), as these should go in the references.
11. **References:** Bibliographical citations should be reviewed in the form of references to the text. Under no circumstances should references mentioned in the text not be included. Their number should be sufficient to contextualize the theoretical framework with current and important criteria. They will be presented sequentially in order of appearance, as appropriate following the format of the IEEE.

3.2. Guidelines for Bibliographical references

Journal articles:

[1] J. Riess, J. J. Abbas, "Adaptive control of cyclic movements as muscles fatigue using functional neuromuscular stimulation". IEEE Trans. Neural Syst. Rehabil. Eng vol. 9, pp.326–330, 2001. [Onine]. Available: https://doi.org/10.1109/7333.948462

Books:

[1] G. O. Young, "Synthetic structure of industrial plastics" in Plastics, 2nd ed., vol. 3, J. Peters, Ed. New York: McGraw–Hill, 1964, pp. 15–64.

Technical reports:

[1] M. A. Brusberg and E. N. Clark, "Installation, operation, and data evaluation of an oblique–incidence ionosphere sounder system," in Radio Propagation Characteristics of the Washington–Honolulu Path, Stanford Res. Inst., Stanford, CA, Contract NOBSR–87615, Final Rep., Feb. 1995, vol. 1

Articles presented in confeences (unpubished):

[1] Vázquez, Rolando, Presentación curso "Realidad Virtual". National Instruments. Colombia, 2009.

Articles of memories of Conferences (Published):

[1] L. I. Ruiz, A. García, J. García, G. Taboada. "Criterios para la optimización de sistemas eléctricos en refinerías de la industria petrolera: influencia y análisis en el equipo eléctrico," IEEE CONCAPAN XXVIII, Guatemala 2008.

Thesis:

[1] L.M. Moreno, "Computación paralela y entornos heterogéneos," Tesis doctoral, Dep. Estadística, Investigación Operativa y Computación, Universidad de La Laguna, La Laguna, 2005.

Guidelines:

[1] IEEE Guide for Application of Power Apparatus Bushings, IEEE Standard C57.19.100–1995, Aug. 1995.

Patents:

[1] J. P. Wilkinson, "Nonlinear resonant cir-

cuit devices, U.S. Patent 3 624 125, July 16, 1990.

Manuals:

[1] Motorola Semiconductor Data Manual, Motorola Semiconductor Products Inc., Phoenix, AZ, 1989.

Internet resources:

[1] E. H. Miller, "A note on reflector arrays" [Online]. Available. https://goo.gl/4cJkCF

3.3. Epigraphs, Figures and Charts

The epigraphs of the body of the article will be numbered in Arabic. They should go without a full box of capital letters, neither underlined nor bold. The numbering must be a maximum of three levels: 1. / 1.1. / 1.1.1. At the end of each numbered epigraph will be given an enter to continue with the corresponding paragraph.

The charts must be included in the text according to order of appearance, numbered in Arabic and subtitled with the description of the content, the subtitle should go at the top of the table justified to the left.

Figures can be linear drawings, maps or black and white halftone or color photographs in 300 dpi resolution. Do not combine photographs and line drawings in the same figure.

Design the figures so that they fit eventually to the final size of the journal 21 x 28 cm. Make sure inscriptions or details, as well as lines, are of appropriate size and thickness so that they are not illegible when they are reduced to their final size (numbers, letters and symbols must be reduced to at least 2.5 mm in height After the illustrations have been reduced to fit the printed page). Ideally, the linear illustrations should be prepared at about a quarter of their final publication size.

Different elements in the same figure should be spelled a, b, c, etc.

Photographs should be recorded with high contrast and high resolution. Remember that photographs frequently lose contrast in the printing process. Line drawings and maps should be prepared in black.

The text of the figures and maps must be written in easily legible letters.

If the figures have been previously used, it is the responsibility of the author to obtain the corresponding permission to avoid subsequent problems related to copyright.

Each figure must be submitted in a separate file, either as bitmap (.jpg, .bmp, .gif, or .png) or as vector graphics (.ps, .eps, .pdf).

4. Submission process

The manuscript must be sent through the OJS system of the journal, <`https://goo.gl/JF7dWT`>,the manuscript should be uploaded as an original file in .pdf without author data and anonymized according to the above; In complementary files the complete manuscript must be loaded in .doc or .docx (Word file), that is to say with the data of the author (s) and its institutional ascription; Also the numbered figures should be uploaded in independent files according to the corresponding in the manuscript (as bitmap .jpg, .bmp, .gif, or .png or as vector graphics .ps, .eps, .pdf). It is also obligatory to upload the cover letter and grant of rights as an additional file.

All authors must enter the required information on the OJS platform and only one of the authors will be responsible for correspondence.

Once the contribution has been sent the system will automatically send the author for correspondence a confirmation email of receipt of the contribution.

5. Editorial process

Once the manuscript has been received in OJS, a first check by the editorial team of the following points:

- The topic is in accordance with the criteria of the journal.
- Must have the IMRDC structure.
- Must be in the INGENIUS format.
- Must use the IEEE citation format.
- All references should be cited in the text of the manuscript as well as charts, figures and equations.
- The manuscript is original; for this, software is used to determine plagiarism.

The assessment described above can take up to 4 weeks.

If any of the above is not complete or there is inconsistency, an email will be sent to the author to make the requested corrections.

The author will make the corrections and resend the contribution through an email in response to the notification and will also upload the corrected manuscript into OJS supplementary files.

The editorial team will verify that the requested corrections have been incorporated, if it complies, the manuscript will start the second part of the process that may be followed by the author through OJS, otherwise the author will be notified and the manuscript will be archived.

The second phase of the process consists of the evaluation under the methodology of double-blind review, which includes national and foreign experts considering the following steps:

- The editor assigns two or more reviewers for the article.
- After reviewing the article, the reviewers will submit the evaluation report with one of the following results.
  - Publishable
  - Publishable with suggested changes
  - Publishable with mandatory changes
  - Non publishable
- The editor once received the evaluation by the reviewers will analyze the results and determine if the article is accepted or denied.
- If the article is accepted, the author will be notified to make corrections if required and the corresponding editorial process will be continued.
- If the article is denied, the author will be notified and the manuscript will be archived.
- In the two previous cases the result of the evaluation of the reviewers and their respective recommendations will be sent.

The second phase of the process lasts at least 4 weeks, after which they will be notified to the author giving instructions to continue with the process.

6. Publication

The INGENIUS Journal publishes two issues per year, on January 1st and July 1st, so it is important to consider the dates for sending the articles and their corresponding publication. Articles received until October will be considered for the January publication and those received until April for the July publication.

UNIVERSIDAD POLITÉCNICA SALESIANA DEL ECUADOR
Javier Herrán Gómez, sdb
Rector

Turuhuayco 3-69 y Calle Vieja
Postal code 2074
Cuenca, Ecuador
Teléfono: (+593 7) 205 00 00
Fax: (+593 7) 408 89 58
Email: srector@ups.edu.ec

Exchange

Exchange with other periodicals is accepted.

Address:
Secretaría Técnica de Comunicación
Universidad Politécnica Salesiana
Turuhuayco 3-69 y Calle Vieja
Postal code 2074
Cuenca, Ecuador
Phone: (+593 7) 205 00 00 Ext. 1182
Fax: (+593 7) 408 89 58
Email: rpublicas@ups.edu.ec
www.ups.edu.ec
Cuenca – Ecuador

Ingenius, Journal Science of Technology,
Semester publication, N.° 20, july/december 2018
John Calle Sigüencia, Editor in chief
revistaingenius@ups.edu.ec

Printed
Centro Gráfico Salesiano: Antonio Vega Muñoz 10-68 y General Torres.
Phone: (+593 7) 283 17 45
Cuenca – Ecuador
Email: centrograficosalesiano@lns.com.ec

OTHER PUBLICATIONS OF THE UNIVERSITY

UNIVERSITAS, Revista de Ciencias Sociales y Humanas.

LA GRANJA, Revista de Ciencias de la Vida.

ALTERIDAD, Revista de Educación.

RETOS, Revista de Ciencias de la Administración y Economía.

UTOPÍA, Revista de Pastoral Juvenil Universitaria.

SOPHIA, Colección de Filosofía de la Educación.

ABYA YALA | UNIVERSIDAD POLITÉCNICA SALESIANA

SALESIANOS DON BOSCO